

PHENOMENOLOGY OF LIGHT PARTICLES ON EARTH AND IN
THE SKY

Zur Erlangung des akademischen Grades eines
DOKTORS DER NATURWISSENSCHAFTEN (Dr. rer. nat.)
von der KIT-Fakultät für Physik
des Karlsruher Instituts für Technologie (KIT)
angenommene
DISSERTATION
von
M.Sc. MATTHIAS CHRISTIAN LINSTER

Tag der mündlichen Prüfung: 16. Juli 2021
Referent: Prof. Dr. Ulrich Nierste
Korreferent: Prof. Dr. Thomas Schwetz-Mangold
Betreuende Wissenschaftler: Dr. Robert Ziegler
Dr. Wolfgang G. Hollik



This work is licensed under CC BY-SA 4.0. To view a copy of this license, visit <http://creativecommons.org/licenses/by-sa/4.0/>.

Matthias Linster: *Phenomenology of Light Particles on Earth and in the Sky*, © 28. November 2021

ABSTRACT

In this thesis, three aspects of the phenomenology of light particles in extensions of the Standard Model are discussed. First, novel bounds on the interactions of new light particles with Standard Model fermions are derived from molecular spectroscopy, which puts stringent limits on couplings of new scalar, vector and axialvector particles with keV masses. Second, several neutrino observables are predicted using a simple and well-motivated class of flavor models, yielding a narrow range for the absolute neutrino mass scale which will be probed by near-future experiments. Finally, novel limits are obtained for flavor-violating axion couplings to light quarks from the observation of the SN1987A supernova, which constrains energy losses in the form of light particles emitted from the proto-neutron star through Λ hyperon decays and bremsstrahlung.

ZUSAMMENFASSUNG

In dieser Arbeit werden drei Aspekte der Phänomenologie leichter Teilchen in Erweiterungen des Standardmodells diskutiert. Zuerst werden neuartige Grenzen an die Wechselwirkungen neuer leichter Teilchen mit Fermionen des Standardmodells aus der Molekülspektroskopie abgeleitet, was starke Schranken an die Kopplungen neuer Skalar-, Vektor- und Axialvektorteilchen mit keV-Massen setzt. Anschließend werden mehrere Neutrino-Observablen mit Hilfe einer einfachen und gut motivierten Klasse von Flavor-Modellen vorhergesagt, wodurch ein schmaler bevorzugter Bereich für die absolute Neutrino-Massenskala resultiert, der mit zukünftigen Experimenten erforscht werden kann. Schließlich werden neue Grenzen an flavor-verletzende Kopplungen von Axionen an leichte Quarks aus der Beobachtung der Supernova SN1987A bestimmt, die den Energieverlust durch leichte Teilchen, die in Λ -Hyperon-Zerfällen und -Bremsstrahlung produziert werden, beschränkt.

CONTENTS

INTRODUCTION	
1	INTRODUCTION 3
I LIGHT NEW PHYSICS ON EARTH: A STUDY OF MOLECULAR SPECTRA	
2	MOLECULAR SPECTROSCOPY 13
2.1	Theoretical Status 13
2.2	Experimental Status 21
2.3	Comparison Between Theory and Experiment 23
3	NEW PHYSICS EFFECTS ON MOLECULAR SPECTRA 25
3.1	Calculation of New Physics Effects 25
3.2	Scalar and Pseudoscalar Mediators 30
3.3	Vector and Axialvector Mediators 34
3.4	Comparison to Other Experiments 37
3.5	Estimation of Two-Particle Exchanges 38
4	CONCLUSION AND OUTLOOK 43
II NEUTRINO PHYSICS ON EARTH AND IN THE SKY: NEUTRINO MASSES FROM A $U(2)$ FLAVOR SYMMETRY	
5	A $U(2)$ MODEL OF FLAVOR 47
5.1	Motivation 47
5.2	Fermion Masses and Mixings in $U(2)$ -like Scenarios 49
5.3	Majorana Neutrinos in $U(2)$ -like Scenarios 53
6	PHENOMENOLOGY OF NEUTRINO OBSERVABLES 57
6.1	The Status of Neutrino Properties 57
6.2	Scenarios for $U(2)$ -like Symmetries 58
6.3	Description of the Statistical Analysis 63
6.4	Results 65
7	CONCLUSION AND OUTLOOK 71
III LIGHT NEW PHYSICS IN THE SKY: SUPERNOVA BOUNDS ON FLAVOR-VIOLATING COUPLINGS	
8	LIGHT PARTICLES IN SUPERNOVAE 75
8.1	Core-Collapse Supernovae 75
8.2	The Neutrino Signal as a Bound for New Physics 79
9	SN1987A CONSTRAINTS ON FLAVOR-VIOLATING COUPLINGS 83
9.1	Energy-Loss Formula for a New Particle 83
9.2	Hyperon Decays 90
9.3	Hyperon Bremsstrahlung 97
10	CONCLUSION AND OUTLOOK 107

CONCLUDING REMARKS

11 CONCLUDING REMARKS 111

APPENDIX

A MOLECULAR SPECTROSCOPY 117

- A.1 Calculation of non-Relativistic Potentials 117
- A.2 Spin Matrix Elements 121
- A.3 List of Experimental Data 124

B NEUTRINO OBSERVABLES FROM A $U(2)$ TEXTURE 127

- B.1 Relations Between Neutrino and PMNS Parameters 127

C SUPERNOVA CONSTRAINTS 131

- C.1 The Principle of Detailed Balance 131
- C.2 Lambda Production Rates from Decays 132
- C.3 Production Rates for Lambda Decays 134
- C.4 Independent Scalar Products for Bremsstrahlung 136
- C.5 Phase Space of Hyperon Bremsstrahlung 137

BIBLIOGRAPHY 141

LIST OF FIGURES

Figure 1.1	Visualization of the frontiers in particle physics.	6
Figure 2.1	Visualization of our theory uncertainty estimate.	20
Figure 2.2	Visualization of a molecular spectrum.	21
Figure 2.3	Visualization of different spectroscopy concepts.	22
Figure 3.1	Electron-nucleus scattering mediated by a scalar particle.	27
Figure 3.2	Upper limits on the scalar and pseudoscalar couplings g_{ij}^S and g_{ij}^P from molecular spectroscopy.	32
Figure 3.3	Upper limits on the vector and axialvector couplings g_{ij}^V and g_{ij}^A from molecular spectroscopy.	36
Figure 3.4	Two-neutrino exchange Feynman diagram in the full and the effective theory.	38
Figure 3.5	W box contribution to the two-neutrino exchange.	40
Figure 3.6	Two-Goldstone boson exchange Feynman diagram in the full and the effective theory.	41
Figure 6.1	Allowed parameter space in the $m_{\beta\beta}$ - $\sum_i m_i$ plane at 95.4% confidence level.	59
Figure 6.2	$m_{\beta\beta}$ - $\sum_i m_i$ parameter space at 95.4% confidence level in $U(2)$ scenarios.	67
Figure 6.3	Predictions for the Dirac CP phase δ in terms of $\sin^2(\theta_{23})$ of the PMNS matrix.	68
Figure 8.1	Temperature and composition profiles about 1 s after the core bounce of a progenitor star.	78
Figure 8.2	Simulated neutrino signal of a supernova.	79
Figure 8.3	Temperature at a radius of $R = 7.5$ km with time.	80
Figure 9.1	Visualization of the different trapping regimes.	86
Figure 9.2	Profiles of the effective mass m_i^* of protons p and neutrons n and their vector self-energies V_i in a supernova remnant.	90
Figure 9.3	Feynman diagram for the tree-level decay of a Λ hyperon.	91
Figure 9.4	Luminosities in terms of the branching ratio $\text{Br}(\Lambda \rightarrow n + X)$ of Λ hyperon decays.	95
Figure 9.5	Possible Feynman diagrams for Λ -neutron bremsstrahlung.	99
Figure 9.6	Excluded region for the effective axion scale $F_{\Lambda n}$ from Λ bremsstrahlung.	105
Figure A.1	Feynman diagram for the scalar mediator exchange.	117

LIST OF TABLES

Table 2.1	Comparison of theoretical predictions and experimental values for several hydrogen lines. 23
Table 2.2	Comparison of theoretical predictions and experimental values for several tritium lines. 24
Table 5.1	Representations of the Standard Model fields in a $U(2)$ model of flavor. 49
Table 6.1	Predictions for the neutrino parameters in the Diagonal Charged Lepton scenario. 62
Table 6.2	Summary of the input parameters of the three $U(2)$ scenarios. 64
Table 6.3	Predictions for the neutrino observables in $U(2)$ models of flavor. 66
Table 9.1	Upper limits on the branching ratio $\text{Br}(\Lambda \rightarrow n + X)$ of Λ baryon decays from the SN1987A signal. 96
Table A.1	List of all molecular lines used in the analysis of this thesis. 124

INTRODUCTION

INTRODUCTION

The fundamental constituents and interactions of Nature have always fascinated humankind—not only physicists—since they are connected to deep questions about our Universe. During more than 2000 years of exploration beginning with the ancient Greeks, vast progress has been made in our understanding of the microscopic world, uncovering more and more of the underlying structure. This journey culminated in the *Standard Model of Elementary Particle Physics* which is the best theory of fundamental interactions to date.

Despite emerging from a simple construction principle based on gauge symmetries, the Standard Model accounts for a variety of complex phenomena with unprecedented precision. However, even the best physical theory comes with a limited range of applicability and among the physicist's duties is the investigation of the borders of a theory. There are two approaches to identify the shortcomings of a model: On the one hand, one can perform experiments to compare theoretical predictions against reality. Any deviation found in this way needs to be explained by a more complete model. On the other hand, theorists can look for aspects of the model which seem unsatisfactory or try to identify patterns in the available data even if it does not contradict the predictions. While these so obtained puzzles might be red herrings without resolutions, they could also hint to new dynamics, thus providing deeper insight. Indeed, we find examples for both problems and puzzles in the Standard Model, requiring and motivating New Physics Beyond the Standard Model.

THE BAD One of the biggest shortcomings of the Standard Model is the fact that it can only account for a small fraction of about 4% of the energy density of the Universe [1]. Of the remaining 96%, about 27% are attributed to a new kind of matter called *Dark Matter*, which to date has been only indirectly observed via its gravitational interaction. The history of Dark Matter goes back to the works of Fritz Zwicky [2] in 1933 where he concluded that the motions of galaxies in the Coma cluster are not explainable by the visible matter and General Relativity alone. It took until the 1970s until this problem was widely accepted, when Vera Rubin connected a similar discrepancy in the rotation curves of stars within galaxies to Dark Matter [3].

Nowadays, there is evidence for Dark Matter at different scales, from dwarf galaxies [5] and Milky Way sized galaxies [6] to galaxy clusters [7]. Moreover, Dark Matter explains structure formation in the universe [8], whose imprints on the Cosmic Microwave Background

*See Reference [4]
for a historical
perspective on Dark
Matter.*

(CMB) were recently confirmed by the PLANCK satellite [1]. A novel form of matter provides the best explanation of these and further observations to date.

Another important shortcoming of Standard Model are neutrino masses which are not included for several reasons. First, the precise nature of neutrinos is still unclear with both Dirac and Majorana neutrinos being conceivable options. Consequently, there are many mechanisms possible to generate neutrino mass terms [9] and this ambiguity would lead to many “Standard Models” which are indistinguishable in their low-energy phenomenology accessible to experiments. In combination with the tiny value of the mass that led to effects too weak to be measured at the time of the construction of the Standard Model, it was convenient to set neutrino masses to zero.

However, the observation of neutrino oscillations at the beginning of this century [10, 11] requires at least two of the three neutrinos to be massive and thus is evidence of Beyond the Standard Model dynamics. Unfortunately, experiments could not fully reveal the nature of neutrinos until now, despite vast progress in experimental neutrino physics entering a precision era [12].

The list of problems can be further extended by established mysteries such as the unexplained baryon asymmetry of the Universe, but also by a growing list of experimental anomalies. Examples for the latter are the excess in electronic recoil events in XENON1T [13], the neutron lifetime anomaly [14, 15], the recently confirmed anomaly in the anomalous magnetic moment of the muon [16] or the reactor neutrino anomaly [17].

In this context, anomalies refer to measurements which either deviate from the theoretical prediction but not yet significantly or need to be confirmed independently.

THE UGLY One example of a puzzle in the Standard Model where a resolution is desirable is the so-called *Flavor Puzzle* [18]. It refers to the question of why there are so large hierarchies in the masses and mixing angles of quarks and masses of charged leptons, while the lepton mixing matrix features only mild hierarchies. An explanation of the large spread of at least twelve orders of magnitude between neutrino masses and the top quark mass as well as the pattern of the Cabibbo-Kobayashi-Maskawa (CKM) matrix would deepen our understanding of the world, since we would not exist if these hierarchies were absent [19].

Another intriguing puzzle of the Standard Model is the absence of CP violation in the strong interaction. CP violation is introduced in Quantum Chromodynamics (QCD) by the topological $G_{\mu\nu}^a \tilde{G}^{a,\mu\nu}$ operator with the gluonic field strength tensor $G_{\mu\nu}^a$ and its dual $\tilde{G}_{\mu\nu}^a$. On the one hand, this term parametrizes the non-trivial structure of the Quantum Chromodynamics (QCD) vacuum [20], on the other hand it is generated by axial $U(1)_A$ transformations of the quark fields due to the chiral anomaly [21, 22]. Due to the latter it seems at first sight that the parameter of the $G\tilde{G}$ operator could be shifted arbitrarily so

The gauge invariant vacua of the strong interaction are given by the Bloch states $|\vartheta\rangle$ with an angle $\vartheta \in [0, 2\pi)$ [20].

that the operator would not yield an effect in experiments. However, there exists a combination $\bar{\vartheta} = \vartheta + \arg(\det(Y_u Y_d))$ of the vacuum angle ϑ and the argument of the determinant of the quark Yukawa matrices $Y_{u,d}$ for up-type and down-type quarks, which is invariant under all transformations [20].

It is this $\bar{\vartheta}$ parameter that multiplies the CP-violating $G\tilde{G}$ term and thus yields physical CP-violating effects. The most sensitive observable to this parameter is the electric dipole moment of the neutron, yielding an upper limit of $|\bar{\vartheta}| \lesssim \mathcal{O}(10^{-11})$ [20]. The question of why this quantity is so small is referred to as the *Strong CP Puzzle*, in particular since its value has to be compared to the large $\mathcal{O}(1)$ CP-violating phase of the electroweak sector.

These are just two examples of many puzzles in the Standard Model. What all puzzles have in common is that there might not exist a mechanism explaining them. For instance, the two puzzles described above are connected to free parameters of the Standard Model which possibly could have been chosen randomly at the Big Bang so that their small values are purely due to chance. However, models tackling these puzzles are often also linked to the fundamental problems of the Standard Model like for instance Dark Matter and thus provide interesting directions for model building. Furthermore, the identification of structures might allow to infer information about currently unknown sectors, helping in the search for Beyond the Standard Model physics.

THE GOOD A plethora of ideas have been proposed as solutions of these problems and puzzles. For example, there are many suggestions explaining the deficiencies usually attributed to Dark Matter. While some explanations favor a modification of gravity [24], there are also numerous ideas within the particle framework: The mass range of proposed Dark Matter particles spans from fuzzy Dark Matter as light as 10^{-22} eV [25] to primordial black holes with masses of order of the solar mass [26]. Popular candidates are so-called *Weakly Interacting Massive Particles* (WIMPs) with masses at the electroweak scale [27], which are well motivated from the cosmological point of view due to the freeze-out mechanism [28] and occur naturally for example in supersymmetric models [29].

The negative results from direct searches for new particles at the electroweak scale in the past decade gave new impetus to models beyond Weakly Interacting Massive Particles (WIMPs)—although the latter are far from being excluded. The search for Weakly Interacting Massive Particles (WIMPs) corresponds to an exploration of the *energy frontier*, see Figure 1.1, where large energies or high masses are needed to either produce heavy states or to yield a significant effect in a detector, for example in the form of recoil energy. While this is definitely an important search path, one should explore the full parameter space for New Physics. Besides high energies, the regime of light particles

Note that $\bar{\vartheta}$ is only invariant if all quarks are massive which is nowadays established [23].

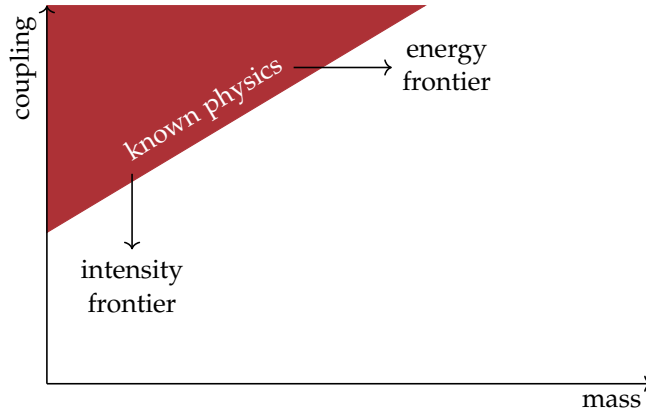


Figure 1.1: Visualization of the different frontiers. Heavy particles can be found by direct detection experiments with large energies at the energy frontier, while light particles with weak couplings need high precision at the intensity frontier.

with small couplings can be interesting in the context of the problems and puzzles of the Standard Model, where limited precision prevented experiments in the past from resolving the tiny effects of such light dynamics.

However, advances in technology allow for increasing experimental precision, making searches for these feebly coupled light states feasible. Therefore, there is nowadays rising interest to also explore this complementary part of the parameter space at the *intensity frontier*, see Figure 1.1. This is also the case since light particles with masses below 1 GeV are well motivated: Many proposed particles can account for the Dark Matter relic density—for example via the freeze-in mechanism [30]—and arise naturally in solutions of theoretical puzzles. Moreover, light particles were suggested as explanations for several experimental anomalies such as the reactor anomaly [17], the neutrino lifetime anomaly [31], the XENON1T excess [13] or the anomalous magnetic moment of the muon [32]. Another motivation is String Theory, where the compactification of extra dimensions leads to many light states as moduli fields [33].

A PROTOTYPE EXAMPLE Light particles often arise as Goldstone bosons from the spontaneous breaking of continuous global symmetries. As a prime example of a well-motivated light particle of this type, we briefly discuss the *QCD axion*, see for instance Reference [20] for a recent review.

In 1977, Helen Quinn and Roberto Peccei proposed a spontaneously broken symmetry $U(1)_{\text{PQ}}$ as a solution of the Strong CP Puzzle, where the $\bar{\theta}$ parameter is dynamically set to zero [34, 35]. Specifically, a potential is generated for the axion field—which is the Goldstone boson arising from the breaking of the $U(1)_{\text{PQ}}$ symmetry [36, 37]—from non-perturbative Quantum Chromodynamics (QCD) effects. As

a consequence, the axion field acquires a vacuum expectation value cancelling the $\bar{\vartheta}$ parameter [20]. Since the axion is a Goldstone boson, its couplings are inversely proportional to the breaking scale f_a of the Peccei-Quinn symmetry $U(1)_{PQ}$ and are thus strongly suppressed for large scales f_a . Similarly, an axion mass $m_a \sim \frac{1}{f_a}$ inversely proportional to the axion scale f_a is generated from the non-perturbative axion potential. Axions can also be linked to family symmetries [38–41], where an axion candidate arises from the spontaneous breaking of a flavor symmetry addressing the Flavor Puzzle.

Despite being very light and weakly coupled, it has soon been realized that the axion can account for the Dark Matter relic density by means of the *Misalignment Mechanism* [20]. In particular, the light axion field behaves like a classical field due to large occupation numbers. At first, the axion field has a constant value $\bar{\vartheta}_0$ due to the large Hubble friction and vanishing mass. After the Quantum Chromodynamics (QCD) phase transition, a mass is generated from the non-perturbative potential so that the axion field starts to oscillate once its mass has overcome Hubble friction. The energy stored in these oscillations behaves like cold Dark Matter in the further evolution, making the axion field a candidate for Dark Matter.

A generalization of axions is given by *axion-like particles* (ALPs) which are pseudoscalar particles whose mass is independent of the breaking scale f_a of the symmetry. While this explicit breaking of the Peccei-Quinn symmetry spoils the solution of the Strong CP Puzzle, axion-like particles could still provide an answer to several problems of the Standard Model such as Dark Matter via the Misalignment Mechanism described above.

EXPERIMENTAL SEARCHES Due to their rich phenomenology, light particles have been looked for in many experiments, see for example Reference [42] for a review. The spectrum of experiments ranges from direct laboratory experiments to indirect probes in astrophysics and cosmology.

Direct laboratory experiments have the advantage of being performed in a controlled environment, increasing the reliability of results and of uncertainty estimates. For instance, particle masses in the keV range correspond to atomic length scales so that their effects influence the energy levels of atoms and molecules probed in laboratory spectroscopy experiments. Tight bounds have been derived using atomic and molecular spectroscopy [43–48] or neutron scattering [49] on forces mediated by such particles.

Neutrino masses are looked for both in laboratory experiments and indirectly through cosmological effects [1]. For instance, a model-independent probe is given by the measurement of the tritium beta decay spectrum like in the KATRIN experiment [50, 51], while searches for neutrinoless double beta decays [52, 53] look for Majorana neu-

The small mass is a consequence of the Goldstone nature of the axion.

The equation of motion of a scalar field a reads $\ddot{a} + 3H(\dot{t})\dot{a} + m^2 a = 0$ with the decreasing Hubble constant $H(t)$ parametrizing the expanding universe. If $H^2 \ll m^2$, the friction term can be neglected, while in the opposite regime $H^2 \gg m^2$ oscillations are strongly damped.

A massive scalar mediator generates a Yukawa potential $V_Y(r) = \frac{\alpha}{r} e^{-mr}$ with coupling α , which is strongly suppressed at distances $r \gg m^{-1}$ and indistinguishable from the Coulomb potential at distances $r \ll m^{-1}$. Thus, a significant effect occurs at distances $r \sim m^{-1}$.

trinos. The most stringent bound on the sum of neutrino masses is currently derived from satellites observing the Cosmic Microwave Background (CMB) [1], where the mass determination however depends on the validity of the Λ CDM cosmological model.

Light particles with weak couplings like axions are hard to test in laboratory experiments due to the high precision needed to observe rare effects. Nevertheless, tight laboratory bounds are available [20], especially for axions with flavor-violating couplings [54]. An indirect test of such particles is provided by observations of stars where light particles can be produced in large amounts, so that the observation of stars is a prime example for a probe at the intensity frontier in Figure 1.1. In this case, the presence of light particles results in a significant energy loss which alters the dynamics of the star and yields tight limits on New Physics [55].

Many more experiments have been performed at the intensity frontier. Modifications of the gravitational potential have been studied in torsion-balance experiments [56] or by testing the Casimir force [57]. Beam dump experiments have been used to study light particles with a finite lifetime like axion-like particles (ALPs) [58, 59]. Moreover, collider experiments like Belle II [60] and even the Large Hadron Collider (LHC) [61, 62] achieve high precision due to increasing luminosity, especially in flavor observables like B meson decays. Plenty of experimental setups are testing the axion parameter space. Examples are helioscopes [63] and haloscopes [64] which are searching for axions from the Sun and Dark Matter halo, respectively. With many more approaches to be listed, present and future investigations offer a great discovery potential for these interesting types of particles.

OUTLINE OF THIS THESIS In this thesis, we discuss various aspects of the phenomenology of light particles, both in laboratory experiments and astrophysics. Specifically, we derive bounds on the parameter space of several types of light new particles using molecular spectroscopy in Part I and the SN1987A supernova signal in Part III, while we analyze the phenomenology of neutrino observables in a well-motivated framework in Part II. Each part is divided into three chapters where an overview over the current status and theoretical basics is given in the first one, followed by the detailed analysis in the second chapter. In the last one, we conclude each part and give an outlook.

In Part I, we study the effects of forces mediated by light new particles on the rotational and vibrational excitations of hydrogen-like molecules. To date, only modifications of the couplings between the two nuclei by scalar mediators have been considered in the literature so that the full potential of molecules has not yet been explored. After reviewing the Standard Model calculation and experimental status in Chapter 2, we present a systematic treatment of the effects of several

types of mediators at the keV scale in Chapter 3, considering also couplings between two electrons and between an electron and a nucleus. Finally, we conclude this part in Chapter 4.

It would be desirable if predictions for the neutrino mass scale were available so that future experiments can be constructed which are sensitive to the most interesting regions of the parameter space. One way of obtaining such predictions is the identification of patterns in the Standard Model parameters through flavor symmetries, which can be then applied to the neutrino sector [65]. We discuss predictions for neutrino observables obtained from well-motivated $U(2)$ -like flavor symmetries in Part II of this thesis. In particular, we present the structure of $U(2)$ models in Chapter 5, focussing on the lepton sector. In Chapter 6, we discuss the resulting predictions for the neutrino mass scale and CP phase, particularly taking the effects of charged leptons into account which are usually omitted in analyses based on pure texture approaches without underlying flavor symmetries. We conclude this part and given an outlook in Chapter 7.

While limits on axions and axion-like particles (ALPs) from stars have been intensively explored in the past [20], the effects of flavor-violating axions on stars have not been studied until recently [66]. In particular, the study of Λ baryons which have a sizable abundance in stars allows for a test of the strange-down coupling, with constraints surpassing laboratory bounds on the axialvector interaction by several orders of magnitude [54]. In Part III of this thesis, we derive such bounds from the observation of the SN1987A supernova. In particular, we review core-collapse supernovae and their neutrino signal which is used to derive limits on light particles in Chapter 8. In Chapter 9, we determine the energy loss due to the emission of axions from decays of Λ baryons and give an outlook on bounds for axion-like particles (ALPs) from Λ bremsstrahlung. We conclude this part in Chapter 10. Finally, we summarize this thesis in Chapter 11.

Part I

LIGHT NEW PHYSICS ON EARTH: A STUDY OF
MOLECULAR SPECTRA

MOLECULAR SPECTROSCOPY

In the search for new light particles, molecules provide suitable study objects [67–69]. A new light mediator particle would modify the Coulomb potential responsible for molecular binding. As a consequence, molecular energy levels and transition energies will change which could possibly be observed in precision spectroscopy experiments.

Although such determinations of transition frequencies are challenging on both experimental and theory side, there are precise state-of-the-art predictions and measurements available. In this chapter, we review the theoretical and experimental status in Sections 2.1 and 2.2, respectively. Finally, we briefly compare both predictions and corresponding measurements in Section 2.3.

This chapter is based on the publication

Wolfgang Gregor Hollik, Matthias Linster, and Mustafa Tabet. “A Study of New Physics Searches with Tritium and Similar Molecules.” *Eur. Phys. J. C* 80.7 (2020), p. 661. DOI: [10.1140/epjc/s10052-020-8215-0](https://doi.org/10.1140/epjc/s10052-020-8215-0). arXiv: [2004.11274](https://arxiv.org/abs/2004.11274) [hep-ph] .

2.1 THEORETICAL STATUS

As hydrogen-like molecules are four-particle systems, the precise calculation of their energy levels is a difficult task even in the approximation of only a Coulomb interaction in a non-relativistic setup. The Hamilton operator of such a molecule of two heavy nuclei N_1 and N_2 with $N_i = \text{H, D, T}$ surrounded by two light electrons e_1^- and e_2^- can be split into an electronic and a nuclear part [71],

$$\hat{H} = \hat{H}_{\text{el}} + \hat{H}_{\text{N}}. \quad (2.1)$$

In this separation, the electronic part \hat{H}_{el} describes the motion of the electrons in the Coulomb field of nuclei at positions \mathbf{R}_A and \mathbf{R}_B in terms of the center-of-mass coordinates of the nuclei. Denoting the electrons by numeric labels $i = 1, 2$ and the nuclei by the letters $\lambda = A, B$, the electronic Hamiltonian \hat{H}_{el} reads [71]

$$\hat{H}_{\text{el}} = \frac{\mathbf{P}_1^2}{2m_e} + \frac{\mathbf{P}_2^2}{2m_e} + \alpha_{\text{em}} \left\{ \frac{1}{r_{12}} + \frac{1}{R} - \left(\frac{1}{r_{1A}} + \frac{1}{r_{2B}} + \frac{1}{r_{1B}} + \frac{1}{r_{2A}} \right) \right\}, \quad (2.2)$$

Hydrogen-like molecules are bound states of two hydrogen isotopes, that is of either hydrogen (H), deuterium (D) or tritium (T).

Given electronic positions \mathbf{r}_1 and \mathbf{r}_2 we have $r_{12} = |\mathbf{r}_1 - \mathbf{r}_2|$, $r_{i\lambda} = |\mathbf{r}_i - \mathbf{R}_\lambda|$ and $R = |\mathbf{R}_A - \mathbf{R}_B|$.

where $\alpha_{\text{em}} \simeq \frac{1}{137}$ is the electromagnetic fine structure constant, m_e is the electron mass and $\mathbf{P}_{1,2}$ are the momentum operators of the electrons. Moreover, r_{12} , $r_{i\lambda}$, and R are the distances between the two electrons, between electron i and nucleus λ , and between the two nuclei, respectively. The nuclear Hamiltonian \hat{H}_N includes the remaining kinetic energy of the nuclei as well as a kinetic coupling between the electrons and nuclei [71],

$$\hat{H}_N = -\frac{1}{2\mu_N} (\nabla_R^2 + \nabla_{\text{el}}^2) + \left(\frac{1}{M_A} - \frac{1}{M_B} \right)^2 \nabla_R \cdot \nabla_{\text{el}} \quad (2.3)$$

with $\nabla_{\text{el}} = \frac{1}{2} (\nabla_1 + \nabla_2)$, the reduced mass $\mu_N = \frac{M_A M_B}{M_A + M_B}$ of the nuclei and the gradients $\nabla_{R,1,2}$ with respect to the nuclear relative coordinate $\mathbf{R} = \mathbf{R}_A - \mathbf{R}_B$, and the electronic positions $\mathbf{r}_{1,2}$, respectively.

Over the course of the last hundred years, many physicists attempted to obtain the molecular energy spectrum of the Hamilton operator (2.1). Before briefly reviewing milestones in the precise determination of the energy levels, we present estimates of the sizes of the expected effects.

ESTIMATES OF THE EFFECTS Compared to atomic spectra, their molecular counterparts have a richer structure due to the second nucleus allowing for vibrational and rotational excitations. Spectral lines corresponding to electronic, vibrational and rotational transitions are well separated in their size with the former being the largest and the latter being the smallest effect. One can understand the hierarchy between rotational and vibrational transitions as follows:

The inter-nuclear force causing vibrations around the equilibrium distance R^* of the two nuclei can be modeled by a Morse potential [72],

$$V_{\text{Morse}}(R) = D_e \left(1 - e^{-\frac{R-R^*}{w}} \right)^2, \quad (2.4)$$

where D_e is the depth and w is the width of the potential. Estimating the depth D_e of the well to be similar to the lowest energy state $E^{(0,0)} \simeq 36\,000 \text{ cm}^{-1}$ [71] and the well width w to be of order of the equilibrium distance R^* , that is $D_e \sim E_{(0,0)}$ and $w \sim R^*$, we find

$$\Delta E_{\Delta v=1} \sim \hbar \sqrt{\frac{2E_{(0,0)}}{M_N (R^*)^2}} \sim 3000 \text{ cm}^{-1} \quad (2.5)$$

for the transition energy $\Delta E_{\Delta v=1} = \hbar\omega$ between two neighboring vibrational levels.

Similarly, one can estimate the rotational energy difference by using the centrifugal potential

$$V_J(R) \sim \frac{J(J+1)}{2M_N R^2}. \quad (2.6)$$

Note that $1 \text{ eV} \simeq 8065.544\,45 \text{ cm}^{-1}$ and thus $E^{(0,0)} \simeq 4.5 \text{ eV}$. The dissociation energy refers to the separation of the molecule into two hydrogen atoms.

yielding the scale of rotational transition energies ΔE_{rot}

$$\Delta E_{\text{rot}} \sim 400 \text{ cm}^{-1}. \quad (2.7)$$

In conclusion, the electronic levels in a molecule which are also present in atoms separate into bands, making molecular spectroscopy more sensitive to phenomena at smaller energy scales compared to atomic spectroscopy. Moreover, vibrational transitions can be probed with higher statistics by measuring the same vibrational transition for different values of the angular momentum J , which is especially advantageous for rotationally invariant quantities.

EARLY ATTEMPTS OF A SOLUTION The first attempts to find the eigenvalues of the Hamiltonian (2.1) date back to the late 1920s. Heitler and London assumed fixed positions for the nuclei to find the electronic ground state of the electronic Hamilton operator (2.2) [73]. They applied perturbation theory to the symmetrized state where each of the two electrons forms a hydrogen atom with one of the nuclei. In this approach, they regard the inter-nuclear force as a small perturbation, which is a poor approximation for hydrogen due to the small binding lengths [74].

Such a state is expected to be a good approximation for largely separated nuclei.

In the same year, Born and Oppenheimer determined the effect of nuclear motion by performing a series expansion in the small ratio $\sqrt[4]{\frac{m_e}{M_N}}$ [75]. This assumption of heavy and therefore slowly moving nuclei is usually referred to as the *adiabatic approximation*. They found that the effects of nuclear vibrations and rotations occur at different orders in their expansion, with vibrations being a second-order and rotations being a fourth-order effect. Hence, there is a clear hierarchy between the effects of the electronic energy level and the vibrational and rotational state of the nuclei, with the former yielding the largest separation and the latter the smallest.

See also our estimates for the separation in the preceding paragraph.

In 1933, James and Coolidge improved the determination of the electronic wave functions and energy levels using a variational approach [74]. Choosing a suitable test wave function ψ_u with parameter u , one calculates the expectation value of the Hamiltonian (2.2), which is always larger than or equal to the ground state energy E_0 ,

$$\langle \hat{H}_{\text{el}} \rangle_u = \langle \psi_u | \hat{H}_{\text{el}} | \psi_u \rangle \geq E_0. \quad (2.8)$$

Consequently, an estimate of the ground state energy can be obtained by minimizing the expectation value $\langle \hat{H}_{\text{el}} \rangle_u$ with respect to the variational parameter u , that is

$$E_0 \simeq \min_{u \in \mathbb{R}} \langle \hat{H}_{\text{el}} \rangle_u. \quad (2.9)$$

In particular, James and Coolidge proposed to expand the test wave function ψ_u for hydrogen-like molecules in a set of basis functions $\psi_{n_0, n_1, n_2, n_3, n_4}^0$ [74],

$$\psi_u(\mathbf{r}_1, \mathbf{r}_2; \mathbf{R}_A, \mathbf{R}_B) = \hat{S} \sum_{n_0, \dots, n_4} C_{n_0, \dots, n_4} \psi_{n_0, \dots, n_4}^0(\mathbf{r}_1, \mathbf{r}_2, \mathbf{R}_A, \mathbf{R}_B; u), \quad (2.10)$$

where the non-negative integers $n_i = 0, 1, \dots$ for $i = 0, 1, \dots, 4$ characterize the basis function and the $C_{n_0, n_1, n_2, n_3, n_4}$ are series coefficients. The operator \hat{S} ensures the correct symmetry of the wave function to comply with the Pauli principle.

In their work, James and Coolidge used the basis comprising the functions [74]

$$\begin{aligned} \psi_{n_0, n_1, n_2, n_3, n_4}^0(\mathbf{r}_1, \mathbf{r}_2, \mathbf{R}_A, \mathbf{R}_B; u) &= R^{-3-\sum_i n_i} e^{-u(r_{1A}+r_{1B}+r_{2A}+r_{2B})} \\ &\times r_{12}^{n_0} (r_{1A} - r_{1B})^{n_1} (r_{2A} - r_{2B})^{n_2} (r_{1A} + r_{1B})^{n_3} (r_{2A} + r_{2B})^{n_4}, \end{aligned} \quad (2.11)$$

which is usually referred to as the *symmetric James-Coolidge basis*. On the one hand, this choice reflects the long-distance behavior of a decaying exponential probability as seen in hydrogen atoms and on the other hand the elliptical symmetry of hydrogen-like molecules. The latter is apparent if one expresses the basis functions $\psi_{n_0, \dots}^0$ in terms of elliptical coordinates,

Recall that the wave function should separate into two hydrogen atoms for large nuclear distances R .

$$\tilde{\zeta}_i = \frac{1}{R}(r_{iA} + r_{iB}), \quad \eta_i = \frac{1}{R}(r_{iA} - r_{iB}), \quad \phi_i = \arctan\left(\frac{[\mathbf{r}_i]_y}{[\mathbf{r}_i]_x}\right) \quad (2.12)$$

for electron $i = 1, 2$. Here, the positions of the nuclei are the focal points of the ellipsis which are assumed to lie on the z -axis and ϕ_i represents the azimuthal angle in the plane orthogonal to the nuclear axis.

Once a finite set of basis functions has been chosen, one first determines the coefficients C_{n_0, \dots, n_4} such that the Schrödinger equation of the electronic Hamiltonian (2.2) is fulfilled. Next, the energy expectation value is calculated and minimized with respect to the variational parameter u . This leads to a prediction for the ground state energy, which can be further improved by adding more basis functions.

Another major improvement in the accuracy of the prediction of the ground state energy of molecular hydrogen was achieved by Kołos and Wolniewicz in the 1960s, see for example References [76–80]. Extending the previous works by Born and Oppenheimer and by James and Coolidge, they were not only able to evaluate the integrals to higher precision, but also added non-adiabatic and relativistic corrections to their prediction. As a result, they achieved 5-digit precision matching the experimental uncertainties at that time [80].

Note that their evaluation was in tension with data at that time [80].

Nowadays, the calculation of energy levels and the electronic wave function is automatized in the program H2solv [81], which allows to predict the ground state energy of molecular hydrogen and its isotopologues to a precision limited only by computing power. In particular, the authors of H2solv have demonstrated the possible accuracy with their code by determining the hydrogen ground state energy to a precision of 18 digits employing a basis of about 60 000 functions [81].

Hydrogen isotopologues are the possible molecules that can be formed from hydrogen isotopes as nuclei.

MODERN NON-ADIABATIC PERTURBATION THEORY In the last 20 years, vast progress has been made by Pachucki and collaborators [82–91] with the development of the so-called *Non-adiabatic Perturbation Theory*, see References [71, 92] for reviews. Their approach allows for a clear separation of all non-adiabatic effects and their systematic inclusion in the theory prediction.

The starting point is the assumption that the leading term of the full wave function of a hydrogen-like molecule separates into an electronic and nuclear part as in the adiabatic approximation [71],

$$\Psi(\mathbf{r}_1, \mathbf{r}_2, \mathbf{R}_A, \mathbf{R}_B) \approx \varphi_{\text{el}}(\mathbf{r}_1, \mathbf{r}_2; \mathbf{R}) \chi_{\text{N}}(\mathbf{R}). \quad (2.13)$$

Here, φ_{el} denotes the electronic wave function solving the Schrödinger equation of the electronic Hamiltonian (2.2) with fixed distance R between the nuclei,

$$(\hat{H}_{\text{el}} - \mathcal{E}(R)) \varphi_{\text{el}} = 0, \quad (2.14)$$

while χ_{N} is the nuclear wave function determined below.

In Non-adiabatic Perturbation Theory, the effect of non-stationary nuclei on the electrons is added to the wave function as a small perturbation $\delta\Psi_{\text{na}}$ [71],

$$\Psi(\mathbf{r}_1, \mathbf{r}_2, \mathbf{R}) = \varphi_{\text{el}}(\mathbf{r}_1, \mathbf{r}_2; \mathbf{R}) \chi_{\text{N}}(\mathbf{R}) + \delta\Psi_{\text{na}}(\mathbf{r}_1, \mathbf{r}_2, \mathbf{R}), \quad (2.15)$$

fulfilling the orthogonality condition $\langle \delta\Psi_{\text{na}} | \varphi_{\text{el}} \rangle_{\text{el}}$ on the electronic subspace. Splitting off the electronic Schrödinger equation $\hat{H}_{\text{el}} - \mathcal{E}(R)$ from the remaining problem, one can formally solve the Schrödinger equation of the full Hamiltonian (2.1) for the non-adiabatic correction $\delta\Psi_{\text{na}}$ as [71]

Here and in the following, $\langle \cdot | \cdot \rangle_{\text{el}}$ means the integration over electronic coordinates only in the scalar product.

$$0 = (\hat{H}_{\text{el}} + \hat{H}_{\text{N}} - E) \Psi \quad (2.16)$$

$$= ((\hat{H}_{\text{el}} - \mathcal{E}) + (\mathcal{E} + \hat{H}_{\text{N}} - E)) (\varphi_{\text{el}} \chi_{\text{N}} + \delta\Psi_{\text{na}}) \quad (2.17)$$

$$\Rightarrow \delta\Psi_{\text{na}} = \frac{1}{(\hat{H}_{\text{el}} - \mathcal{E})'} (\hat{H}_{\text{N}} \varphi_{\text{el}} \chi_{\text{N}} + (\mathcal{E} + \hat{H}_{\text{N}} - E) \delta\Psi_{\text{na}}), \quad (2.18)$$

where $\frac{1}{(\hat{H}_{\text{el}} - \mathcal{E})'} \varphi_{\text{el}} = 0$.

Integrating the Schrödinger equation (2.17) over the electronic coordinates and iteratively plugging in the formal solution (2.18) for $\delta\Psi_{\text{na}}$, one obtains a differential equation for the nuclear wave function reading [71]

$$\left(-\frac{\nabla_R^2}{2\mu_N} + \mathcal{E}(R) + \mathcal{E}^{(2,1)}(R) + \dots - E \right) \chi_N = 0. \quad (2.19)$$

In this formula, the dots symbolize higher-order terms in the non-adiabatic expansion and we defined the first non-adiabatic correction $\mathcal{E}^{(2,1)}(R)$ as

$$\mathcal{E}^{(2,1)}(R) = \langle \varphi_{\text{el}} | \hat{H}_N | \varphi_{\text{el}} \rangle_{\text{el}}. \quad (2.20)$$

In the shown approximation, the nuclear Schrödinger equation (2.19) is the Schrödinger equation of a particle in three dimensions in a radially symmetric potential

$$U(R) = \mathcal{E}(R) + \mathcal{E}^{(2,1)}(R). \quad (2.21)$$

This implies that the angular part of the nuclear wave functions is given by the spherical harmonics Y_J^m ,

$$\chi_N(\mathbf{R}) = \chi_{v,J}(\mathbf{R}) = \frac{u_v(R)}{R} Y_J^m(\vartheta, \varphi), \quad (2.22)$$

so that the molecular levels can be characterized by their angular momentum quantum numbers J and m . Furthermore, the radial motion of the two nuclei is an anharmonic oscillation around the minimum R^* of the potential $U(R)$, where R^* corresponds to the equilibrium nuclear distance. Thus, the radial part $u_v(R)$ is characterized by a quantum number v corresponding to the excitation of the oscillator. The expansion parameter of Non-adiabatic Perturbation Theory is given by the ratio of the electron mass m_e to the reduced nuclear mass μ_N . In order to obtain an order-by-order expansion in this ratio $\frac{m_e}{\mu_N}$, it is convenient to regard the correction $\mathcal{E}^{(2,1)}$ to the inter-nuclear potential $U(R)$ as a perturbation instead of solving the Schrödinger equation (2.19) exactly. Applying first-order perturbation theory, this in turn leads to the non-adiabatic contribution [71]

$$E^{(2,1)} = \langle \chi_{v,J} | \mathcal{E}^{(2,1)}(R) | \chi_{v,J} \rangle = \langle \chi_{v,J} | \langle \varphi_{\text{el}} | \hat{H}_N | \varphi_{\text{el}} \rangle_{\text{el}} | \chi_{v,J} \rangle \quad (2.23)$$

to the leading-order energy $E^{(2,0)}$ which is determined by the solution of the Schrödinger equation (2.19) without $\mathcal{E}^{(2,1)}$ and higher non-adiabatic terms.

Recall that $\langle \cdot | \cdot \rangle_{\text{el}}$ denotes the integration over electronic coordinates only. Due to rotational symmetry, the correction only depends on the magnitude R of the nuclear distance vector.

In the case of a hydrogen molecule H_2 , $R^* \simeq 1.4a_B$ with the Bohr radius a_B .

In the same manner, one can add relativistic, Quantum Electrodynamics (QED) and further non-adiabatic corrections to the energy eigenvalues. For instance, the leading relativistic correction is determined by the Breit-Pauli Hamiltonian $\hat{H}^{(4)}$, as for example given in Reference [89]. Retaining the Born-Oppenheimer wave function as the leading term as in Equation (2.15), we can add a relativistic correction $\delta\Psi_{\text{rel}}$ to the wave function (2.15) and formally replace \hat{H}_{N} by $\hat{H}_{\text{N}} + \hat{H}^{(4)}$ in all equations above to find the relativistic correction as [71]

$$E^{(4,0)} = \langle \chi_{v,J} | (\langle \varphi_{\text{el}} | \hat{H}^{(4,0)} | \varphi_{\text{el}} \rangle_{\text{el}}) | \chi_{v,J} \rangle. \quad (2.24)$$

In contrast to non-adiabatic corrections, relativistic and Quantum Electrodynamics (QED) terms will enter the energy eigenvalue with higher powers of the electromagnetic fine structure constant α_{em} instead of the ratio $\frac{m_{\text{e}}}{\mu_{\text{N}}}$.

As a result, we obtain a two-stage expansion of the total energy of hydrogen-like molecules first in powers of the electromagnetic finestructure constant α_{em} and next in the mass ratio $\frac{m_{\text{e}}}{\mu_{\text{N}}}$ [71],

$$E = \alpha_{\text{em}}^2 \left[E^{(2,0)} + \frac{m_{\text{e}}}{\mu_{\text{N}}} E^{(2,1)} + \left(\frac{m_{\text{e}}}{\mu_{\text{N}}} \right)^2 E^{(2,2)} + \dots \right] \\ + \alpha_{\text{em}}^4 \left[E^{(4,0)} + \frac{m_{\text{e}}}{\mu_{\text{N}}} E^{(4,1)} + \dots \right] + \alpha_{\text{em}}^5 E^{(5,0)} + \alpha_{\text{em}}^6 E^{(6,0)} + \dots \quad (2.25)$$

Here, the expansion parameters α_{em} and $\frac{m_{\text{e}}}{\mu_{\text{N}}}$ have been split off the terms $E^{(i,j)}$. All terms displayed are fully known, while there exists also a partial determination of the leading $\mathcal{O}(\alpha_{\text{em}}^7)$ contribution in the literature [86–91, 93, 94]. Moreover, the correction due to the finite size of the nuclei at $\mathcal{O}(\alpha_{\text{em}}^4)$ is also known [71] but not displayed here.

All corrections are implemented in the computer code `H2spectre` [92, 95], allowing to compute the energy levels of hydrogen-like molecules to state-of-the-art precision. Moreover, `H2spectre` also internally determines the nuclear wave function $\chi_{v,J}(\mathbf{R})$ as obtained from the nuclear Schrödinger equation (2.19). Extracting the internal nuclear wave function $\chi_{v,J}(R)$ from `H2spectre` and combining it with the Born-Oppenheimer wave function φ_{el} from `H2solv` [81] as described above, these codes give access to the full unperturbed wave function (2.13).

RESULTS The relative precision of the energy levels of hydrogen-like molecules achieved with `H2spectre` is of $\mathcal{O}(10^{-8})$. Running the code for example for the rovibrational ground state with $v = J = 0$, this level is predicted to have an energy $E_{(0,0)}$ of

$$E_{(0,0)} = 36\,118.069\,52(24) \text{ cm}^{-1}. \quad (2.26)$$

In particular, the leading relativistic correction will be of $\mathcal{O}(\alpha_{\text{em}}^4)$.

The H2spectre code had to be modified since it does not allow for an extraction of the nuclear wave function $\chi_{v,J}(R)$ by default.

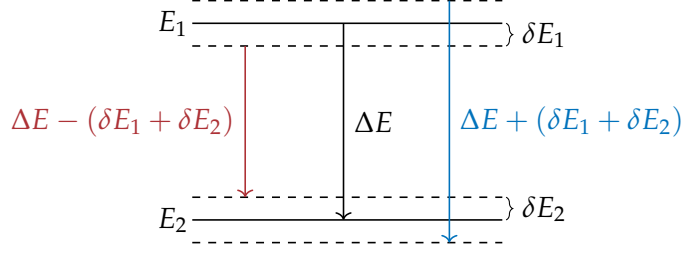


Figure 2.1: Visualization of our theory uncertainty estimate. Given two energy levels $E_{1,2}$ with theory uncertainties $\delta E_{1,2}$, the real energies of these levels are contained in the intervals $[E_i - \delta E_i, E_i + \delta E_i]$ for $i = 1, 2$. As a result, the smallest possible transition energy is given by $\Delta E - (\delta E_1 + \delta E_2)$ with $\Delta E = E_1 - E_2$, while $\Delta E + (\delta E_1 + \delta E_2)$ yields the largest possible energy difference. This motivates that the real transition energy is contained in the interval $[\Delta E - \delta \Delta E, \Delta E + \delta \Delta E]$ and that the theory uncertainty $\delta \Delta E$ of the transition is given by the sum of the two level uncertainties $\delta \Delta E = \delta E_1 + \delta E_2$.

given in units of inverse wave lengths.

Currently, the dominant uncertainty arises from the yet unknown non-adiabatic correction to the Quantum Electrodynamics (QED) effects at $\mathcal{O}(\alpha_{\text{em}}^5)$ according to the uncertainty budget displayed by H2spectre. This effect is difficult to compute due to the Bethe logarithm appearing in the Hamiltonian [71, 92]. All other terms exhibit a relative uncertainty of at most $\mathcal{O}(10^{-9})$. In particular, this holds for the effect of the finite nucleus size which depends on the imprecisely measured nuclear radii [71].

In our work, we employ a more conservative estimate of the theoretical uncertainty for transitions between two different levels than the authors of H2spectre. Since theory uncertainties should reflect the interval in which the real value is located, one must not treat them as statistical quantities. Thus, we linearly add the theory errors, that is given a transition between two levels E_1 and E_2 with uncertainties δE_1 and δE_2 , respectively, we estimate the uncertainty in the transition energy $\Delta E = E_2 - E_1$ as

$$\delta \Delta E = \delta E_1 + \delta E_2, \quad (2.27)$$

see Figure 2.1.

We find theoretical predictions of $\mathcal{O}(4000 \text{ cm}^{-1})$ and $\mathcal{O}(100 \text{ cm}^{-1})$ for vibrational and rotational transitions, respectively, see also Table 2.1. Both values match their corresponding estimates in Equations (2.5) and (2.7). Hence, the full calculation confirms the expectation that each of the electronic levels splits into vibrational levels which themselves contain several rotational levels, see Figure 2.2.

The Bethe logarithm is given by $\frac{\langle \varphi_{\text{el}} | \vec{j} \hat{H}' \ln(2\hat{H}') \vec{j} | \varphi_{\text{el}} \rangle_{\text{el}}}{\langle \varphi_{\text{el}} | \vec{j} \hat{H}' \vec{j} | \varphi_{\text{el}} \rangle_{\text{el}}}$, where $\hat{H}' = \hat{H}_{\text{el}} - \mathcal{E}$ and $\vec{j} = -\frac{\vec{p}_1 + \vec{p}_2}{m_e}$ [71].

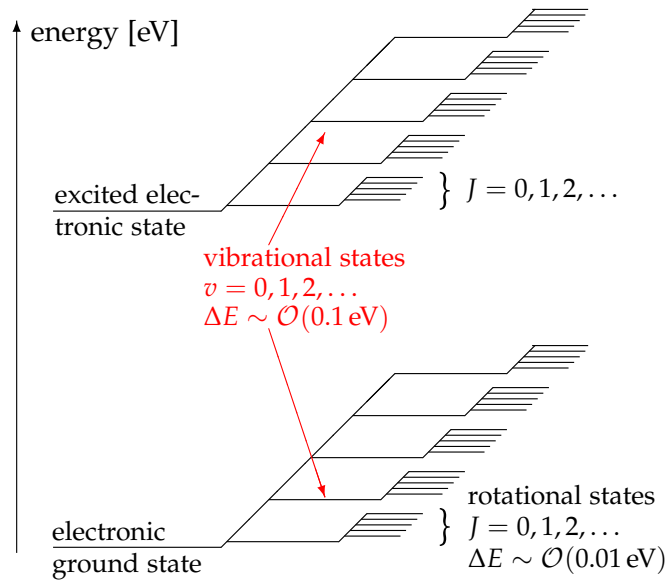


Figure 2.2: Visualization of a molecular spectrum. Each electronic level splits into several vibrational levels, which themselves contain rotational levels. The energy of a purely vibrational transition is of $\mathcal{O}(0.1 \text{ eV})$, while rotational transitions are of $\mathcal{O}(0.01 \text{ eV})$ and thus smaller by about an order of magnitude. The image is adapted from Reference [96].

2.2 EXPERIMENTAL STATUS

Over the course of the century, experimental techniques measuring transition frequencies of molecular hydrogen and its isotopologues have greatly improved and achieved a relative precision of up to $\mathcal{O}(10^{-10})$, see for instance References [97–99]. Experimental measurements of a certain vibrational transition are usually classified by the associated change in the angular momentum quantum number ΔJ with Q , R and S branches referring to $\Delta J = 0, 1, 2$, respectively. Different methods are used since there is no single technique suited for precise measurements of all isotopologues.

DOPPLER-FREE LASER SPECTROSCOPY One problem of precision spectroscopy is the Doppler shift broadening of the spectral lines due to the thermal motion of the gas molecules. To overcome this limitation, *Doppler-free Laser Spectroscopy* was invented in the 1970s, see Reference [100] for a review. If the target molecule is moving at a velocity \mathbf{v} with respect to the laboratory frame, the photon with frequency ω is absorbed with a Doppler-shifted frequency $\omega'_1 = \omega - \mathbf{k} \cdot \mathbf{v}$, where $\vec{\mathbf{k}}$ is the wave vector of the photon in the laboratory frame. To get rid of the unknown velocity-dependent term $-\mathbf{k} \cdot \mathbf{v}$, one can add a second counterpropagating photon to the first one with the inverse wave vector $-\mathbf{k}$ and hence a frequency $\omega'_2 = \omega + \mathbf{k} \cdot \mathbf{v}$ in the rest frame of the molecule, see Figure 2.3a. Once a molecule absorbs these two photons, the resonance condition for a transition with energy ΔE becomes

For example, some techniques need large probe volumes which are not realizable for the instable tritium due to the need of transportation to the spectroscopy laboratory.

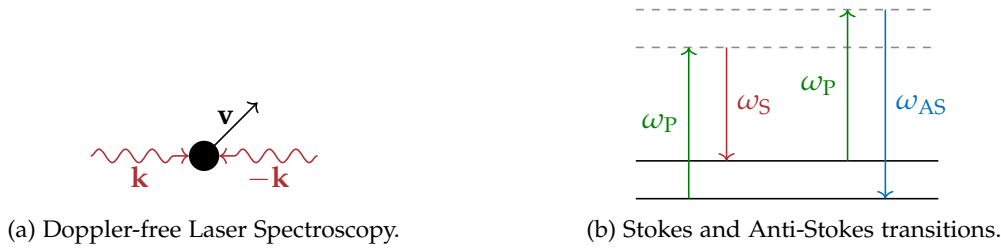


Figure 2.3: Visualization of different spectroscopy concepts. Left: Doppler-free Laser Spectroscopy uses two counterpropagating photons (red) with wave vectors $\pm\mathbf{k}$ to cancel the Doppler shift of the molecule (black dot) moving with velocity \mathbf{v} in the laboratory frame. Right: In Raman Spectroscopy, a pump laser with frequency ω_P excites the ground state (lower solid line) to a virtual level (dashed line), which decays to an excited level (upper solid line) emitting a Stokes photon with frequency ω_S . If the excited level absorbs another pump photon, the so-obtained virtual state can decay back to the ground state by emitting the anti-Stokes photon with frequency ω_{AS} , which is observed in Coherent Anti-Stokes Raman Spectroscopy.

$$\Delta E = \hbar\omega'_1 + \hbar\omega'_2 = \hbar(\omega - \mathbf{k} \cdot \mathbf{v}) + \hbar(\omega + \mathbf{k} \cdot \mathbf{v}) = 2\hbar\omega \quad (2.28)$$

and thus does not exhibit a Doppler shift.

In the case of hydrogen-like molecules, Doppler-free laser spectroscopy has been applied to experimentally determine several energy levels and transition energies of H_2 , D_2 and HD [97–99]. A high relative precision of $\mathcal{O}(10^{-10})$ was achieved with this method.

STIMULATED RAMAN SPECTROSCOPY *Raman Spectroscopy* is another important technique and is described in Reference [101] and references therein. Here, the molecule of interest in its ground state is illuminated by a pump laser of a certain frequency ω_P , exciting the molecule to some virtual state. From this virtual state, the molecule decays back to one of the real atomic levels. If this target level is one of the higher excitations, the photon emitted in this process has a smaller frequency $\omega_S < \omega_P$ than the incident photon and the molecule remains in an excited state after this process, see Figure 2.3b. Measuring this so-called *Stokes photon*, one obtains the transition energy between the ground state and the final state of the molecule as the difference $\Delta\omega = \omega_P - \omega_S$ in the frequencies of the two photons.

If one also provides the Stokes photon externally by a second laser beam, the emission rate of Stokes photons can be resonantly enhanced, leading to a clearer experimental signal. This observation is exploited in *Stimulated Raman Spectroscopy* [101], where one varies the frequency of a second laser beam until a resonantly enhanced Stokes signal is seen. In this case, the second laser beam is at the same frequency as the Stokes photon allowing for precise measurements of transition energies.

Table 2.1: Measurement of several $(v_2, J_2) \rightarrow (v_1, J_1)$ transition energies ΔE_{exp} for molecular hydrogen H_2 and theoretical predictions ΔE_{theo} for these transitions as obtained from H2spectre [92, 95]. The theoretical uncertainty has been estimated according to Equation (2.27). The experimental values are taken from Reference [98].

transition	ΔE_{theo} [cm^{-1}]	ΔE_{exp} [cm^{-1}]
$(1, 0) \rightarrow (0, 0)$	4161.166 12(45)	4161.166 35(15)
$(1, 1) \rightarrow (0, 1)$	4155.253 76(44)	4155.254 00(21)
$(1, 2) \rightarrow (0, 2)$	4143.465 29(44)	4143.465 53(15)

The application of Stimulated Raman Spectroscopy allowed to record the energies of several lines in hydrogen isotopologues with a relative precision of $\mathcal{O}(10^{-6})$ [101].

COHERENT ANTI-STOKES RAMAN SPECTROSCOPY An improvement of Stimulated Raman Spectroscopy is given by the technique of *Coherent Anti-Stokes Raman Spectroscopy* [102]. Here instead, the anti-Stokes line having a larger energy than the pumping frequency ω_p is observed. This line occurs if the final state of the molecule after a Raman transition is excited again to another virtual level by the pump laser and decays back to the ground state afterwards, see Figure 2.3b. Again, a resonant enhancement is observed when the Stokes laser is set to a frequency matching the transition energy of the ground state to some higher excited level of the molecule.

Since the anti-Stokes photon has a higher energy than the incoming pump photon, it is not polluted by fluorescence like the Stokes photon. Hence, the anti-Stokes line is observed in a region with lower background, allowing for a cleaner measurement despite the transition being less likely as a higher-order effect. Moreover, faster signal collection and the possibility of smaller probe volumes make Coherent Anti-Stokes Raman Spectroscopy advantageous if one deals with unstable molecules like T_2 . Indeed, the world’s best spectra of molecular tritium T_2 , DT, and HT were recorded using these techniques [102–105]. In all cases, a relative precision of $\mathcal{O}(10^{-7})$ was achieved.

2.3 COMPARISON BETWEEN THEORY AND EXPERIMENT

Theoretical prediction and experimental measurements agree very well for most isotopologues. For instance, energies for several $v = 1 \rightarrow v = 0$ transitions in molecular hydrogen H_2 agree within one standard deviation, see Table 2.1.

There is, however, a discrepancy between data and prediction in the tritium dataset at the level of 2–3 standard deviations depending on the error estimation, see Table 2.2. An explanation of this tension in terms of a New Physics particle is challenging since the measurements

Table 2.2: Measurement of several transition energies ΔE_{exp} for molecular tritium T_2 for the $Q(J)$ band and theoretical predictions ΔE_{theo} for these transitions as obtained from H2spectre [92, 95]. The theoretical error estimate is calculated according to Equation (2.27). The experimental values are taken from Reference [103].

transition	ΔE_{exp} [cm^{-1}]	ΔE_{theo} [cm^{-1}]	difference [cm^{-1}]
Q(0)	2464.5052(4)	2464.5042(3)	0.0010
Q(1)	2463.3494(3)	2463.3484(3)	0.0010
Q(2)	2461.0388(3)	2461.0392(3)	-0.0004
Q(3)	2457.5803(4)	2457.5814(3)	-0.0011
Q(4)	2452.9817(4)	2452.9821(3)	-0.0004
Q(5)	2447.2510(4)	2447.2509(3)	0.0001

show an angular momentum dependence of the discrepancy, while a New Physics contribution is usually rotationally invariant. In particular, different transitions in the Q band yield different signs in the deviations between theory and experiment.

As a consequence, a resolution of this tension either by further experimental scrutiny or by improvements of the Standard Model prediction is more likely. Indeed, new measurements in a recent study with an improved setup show agreement with the Standard Model result [105]. While there is no direct hint for Beyond the Standard Model physics in data, one can nevertheless infer limits on the New Physics parameter space which complement independent measurements of the same quantities. We study the New Physics potential of molecular spectroscopy in the next chapter.

NEW PHYSICS EFFECTS ON MOLECULAR SPECTRA

A massive new mediator particle would lead to modifications of the Coulomb potential on length scales of the inverse mediator mass. In particular, if the bond length of a molecule is of $\mathcal{O}(1 \text{ \AA})$, this means that molecular spectra are sensitive to new particles with masses in the keV range. The effect of such particles in the non-relativistic world of molecules can be modeled by effective potentials that are added to the Hamilton operator.

We explain the perturbative treatment of New Physics effects on molecular spectra in Section 3.1 before we turn to discuss scalar and pseudoscalar mediators in Section 3.2 as well as vector and axialvector mediators in Section 3.3. In Section 3.4, we compare our bounds to those available in the literature. Finally, we comment on the feasibility of studying two-particle exchanges with molecules in Section 3.5.

This chapter is a revised version of the publication

Wolfgang Gregor Hollik, Matthias Linster, and Mustafa Tabet. “A Study of New Physics Searches with Tritium and Similar Molecules.” *Eur. Phys. J. C* 80.7 (2020), p. 661. DOI: [10.1140/epjc/s10052-020-8215-0](https://doi.org/10.1140/epjc/s10052-020-8215-0). arXiv: [2004.11274](https://arxiv.org/abs/2004.11274) [hep-ph] .

3.1 CALCULATION OF NEW PHYSICS EFFECTS

In contrast to atomic spectroscopy, molecular spectroscopy permits a direct probe of all possible New Physics interactions between all molecular and atomic constituents, that is between two electrons, two nuclei or between an electron and a nucleus. One can incorporate the effect of the exchange of a new particle by adding a low-energy effective potential to the Hamiltonian, which can be treated perturbatively.

EFFECTIVE POTENTIALS The Fourier-transformed effective potential $\tilde{V}(\mathbf{q})$ of a mediator particle with momentum transfer \mathbf{q} is determined from the quantum field theoretical amplitude \mathcal{M} by means of the Born rule [106],

$$\mathcal{M} = -(\xi_1)_\alpha (\xi_2)_\beta (\xi_3^\dagger)_\gamma (\xi_4^\dagger)_\delta [\tilde{V}(\mathbf{q})]_{\gamma\delta,\alpha\beta}. \quad (3.1)$$

Here, ξ_i denote the two-component Pauli spinors of the two incoming fermions 1 and 2 and outgoing fermions 3 and 4 in non-relativistic

This is in contrast to atoms where at least the nucleus-nucleus coupling cannot be probed due to the lack of the second nucleus.

normalization, while $\alpha, \beta, \gamma, \delta$ refer to the spinor components. Due to translational symmetry, the effective potentials only depend on the distance r_{ij} of the two interacting particles i and j . Thus, the full New Physics potential V_{NP} is given by a sum over all combinations of particles in the molecule,

$$V_{\text{NP}}(\{r_{ij}\}) = \sum_{i < j} V_{ij}(r_{ij}). \quad (3.2)$$

For instance, the simplest incarnation of New Physics is the exchange of a scalar particle of mass m , resulting in the well-known Yukawa potential [107],

See also Appendix A.1.1 for a derivation.

$$V_Y(r) = -\frac{\alpha_Y}{r} e^{-mr}. \quad (3.3)$$

Here, α_Y is the fine structure constant of the new interaction which is proportional to the product of the fundamental couplings g_i and g_j of the scalar to the particles i and j , respectively,

$$\alpha_Y = \frac{g_i g_j}{4\pi} = \frac{g_{ij}}{4\pi}. \quad (3.4)$$

As a consequence of their multiplicative nature, couplings $g_{ij} = g_i g_j$ between the same type of particles are always positive, while the coupling between a nucleus and an electron can have both signs.

We expect a significant modification of the leading Coulomb potential in the case where the range of the new force is similar to molecular scales. In particular, bond lengths of $\mathcal{O}(1 \text{ \AA})$ correspond to mediator masses of $m \sim \mathcal{O}(1 \text{ keV})$. If the mediator is much lighter, the potential is too long-ranged to be distinguished from the Coulomb law, while for masses much above the keV scale the force would be too suppressed at molecular scales to yield any measurable effect.

A scalar mediator coupling to both electrons 1 and 2 and nuclei A and B leads to the potential

$$\begin{aligned} & V_{\text{NP-full}}(\mathbf{r}_1, \mathbf{r}_2, \mathbf{R}_A, \mathbf{R}_B) \\ &= \alpha_{\text{em}} \left\{ \left(-1 - \frac{g_{\text{eN}}}{4\pi\alpha_{\text{em}}} e^{-mr_{1A}} \right) \frac{1}{r_{1A}} + \left(-1 - \frac{g_{\text{eN}}}{4\pi\alpha_{\text{em}}} e^{-mr_{1B}} \right) \frac{1}{r_{1B}} \right. \\ & \quad + \left(-1 - \frac{g_{\text{eN}}}{4\pi\alpha_{\text{em}}} e^{-mr_{2A}} \right) \frac{1}{r_{2A}} + \left(-1 - \frac{g_{\text{eN}}}{4\pi\alpha_{\text{em}}} e^{-mr_{2B}} \right) \frac{1}{r_{2B}} \\ & \quad \left. + \left(1 - \frac{g_{\text{ee}}}{4\pi\alpha_{\text{em}}} e^{-mr_{12}} \right) \frac{1}{r_{12}} + \left(1 - \frac{g_{\text{NN}}}{4\pi\alpha_{\text{em}}} e^{-mR} \right) \frac{1}{R} \right\} \end{aligned} \quad (3.5)$$

with the positive electron-electron and nucleus-nucleus couplings g_{ee} and g_{NN} , respectively, and the electron-nucleus coupling g_{eN} . Note

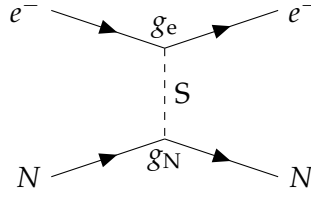


Figure 3.1: Electron-nucleus scattering mediated by a scalar particle. The presence of this process also implies effective couplings between two electrons and two nuclei since it depends on the fundamental couplings g_e and g_N of the mediator to electrons and nuclei, respectively.

that we are considering the coupling to the whole nucleus, while instead the neutron coupling is determined in some of the literature. These works assume that the nucleus coupling is proportional to the neutron number. Therefore, it could be necessary to take into account a factor of up to 4 due to different definitions of the couplings when comparing our results to those of other groups.

The new mediator could also couple not to all of the molecular constituents so that some of the couplings g_{ee} , g_{NN} and g_{eN} may vanish. However, the presence of an electron-nucleus coupling g_{eN} automatically implies that the mediator couples to both electrons and nuclei so that additionally the electron-electron coupling g_{ee} and nucleus-nucleus coupling g_{NN} should be present, see Figure 3.1.

In particular, this would imply that New Physics does not couple to protons, which would require some tuning on the model-building side. Moreover, this would exclude hydrogen from our analysis.

PERTURBATIVE CALCULATION In order to study exclusively one of the possible new interactions, we set all but one coupling g_{ij} to zero. Even though a non-vanishing coupling g_{eN} would also imply non-zero couplings g_{ee} and g_{NN} as described above, the presence of the latter only changes the bound by an $\mathcal{O}(1)$ number due to increased combinatorics when non-hierarchical couplings are assumed.

Since theoretical prediction and experimental measurements currently agree within uncertainties [92], any New Physics effect is expected to be small, not exceeding the current uncertainties. Thus, a treatment of the New Physics potential V_{NP} in first-order perturbation theory is sufficient. We can derive the first-order correction following the arguments which led to the first relativistic correction in Equation (2.24) by formally replacing \hat{H}_N by $\hat{H}_N + V_{\text{NP}}$. As a result, the New Physics correction $E_{v,J}^{\text{NP}}$ to a rovibrational level with quantum numbers (v, J) and Standard Model energy $E_{v,J}^{\text{SM}}$ reads

$$E_{v,J}^{\text{NP}} = \langle \chi_{v,J} | (\langle \varphi_{\text{el}} | V_{\text{NP}} | \varphi_{\text{el}} \rangle_{\text{el}}) | \chi_{v,J} \rangle \quad (3.6)$$

so that the full energy $E_{v,J}$ of the level including the effects of the new mediator is given by

$$E_{v,J} = E_{v,J}^{\text{SM}} + E_{v,J}^{\text{NP}}. \quad (3.7)$$

Analogously to all corrections, φ_{el} and $\chi_{v,J}$ correspond to the Born-Oppenheimer wave functions for the electronic and nuclear part and can be extracted from the codes `H2solv` [81] and `H2spectre` [92, 95], respectively.

The case of a pure nuclear force, that is a force between the two nuclei only depending on their distance R , is simple to evaluate since the scalar product of the properly normalized electronic wave functions evaluates to unity, leaving

$$E_{v,J}^{\text{NP}} = \langle \chi_{v,J} | V_{\text{NP}}(R) | \chi_{v,J} \rangle. \quad (3.8)$$

Only for an interaction involving at least one electron we need the electronic wave function φ_{el} and the calculation becomes more involved. In this case, we first need to evaluate the electronic matrix element

$$\mathcal{E}_{\text{NP}}(R) = \langle \varphi_{\text{el}} | V_{\text{NP}}(r_{12}, r_{1A}, r_{1B}, r_{2A}, r_{2B}, R) | \varphi_{\text{el}} \rangle_{\text{el}} \quad (3.9)$$

by inserting the wave function φ_{el} from `H2solv` [81] and performing the six-dimensional integral over the electronic coordinates. Afterwards, we solve the nuclear integral

$$E_{v,J}^{\text{NP}} = \langle \chi_{v,J} | \mathcal{E}_{\text{NP}}(R) | \chi_{v,J} \rangle \quad (3.10)$$

using the nuclear wave function $\chi_{v,J}$ from `H2spectre` [92, 95].

There is an additional complication for spin-dependent potentials as the matrix depends on the nuclear spin state $|f_1, m_{f,1}, f_2, m_{f,2}\rangle$ in this case. Here, f_i is the total nuclear spin of nucleus i and $m_{f,i}$ is the corresponding projection on the z-axis. Since the full nuclear state must be either symmetric (for deuterium) or antisymmetric (for hydrogen or tritium) under the exchange of indistinguishable particles, the nuclear spin state depends on the symmetry of the spatial wave function. In particular, only the angular part proportional to the spherical harmonics Y_J^m with parity $(-1)^J$ changes under the interchange of the nuclei. Hence, the exact nuclear spin states depend not only on the isotopologue but also on the angular momentum J . For more details on the calculation of the spin matrix elements see Appendix A.2.

In all cases, the ground state energy might be degenerate by the multiplicity of the nuclear spin states allowed. Hence, degenerate perturbation theory has to be applied and we have to diagonalize the New Physics contribution in the degenerate spin space to find the real energy corrections. This also holds for the mixed molecules HD, HT, and DT, where there is no restriction on the nuclear spin state from the Pauli principle. By contrast, there is no such problem for electrons as the electronic spin state is always the anti-symmetric singlet state due to the symmetric position space wave function in the ground state.

Note that one of the angular integrals is trivial due to the rotational symmetry of the problem around the nuclear axis.

Recall that hydrogen and tritium nuclei have spin $\frac{1}{2}$, while deuterium has spin 1.

The relevant energy is the one of the unperturbed state in Equation (2.13).

For instance, the nuclear spins of HT could be either in the singlet or triplet state, both having the same unperturbed energy.

Finally, the energy of a transition between levels (v_1, J_1) and (v_2, J_2) can be obtained from their energy difference,

$$\Delta E_{(v_1, J_1) \rightarrow (v_2, J_2)} = E_{v_2, J_2} - E_{v_1, J_1}, \quad (3.11)$$

where $E_{v, J} = E_{v, J}^{\text{SM}} + E_{v, J}^{\text{NP}}$ is the level energy including the New Physics correction.

Since experimental measurements confirm the Standard Model predictions, any New Physics effect should be at most of the order of the Standard Model uncertainty $\delta E_{v, J}^{\text{SM}}$. In perturbation theory, the error $\delta E_{v, J}^{\text{NP}}$ should be much smaller than the New Physics contribution $E_{v, J}^{\text{NP}}$ itself, $\delta E_{v, J}^{\text{NP}} \ll \Delta E_{v, J}^{\text{NP}} \sim \delta E_{v, J}^{\text{SM}}$. As a consequence, we keep the Standard Model uncertainty on the energy level as a good approximation of the theory uncertainty even in the New Physics case,

$$\delta E_{v, J} = \delta E_{v, J}^{\text{SM}} + \delta E_{v, J}^{\text{NP}} \approx \delta E_{v, J}^{\text{SM}}. \quad (3.12)$$

In particular, we linearly add the uncertainties for transitions as in Equation (2.27).

TECHNICAL IMPLEMENTATION Since the electronic wave function is not known analytically, we employ numerical integration techniques to solve the integrals in the electronic matrix element (3.9). In particular, we use the VEGAS algorithm as implemented in the GNU Scientific Library and the LocalAdaptive numerical integration routine in Mathematica as a check.

Since the New Physics potential depends on the new coupling g_{ij} and the mass m of the new mediator, the electronic energy correction $\mathcal{E}_{\text{NP}}(R)$ will depend on the three parameters (R, m, g_{ij}) . However, the dependence on the coupling g_{ij} can be factored out so that only the dependence on (R, m) is non-trivial. In order to avoid time-consuming numerical integrations during the parameter scan, we calculate the electronic matrix element $\mathcal{E}_{\text{NP}}(R)$ on a grid in (R, m) once. Afterwards, we approximate the full dependence on these parameters by an interpolation with splines of degree two using the RectBivariateSpline class in SciPy.

Finally, we compute the nuclear matrix element (3.10) analogously to the determination of all higher-order corrections in H2spectre using the radial nuclear wave function u_v in a discrete value representation with grid spacing ΔR [92, 95]. In order to obtain the nuclear wave function, we modified the H2spectre code by adding an exporting routine. Then, the energy correction reads [92, 95]

$$E_v^{\text{NP}} = \Delta R \cdot \sum_i \mathcal{E}_{\text{NP}}^i \cdot (u_v^i)^2, \quad (3.13)$$

where $u_v^i = u_v(R_i)$ and $\mathcal{E}_{\text{NP}}^i = \mathcal{E}_{\text{NP}}(R_i)$ are the radial nuclear wave function and electronic matrix element evaluated at the grid points R_i ,

This corresponds to an approximation of the integral by a sum of the integrand evaluated at sampling points.

respectively. Note that we assumed a radially symmetric New Physics potential where the energy correction is independent of angular momentum J . Moreover, the same expression also applies to the case of the pure nuclear force as given in Equation (3.8) if \mathcal{E}_{NP} is replaced by the potential V_{NP} .

We have automated the calculation in a Python program package `hyc.py` [108] which expects the type of potential, the coupling g and mass m of the mediator and the isotopologue as inputs and yields level or transition energies and their uncertainties. `hyc.py` can be run standalone with the desired transitions defined in the program code or it can be imported as a package from own code. In order to calculate many transitions efficiently, `hyc.py` heavily uses NumPy's vectorization feature, allowing to pass multiple transitions at once to the code.

CONDITION FOR NEW PHYSICS BOUNDS Since the measurements confirm the Standard Model value, we place bounds on the parameter space by requiring that the transition energy including New Physics effects is still compatible with the experimental value ΔE_{exp} within three standard deviations σ_{exp} . We assume that the theory value of a transition energy $\Delta E = \Delta E_{(v_1, J_1) \rightarrow (v_2, J_2)}$ is contained in the interval

$$[\Delta E - \delta\Delta E, \Delta E + \delta\Delta E] \quad (3.14)$$

given by the theory uncertainty $\delta\Delta E$ which is calculated as in Equation (2.27).

In conclusion, a parameter point (m, g_{ij}) for a new mediator with mass m and coupling g_{ij} is excluded if its energy is not contained in the interval

$$[\Delta E_{\text{exp}} - 3\sigma_{\text{exp}} - \delta\Delta E, \Delta E_{\text{exp}} + 3\sigma_{\text{exp}} + \delta\Delta E] . \quad (3.15)$$

This criterion allows us to derive upper bounds on the couplings g_{ij} for a given mediator mass m by checking against all measurements listed in Appendix A.3.

3.2 SCALAR AND PSEUDOSCALAR MEDIATORS

Scalar and pseudoscalar particles are among the simplest extensions of the Standard Model and could resolve several problems such as Dark Matter or the Strong CP Puzzle. For instance, this class of particles includes additional light Higgs bosons [109, 110] as well as remnants of spontaneously or softly broken continuous global symmetries such as the Majoron [111]. A prime example of a pseudoscalar arising from a broken global $U(1)$ symmetry is the axion [34–37], which also occurs in models addressing the Flavor Puzzle [38–41].

Note that confidence levels of 90% or two sigma are chosen in some of the literature.

Scalar and pseudoscalar couplings g_ψ^S and g_ψ^P of a spinless mediator φ to fermions ψ are described by the Lagrangian

$$\mathcal{L}_{\text{int}} = \bar{\psi}(g_\psi^S + g_\psi^P \gamma_5)\psi\varphi. \quad (3.16)$$

If such a mediator with mass m and either purely scalar or purely pseudoscalar coupling $g_{ab}^S = g_a^S g_b^S$ or $g_{ab}^P = g_a^P g_b^P$, respectively, is exchanged between two spin- $\frac{1}{2}$ fermions a and b with masses $m_{a,b}$, the low-energy potentials read [112]

$$V_S(\mathbf{r}) = -g_{ab}^S \frac{e^{-mr}}{4\pi r}, \quad (3.17a)$$

$$V_P(\mathbf{r}) = -g_{ab}^P \frac{m^2}{4m_a m_b} \left[(\boldsymbol{\sigma}_a \cdot \boldsymbol{\sigma}_b) \left(\frac{1}{m^2 r^2} + \frac{1}{mr} + \frac{4\pi r}{3m^2} \delta^{(3)}(\mathbf{r}) \right) - (\boldsymbol{\sigma}_a \cdot \hat{\mathbf{r}})(\boldsymbol{\sigma}_b \cdot \hat{\mathbf{r}}) \left(1 + \frac{3}{m^2 r^2} + \frac{3}{mr} \right) \right] \frac{e^{-mr}}{4\pi r}. \quad (3.17b)$$

Here, $\boldsymbol{\sigma}_{a,b} = (\sigma_x, \sigma_y, \sigma_z)$ is the tuple of Pauli matrices referring to the spin subspace of fermion a or b and $\hat{\mathbf{r}}$ denotes the unit vector pointing from particle a to particle b. For a derivation of these potentials, see also Appendices A.1.1 and A.1.2.

Notice that the scalar potential is always attractive and therefore lowers the level energy, while the pseudoscalar potential can change sign due to the relative minus sign between the first and second line. As a consequence, strong bounds could be obtained if the Standard Model prediction is close to the left boundary of the exclusion interval in Equation (3.15). Then, a calculated value will lie outside the allowed interval already if the energy is lowered only slightly.

In contrast to the scalar case, all terms in the pseudoscalar potential are spin-dependent. Moreover, we can define an effective pseudoscalar coupling

$$g_{ab}^{P,\text{eff}} = g_{ab}^P \frac{m^2}{4m_a m_b} \quad (3.18)$$

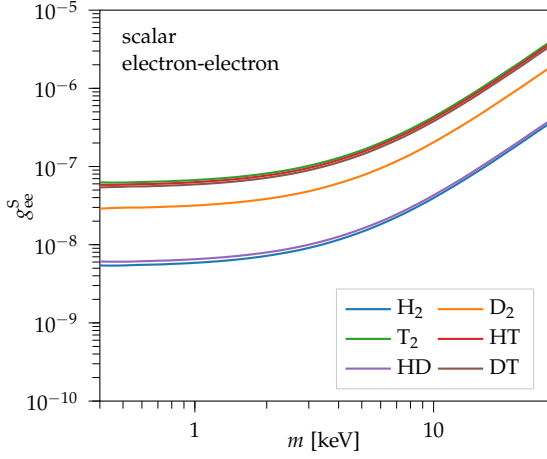
since the coupling g_{ab}^P is always accompanied by the mass ratios of the mediator and the fermions. As a sizable effect of a pseudoscalar exchange on molecular scales is only expected for mediator masses $m \sim \mathcal{O}(\text{keV})$, this results in a suppression of the electron-electron coupling by at least four orders of magnitude. Hence, we do not expect any strong bounds on pseudoscalar mediators, especially not for interactions involving nucleons. Furthermore, the pseudoscalar potential in Equation (3.17b) assumes spin- $\frac{1}{2}$ fermions and, hence, should not be applied for molecules involving spin-1 deuterium nuclei.

In particular, an equivalent derivative coupling $\frac{\partial_\mu \varphi}{\Lambda} \bar{\psi} \gamma^\mu (g_\psi^S + g_\psi^P \gamma_5) \psi$ with mass scale Λ is often used for pseudoscalar particles.

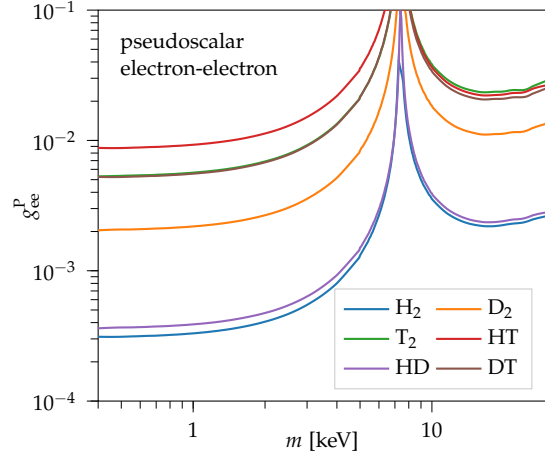
In principle, one could use the potential in the case of the heteronuclear molecules HD and DT by only considering the coupling to hydrogen or tritium. However, this would mean a tuning to a vanishing deuterium coupling. Moreover, we expect similar results as for the other molecules.

In general the mediator features both types of couplings, giving also rise to a mixed scalar-pseudoscalar potential [112].

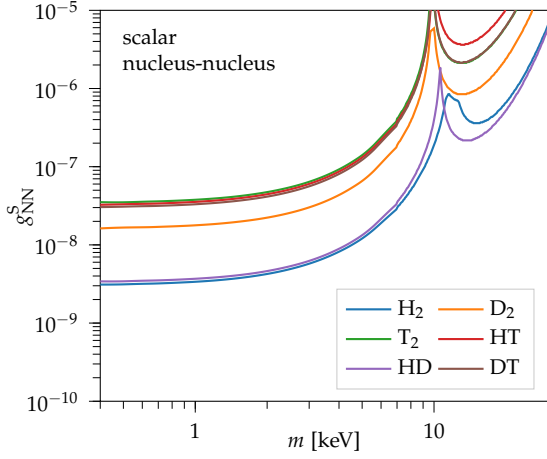
On the contrary, the bounds will be rather weak if the Standard Model prediction is larger than the experimental value.



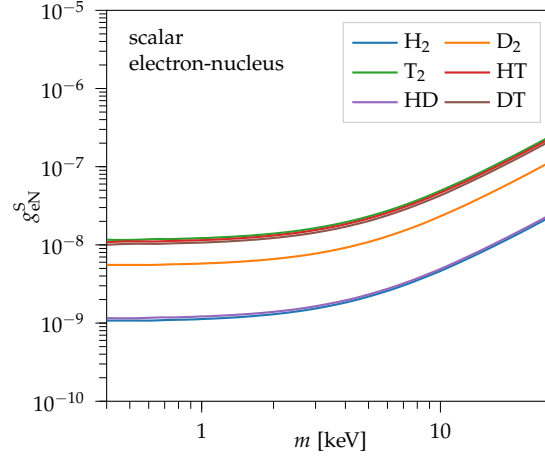
(a) Scalar electron-electron interaction. The curves for T_2 , HT , and DT as well as the ones for H_2 and HD are almost identical.



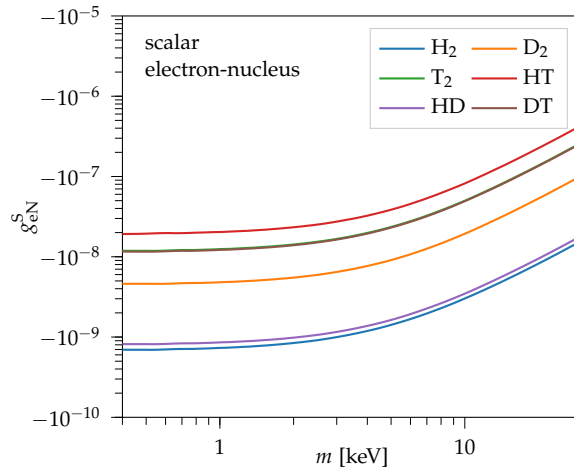
(b) Pseudoscalar electron-electron interaction. The curves for T_2 and DT are almost identical.



(c) Scalar nucleus-nucleus interaction. The curves for T_2 and DT are almost identical, while the one for HT differs only above masses of 10 keV from them.



(d) Scalar electron-nucleus interaction with positive coupling $g_{eN}^S > 0$. The curves for H_2 and HD as well as the ones for T_2 , HT and DT are almost identical.



(e) Scalar electron-nucleus interaction with negative coupling $g_{eN}^S < 0$. The curves for T_2 and DT are almost identical.

Figure 3.2: Upper limits on the scalar and pseudoscalar couplings g_{ij}^S and g_{ij}^P as obtained from molecular spectroscopy by the combination of all available data listed in Appendix A.3.

ELECTRON-ELECTRON COUPLING For a pure coupling between two electrons, we find restrictive bounds on the scalar coupling g_{ee}^S of $g_{ee}^S \lesssim \mathcal{O}(10^{-8})$ for mediator masses m below $m \lesssim 10$ keV, see Figure 3.2a. The best constraints arise from measurements of H₂ and HD, while those from tritiated isotopologues are weaker by about one order of magnitude. Although the measurements have about the same precision, this observation is due to the fact that the central values of the H₂ and HD measurements are smaller than the theoretical prediction and that the attractive scalar potential lowers the energy. Note that for masses $m \lesssim \mathcal{O}(10^{-1}$ keV) the exponential in the Yukawa potential can be neglected at molecular scales, $\frac{e^{-mr}}{r} \simeq \frac{1}{r}$. Thus, the New Physics potential would have the same shape as the Coulomb potential, resulting in a redefinition of the electromagnetic fine structure constant [113]. As a consequence, the New Physics effect would already be contained in the low-energy value of the electromagnetic fine structure constant and should not be added again as in this analysis. Therefore, no bounds can be inferred in the low mass regime, contrary to what one would expect when one extrapolates the exclusion plots to masses below $\mathcal{O}(10^{-1}$ keV).

In the case of a pseudoscalar coupling, we indeed find the mass suppression leading to weaker bounds by about five orders of magnitude, see Figure 3.2b. There is also a cancellation between the terms with different spin structures occurring at mediator masses of about $m \sim 7$ keV so that the bound becomes ineffective at that point. The use of polarized probes can help to disentangle the two terms, however, competitive bounds on pseudoscalar particles are still not to be expected from molecular spectroscopy due to the mass suppression.

NUCLEUS-NUCLEUS COUPLING Due to the huge mass suppression of $g_{NN}^{\text{Peff}} \sim 10^{-12} g_{NN}^{\text{P}}$ in the pseudoscalar potential, we do not get any bounds on the pseudoscalar coupling. In the case of the scalar coupling, we find limits of about the same size of up to $g_{NN}^S \sim \mathcal{O}(10^{-8})$ for the nucleus-nucleus coupling as for the electron-electron coupling, see Figure 3.2c. Again, the best constraints arise from H₂ and HD while bounds from molecules containing tritium are weaker by one order of magnitude. Kinks in the plot indicate that another line becomes more constraining. Moreover, the two levels involved in the transition receive New Physics contributions of the same size for mediators with masses of about 10 keV which thus cancel in the transition energy. This explains the apparent divergences in the curves in Figure 3.2c.

Comparing to the literature, the authors of References [43, 104] quote upper bounds on the scalar coupling of $g_{NN}^S \sim 10^{-10}$ which are stronger than our results. The main reasons for this apparent discrepancy are on the one hand our more conservative exclusion criterion and on the other hand that we consider an effective coupling to the whole nucleus instead of the single nucleons. Due to the latter fact,

we do not split off the nucleon numbers A from the couplings and the bounds in References [43, 104] are better than ours by a factor of $A^2 = 9$ for tritium-tritium interactions.

ELECTRON-NUCLEUS COUPLING In the case of the electron-nucleus coupling, only a scalar coupling is possible since the matrix element of the pseudoscalar potential vanishes in the electronic ground state, see Appendix A.2. Our exclusion limits for the scalar coupling can be found in Figures 3.2d and 3.2e, showing the limits for both possible signs of the coupling. In contrast to a purely electronic or pure nuclear force, the bounds are slightly stronger with constraints of up to $|g_{eN}^S| \lesssim \mathcal{O}(10^{-9})$. This is not surprising since there are four possible combinations of one electron with one nucleon, yielding a combinatorical factor of four compared to the other two cases. Bearing in mind that an electron-nucleus coupling also implies an electron-electron and nucleus-nucleus coupling, the bounds should further improve by an $\mathcal{O}(1)$ number. Again, the best constraints stem from H_2 and HD measurements.

3.3 VECTOR AND AXIALVECTOR MEDIATORS

Another popular possibility for New Physics interactions are Spin-1 mediators with vector or axialvector couplings. The most prominent example in this category is the Dark Photon stemming from a new gauged $U(1)'$ symmetry [114]. The gauge-invariant kinetic mixing term $F_{\mu\nu}F'^{\mu\nu}$ allows for small vector or axialvector couplings to Standard Model fermions. Moreover, rather heavy vector mediators arise in the Stueckelberg mechanism which, however, also leads to pseudoscalar axion-like particles (ALPs) [115, 116].

The Lagrangian for such a spin-1 mediator V^μ with mass m interacting with fermions ψ with couplings $g_\psi^{V,A}$ is given by

$$\mathcal{L}_{\text{int}} = \bar{\psi}\gamma^\mu(g_\psi^V + g_\psi^A\gamma_5)\psi V_\mu. \quad (3.19)$$

Considering only purely vector couplings $g_{ab}^V = g_a^V g_b^V$ or axialvector couplings $g_{ab}^A = g_a^A g_b^A$ of the mediator to Standard Model fermions a and b , we find the non-relativistic potentials [112]

$$\begin{aligned}
V_V(\mathbf{r}) &= \frac{g_{ab}^V}{4\pi} \frac{e^{-mr}}{r} \\
&+ g_{ab}^V \frac{m^2}{4m_a m_b} \left[\boldsymbol{\sigma}_a \cdot \boldsymbol{\sigma}_b \left(\frac{1}{m^2 r^2} + \frac{1}{mr} + 1 - \frac{8\pi r}{3m^2} \delta^{(3)}(\mathbf{r}) \right) \right. \\
&\quad \left. - (\boldsymbol{\sigma}_a \cdot \hat{\mathbf{r}})(\boldsymbol{\sigma}_b \cdot \hat{\mathbf{r}}) \left(\frac{3}{m^2 r^2} + \frac{3}{mr} + 1 \right) \right] \frac{e^{-mr}}{4\pi r}, \quad (3.20a) \\
V_A(\mathbf{r}) &= -g_{ab}^A \left[\boldsymbol{\sigma}_a \cdot \boldsymbol{\sigma}_b \left(1 + \frac{1}{m^2 r^2} + \frac{1}{mr} + \frac{4\pi r}{3m^2} \delta^{(3)}(\mathbf{r}) \right) \right. \\
&\quad \left. - (\boldsymbol{\sigma}_a \cdot \hat{\mathbf{r}})(\boldsymbol{\sigma}_b \cdot \hat{\mathbf{r}}) \left(1 + \frac{3}{m^2 r^2} + \frac{3}{mr} \right) \right] \frac{e^{-mr}}{4\pi r}. \quad (3.20b)
\end{aligned}$$

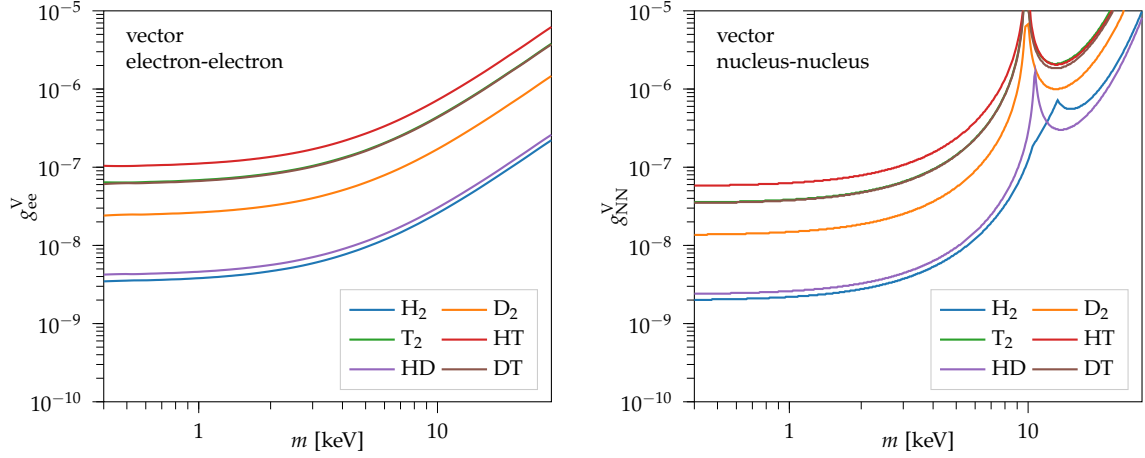
Again also a mixed vector-axialvector potential would be possible if the mediator features both type of couplings [112].

Here, $\boldsymbol{\sigma}_{a,b} = (\sigma_x, \sigma_y, \sigma_z)$ denotes the tuple of Pauli matrices acting on the spin subspace of fermion a and b and $\hat{\mathbf{r}}$ is the unit vector of the vector connecting the two particles a and b. Note that again these potentials only apply if the interacting particles are spin- $\frac{1}{2}$ fermions, excluding couplings to deuterium nuclei.

The spin-dependent terms in the vector mediator potential V_V are mass-suppressed like in the pseudoscalar case so that it can be approximated by the leading Yukawa potential. Due to this fact we do not expect qualitatively different limits than those shown for scalar couplings in Figure 3.2, although the different sign compared to the scalar potential in Equation (3.17a) leads to a slight modification of the bounds. Moreover, since the dominant term is spin-independent, we can apply the vector potential also to deuterium. For the axialvector force, all terms are spin-dependent, while the mass suppression is absent so that large effects are expected.

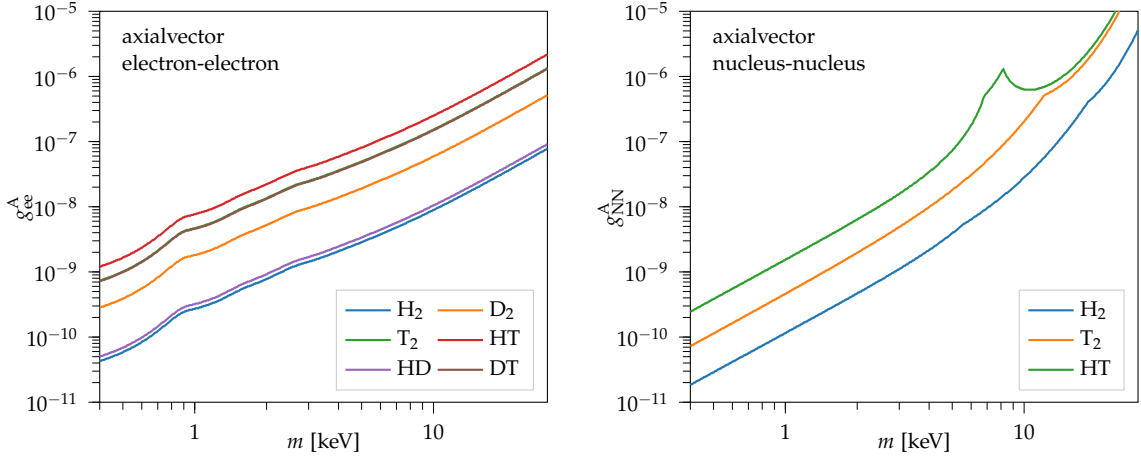
ELECTRON-ELECTRON COUPLING The constraints on the vector electron-electron coupling as shown in Figure 3.3a are similar to those of a scalar coupling as a result of the leading Yukawa term in the vector potential. However, the opposite signs result in a slight difference as a consequence of the central theory value not exactly matching the experimental value. Hence, the exclusion interval around the theory value is asymmetric allowing for larger or lower New Physics contributions depending on the direction.

Again, measurements of H_2 and HD are most limiting with upper bounds on the vector coupling g_{ee}^V of $\mathcal{O}(10^{-8})$ for mediator masses $m \lesssim \mathcal{O}(10 \text{ keV})$. As before, constraints should not be trusted if the mass m of the new particle is much below the keV regime since the electromagnetic fine structure constant would be modified there [113]. For the axialvector electron-electron interaction we now find strong bounds as expected. Axialvector couplings g_{ee}^A of up to $\mathcal{O}(10^{-10})$ are excluded for mediators masses $m \lesssim \mathcal{O}(1 \text{ keV})$, while for larger masses $m \lesssim \mathcal{O}(10 \text{ keV})$ the excluded region still reaches up to $\mathcal{O}(10^{-8})$ in the coupling, see Figure 3.3c.



(a) Vector electron-electron interaction. The curves for T_2 and DT are almost identical.

(b) Vector nucleus-nucleus interaction. The curves for T_2 and DT are almost identical.



(c) Axialvector electron-electron interaction. The curves for T_2 and DT as well as the ones for H_2 and HD are almost identical.

(d) Axialvector nucleus-nucleus interaction.

Figure 3.3: Upper limits on the vector and axialvector couplings g_{ij}^V and g_{ij}^A as obtained from molecular spectroscopy by the combination of all available data in Appendix A.3.

NUCLEUS-NUCLEUS COUPLING The overall picture for the vector nucleus-nucleus coupling is similar to the electron-electron counterpart, see Figure 3.3b. Still, molecules containing tritium give loose constraints so that again H_2 and HD yield the best limits of $g_{\text{NN}}^{\text{V}} \sim \mathcal{O}(10^{-9})$. Similarly to the electron-electron coupling, the vector nucleus-nucleus coupling is slightly better constrained than the scalar nucleus-nucleus coupling as a consequence of the different sign in the Yukawa potential.

In the case of the axialvector nucleus-nucleus coupling, the bounds are similar to the electron-electron axialvector coupling with a limit of up to $\mathcal{O}(10^{-10})$ for mediator masses below 1 keV. Since the spin-dependent potentials are only valid for fermionic nuclei, we only show the bounds for molecular hydrogen H_2 and tritium T_2 as well as HT in Figure 3.3d. While the best constraints still arise from hydrogen, tritium limits are now only slightly worse, in contrast to the other cases.

ELECTRON-NUCLEUS COUPLING Since the dominant vector contribution is the Yukawa potential, the bounds for the electron-nucleus coupling are the same as for the scalar correspondent as shown in Figures 3.2d and 3.2e. Note however that the leading Yukawa part has opposite sign so that Figure 3.2d represents the case of a negative vector coupling g_{eN}^{V} , while Figure 3.2e corresponds to a positive coupling g_{eN}^{V} . Again, the limits are slightly better than those for the vector electron-electron or vector nucleus-nucleus coupling due to the increased number of combinations, yielding bounds of $\mathcal{O}(10^{-9})$. Analogously to the pseudoscalar case, we cannot place any bounds on the electron-nucleus axialvector coupling since the spin dependence cancels in the electronic ground state, see Appendix A.2.

3.4 COMPARISON TO OTHER EXPERIMENTS

The New Physics potential of scalar mediators has been explored with other methods. In particular, the electron-neutron coupling has been analyzed in the context of atomic spectroscopy [45], atomic isotope shifts [46, 48], and Rydberg atoms [47]. From these studies, upper bounds on the electron-neutron coupling of $\mathcal{O}(10^{-13})$ were derived with possible improvements of two orders of magnitude to be expected by future experiments [45]. Note that these bounds cannot be directly compared to those given in this work since we do not extract the coupling to neutrons directly but only consider the coupling to the whole nucleus. However, we expect our limits to be of the same order due to the low neutron numbers of the nuclei considered in this work. The same picture applies to the nucleus-nucleus coupling where there are limits from neutron scattering [49] which are several orders of magnitude better than those obtained in this work. However, we derive

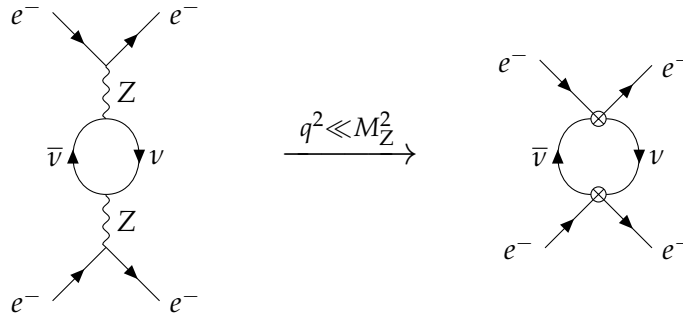


Figure 3.4: In the low-energy theory where the momentum transfer q is much smaller than the Z boson mass M_Z , the effective four-fermion interaction of fermions with neutrinos becomes an interaction between the two fermions mediated by the exchange of two neutrinos.

nucleus couplings so that we also get a bound on a coupling to protons from H_2 which is not tested in neutron scattering.

In the case of the electron-electron coupling, atomic spectroscopy in Helium atoms derives upper limits of $\mathcal{O}(10^{-9})$ [45] so that molecular spectroscopy is competitive. Still, measurements of the anomalous magnetic moment of the electron yield more stringent bounds—although the effect of a new interaction enters this observable indirectly at loop level.

Indirect astrophysical searches for example from the cooling of stars provide constraints on these couplings that are much stronger than those from any laboratory experiment [55, 117, 118]. We explore supernova bounds for pseudoscalar mediators with flavor-violating couplings in Part III of this thesis. Moreover, there are also stringent bounds from cosmology, see for instance Reference [119]. Still, laboratory methods provide important insights as being performed in a controlled experimental environment, while astrophysical and cosmological determinations suffer from large uncertainties.

3.5 ESTIMATION OF TWO-PARTICLE EXCHANGES

While the exchange of a heavy Standard Model Higgs or electroweak gauge boson leads to a Yukawa-like potential which is too short-ranged to be observed in molecular spectroscopy, it was claimed in the literature that the effective coupling of fermions to neutrinos mediated for example by a Z boson exchange, see Figure 3.4, leads to a measurable effect [68, 120–129]. This observation is supported by an analysis done by Stadnik in Reference [125] for hydrogen atoms and positronium.

Based on early works by Feinberg and Sucher [120] as well as Hsu and Sikivie [122], Grifols et al. derived the long-range potentials for massive Dirac or Majorana-type neutrinos to be [123]

$$V_D(r) = \frac{G_{\text{eff}}^2 m_\nu^3}{16\pi^3 r^2} K_3(2m_\nu r) \stackrel{m_\nu r \gg 1}{\approx} \frac{G_{\text{eff}}}{32\pi^2} \sqrt{\frac{m_\nu^5}{\pi r^5}} e^{-2m_\nu r}, \quad (3.21)$$

$$V_M(r) = \frac{G_{\text{eff}}^2 m_\nu^3}{8\pi^2 r^3} K_2(2m_\nu r) \stackrel{m_\nu r \gg 1}{\approx} \frac{G_{\text{eff}}}{16\pi^2 r^2} \sqrt{\frac{m_\nu^3}{\pi r^3}} e^{-2m_\nu r}. \quad (3.22)$$

Here, the functions $K_n(x)$ are the modified Bessel functions [130] and we show the long-range behavior, which matches the intuition that there is an exponential suppression of twice the neutrino mass, analogously to the mediator mass before. The short-range behavior of these potentials which is also corresponding to the massless neutrino limit, however, features a strong r^{-5} divergence, yielding the expression by Weinberg and Sucher [120],

$$V(r) = \frac{G_{\text{eff}}^2}{16\pi^3 r^5}, \quad (3.23)$$

for both Dirac and Majorana neutrinos.

This highly singular behavior for short distances is an artifact of the effective theory where the electroweak gauge bosons are integrated out and requires a careful treatment. In particular, one should introduce a cut-off to account for the limited validity of the theory in the high-energy regime. Naively, the cut-off parameter should be of order of the Z boson mass M_Z . Such a high value would however assume that the wave function also captures effects of length scales much smaller than the inverse electron mass m_e^{-1} , contradicting the assumption of the non-relativistic approximation. Therefore, a cut-off of $r \gtrsim (m_e \alpha_{\text{em}})^{-1}$ would be appropriate as it is the scale at which effects are integrated out in the non-relativistic effective theory of Quantum Electrodynamics (NRQED) [131].

In the case of molecular physics, we can estimate the dependence of the New Physics energy shift in Equation (3.10) on the cut-off as follows. We shift $\mathbf{r}_2 \rightarrow \mathbf{r}_1 - \mathbf{r}_2 = \mathbf{r}_{12} = \mathbf{r}$ in the integral over the coordinates of the second electron and introduce a cut-off r_{cut} for the distance $\mathbf{r} = \mathbf{r}_{12}$. Since also basis functions ψ_{n_0, \dots, n_4}^0 with $n_0 = 0$ are included in the expansion of the electronic ground state wave function, see Equation (2.11), the leading term of the wave function is constant in $r = |\mathbf{r}_{12}|$. Thus, we can infer the cut-off dependence by power counting

$$E_{v,J}^{\text{NP}} \stackrel{r \rightarrow 0}{\sim} \int d^3 r_2 \frac{1}{r^5} = \int_{r_{\text{cut}}} d^3 r \frac{1}{r^5} \sim \frac{1}{r_{\text{cut}}^2}, \quad (3.24)$$

where we dropped all factors constant in r .

Thus, we find a quadratic dependence of the result on the cut-off r_{cut} so that changes in the arbitrary scale result in large differences. This signals an incorrect treatment of the ultraviolet divergence and

Note that the other integrals are finite due to the exponential suppression in the wave function.

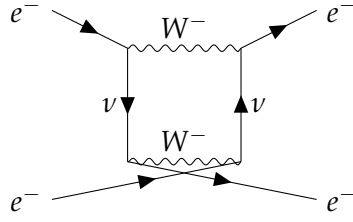


Figure 3.5: One of the possible W box diagrams contributing to the two-neutrino exchange potential. The curly lines represent W bosons.

we conclude that the use of the potentials (3.21) and (3.22) does not provide reliable results. As a consequence, we also doubt the strong bounds derived by Stadnik claiming that the Standard Model value for G_{eff} is within reach of experiments since his conclusions actually rely on the fact that his contribution diverges quadratically [125]. This has also been noticed by other authors [132, 133].

A careful treatment would involve a proper matching in the tower of effective theories and a suitable regularization of the occurring divergences, for instance by dimensional regularization. For the scope of this thesis, we restrict ourselves to a rough upper estimate of the effect by looking at the short-distance behavior of one of the W box diagrams as depicted in Figure 3.5.

Denoting the W boson mass by M_W and the Fermi constant by G_F , this diagram is of $\mathcal{O}(G_F^2 M_W^2)$ in the coupling as it is also the case for the neutrino exchange shown above. However, we expect a further suppression if we consider for example sterile neutrinos instead of the Standard Model neutrinos due to small mixing factors. In this sense, one should view the discussion below as a generous upper limit that is orders of magnitude larger than the actual result.

Evaluating the short-distance behavior of the box diagram, see Appendix A.1.3, we derive the low-energy effective contact potential

$$V_{W\text{-box}}(r) = \frac{4}{3} \pi G_F^2 M_W^2 \delta^{(3)}(\mathbf{r}). \quad (3.25)$$

Plugging in numbers, we find an energy correction of $\mathcal{O}(10^{-11} \text{ cm}^{-1})$, which is far below the current experimental sensitivity. Hence, we can completely neglect the two-neutrino exchange in the case of molecules and, more generally, in all atomic systems where the Coulomb force is present.

LONG-RANGE FORCES INDUCED BY HIGGS BOSONS Another interesting possibility for a long-range potential is the exchange of two light pseudo-Goldstone bosons a coupling to the Standard Model Higgs boson H via a scalar interaction given by the Lagrangian $\mathcal{L}_{\text{Haa}} = g_{\text{Haa}} a a H$ [124], see Figure 3.6. While the low-energy potential reduces to a well-behaved r^{-3} form in this case, the effective coupling

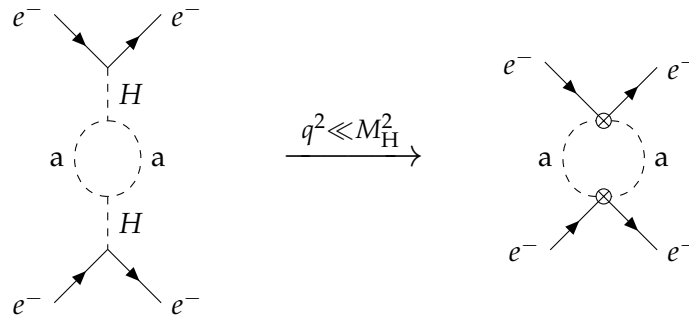


Figure 3.6: In the low-energy theory where the momentum transfer q is much smaller than the Higgs boson mass M_H , the effective interaction of electrons with the scalar pseudo-Goldstone bosons becomes an interaction between the two electrons mediated by the exchange of two pseudo-Goldstone bosons.

will be proportional to the second power of the electron Yukawa coupling to the Higgs [124]. This introduces a large suppression and, hence, all effects on molecular spectra are again negligible.

CONCLUSION AND OUTLOOK

In this work, we have performed the first systematic study of constraints on New Physics couplings arising from the spectroscopy of rovibrational molecular levels. In contrast to other direct probes, molecular spectroscopy offers the unique possibility to study different couplings in one measurement, namely the couplings between two electrons, between two nuclei or between one electron and one nucleus. While the nucleus-nucleus coupling has been studied before in the case of the Yukawa potential associated with a scalar force mediator exchange, we have extended the discussion by including pseudoscalar, vector, and axialvector mediators and by analyzing the other couplings. Moreover, we have briefly discussed the case of two-particle exchanges originating from effective couplings to the heavy gauge bosons and Higgs boson.

For this purpose, we have calculated the effect of a New Physics particle perturbatively starting from ab initio Standard Model predictions which are available in the form of computer codes in the literature. Currently, the Standard Model predictions agree with experimental measurements despite the already high relative precision of $\mathcal{O}(10^{-8})$ of both calculation and experiment. Hence, we do not expect any signal of New Physics to be seen in existing spectroscopy data and use the current data to derive upper bounds on the new couplings.

As a result, we have found that the best bounds can be obtained from the current measurements of molecular hydrogen H_2 and hydrogen-deuterium molecules HD for all couplings. Molecules containing tritium give worse constraints by about one order of magnitude which is a consequence of the position of the theory prediction in our exclusion interval rather than experimental precision. Note that the tension in tritium data has been resolved by new data so that the New Physics bounds are weakened, which is in contrast to the expectation that the higher nucleus mass could be advantageous for tritium molecules.

We find bounds of up to $g_{ee,NN} \sim \mathcal{O}(10^{-11})$ for axialvector nucleus-nucleus and electron-electron couplings and up to $\mathcal{O}(10^{-9})$ for the other types. These results are compatible with atomic spectroscopy which, however, yields tighter constraints by about three orders of magnitude. Adding to existing literature results, our analysis discusses the spin-dependent pseudoscalar and axialvector forces. The same conclusion also applies to the nucleus-nucleus interaction, where our results are compatible with those from neutron scattering but less constraining. Concerning the electron-electron interaction, molecular bounds match the accuracy of those obtained from Helium spec-

troscopy. Measurements of the anomalous magnetic moment of the electron show greater sensitivity to the electron-electron coupling, but are indirect probes through loop-effects.

Astrophysical measurements provide constraints which are several orders of magnitude better than all bounds from laboratory experiments. The precise applicability of these bounds for mediators in the keV range is not entirely clear since for instance the core of a white dwarf features a temperature of $\mathcal{O}(\text{keV})$. As also star models suffer from large uncertainties, it is nevertheless valuable to have a direct laboratory experiment in a controlled environment.

There are several possibilities to extend this work. First, a full calculation of the non-adiabatic Quantum Electrodynamics (QED) correction would reduce the theory uncertainty by one order of magnitude, allowing for tighter constraints. Moreover, improvements in experimental techniques or the use of polarized probes would further test the Standard Model. Lastly, it would be interesting to further analyze the fate of two-particle exchanges in a dedicated study involving a proper matching in the tower of effective field theories to evaluate the claims of strong limits in the literature.

Part II

NEUTRINO PHYSICS ON EARTH AND IN THE
SKY: NEUTRINO MASSES FROM A $U(2)$ FLA-
VOR SYMMETRY

A $U(2)$ MODEL OF FLAVOR

Models based on a $U(2)$ flavor symmetry not only provide an explanation of the Flavor Puzzle, but also predictions for currently unknown neutrino observables. In this chapter, we introduce this general class of models and discuss the prototype model and its variants. We motivate the use of a $U(2)$ flavor symmetry in Section 5.1, before we analyze concrete realizations in the case of quarks and charged leptons in Section 5.2 and neutrinos in Section 5.3.

This chapter is based on the publications

Matthias Linster and Robert Ziegler. “A Realistic $U(2)$ Model of Flavor.” *JHEP* 08 (2018), p. 058. DOI: [10.1007/JHEP08\(2018\)058](https://doi.org/10.1007/JHEP08(2018)058). arXiv: [1805.07341](https://arxiv.org/abs/1805.07341) [hep-ph]

and

Matthias Linster, Jacobo Lopez-Pavon, and Robert Ziegler. “Neutrino Observables from a $U(2)$ Flavor Symmetry.” *Phys. Rev. D* 103.1 (2021), p. 015020. DOI: [10.1103/PhysRevD.103.015020](https://doi.org/10.1103/PhysRevD.103.015020). arXiv: [2009.10437](https://arxiv.org/abs/2009.10437) [hep-ph] .

5.1 MOTIVATION

One of the most intriguing puzzles of the Standard Model is the presence of a large hierarchical pattern in the parameters relevant for Flavor Physics. In particular, electron and top mass are separated by about six orders of magnitude [23], while neutrinos are at least another six orders of magnitude lighter than electrons [23, 50]. Furthermore, the three quark mixing angles yielding the Cabibbo-Maskawa-Kobayashi (CKM) matrix are spread over three orders of magnitude ranging from $\mathcal{O}(10^{-3})$ to $\mathcal{O}(10^{-1})$ [135]. One might now expect that the Pontecorvo-Maki-Nakagawa-Sakata (PMNS) matrix describing lepton mixing is subject to similar hierarchies, however, with two angles being $\mathcal{O}(1)$ and one of $\mathcal{O}(10^{-1})$ this is not the case [12, 136], deepening the mystery.

The quest for an explanation of this pattern, the so-called Flavor Puzzle, has attracted many physicists in the past, see Reference [18] for a review. Understanding a possible mechanism governing the value of the Standard Model parameters could, for example, hint to the absolute scale of neutrino masses [41] or predict the flavor structure of both light and heavy degrees of freedom in Beyond the Standard Model theories. Hence, solutions to the Flavor Puzzle can be linked to explanations of long-standing anomalies such as in B

meson decays [137, 138] or puzzles like the Strong CP Puzzle [38–41], providing a deeper insight into our world.

A plethora of ideas have been proposed as explanations for the Flavor Puzzle. Particularly nice resolutions are given by theories with flavor symmetries, for example in Froggatt-Nielsen-type models [139], where the spontaneous breaking of the flavor symmetry leads to hierarchical Yukawa matrices. Further attempts are based on extra dimensions with a hierarchy generated from the geometry of the extra dimension [140–142] or on a radiative generation of fermion masses [143–146], so that the Yukawa couplings of the first and second family are loop-suppressed. For reviews of these and other ideas see also References [18, 65, 147].

Specifically, models with a $U(2)$ flavor symmetry provide nice realizations of Froggatt and Nielsen’s idea and have been first proposed by Barbieri et al. [148, 149] in setups compatible with both supersymmetry (SUSY) and $SO(10)$ Grand Unification. However, these models were soon ruled out by precision data from B factories indicating a violation of the model prediction $\left| \frac{V_{ub}}{V_{cb}} \right| = \frac{m_u}{m_c}$ with the CKM matrix elements V_{ij} and up and charm quark masses m_u and m_c [150]. The same conclusion holds for a variant of these original $U(2)$ models where the $SU(2)$ factor is replaced by a discrete symmetry D_3 [151], which would have had the advantage of explaining the absence of additional Goldstone bosons from the spontaneous breaking of the flavor symmetry.

Still, it has been noticed during the last decade that the $U(2)$ framework is viable if one lifts the restriction to $SO(10)$ Grand Unification and demands compatibility with $SU(5)$ only [41, 152]. These models provide an excellent fit to current data and do not require supersymmetry at all [41]. Furthermore, viable models based on such a $U(2)$ flavor symmetry can be linked to other interesting phenomena such as axions [41] or explanations of the persisting B anomalies in scenarios with light Z' bosons [137] or leptoquarks [138].

These viable $U(2)$ models have also been successfully applied to the neutrino sector, yielding predictions for the absolute neutrino mass scale [41]. By choosing appropriate representations for the Standard Model fermions, Dirac-type neutrinos can be easily realized in the model. In particular, the overall neutrino mass scale is determined by the choice of sufficiently large $U(1)$ charges of the right-chiral neutrino fields, where the exact size of these charges can be inferred from the requirement that the observed neutrino mass differences should be reproduced by the model.

Majorana-type neutrinos in such a $U(2)$ scenario would need some tuning since the Weinberg operator [153] vanishes at leading order due to the antisymmetric $SU(2)$ -invariant [41]. A way out is provided if one restricts the $SU(2)$ factor to the discrete subgroup D_6 , which shares the phenomenologically essential features of $SU(2)$ but allows

Table 5.1: Representations of a $U(2)$ flavor symmetry for the Standard Model fields [41]. Q , u^c , and d^c denote the left-chiral quark doublet, up and down quark singlet, respectively, while L and ℓ^c represent the left-chiral lepton doublet and singlet, respectively. The index a indicates that the first two generations are combined into an $SU(2)$ doublet, while the index 3 refers to the third generation. H is the Standard Model Higgs field.

	Q_a	u_a^c	d_a^c	Q_3	u_3^c	d_3^c	L_a	ℓ_a^c	L_3	ℓ_3^c	H	φ	χ
$SU(2)$	2	2	2	1	1	1	2	2	1	1	1	2	1
$U(1)$	1	1	1	0	0	1	1	1	1	0	0	-1	-1

for the Weinberg operator due to a symmetric group invariant [41]. In this setup, the choice of the representations of the Standard Model fields *predicts* the neutrino mass matrix to be anarchic, leading to an even better fit to data despite fewer parameters [41].

An anarchic matrix features entries of the same size.

5.2 FERMION MASSES AND MIXINGS IN $U(2)$ -LIKE SCENARIOS

In this section, we briefly review the realistic $U(2)$ models introduced in References [41, 152]. The starting point of $U(2)$ models is the observation that the largest breaking of the $U(3)^5$ flavor symmetry of the kinetic part of the Standard Model is due to the large Yukawa coupling of the top quark. This separates the third generation from the first two, which motivates a remaining $U(2)$ symmetry for the latter. In particular, this idea is realized when the first two generations form a doublet, while the third generation resides in a singlet representation. Put differently, the three-dimensional representation comprising the families is decomposed as $\mathbf{3} = \mathbf{2} \oplus \mathbf{1}$.

One $U(3)$ symmetry for each type of Standard Model fields Q , u^c , d^c , L and ℓ^c .

The flavor symmetry cannot be exactly realized since otherwise the Yukawa couplings would in general be forbidden. Therefore, we introduce a spontaneous breaking by two spurion fields φ and χ called *flavons*, which are responsible for the breaking of the $SU(2)$ and $U(1)$ factors, respectively. If their vacuum expectation values v_φ and v_χ are smaller than the scale Λ of the UV completion, the ratios of these vacuum expectation values and the new scale Λ will be small numbers $\varepsilon_\varphi = \frac{v_\varphi}{\Lambda} \ll 1$ and $\varepsilon_\chi = \frac{v_\chi}{\Lambda} \ll 1$. These two small parameters ε_φ and ε_χ are the only small parameters in the setup and will explain all hierarchies in the flavor parameters.

A SPECIFIC MODEL Choosing the representations of the Standard Model fermion fields as in Table 5.1, the up-type quark Yukawa Lagrangian reads [41]

$$\begin{aligned}
\mathcal{L}_Y^u = & -\frac{\lambda_{11}^u}{\Lambda^6} \varphi_a^\dagger (Q_a H) \varphi_b^\dagger u_b^c \chi^4 & -\frac{\lambda_{12}^u}{\Lambda^2} \varepsilon_{ab} (Q_a H) u_b^c \chi^2 \\
& -\frac{\lambda_{22}^u}{\Lambda^2} \varepsilon_{ab} \varphi_a (Q_b H) \varepsilon_{\alpha\beta} \varphi_\alpha u_\beta^c & -\frac{\lambda_{13}^u}{\Lambda^3} \varphi_a^\dagger (Q_a H) u_3^c \chi^2 \\
& -\frac{\lambda_{23}^u}{\Lambda^2} \varepsilon_{ab} \varphi_a (Q_b H) u_3^c & -\frac{\lambda_{31}^u}{\Lambda^3} (Q_3 H) \varphi_a^\dagger u_a^c \chi^2 \\
& -\frac{\lambda_{32}^u}{\Lambda} (Q_3 H) \varepsilon_{ab} \varphi_a u_b^c & -\lambda_{33}^u (Q_3 H) u_3^c \\
& + \text{h.c.}
\end{aligned} \tag{5.1}$$

where $\varepsilon = (\varepsilon_{ab})$ is the two-dimensional Levi-Civita tensor in matrix form. Moreover, Q_a and u_a^c are the quark doublet and up-type quark singlet of generation $a = 1, 2, 3$, respectively, while H is the Higgs field and $(Q_i H)$ denotes the $SU(2)_L$ singlet contraction of the electroweak gauge group. The complex Wilson coefficients λ_{ij}^u should be chosen as being $\mathcal{O}(1)$ in order not to introduce any further hierarchy.

Once the flavor symmetry is broken and the flavons φ and χ acquire their vacuum expectation values $v_\varphi = \varepsilon_\varphi \Lambda$ and $v_\chi = \varepsilon_\chi \Lambda$, the Standard Model Yukawa couplings are restored. As a consequence, the up-type quark Yukawa matrix is given by [41]

We consider numbers between $\frac{1}{3}$ and 3 as desirable for $\mathcal{O}(1)$ quantities.

$$Y^u = \begin{pmatrix} \lambda_{11}^u \varepsilon_\varphi^2 \varepsilon_\chi^4 & \lambda_{12}^u \varepsilon_\varphi^2 & \lambda_{13}^u \varepsilon_\varphi \varepsilon_\chi^2 \\ -\lambda_{12}^u \varepsilon_\varphi^2 & \lambda_{22}^u \varepsilon_\varphi^2 & \lambda_{23}^u \varepsilon_\varphi \\ \lambda_{31}^u \varepsilon_\varphi \varepsilon_\chi^2 & \lambda_{32}^u \varepsilon_\varphi & \lambda_{33}^u \end{pmatrix} \approx \begin{pmatrix} 0 & \lambda_{12}^u \varepsilon_\varphi^2 & 0 \\ -\lambda_{12}^u \varepsilon_\varphi^2 & \lambda_{22}^u \varepsilon_\varphi^2 & \lambda_{23}^u \varepsilon_\varphi \\ 0 & \lambda_{32}^u \varepsilon_\varphi & \lambda_{33}^u \end{pmatrix}, \tag{5.2}$$

where we neglected the $(1,1)$, $(1,3)$ and $(3,1)$ entries in the last step which result in subleading contributions to quark masses and mixing angles. From the Yukawa coupling matrix it is apparent that the spurion vacuum expectation values introduce a hierarchical pattern in the Yukawa couplings even when the Wilson coefficients λ_{ij}^u are chosen as of $\mathcal{O}(1)$.

Similarly, one can derive the Yukawa matrices for down-type quarks,

$$Y^d \sim \begin{pmatrix} 0 & \varepsilon_\chi^2 & 0 \\ -\varepsilon_\chi^2 & \varepsilon_\varphi^2 & \varepsilon_\varphi \varepsilon_\chi \\ 0 & \varepsilon_\varphi & \varepsilon_\chi \end{pmatrix}, \tag{5.3}$$

omitting the $\mathcal{O}(1)$ Wilson coefficients λ_{ij}^d in each entry and showing only the leading elements.

The Yukawa matrices $Y^{u,d}$ are diagonalized by a singular value decomposition,

Note that the $(1,2)$ and $(2,1)$ entry are linked as $Y_{12}^{u,d} = -Y_{21}^{u,d}$ so that both depend on the same Wilson coefficient λ_{12}^d .

$$(V_L^{u,d})^\dagger Y^{u,d} V_R^{u,d} = \text{diag}(y_1^{u,d}, y_2^{u,d}, y_3^{u,d}), \tag{5.4}$$

with unitary matrices $V_{L,R}^{u,d}$. These unitary matrices can be parametrized in terms of three rotation angles, which are forced to be hierarchical by the hierarchical structure of the Yukawa matrices. For instance, the right-handed (2,3) rotation angle $\vartheta_{23}^{R,d}$ in the down-type sector is of $\mathcal{O}(1)$, $\vartheta_{23}^{R,d} \sim 1$, while the left-handed (2,3) rotation angle $\vartheta_{23}^{L,d}$ in the down-type sector is of $\mathcal{O}(\varepsilon_\varphi)$, $\vartheta_{23}^{L,d} \sim \varepsilon_\varphi \ll 1$, and thus small [41].

There are a three common properties of viable $U(2)$ Yukawa textures:

1. One needs a large right-handed rotation angle $\vartheta_{23}^{R,d}$ in the (2,3) sector of down-type quarks in order to fix the incorrect prediction of the first $U(2)$ models [41, 137, 152].
2. The (1,1), (1,3) and (3,1) entries can be approximated by zero at leading order, which mimics supersymmetric scenarios where these texture zeros are exact [152].
3. The (1,2) and (2,1) entries are linked as $Y_{12}^\alpha = -Y_{21}^\alpha$ for $\alpha = u, d$ by means of the antisymmetric $SU(2)$ invariant.

These properties are special features of the $2 \oplus 1$ representation structure and we will use these observations to constrain the form of the charged lepton mass matrix in the following.

CHARGED LEPTON MASSES A charged lepton Yukawa matrix with a $U(2)$ texture is determined by the choice of the representations of the lepton doublet L and the lepton singlet ℓ^c and should share the basic features observed for the quark sector. In particular, there are two viable choices for models of Grand Unification [41, 138, 152]:

1. **SU(5) GRAND UNIFICATION** In an $SU(5)$ -compatible model [41], the lepton doublet L shares the quantum numbers of the down-type quark singlet d^c , while the lepton singlet has those of the quark doublet Q . As a consequence, the orders of magnitude of the charged lepton matrix entries are the same as for the down-type quark matrix but with left and right rotations interchanged. Hence, the rotation angle $\vartheta_{23}^{L,\ell}$ of the left-handed (2,3) sector is of $\mathcal{O}(1)$ for charged leptons, while the right-handed (2,3) rotation $\vartheta_{23}^{R,\ell}$ is small, that is $\vartheta_{23}^{L,\ell} \sim \vartheta_{23}^{R,d} \sim 1$ and $\vartheta_{23}^{R,\ell} \sim \vartheta_{23}^{L,d} \sim \varepsilon_\varphi \ll 1$.
2. **PATI-SALAM UNIFICATION** In the case of a Pati-Salam scenario, the lepton doublet L is combined with the quark doublet Q in one representation, while the lepton singlet shares the quantum numbers of the down-type singlet d^c [138]. Consequently, we find the same structure as for the down-type quark Yukawa matrix in Equation (5.3) with a small left-handed (2,3) rotation $\vartheta_{23}^{L,\ell} \sim \vartheta_{23}^{L,d} \sim \varepsilon_\varphi \ll 1$ and an $\mathcal{O}(1)$ right-handed (2,3) rotation $\vartheta_{23}^{R,\ell} \sim \vartheta_{23}^{R,d} \sim 1$, which is opposite to the $SU(5)$ case.

Recall that $d^c, L \in \mathbf{5}$, while $Q, u^c, \ell^c \in \mathbf{10}$ in $SU(5)$ Grand Unification models.

Recall that due to color and lepton number being treated on equal footing, L becomes the “fourth color” of Q , while d^c is combined with ℓ^c , which is the correspondent of the lower component of the lepton doublet L , into an $SU(4)$ representation.

Denoting the charged lepton mass matrix as

$$M_\ell = \begin{pmatrix} 0 & m_{12}^\ell & 0 \\ -m_{12}^\ell & m_{22}^\ell & m_{23}^\ell \\ 0 & m_{32}^\ell & m_{33}^\ell \end{pmatrix}, \quad (5.5)$$

it can be diagonalized by a singular value decomposition,

$$(V_L^\ell)^\dagger M_\ell V_R^\ell = \text{diag}(m_e, m_\mu, m_\tau) \quad (5.6)$$

with electron, muon and tau masses m_e , m_μ and m_τ , respectively. The rotation matrices $V_{L,R}^\ell$ are unitary 3×3 -matrices that can be parametrized by three angles $\vartheta_{12}^{h,\ell}$, $\vartheta_{13}^{h,\ell}$ and $\vartheta_{23}^{h,\ell}$ as well as 6 phases $\alpha_{1,2}^{h,\ell}$, $\beta_{1,2,3}^{h,\ell}$ and $\delta^{h,\ell}$ with $h = L, R$. A convenient choice for the rotation matrix is the standard form of the Particle Data Group (PDG) [23], given by

$$V_h^\ell = P_h^{\ell'} V_{23}^{h,\ell} V_{13}^{h,\ell} V_{12}^{h,\ell} P_h^\ell. \quad (5.7)$$

Here, $P_h^\ell = \text{diag}(e^{i\alpha_1^{h,\ell}}, e^{i\alpha_2^{h,\ell}}, 1)$ and $P_h^{\ell'} = \text{diag}(e^{i\beta_1^{h,\ell}}, e^{i\beta_2^{h,\ell}}, e^{i\beta_3^{h,\ell}})$ are diagonal phase matrices and the rotation matrices read

$$V_{12}^{h,\ell} = \begin{pmatrix} c_{12}^{h,\ell} & s_{12}^{h,\ell} & 0 \\ -s_{12}^{h,\ell} & c_{12}^{h,\ell} & 0 \\ 0 & 0 & 1 \end{pmatrix}, \quad V_{23}^{h,\ell} = \begin{pmatrix} 1 & 0 & 0 \\ 0 & c_{23}^{h,\ell} & s_{23}^{h,\ell} \\ 0 & -s_{23}^{h,\ell} & c_{23}^{h,\ell} \end{pmatrix}, \quad (5.8)$$

$$V_{13}^{h,\ell} = \begin{pmatrix} c_{13}^{h,\ell} & 0 & s_{13}^{h,\ell} e^{-i\delta^{h,\ell}} \\ 0 & 1 & 0 \\ -s_{13}^{h,\ell} e^{i\delta^{h,\ell}} & 0 & c_{13}^{h,\ell} \end{pmatrix}$$

with the abbreviations $c_{ij}^{h,\ell} = \cos(\vartheta_{ij}^{h,\ell})$ and $s_{ij}^{h,\ell} = \sin(\vartheta_{ij}^{h,\ell})$.

The properties 2 and 3 above impose four complex constraints on the charged lepton matrix M_ℓ , indicating that not all parameters are independent quantities [41, 137]. Indeed, exploiting these conditions, the 6 rotation angles $\vartheta_{12,13,23}^{h,\ell}$ can be expressed in terms of just two angles, which can be chosen as the left- and right-handed (2,3) rotations $\vartheta_{23}^{L,\ell}$ and $\vartheta_{23}^{R,\ell}$ [137]. Specifically, we find for the unified scenarios:

1. SU(5) GRAND UNIFICATION Here, the right-handed (2,3) rotation is small, $s_{23}^{R,\ell} \ll 1$, while the left-handed angle $\vartheta_{23}^{L,\ell}$ is a free parameter of $\mathcal{O}(1)$. As a consequence, the sine of the (1,2) angle is given by [41]

$$s_{12}^{L,\ell} \approx \sqrt{\frac{m_e}{c_{23}^{L,\ell} m_\mu}} \quad (5.9)$$

That is
 $m_{11}^\ell = m_{13}^\ell = m_{31}^\ell = 0$
and $m_{12}^\ell = -m_{21}^\ell$.

with $c_{23}^{L,\ell} \gtrsim \frac{m_e}{m_\mu}$ and the (1,3) rotation is small, $s_{13}^{L,\ell} \ll 1$. Hence, the (1,3) rotation can be neglected, while the (1,2) and (2,3) rotations could be sizable. Ignoring phases, this yields the left-handed rotation matrix

$$V_5^{L,\ell} \approx V_{23}^{L,\ell} V_{12}^{L,\ell} = \begin{pmatrix} c_{12}^{L,\ell} & s_{12}^{L,\ell} & 0 \\ -c_{23}^{L,\ell} s_{12}^{L,\ell} & c_{23}^{L,\ell} c_{12}^{L,\ell} & s_{23}^{L,\ell} \\ s_{23}^{L,\ell} s_{12}^{L,\ell} & -s_{23}^{L,\ell} c_{12}^{L,\ell} & c_{23}^{L,\ell} \end{pmatrix}. \quad (5.10)$$

In this approximation, only two independent linear combinations β_1 and β_2 of the twelve phases enter the physical quantities of interest. As a result, the left-handed charged lepton rotations are at leading order characterized by three real parameters only: the angle $\vartheta_{23}^{L,\ell}$ and the two effective phases β_1 and β_2 .

2. **PATI-SALAM UNIFICATION** Here, both left-handed (2,3) and (1,3) rotations are small, $s_{23}^{L,\ell} \ll 1$ and $s_{13}^{L,\ell} \ll 1$. This leaves us with [138]

$$s_{12}^{L,\ell} \approx \sqrt{\frac{c_{23}^{R,\ell} m_e}{m_\mu}} \quad (5.11)$$

to consider, where the right-handed (2,3) rotation is of $\mathcal{O}(1)$. Up to phases, we find the left-handed rotation matrix in this scenario to be

$$V_{\text{PS}}^{L,\ell} \approx V_{12}^{L,\ell} = \begin{pmatrix} c_{12}^{L,\ell} & s_{12}^{L,\ell} & 0 \\ -s_{12}^{L,\ell} & c_{12}^{L,\ell} & 0 \\ 0 & 0 & 1 \end{pmatrix}. \quad (5.12)$$

Moreover, the number of physical phases reduces to one which we denote by β . Thus, the left-handed charged lepton rotation is described by only two parameters at leading order, namely the angle $\vartheta_{23}^{R,\ell}$ and the effective phase β .

In both cases, the right-handed rotation matrices can be obtained similarly but are not of interest in the following.

5.3 MAJORANA NEUTRINOS IN U(2)-LIKE SCENARIOS

Proving successful in the quark sector, it is interesting to apply the $U(2)$ symmetry to neutrinos to check whether the yet unknown mass scale and phases in the PMNS matrix could be predicted. However, this analysis depends on whether neutrinos are of Dirac or Majorana type, so we have to analyze these cases separately.

Analogously to the CKM matrix only the left-handed rotations enter the PMNS matrix as a consequence of the absent right-chiral weak interactions.

DIRAC NEUTRINOS Dirac-type neutrinos are straightforward to include [41]: First, we introduce the right-chiral neutrino field N_i^c as a gauge singlet to the Standard Model field content with i being the generation index. Next, we choose representations under the flavor $U(2)$ group for these new fields. A reasonable choice is given by a $U(2)$ doublet for the first two generations and a singlet for the third family as for the other fermions [41], but with unfixed $U(1)$ charges X_a^N for the doublet and X_3^N for the singlet. Since the PMNS matrix features only a mild hierarchy, one expects equal charges $X_a^N = X_3^N$ to work well in order to obtain large mixing angles from the neutrino sector, which are needed to dominate over the partly small left-handed rotations of charged leptons.

Indeed, equal charges of $X_a^N = X_3^N = 5, 6$ provide the best fit to data which includes the measured neutrino parameters [41]. The large charges are needed to suppress the overall neutrino mass scale, which is essentially given by the square roots of the small mass-squared differences $\Delta m_{21}^2 = 7.42 \times 10^{-5} \text{ eV}^2$ and $\Delta m_{31}^2 = 2.514 \times 10^{-3} \text{ eV}^2$ [12, 136] due to a small hierarchy induced by the flavor symmetry.

MAJORANA NEUTRINOS Majorana neutrinos are particularly appealing since they could be linked to several puzzles in the Standard Model. For instance, Majorana neutrinos arise in the seesaw mechanism possibly explaining the smallness of neutrino masses or could allow for the generation of lepton number in the early universe due to their lepton number violating nature in a process called *Leptogenesis*, see Reference [9] for a review.

Instead of discussing one of the many possible UV-complete theories, it is convenient to consider the dimension-five Weinberg operator [153]

$$\mathcal{L}_{\text{Weinberg}} = -\frac{y}{2M}(LH)(LH), \quad (5.13)$$

where y is a dimensionless Yukawa coupling, M is the Majorana mass scale and (LH) is the electroweak $SU(2)_L$ singlet contraction of the Standard Model lepton and Higgs doublets L and H , respectively. The Weinberg operator provides a model-independent way to incorporate a Majorana neutrino mass term in the theory without the need for additional fields.

Augmenting the Weinberg operator with a $U(2)$ flavor symmetry we encounter a problem: Since the representation of the lepton doublet L is already fixed by the requirement that charged lepton masses are reproduced, there is no freedom to choose representations to obtain the correct neutrino parameters. Instead, the neutrino mass pattern is predicted by the Standard Model representations. In the case of the viable $U(2)$ models reviewed in the previous section, however, the leading term in the $(1,2)$ and $(2,1)$ entries of the Yukawa matrices vanishes due to the antisymmetric $SU(2)$ invariant, $\varepsilon_{ab}L_aL_b = 0$,

leading to a vanishing Weinberg operator. Therefore, the (1,2) and (2,1) components receive a further suppression by ε_φ^2 so that the (1,2) PMNS angle $\vartheta_{12} \sim \mathcal{O}(\varepsilon^2)$ is much smaller than the observed value of $\vartheta_{12} \sim 0.6$ [41].

As a consequence, Majorana neutrinos in realistic models would need some degree of fine-tuning in the Yukawa couplings not being $\mathcal{O}(1)$ anymore [41]. A way out is provided by replacing the $SU(2)$ factor of the flavor symmetry by the discrete dihedral group D_6 [41]. Within this group, one can assign representations to all fields such that the basic texture of the Yukawa matrices (5.2), (5.3) and (5.5) is maintained but with symmetric instead of antisymmetric (1,2) and (2,1) entries, that is with $Y_{12}^i = Y_{21}^i$ for $i = u, d, \ell$. Consequently, the symmetric (1,2) entries in the Weinberg operator are now allowed at leading order. While quark masses and mixings as well as charged lepton masses are still reproduced despite the different sign, the Weinberg operator now leads to an anarchic Yukawa texture [41]

$$Y^\nu \approx \frac{v}{M} \begin{pmatrix} 0 & \lambda_{12}^y \varepsilon_\chi^2 & 0 \\ \lambda_{12}^y \varepsilon_\chi^2 & \lambda_{22}^y \varepsilon_\varphi^2 & \lambda_{23}^y \varepsilon_\varphi \varepsilon_\chi \\ 0 & \lambda_{23}^y \varepsilon_\varphi \varepsilon_\chi & \lambda_{33}^y \varepsilon_\chi^2 \end{pmatrix} \quad (5.14)$$

with the electroweak vacuum expectation value v . This corresponds to the well-studied “ A_2 ” texture [154–163] with two texture zeros, which are, however, again only approximate zeros and not exact ones. The use of the Weinberg operator for neutrino mass generation makes the model very predictive: The mild hierarchies in the neutrino sector are a *consequence* of the representations of the charged leptons and not an additional input. Moreover, the model leads to a better fit to data than the Dirac version despite the reduced number of free parameters due to the symmetric nature of the Weinberg operator [41].

In the neutrino Yukawa matrix (5.14), all relevant entries of the same order and the properties of a $U(2)$ texture are still maintained, except that the matrix is now symmetric. As a complex symmetric matrix, it can be diagonalized by a Takagi decomposition,

$$(V^\nu)^\top Y^\nu V^\nu = \text{diag}(y_1, y_2, y_3), \quad (5.15)$$

with a single unitary matrix V^ν .

The comparison of this model to all available data, that is the masses of quarks and charged leptons, the mass-squared differences of neutrino masses and the parameters of the CKM and PMNS matrix, leads to an excellent fit with all Wilson coefficients λ_{ij}^a for $a = u, d, \ell, N$ being between $\frac{1}{3}$ and 2 [41]. If one scans the parameter space of successful fits, one finds a narrow range allowed for the neutrino mass scale [41]. In particular, the sum of neutrino masses is found to be less than $\sum m_\nu \lesssim 78 \text{ meV}$ and thus near the minimal possible value [41].

This is due to two additional insertions of the φ_a spurion.

The dihedral group D_6 is the symmetry group of a regular hexagon.

The scale of the neutrino Yukawa couplings y^ν is given by $y^\nu \sim \frac{v}{M} \varepsilon^2$ which reproduces the observed values for $M \sim 10^{10} \text{ GeV}$ [41].

Recall that $\sum m_\nu \gtrsim 58 \text{ meV}$ where the minimum is saturated for the lightest neutrino being massless.

In this work, we statistically analyze whether these predictions can be further pinned down and whether predictions for the unknown phases can be made. Furthermore, we extend the predictions for neutrino observables to the Pati-Salam-type models in order to check their robustness with respect to variations of the model.

The predictions of flavor symmetries for neutrino observables could not only hint at the values of the currently unknown parameters, but also provide an important test for such models.

In this chapter, we study the consequences of a $U(2)$ -like flavor symmetry on neutrino mass observables and the Dirac CP phase of the lepton sector. We begin with a short review of the current experimental status of these quantities in Section 6.1. Next, we show that the $U(2)$ texture implies a relation between the mass parameters and phases and the neutrino rotation angles, and we introduce scenarios parametrizing the influence of the charged lepton sector in Section 6.2. Finally, we present the statistical methods applied in this work in Section 6.3, before we discuss the results in Section 6.4.

This chapter is based on the publication

Matthias Linster, Jacobo Lopez-Pavon, and Robert Ziegler.
 “Neutrino Observables from a $U(2)$ Flavor Symmetry.”
Phys. Rev. D 103.1 (2021), p. 015020. DOI: [10.1103/PhysRevD.103.015020](https://doi.org/10.1103/PhysRevD.103.015020). arXiv: [2009.10437](https://arxiv.org/abs/2009.10437) [hep-ph] .

6.1 THE STATUS OF NEUTRINO PROPERTIES

Despite the weakness of neutrino interactions, neutrino experiments have entered the precision era with percent-level uncertainties [12, 136]. Currently, five neutrino parameters are known with high precision: the three mixing angles ϑ_{ij} of the PMNS matrix and the two mass-squared differences $\Delta m_{ij}^2 = m_i^2 - m_j^2$. Nevertheless, there are quantities that still need to be measured.

The Dirac CP phase δ is up to a precise determination in the coming years and global analyses already start to pin down its value—although not yet at a statistically significant level [12, 136]. In particular, there is a tension between recent data from T2K [164] and NOvA [165] long baseline neutrino oscillation experiments, which yield central values of $\delta \approx 250^\circ$ and $\delta \approx 150^\circ$, respectively, for normal ordered neutrinos. There would be a 3σ evidence for CP violation if inverted hierarchy was realized in nature [12, 136]. Next generation experiments like T2HK [166] and DUNE [167] are expected to achieve a 10–20° precision on the CP violating phase δ , which helps to distinguish the orderings.

Another important open question concerns neutrino masses: While the mass-squared differences can be inferred from the oscillation frequencies, the absolute scale has to be extracted from other experiments. The

Note however that there is still a large uncertainty for the (2,3) angle ϑ_{23} at the 3σ level.

Recall that the mass orderings $m_1 < m_2 < m_3$ (normal ordering) and $m_3 < m_1 < m_2$ (inverted ordering) cannot be distinguished by current data, although normal ordering is slightly preferred [12, 136].

current best bound of $m_\beta \lesssim 0.8 \text{ eV}$ on the effective beta decay mass $m_\beta = \sqrt{\sum_i |U_{ei}|^2 m_i^2}$ with the PMNS matrix U was recently obtained by the KATRIN collaboration [51]. Their expected sensitivity after the full run is about 0.2 eV at 90 % confidence level, with a possible further improvement down to 0.04 eV by the future Project 8 Neutrino-Mass Experiment [168].

In particular, the Λ CDM model is assumed.

On the other hand, cosmological observations and in particular the analysis of the Cosmic Microwave Background (CMB) combined with Baryon Acoustic Oscillations (BAO) yield much stronger limits on the sum of neutrino masses of $\sum_i m_i \lesssim 0.12 \text{ eV}$ [1], although this is only an indirect bound depending on assumptions on the cosmological model. Cosmic Microwave Background (CMB) satellites nearly disfavor the full parameter space $(\sum_i m_i)_{\text{IO}} \gtrsim 0.1 \text{ eV}$ of inverted hierarchy at 95 % confidence level. Further improvements are expected by next-generation satellites like EUCLID [169] and DESI [170] which aim at a measurement of the sum with an uncertainty of 0.02 eV.

If neutrinos are of Majorana-type, the possibility to look for neutrinoless double beta decay ($0\nu\beta\beta$) arises, which is sensitive to the effective Majorana mass $m_{\beta\beta} = |\sum_i U_{ei}^2 m_i|$. KamLAND-Zen reports an upper bound of $m_{\beta\beta} \lesssim 0.061\text{--}0.165 \text{ eV}$ at 90 % confidence level [52], where the range arise from large uncertainties in nuclear matrix elements. Next-generation experiments like LEGEND [171] and nEXO [172] target at an improvement of about one order of magnitude, thus allowing to probe the entire parameter space of inverted hierarchy neutrinos.

The current constraints on the $m_{\beta\beta}$ - $\sum m_i$ parameter space at 95.4 % confidence level are displayed in Figure 6.1. Note that the effective beta decay mass m_β is directly related to the sum up to small uncertainties in the PMNS angles, since any phases drop out in the modulus of the PMNS matrix elements. Hence, plots with m_β do not contain any additional significant information compared to those with the sum $\sum_i m_i$.

6.2 SCENARIOS FOR $U(2)$ -LIKE SYMMETRIES

It is appealing to predict the undetermined neutrino quantities from the ones that are already measured in the context of motivated models with only a few parameters. In this work, we analyze the predictions if one additionally imposes a $U(2)$ -like flavor symmetry as described in Chapter 5. Indeed, neutrino observables provide an interesting test of $U(2)$ -like flavor symmetries besides the successful fit of quark and charged lepton masses and CKM parameters.

In order to do so, we recognize that the characteristic $U(2)$ Yukawa textures are linked to the particle masses by unitary rotation matrices $V_{L,R}^\ell$ and V^ν , see Equations (5.6) and (5.15), which themselves yield the PMNS matrix

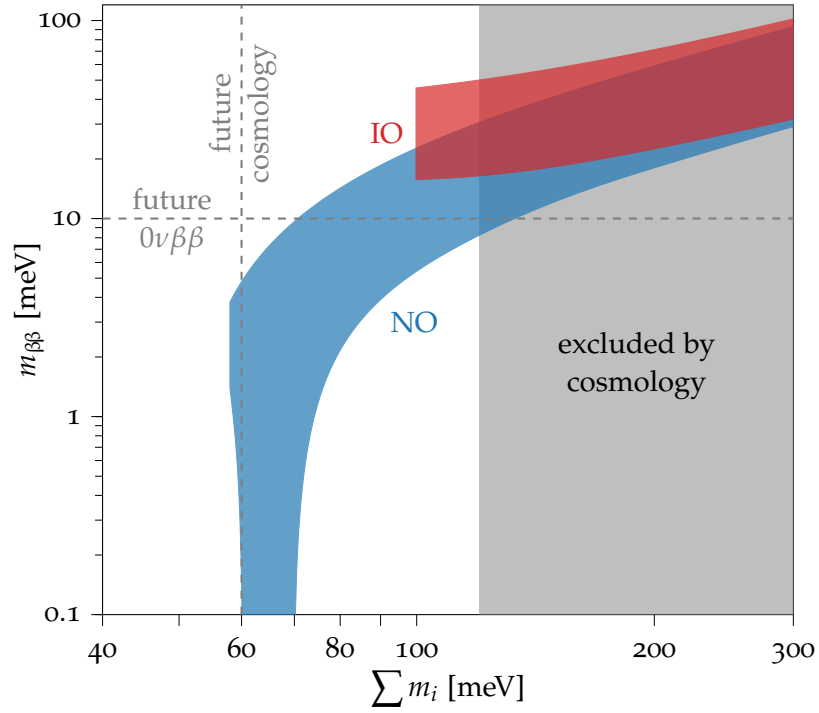


Figure 6.1: Allowed parameter space in the $m_{\beta\beta}$ - $\sum_i m_i$ plane at 95.4% confidence level as obtained by minimizing the NuFIT likelihood [12, 136] at each point. We do not show the current limits from the neutrino-less beta decay ($0\nu\beta\beta$) experiments due to large uncertainties in the nuclear matrix elements. The dashed lines indicate projected sensitivities of future experiments. This plot has been adapted from Reference [134] by removing the model constraints.

$$U = (V_L^\ell)^\dagger V^\nu. \quad (6.1)$$

The unitary PMNS matrix U can be decomposed as in Equation (5.7) so that in principle it depends on three angles ϑ_{ij} and six phases $\delta, \alpha_{1,2}$ and $\beta_{1,2,3}$. The rephasing freedom of charged leptons allows to absorb the β_i phases into the charged lepton fields, hence only the Dirac CP phase δ and the two Majorana phases $\alpha_{1,2}$ are physical in the case of Majorana neutrinos.

Therefore, the PMNS parameters can be obtained in terms of the rotations V_L^ℓ and V^ν which connect flavor and mass basis and which are determined by the $U(2)$ symmetry. We will analyze these relations in the following.

A Majorana field ψ_M cannot absorb a phase factor due to the reality condition $\psi_M^c = \psi_M$. The absence of this condition for Dirac spinors also allows to absorb the Majorana phases α_i into the neutrino fields for Dirac neutrinos.

NEUTRINO MASSES AND PHASES FROM A $U(2)$ TEXTURE As discussed in Section 5.3, a Majorana mass matrix with $U(2)$ texture, see Equation (5.14),

$$M^\nu = \begin{pmatrix} 0 & m_{12}^\nu & 0 \\ m_{12}^\nu & m_{22}^\nu & m_{23}^\nu \\ 0 & m_{23}^\nu & m_{33}^\nu \end{pmatrix} = (V^\nu)^* \text{diag}(m_1, m_2, m_3) (V^\nu)^\dagger, \quad (6.2)$$

features two approximate texture zeros $M_{11}^\nu, M_{13}^\nu \approx 0$. Parametrizing the neutrino rotation matrix as in Equation (5.7), the vanishing $(1,1)$ and $(1,3)$ entries impose two complex conditions on the rotation parameters,

$$\frac{m_1}{m_3} e^{i\tilde{\alpha}_1} + (t_{12}^\nu)^2 \frac{m_2}{m_3} e^{i\tilde{\alpha}_2} + \frac{(t_{13}^\nu)^2}{(c_{12}^\nu)^2} e^{-i\delta^\nu} = 0, \quad (6.3)$$

$$\frac{m_1}{m_3} e^{i\tilde{\alpha}_1} - \frac{m_2}{m_3} e^{i\tilde{\alpha}_2} + A = 0. \quad (6.4)$$

Here, we abbreviated $t_{ij}^\nu = \tan(\vartheta_{ij}^\nu)$, $\tilde{\alpha}_i = 2\alpha_i^\nu + \delta^\nu$ and defined

$$A = \frac{t_{13}^\nu}{c_{13}^\nu c_{12}^\nu s_{12}^\nu t_{23}^\nu}. \quad (6.5)$$

Taking real and imaginary parts and combining these two complex equations, one can express four real quantities in terms of the others. Since the rotation angles will be related to the already measured PMNS angles, it is particularly convenient to find expressions for the unknown neutrino mass scale m_1 and the three phases $\tilde{\alpha}_{1,2}$ and δ^ν . As a result, we find an equation

Note that you can relate the other masses $m_{2,3}$ to m_1 by $m_i^2 = \Delta m_{i1}^2 + m_1^2$.

$$(t_{13}^\nu)^4 = \frac{m_1^2}{m_1^2 + \Delta m_{31}^2} + (s_{12}^\nu)^2 \frac{\Delta m_{21}^2}{m_1^2 + \Delta m_{31}^2} - (s_{12}^\nu)^2 (c_{12}^\nu)^2 A^2 \quad (6.6)$$

yielding the mass m_1 in terms of the neutrino angles θ_{ij}^ν and mass-squared differences Δm_{ij}^2 . Afterwards, the solution to this equation can be used to determine the phases up to signs as

$$\cos(\delta^\nu) = \frac{A}{2(t_{13}^\nu)^2} \left[1 - 2(s_{12}^\nu)^2 - \frac{\Delta m_{21}^2}{m_3^2 A^2} \right], \quad (6.7)$$

$$\cos(\tilde{\alpha}_1) = \frac{\Delta m_{21}^2 - m_3^2 A^2}{2m_1 m_3 A}, \quad (6.8)$$

$$\cos(\tilde{\alpha}_2) = \frac{\Delta m_{21}^2 + m_3^2 A^2}{2m_2 m_3 A}, \quad (6.9)$$

where $m_i = \sqrt{\Delta m_{i1}^2 + m_1^2}$ for $i = 2, 3$. Due to the symmetry of the cosine, two signs are possible for each phase which leads to eight possible sign combinations. However, all phases must have equal sign as can be seen as follows:

1. The imaginary part of Equation (6.4) can be rearranged as

$$\frac{\sin(\tilde{\alpha}_1)}{\sin(\tilde{\alpha}_2)} = \frac{m_2}{m_1} > 0 \quad (6.10)$$

so that $\tilde{\alpha}_1$ and $\tilde{\alpha}_2$ must have equal sign,

$$\text{sign}(\tilde{\alpha}_1) = \text{sign}(\tilde{\alpha}_2). \quad (6.11)$$

2. Taking the imaginary part of Equation (6.3), one finds

$$\sin(\delta^\nu) = \frac{(c_{12}^\nu)^2}{(t_{13}^\nu)^2} \left[\frac{m_1}{m_3} \sin(\tilde{\alpha}_1) + (t_{12}^\nu)^2 \frac{m_2}{m_3} \sin(\tilde{\alpha}_2) \right], \quad (6.12)$$

where the right-hand side is larger than zero in the case of positive $\sin(\tilde{\alpha}_1) > 0$ and $\sin(\tilde{\alpha}_2) > 0$ and smaller than zero otherwise. Hence, also δ^ν must have the same sign as the phases $\tilde{\alpha}_{1,2}$. Hence,

$$\text{sign}(\delta^\nu) = \text{sign}(\tilde{\alpha}_1) = \text{sign}(\tilde{\alpha}_2). \quad (6.13)$$

In conclusion, given a set of the neutrino angles and mass-squared differences there exist either two possible solutions for the neutrino mass scale and phases or none at all.

DIAGONAL CHARGED LEPTON SCENARIO In a first approximation, one can neglect the contribution of charged leptons to the PMNS matrix U as defined in Equation (6.1), that is by approximating $U \approx V^\nu$. We call this case the *Diagonal Charged Lepton scenario*. Since charged leptons are expected to yield only a small correction to neutrino observables, the results of this scenario will serve as a useful reference point for cases with charged lepton effects included.

This expectation results from the need of a hierarchical Yukawa matrix to explain the charged lepton masses.

Table 6.1: Predictions for the neutrino parameters in the Diagonal Charged Lepton scenario for normal (NO) and inverted ordering (IO), assuming NuFIT central values. The values are published in Reference [134].

	m_1 [meV]	δ [°]	$\sum_i m_i$ [meV]	m_β [meV]	$m_{\beta\beta}$ [meV]
NO	5	(76, 284)	65	10	0
IO	not possible				

In this scenario, the PMNS parameters will coincide with the ones from the neutrino rotation matrix V^ν , $\vartheta_{ij} = \vartheta_{ij}^\nu$, $\delta = \delta^\nu$ and $\alpha_{1,2} = \alpha_{1,2}^\nu$. Therefore, Equations (6.6)–(6.9) yield the first neutrino mass m_1 as well as the three phases δ and $\alpha_{1,2}$ immediately in terms of the already measured PMNS parameters. This fact makes this scenario very predictive with the only unknown being the sign of the phases.

Indeed, we obtain the predictions in Table 6.1 when we plug in the current NuFIT central values [12, 136]. The low overall mass scale results in a sum $\sum_i m_i$ near the minimal possible value. Hence, the sum automatically satisfies the current bound from cosmology [1], while the effective beta decay mass m_β is too low to be observed by KATRIN [51] or Project 8 [168]. For the Dirac phase, we obtain a value near the one obtained by T2K [164].

The zero (1,1) entry of the $U(2)$ texture implies a vanishing effective Majorana mass,

$$m_{\beta\beta} = \left| \sum_i U_{ei}^2 m_i \right| = m_3 (c_{12}^\nu)^2 (c_{13}^\nu)^2 |M_{11}^\nu| = 0. \quad (6.14)$$

Hence, also the Majorana mass $m_{\beta\beta}$ is well below the experimental reach. From this observation and Figure 6.1, it is evident that both the sum of neutrino masses $\sum_i m_i$ and the effective beta decay mass m_β also need to be small since a vanishing Majorana mass $m_{\beta\beta}$ is only possible for a narrow range of the sum. Moreover, inverted hierarchy is also excluded since the different terms in the Majorana mass cannot cancel if m_3 is too small so that $m_{\beta\beta}$ will be non-zero, see Figure 6.1. The results of a more extensive analysis including uncertainties are presented in Section 6.4.

This would actually imply that the neutrino-less double beta decay is absent, since its decay rate is proportional to the Majorana mass, $\Gamma_{0\nu\beta\beta} \sim m_{\beta\beta}^2$ [9].

U(2) SCENARIOS In realistic scenarios, charged leptons could yield a sizable effect and cannot be neglected when one of the left-handed rotation angles is large. In particular, additional phases in the charged lepton sector can smear out the predictions for the Dirac CP phase δ or the Majorana phases $\alpha_{1,2}$ and the valid range for the overall neutrino mass scale might be modified. In order to estimate the effect of charged leptons, one needs to make assumptions on the texture of their Yukawa matrix.

In this work, we assume a $U(2)$ texture also for the charged lepton sector. In principle, viable unified $U(2)$ models allow for two possible textures being compatible with either $U(5)$ or Pati-Salam Grand Unification, see Section 5.2. As it was discussed, the conditions on a $U(2)$ texture allow us to relate the rotation parameters, severely constraining the charged lepton rotation matrix. In particular, the $U(5)$ case is described by the rotation matrix in Equation (5.10) with one additional rotation angle $\vartheta_{23}^{L,\ell}$ and two additional phases $\beta_{1,2}$, while Pati-Salam models depend only on one angle $\vartheta_{23}^{R,\ell}$ and one additional phase β , giving the rotation matrix in Equation (5.12).

Since only the left-handed rotations are important for phenomenology, we note that all left-handed angles in the Pati-Salam case, which we refer to as the $U(2)_{\text{PS}}$ or *Pati-Salam scenario*, are small. This holds in particular for the (1,2) angle which is bounded by $s_{12}^{L,\ell} \leq \sqrt{\frac{m_e}{m_\mu}} \simeq 0.07$. As a consequence, we do not expect any large deviations of the Pati-Salam scenario from the Diagonal Charged Lepton scenario, except that the additional phases now spoil the vanishing Majorana mass $m_{\beta\beta}$ and the predictions for the CP phase δ . For later use, we express the neutrino parameters needed for the calculation of the neutrino masses according to Equation (6.6) in terms of the PMNS angles and phases in Appendix B.1.

By contrast, both the (1,2) and the (2,3) rotation in the $U(5)$ case, which we call the $U(2)_5$ or $U(5)$ *scenario*, can be sizable. Therefore, the contribution of the charged lepton sector to the PMNS matrix and its related observables could be large so that we expect a deviation from the Diagonal Charged Lepton scenario. As a consequence, inverted hierarchy neutrinos might be allowed. Again, we show the neutrino rotation parameters in terms of the PMNS parameters in Appendix B.1. Since the charged lepton rotation angles and phases are free parameters that cannot be determined experimentally in the Standard Model, predictions of the central values for the neutrino observables cannot be obtained for the $U(2)$ scenarios, which was possible in the Diagonal Charged Lepton scenario. Hence, we will perform a statistical analysis in Section 6.4.

6.3 DESCRIPTION OF THE STATISTICAL ANALYSIS

In order to pin down the predictions of $U(2)$ -like models for neutrino observables, we perform a Bayesian analysis in the following. This method also allows us to obtain information on the uncertainty intervals and possible correlations which could help to confirm or exclude certain models. We restrict our analysis to the three scenarios presented in Section 6.2.

PARAMETERS OF THE SCENARIOS The three scenarios differ in the number of free parameters. Common parameters to all scenarios are

Note that the charged lepton parameters might be correlated to other observables in the presence of additional dynamics such as a light axion field [41].

Table 6.2: Summary of the input parameters of the three scenarios where DCL refers to the Diagonal Charged Lepton scenario, see Section 6.2 for more details. Note that $\ell = 1$ for normal ordering and $\ell = 2$ for inverted ordering.

Parameter	DCL	$U(2)_{\text{PS}}$	$U(2)_5$	prior
PMNS parameters	$\vartheta_{12}, \vartheta_{13}, \vartheta_{23}, \Delta m_{21}^2, \Delta m_{3\ell}^2$	NuFIT χ^2 [12, 136]		
charged lepton angle	—	$\vartheta_{23}^{\text{R},\ell}$	$\vartheta_{23}^{\text{L},\ell}$	flat
charged lepton phases	—	β	β_1, β_2	flat

the angles ϑ_{12} , ϑ_{13} and ϑ_{23} of the PMNS matrix and the mass-squared differences Δm_{21}^2 and Δm_{31}^2 , for which information is provided by global fits such as NuFIT [12, 136]. In principle, one could also add the Dirac CP phase δ to the list of input parameters, but we refrain from doing so since the uncertainties on this parameter are large and there is a slight tension in T2K [164] and NOvA [165] data at the moment. While we think that this procedure is currently appropriate, one should include the CP phase δ to the list of inputs as soon as its uncertainty has significantly decreased.

While the PMNS angles and the mass differences form the full input for the Diagonal Charged Lepton scenario, the $U(2)_5$ and $U(2)_{\text{PS}}$ scenarios feature additional variables related to the charged lepton sector. In particular, these are one angle $\vartheta_{23}^{\text{R},\ell}$ or $\vartheta_{23}^{\text{L},\ell}$ for the $U(2)_{\text{PS}}$ or $U(2)_5$ case, respectively, as well as one or two phases β or $\beta_{1,2}$ for the $U(2)_{\text{PS}}$ and $U(2)_5$ scenarios, respectively. We assume flat prior distributions for these input parameters.

The parameters and their assumed prior distributions are summarized in Table 6.2.

STATISTICAL ANALYSIS In this work, we perform a Bayesian analysis of the scenarios for a given neutrino mass ordering according to the following steps:

1. We draw a random sample of the model parameters from the probability distributions indicated in Table 6.2. In particular, we use the NuFIT χ^2 to infer the probability distributions for the PMNS parameters and the mass-squared differences, where we use the two-dimensional projection for $(s_{23}, \Delta m_{31}^2)$ and the one-dimensional projections for all other parameters. The unknown charged lepton parameters are chosen from flat priors on their range of validity in the case of the $U(2)$ scenarios.
2. The neutrino rotation parameters are given by the PMNS parameters in the Diagonal Charged Lepton scenario, while we calculate them in the $U(2)_{\text{PS}}$ and $U(2)_5$ scenarios from formulas (B.6)–(B.8) and (B.16)–(B.18), respectively. This allows us to

The probability distribution p as a function of the PMNS parameters and mass-squared differences can be obtained as $p = N e^{-\frac{1}{2}\chi^2}$ with a proper normalization N .

derive the lightest neutrino mass m_1 using Equation (6.6), the Dirac CP phase (6.7) and the two Majorana phases from Equations (6.8) and (6.9).

3. Next, we compute the sum of neutrino masses $\sum_i m_i$, the effective beta decay mass m_β and the effective Majorana mass $m_{\beta\beta}$ and determine their posterior distributions using histograms with a suitable binning. If there are two solutions we add them with a weight of $\frac{1}{2}$.
4. Finally, we derive constraints at $p\%$ confidence level by choosing a threshold number such that all bins with a count larger than this threshold sum up to $p\%$ of the points generated.

This is statistically equivalent to the random choice of one of the solutions.

In the case of the Diagonal Charged Lepton scenario, we also performed a frequentist analysis by minimizing the NuFIT likelihood for each point in the parameter space. While this approach is numerically challenging due to the non-linear constraints imposed on the neutrino parameters and the flat directions for the unknown parameters, we obtain similar results for the frequentist and Bayesian approach in the Diagonal Charged Lepton scenario. Based on this observation, we do not expect large deviations in a frequentist analysis of the $U(2)$ -motivated models compared to the Bayesian method.

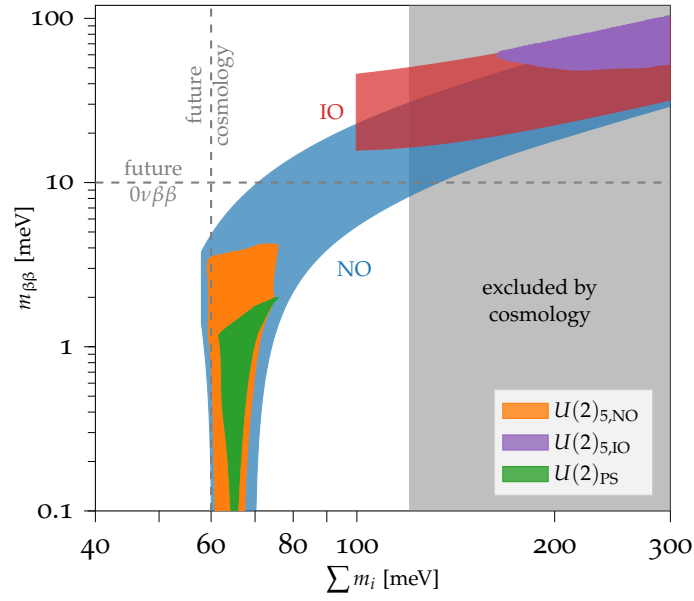
TECHNICAL IMPLEMENTATION Our sampling code has been implemented in the programming language C++, combining several external libraries for specific tasks. In particular, we approximate the χ^2 data points provided by NuFIT [12, 136] using linear interpolation with splines in one or two dimensions using the GNU Scientific Library. In order to solve the equations, we employ the Hybrids algorithm from that library, which we start 100 times at different initial points sampled from a quasi random Sobol sequence to obtain all solutions. Specifically, we use the Sobol sequence implementation in CERN's ROOT framework [173, 174], which also provides us with classes for histograms and data export. The ROOT framework is also used to sample points from the NuFIT likelihood, where we pass the interpolated functions to TF1 and TF2 objects offering a sampling of points distributed according to the function defined. A random subset of the generated points is extracted and exported to Mathematica, where we assert the numerical reliability.

6.4 RESULTS

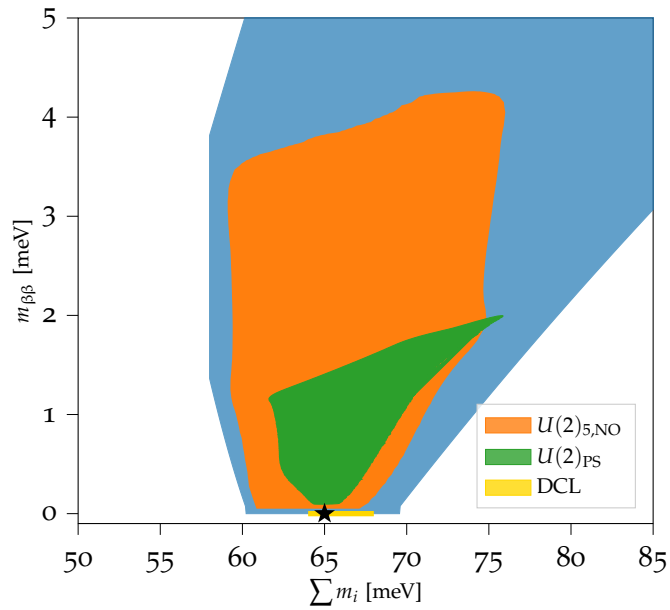
We have performed the analysis for the three scenarios separately, each with normal and inverted hierarchy. The results are shown in Table 6.3 as well as in Figures 6.2 and 6.3. Note that we do not show plots for the effective beta decay mass m_β since it is correlated with the sum of neutrino masses.

Table 6.3: Predictions for the neutrino observables as obtained from the Bayesian analysis described in Section 6.3. The confidence intervals are defined as containing 68.3%, 95.4% and 99.7% of the points for 1σ , 2σ and 3σ , respectively, and the central value quoted corresponds to the most likely value. Note that we found no solution for inverted hierarchy in the Diagonal Charged Lepton (DCL) and Pati-Salam scenario $U(2)_{\text{PS}}$. The values are published in Reference [134].

Scenario	NO/IO	$\sum m_i$ [meV]	m_β [meV]	$m_{\beta\beta}$ [meV]
DCL	NO	$65.0^{+0.9}_{-0.6}$	$10.0^{+0.3}_{-0.2}$	0^{+0}_{-0}
		$(64 \rightarrow 68)_{2\sigma}$	$(10 \rightarrow 11)_{2\sigma}$	$(0 \rightarrow 0)_{2\sigma}$
		$(63 \rightarrow 69)_{3\sigma}$	$(9 \rightarrow 12)_{3\sigma}$	$(0 \rightarrow 0)_{3\sigma}$
$U(2)_{\text{PS}}$	NO	$65.7^{+3.8}_{-2.1}$	$9.8^{+1.6}_{-0.3}$	$1.2^{+0.5}_{-0.3}$
		$(62 \rightarrow 72)_{2\sigma}$	$(9 \rightarrow 13)_{2\sigma}$	$(0 \rightarrow 2)_{2\sigma}$
		$(62 \rightarrow 75)_{3\sigma}$	$(9 \rightarrow 14)_{3\sigma}$	$(0 \rightarrow 2)_{2\sigma}$
$U(2)_5$	NO	$63.7^{+4.4}_{-2.1}$	$9.5^{+1.5}_{-0.3}$	$1.8^{+1.3}_{-0.8}$
		$(60 \rightarrow 74)_{2\sigma}$	$(9 \rightarrow 13)_{2\sigma}$	$(0 \rightarrow 4)_{2\sigma}$
		$(59 \rightarrow 272)_{3\sigma}$	$(9 \rightarrow 85)_{3\sigma}$	$(0 \rightarrow 54)_{3\sigma}$
	IO	$224.2^{+173.8}_{-36.1}$	77^{+54}_{-10}	$68.0^{+31.0}_{-12.2}$
		$(173 \rightarrow 1070)_{2\sigma}$	$(65 \rightarrow 303)_{2\sigma}$	$(49 \rightarrow 255)_{2\sigma}$
		$(167 \rightarrow 5584)_{3\sigma}$	$(63 \rightarrow 497)_{3\sigma}$	$(1 \rightarrow 299)_{3\sigma}$



(a) Logarithmic axes.



(b) Linear axes.

Figure 6.2: $m_{\beta\beta}$ - $\sum_i m_i$ parameter space at 95.4% confidence level in logarithmic (top) and linear scaling (bottom). The Diagonal Charged Lepton (DCL) scenario is marked in yellow with the most likely value indicated by a star, the Pati-Salam scenario $U(2)_{PS}$ in green and the $U(5)$ -compatible scenario $U(2)_5$ in orange for normal and in purple for inverted ordering. Inverted ordering is not possible for the other scenarios. We also show the experimentally allowed regions for normal (blue) and inverted ordering (red), see also Figure 6.1. The gray region is excluded by cosmology, while expected future upper limits from cosmology and neutrinoless double beta decay ($0\nu\beta\beta$) experiments are marked with dashed lines. The plots are published in Reference [134].

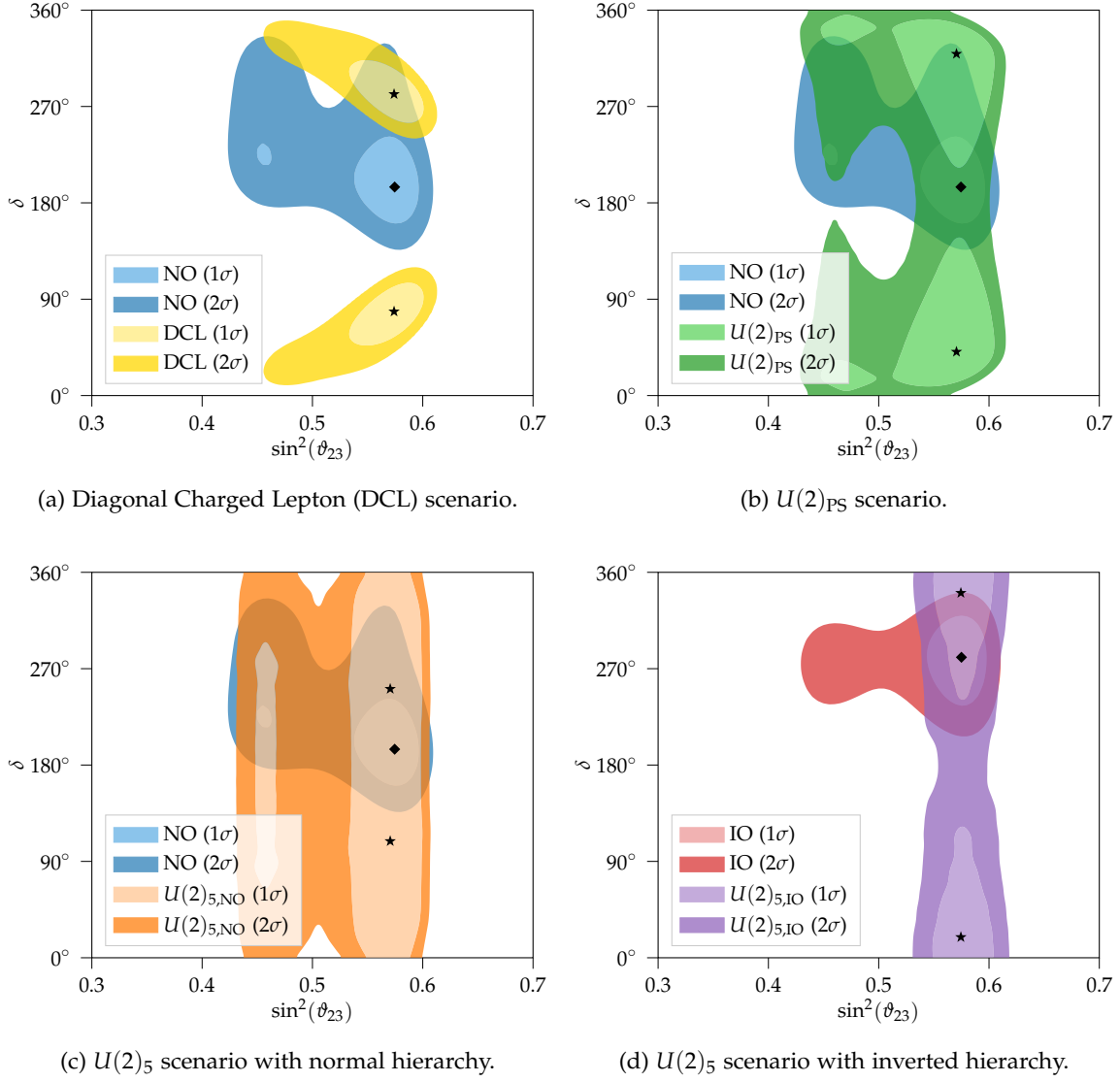


Figure 6.3: Predictions for the Dirac CP phase δ in terms of $\sin^2(\theta_{23})$ of the PMNS matrix. The blue and red regions show the allowed parameter space from NuFIT for normal and inverted ordering, respectively. The other colors correspond to the scenarios as indicated in the caption below the plots. In each case, light colors correspond to 68.3% and dark colors to 95.4% confidence level. The plots have been published in Reference [134].

NEUTRINO MASS OBSERVABLES Our results confirm the expectations outlined in Section 6.2. The Diagonal Charged Lepton scenario corresponding to the pure A_2 texture [154–163] allows for a small mass range of 63–69 meV at the 3σ level only in the case of normal ordering. As a consequence, all predictions automatically fall below the current bounds, even below the stringent bound from cosmology. This also holds for the case of the Pati-Salam scenario $U(2)_{\text{PS}}$, where, however, the 3σ mass range of up to 75 meV is slightly larger due to the additional angle from the charged lepton sector. Moreover, the effective Majorana mass $m_{\beta\beta}$ does not vanish in this case but is far below the reach of current and near-future experiments, even at the 3σ level.

As expected, the situation is different for the $U(5)$ -compatible scenario. Due to the additional left-handed rotation the 3σ range extends up to sums of 272 meV and thus into the region excluded by cosmological searches. The corresponding beta decay mass of $m_\beta \lesssim 85$ meV is still too low to be measured by KATRIN [51], but possibly in the reach of Project 8 [168]. However, our analysis shows that even though such large values are conceivable, they are improbable since the 2σ interval suggests that the sum should be smaller than 74 meV, that is that a long tail of the distribution is responsible for the large 3σ range. These observations confirm the ones in Reference [41] where the valid fits span a range of 59–78 meV, which is approximately the 2σ region in this full analysis. Finally, the effective Majorana mass $m_{\beta\beta}$ is tightly constrained at the 2σ level and therefore below the expected sensitivities of future experiments.

Furthermore, the possibility of inverted hierarchy arises in the $U(2)_5$ scenario due to the large left-handed rotation. If the $U(2)_5$ scenario with inverted ordering was realized in nature, this would lead to a tension with cosmological observations since the whole viable parameter space with sums larger than 167 meV at 3σ is already excluded. On the other hand, a discovery of inverted order neutrinos would imply that a $U(2)$ texture is ruled out completely.

DIRAC CP PHASE In the case of the Diagonal Charged Lepton scenario, there is a correlation between the size of the $(2,3)$ angle ϑ_{23} of the PMNS matrix and the CP phase δ , see Figure 6.3a. As discussed, the model makes no prediction as to the sign of the CP phase so that we find an axial symmetry about 180° . However, we also notice a slight tension of about 2σ between the most probable model value and the current best fit point from NuFIT [12, 136]. If future experiments confirm the current central value from global fits, this would imply that a charged lepton effect is needed for a viable A_2 texture in the neutrino sector. Note also that the Diagonal Charged Lepton scenario prefers the octant where $\vartheta_{23} > \frac{\pi}{4}$, while the global fits still allow a tiny range in the other octant at the 1σ level.

The additional phase in the $U(2)_{\text{PS}}$ case spoils the predictivity of the Diagonal Charged Lepton scenario by allowing all values for the Dirac CP phase δ at the 2σ level. However, CP-conserving values are disfavored at slightly more than 1σ . While the current best fit point from global fits is in an approximately 2σ tension with the most probable value of the scenario, the 1σ regions from the fits and the model prediction now overlap. It is interesting to note that for PMNS angles $\vartheta_{23} \lesssim \frac{\pi}{4}$ a range of the CP phase around the CP-conserving value of $\delta = 180^\circ$ is disfavored at the 2σ level.

In the normal ordered $U(2)_5$ scenario, the two charged lepton phases result in the whole range for the Dirac phase δ being allowed at the 1σ level, although the most probable value is still disfavored at slightly more than 1σ when considering the experimental uncertainties. It is interesting to see that the most probable value is closest to the current best fit point from NuFIT [12, 136] compared to the other scenarios discussed in this work. In the inverted hierarchy case, only the second octant for the angle ϑ_{23} is allowed at the 2σ level. Again, no values for the phase δ are excluded, although the region around the CP-conserving value 180° is disfavored.

It would be interesting to reconsider all scenarios once both the CP phase δ and the angle ϑ_{23} are measured with better precision. The CP phase should be treated as an input then and it might be possible to compare the goodness of fits for all scenarios.

CONCLUSION AND OUTLOOK

In this part, we have studied the predictions for neutrino observables in a broad class of models exhibiting a $U(2)$ flavor symmetry. Such a $U(2)$ family symmetry or variants like $D_6 \times U(1)$ prove to be successful in reproducing the observed hierarchies in the quark sector and charged lepton masses. Extensions of this idea to the neutrino sector based on Majorana neutrinos with masses originating from the Weinberg operator provide a viable way to explain the absence of hierarchies in the PMNS matrix using Standard Model fields only.

In order to cover a broad class of $U(2)$ models, we only assumed the same properties for the neutrino Yukawa matrix which also the Yukawa matrices of quarks and charged leptons exhibit. Such a structure can be realized in several models, especially in unified scenarios. The resulting neutrino texture is the well-studied A_2 texture, which has been analyzed in the literature many times—although in pure texture analyses without taking an underlying symmetry structure into account. Therefore, these analyses usually ignore the effect of charged lepton rotations on the PMNS matrix which could alter neutrino observables significantly.

In this work, we have augmented the pure A_2 model with charged lepton effects by assuming $U(2)$ -like structures for all Yukawa matrices. In particular, the charged lepton sector can be characterized by—besides several new phases—essentially two angles at leading order, of which one is small in specific models motivated by theories of Grand Unification. To this extent, we considered three scenarios: a pure A_2 texture and the two unified scenarios $U(2)_{\text{PS}}$ and $U(2)_5$ corresponding to $U(2)$ models with Pati-Salam or $U(5)$ unification, respectively, where either of the two angles is small.

For normal ordering, we find that the pure A_2 scenario predicts a small range of 63–69 meV for the sum of neutrino masses $\sum_i m_i$ at 3σ confidence level, which consequently translates into a narrow window for the effective beta mass m_β and effective Majorana mass $m_{\beta\beta}$. These predictions are also valid for the unified scenarios at the 2σ level. Only the $U(2)_5$ case allows for larger values at 3σ due to the long tail in the distribution, which is a consequence of the large left-handed rotation. This means that all scenarios are below the current and near future laboratory bounds at 95.4% confidence level and only the near future indirect cosmological searches will be able to probe the parameter space. On the other hand, any observation of one of the mass parameters by near-future laboratory experiments would immediately rule out all scenarios.

Inverted hierarchy is only possible in the $U(5)$ Unification model, with all of the parameter space being excluded by measurements of the PLANCK satellite. While these indirect measurements already exclude inverted hierarchy for the $U(2)$ -like scenarios, also the next generation of neutrino-less double beta decay experiments will be able to disfavor the inverted hierarchy parameter space in a controlled laboratory experiment. A detection of inverted hierarchy on the other hand would again rule out $U(2)$ -like models provided that the cosmological measurements prove to be reliable.

Due to the additional phases from the charged lepton sector, the prediction for the Dirac CP phase δ in the pure A_2 scenario gets smeared out in the $U(2)$ cases to the whole parameter space at 2σ confidence. Depending on the precise value for the $(2,3)$ PMNS angle ϑ_{23} , several areas of the parameter space are disfavored. Therefore, it might be interesting to revisit this case again once the precise value of the CP phase and the octant of the $(2,3)$ PMNS angle have been pinned down.

Besides the already mentioned improvements in experiments which would allow to constrain the parameter space further when using their results as further input to the analysis, one could also try to find limits for the observables by correlating the free charged lepton parameters to other observables. For instance, the $U(1)$ factor could be linked to a flavor-violating axion where the rotation parameters enter the flavor-violating couplings to charged leptons, which contribute to flavor-changing decays like muon decays into electrons and axions, $\mu \rightarrow e^- + a$.

Part III

LIGHT NEW PHYSICS IN THE SKY: SUPER-
NOVA BOUNDS ON FLAVOR-VIOLATING COU-
PLINGS

LIGHT PARTICLES IN SUPERNOVAE

The standard cooling picture of the remnant of a core-collapse supernova explosion can be severely influenced by the presence of new light particles. If such a light particle is produced inside the newly formed proto-neutron star and if it is sufficiently long-lived to carry away energy, the emission of neutrinos is affected. The consistency of the neutrino cooling mechanism with the observations of the SN1987A supernova by three neutrino experiments places a tight bound on the additional energy loss due to new particles. This in turn constrains the interactions of the light particle with all Standard Model particles existing inside the proto-neutron star.

We briefly review the supernova explosion mechanism and some properties of the neutron star remnants in Section 8.1, before turning to a short discussion of the way to obtain New Physics bounds in Section 8.2.

8.1 CORE-COLLAPSE SUPERNOVAE

The death of a massive star serves as a starting point to one of the most fascinating phenomena in the universe: a supernova. During the explosion, the star ejects not only most of its mass into interstellar space, but also radiates away the gravitational binding energy of $\mathcal{O}(10^{53} \text{ erg})$ of the compact remnant formed during the collapse of the star's core, mostly in the form of neutrinos and antineutrinos [175]. This process takes only a fraction of a second and is a consequence of an interplay of all four known forces of nature [176]. While the precise mechanism is still debated, recent state-of-the-art simulations by several groups agree that the explosion is predominantly driven by neutrino heating. However, asymmetric initial conditions and hydrodynamical instabilities seem to provide the necessary perturbations for successful explosions in stars with more than 10 solar masses [176, 177]. This consensus among scientists also stems from the lack of convincing alternative explanations based on established physical principles [175]. We present a brief overview of these neutrino-driven core-collapse supernovae which is based on the Reviews [175, 176, 178–180].

START OF THE COLLAPSE The starting point is a heavy star with mass $M \gtrsim 8M_{\odot}$, where M_{\odot} denotes the mass of our Sun. At the end of its lifetime, such a star has an onion-like structure: it consists of several shells of different chemical elements produced at each step in the fusion chain [175]. The reason for this shell-like structure is that

1 erg corresponds to 10^{-7} J.

In particular, one finds iron, silicon, oxygen, carbon, helium and hydrogen from the inside to the outside [175].

Degenerate electrons feature a distribution that can be approximated by a step function, corresponding to a Fermi gas at zero temperature.

Note that the neutrino energy E_ν enters the cross section σ squared, $\sigma \sim G_F^2 E_\nu^2$ with the Fermi constant G_F , which can be seen from dimensional analysis. The proton coupling is suppressed by $1 - 4 \sin^2(\theta_W)$ with the weak mixing angle θ_W [183].

The dissociation of iron happens mainly by photons created due to the increased temperature in the shock region [175].

the conditions needed to ignite heavier elements are at first realized in the center. In particular, stars with masses above approximately $10M_\odot$ succeed in burning silicon to iron [176], which cannot be ignited any further since it is the most tightly bound element [181]. Thus, an iron core is formed at the center which is stabilized by the pressure of degenerate electrons.

While silicon burning is adding iron to the core, the core reaches the Chandrasekhar mass of about $1.4M_\odot$ [182], at which the degeneracy pressure cannot stabilize the core against gravity anymore. As a consequence, the iron core starts to collapse. The increasing density leads to an increase in the electron chemical potential which eventually overcomes the mass gap between neutron and proton [178]. At this point, the electron capture process of protons, $e^- + p \rightarrow n + \nu_e$, becomes efficient, reducing the electron density. Hence, the collapse is even accelerated due to the further reduction of electronic pressure and the iron core turns to more neutron-rich isotopes [178].

The increasing temperature and neutron number N of the nuclei enhances the cross section of neutrino-nucleus scattering so that neutrinos are trapped [183]. Therefore, a neutrino sphere with a radius of $\mathcal{O}(40 \text{ km})$ forms where neutrinos are in thermal equilibrium [180]. This situation is analogous to photons in our Sun: They cannot stream freely within the Sun and are emitted from its surface—the photosphere—so that the photon spectrum is given by a Planck spectrum at the surface temperature, despite much higher temperatures in the inner Sun.

SHOCK FORMATION AND NEUTRINO HEATING About $\mathcal{O}(100 \text{ ms})$ after the collapse started, the core density is so high that the repulsive forces between the nuclei become important [178]. Thus, the collapse is decelerated and eventually stopped, forming an object which is now stabilized by the pressure of nuclear matter. The still inwards falling material from the outer core bounces on the halted inner core, triggering a shock wave to the outer region of the star [175]. On its way outwards, the shock wave dissociates the iron nuclei in the outer core into free protons and neutrons, on which electron capture is more efficient. This leads to the production of neutrinos, which leave the star in a short burst of $\mathcal{O}(10 \text{ ms})$ once the shock wave crosses the surface of the neutrino sphere [183], see Figure 8.2a.

While it was believed in the past that this shock wave triggers the supernova explosion, state-of-the-art simulations by several groups agree that the energy of the shock is exhausted from the dissociation of iron nuclei so that the shock wave halts at a radius of 100–200 km [175]. It is established that the shock is revived by heating from neutrinos emitted from the core [184]. In particular, the inner core continues to accrete material and becomes a proto-neutron star. The increasing temperature increases the energy of the neutrinos emitted from the

neutrino sphere which then hit the free protons and neutrons behind the shock front. This neutrino heating by mainly $\nu_e + n \rightarrow p + e^-$ and $\bar{\nu}_e + p \rightarrow n + e^+$ reactions not only deposits energy in that layer and hence increases the temperature, but also results in a higher lepton number with a larger degeneracy pressure. Moreover, a turbulent flow is created which constantly transports neutrino-heated material to the shock region while bringing cooler material to the region of efficient neutrino-heating [175]. As a result of the increasing thermal pressure which is supported by turbulent pressure, the shock wave is revived and the outer layers of the star get ejected into the interstellar space [175]. While the core-collapse and the revival of the shock wave take several hundreds of milliseconds only, the triggered explosion reaches the surface of the progenitor star after several hours [175].

THE REMNANT OF THE EXPLOSION The further evolution depends on the mass of the dying star. If it is larger than about $25M_\odot$, the proto-neutron star will further collapse to a black hole, while for lower masses it will cool and eventually become a neutron star [178]. Focussing on the latter case, the proto-neutron star with a radius of $\mathcal{O}(10 \text{ km})$ and a mass of $\mathcal{O}(1.5M_\odot)$ is initially rather hot with temperatures of tens of MeV and features a large fraction of protons of about 20% [175].

However, the large temperature and chemical potentials also allow for the production of heavier particles such as muons [185, 186] or even hyperons [187]. In particular, large chemical potentials imply large kinetic energies so that scattering processes could have a center-of-mass energy larger than the mass gap between, for instance, neutron and Λ baryon so that Λ particles may be produced. The thermal production of a particle i with mass m_i can be roughly estimated by assuming Boltzmann distributions for the number densities n_i , that is $n_i \sim e^{-\frac{m_i}{T}}$. For example, this relates neutron and Λ densities as

$$\frac{n_\Lambda}{n_n} = e^{-\frac{m_\Lambda - m_n}{T}} \sim 0.01, \quad (8.1)$$

assuming a temperature of $T \sim 40 \text{ MeV}$. Thus, Λ baryons have a sizable abundance in these proto-neutron stars.

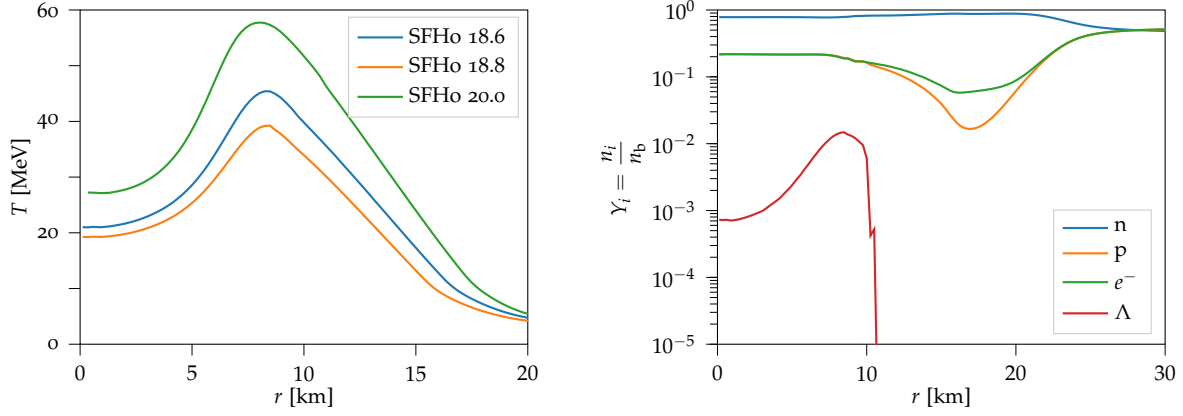
EQUATIONS OF STATE An important ingredient to the prediction of the properties of a neutron star by simulations is the equation of state which relates the thermodynamical quantities characterizing the star to each other, see Reference [188] for a review. The main difficulty in the construction of such an equation of state is the modelling of nuclear interactions, where full calculations based on Quantum Chromodynamics (QCD) are complicated, especially in extremely dense environments. Thus, these processes have to be simplified or fitted to data [188]. There are many proposals of such equations of

In fact, this turbulence [180] and potential initial asymmetries [177] are needed to achieve explosions in stars with masses $\gtrsim 10M_\odot$, where neutrino heating alone is usually not sufficient.

$T = 10 \text{ MeV}$ correspond to 10^{11} K .

Hyperons are baryons consisting of up, down and at least one strange quark, for example the Λ baryon being the isospin-0 bound state of uds quarks.

This approximation with Boltzmann distributions is applicable since all baryons are non-relativistic in stars.



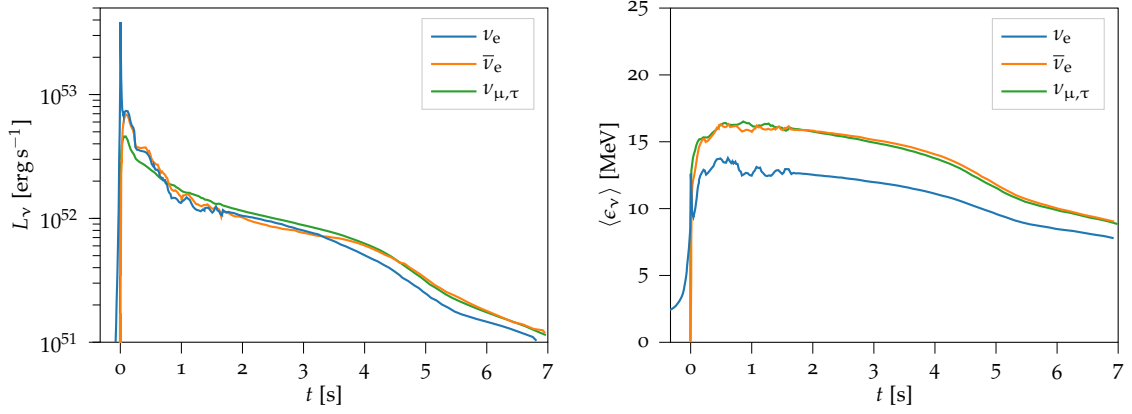
(a) Temperature profiles for different progenitor masses. (b) Composition profiles for different particles after the collapse of a $18.8M_{\odot}$ progenitor star.

Figure 8.1: Temperature (left) and composition (right) profiles about 1 s after the core bounce of the SN1987A supernova proto-neutron star as a function of the radius r . The temperature T is shown for three possible masses of the progenitor star, where the indicated numbers are given in units of the solar mass M_{\odot} . The composition profiles are plotted for the progenitor with mass $18.8M_{\odot}$ for neutrons (n), protons (p), electrons (e^-) and Λ baryons. Note that the apparent net charge between 15 km and 20 km is compensated by the abundances of deuterium and tritium nuclei not shown in the plot. The temperature profiles are based on the supernova simulation in Reference [186], while the compositions have been obtained using the CompOSE framework [194] with the SFHoY equation of state [187] and the supernova input from Reference [186].

state in the literature differing, among other things, in the particle degrees of freedom and the interactions between them. Examples of general-purpose equations of state which can be applied to a large range of the parameter space include LS220 [189, 190], DD2Y [191] or SFHo [192, 193], where the latter two are compatible with all present constraints [188].

In this work, we restrict ourselves to the SFHo equation of state which is available in a variant called SFHoY [187] with hyperons included. There are three input parameters necessary to infer all thermodynamical quantities including the composition of the star: the baryonic energy density q_b , the temperature T and the lepton fraction $Y_{\ell} = Y_e + Y_{\mu}$, where the fractions Y_i are given by the ratio of the number density n_i of the considered particle to the baryon number density n_b , $Y_i = \frac{n_i}{n_b}$ [194]. In the case of supernovae, these input parameters can be obtained from a simulation of the supernova, where we take the recent simulation in Reference [186] that is available from the Garching Core-Collapse Supernova Archive [195] in this work. In particular, the authors simulated the SN1987A supernova for three possible masses $M = 18.6M_{\odot}, 18.8M_{\odot}, 20M_{\odot}$ of the progenitor star. This leads to the temperature profiles and abundances of several particle species as a function of the radius R of the star 1 s after the bounce as shown in Figure 8.1.

All particle numbers are net numbers, for instance the electron number density n_e is the difference of the densities of electrons n_{e^-} and positrons n_{e^+} , $n_e = n_{e^-} - n_{e^+}$. The baryon number density n_b is obtained by summing the number densities of all baryons, $n_b = \sum_i B_i n_i$, where B_i is the baryon number of particle i .



(a) Luminosity L_ν of different neutrino flavors as a function of the time t after the core bounce. (b) Mean energy $\langle \epsilon_\nu \rangle$ of different neutrino flavors as a function of the time t after the core bounce.

Figure 8.2: The neutrino signal of a supernova as obtained in a recent simulation [177]. Both the luminosity L_ν (left) and the mean energy $\langle \epsilon_\nu \rangle$ (right) of electron neutrinos (blue), electron antineutrinos (orange) and heavy lepton neutrinos (green) are shown in terms of the time t after the core bounce. The narrow peak at a time $t \simeq 0$ s corresponds to the short neutrino burst once the shock wave crosses the surface of the neutrino sphere and the slow decline afterwards to the cooling of the neutron star remnant.

In order to calculate the thermodynamical quantities, the computer code CompOSE [194] can be used. The temperature profiles obtained in this way, see Figure 8.1a, are similar in shape but different in scale. Peak temperatures vary between 40–60 MeV, justifying the use of $T \sim 40$ MeV in the Approximation (8.1) above. As expected, neutrons are the most common particle species with a fraction of $Y_n \sim 80\%$, while there still is a large population of protons of $\mathcal{O}(20\%)$, see Figure 8.1b. The simulated abundances of the Λ baryons match the estimate in Equation (8.1). While the Λ fraction Y_Λ reaches its maximum of $\mathcal{O}(10^{-2})$ at the radius where also temperature peaks, it quickly vanishes for radii above about 10 km. This observation indicates that the population of Λ baryons is indeed mainly due to thermal production.

8.2 THE NEUTRINO SIGNAL AS A BOUND FOR NEW PHYSICS

The neutrino-driven core collapse supernova mechanism reviewed in the previous section implies that nearly all of the nascent neutron star’s binding energy of $\mathcal{O}(10^{53}$ erg) is radiated away in the form of neutrinos [183]. Simulations predict a characteristic time evolution of the neutrino emission, see Figures 8.2a and 8.2b. At first, a short neutrino burst occurs as a consequence of the shock wave crossing the surface of the neutrino sphere [117]. The reduced cross section of coherent neutrino scattering due to the dissociation of the heavy elements by the shock wave spoils neutrino trapping which leads to a large number of neutrinos leaving the star.

Only about 1% of the energy is carried away by the ejected material, while photon radiation contains even less energy.

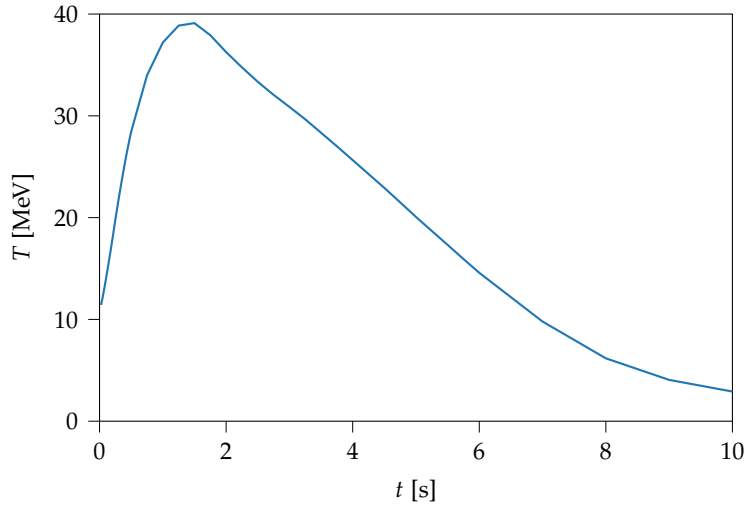


Figure 8.3: Temperature at a radius of $R = 7.5$ km at time t after the core bounce as obtained from the supernova simulation of a progenitor star with mass $18.8M_{\odot}$ in References [186].

While this sudden neutrino burst carries away already about half of the binding energy, the more interesting phase for Beyond the Standard Model physics is the following cooling phase [55]. Since new particles are more likely to be produced in the core of the star where density and temperature are highest, a significant energy loss due to a new particle would occur during that phase. This is due to the fact that the energy of the initial neutrino burst stems mainly from the accretion of material and contraction at the shock front, whereas the cooling neutrinos deplete the energy of the inner core [55]. Since neutrinos are trapped there, this cooling of the inner core starts only after the time which neutrinos need to reach the neutrino sphere.

New particles with weaker couplings, however, might leave the star earlier than neutrinos, thus providing an additional energy loss channel which reduces the temperatures of the core and the neutrino sphere more rapidly [55]. As a consequence, the exponential decay of the neutrino luminosity during the cooling phase of the proto-neutron star can be severely modified in the presence of new particles. Since neutrinos are emitted from the neutrino sphere, their energies are distributed around the temperature of the star of $\mathcal{O}(20 \text{ MeV})$, which quickly drops below 10 MeV after about 10 s, see also Figure 8.3. This expectation is confirmed by a recent simulation of the neutrino energies with mean values of about 10–15 MeV for 5 s after the core bounce, see Figure 8.2b. Additional energy loss would cause the temperature and consequently also the energies of the emitted neutrinos to drop faster. Thus, an observation of a nearby supernova measuring the energies of such cooling-phase neutrinos with time leads to insights into the cooling mechanism [55].

Note that muon and tau neutrinos have slightly higher temperatures since their energy is too low to produce muons or taus in charged current interactions, reducing their scattering cross section [55].

SUPERNOVA SN1987A The only nearby supernova of which the neutrino signal could be detected was observed on February 24, 1987 in an event called SN1987A, where the star Sanduleak –69 202 in the Large Magellanic Cloud underwent a core-collapse supernova. At a distance of about 50 kpc it was still close enough to yield a significant neutrino flux on earth, which was independently seen by the three experiments Kamiokande in Japan [196], Irvine-Michigan-Brookhaven (IMB) in the United States [197] and Baksan in Soviet Union [198]. These detectors have lower detection thresholds of 10–20 MeV so that one expects a neutrino pulse of $\mathcal{O}(10\text{ s})$ in their data corresponding to the predicted time scale of the drop in mean neutrino energies [55], see also Figure 8.2b.

Indeed, the total number of 24 observed neutrinos arrived during a time span of 5–12 s and combined fits are in agreement with the predictions from the core-collapse mechanism [199]. In particular, the Kamiokande group reports a probability for a background fluctuation of less than 10^{-7} [55]. The neutrino luminosity L_ν during the cooling phase is compatible with a value of

$$L_\nu \simeq 3 \times 10^{52} \text{ erg s}^{-1}, \quad (8.2)$$

corresponding to a total energy of $\mathcal{O}(10^{53} \text{ erg})$ integrated over the pulse duration [55].

NEW PARTICLES As discussed above, the presence of a new particle would accelerate the cooling of the core and shorten the neutrino pulse seen by neutrino experiments. Since the cooling time observed in 1987 was compatible with the Standard Model model predictions, the coupling of the new particle can be constrained by requiring that the cooling time is not significantly affected [117]. While a full simulation of proto-neutron star cooling including all new degrees of freedom would be necessary to establish the bound, an estimate is given by the criterion that the luminosity L_X of a new particle X should not exceed the neutrino luminosity L_ν [117], that is

$$L_X \lesssim L_\nu = 3 \times 10^{52} \text{ erg s}^{-1}. \quad (8.3)$$

If the luminosity of the X particle was larger, then considerably less energy would be available to neutrinos so that the neutrino energy would drop below the detection threshold. Although this criterion is ad hoc, it is agreed upon as a good estimate by numerical simulations of axion emission [118].

There are some limitations to the bound [55]. First, the new particle must be produced within the proto-neutron star, which places an upper bound on its mass depending on the temperature of the star

Note that the neutrino pulse observed by the Mont Blanc Observatory several hours before the other signals is not attributed to SN1987A [55].

This bound is sometimes referred to as the “Raffelt criterion”.

and potential mass gaps between initial and final state particles. Furthermore, there is no supernova limit for an arbitrarily small coupling of the new particle because the energy loss would not be efficient if the particle is rarely produced. On the other hand, there is also an upper limit of applicability for this criterion: For large couplings, the new particle would be trapped in the star as is the case for neutrinos [55]. As a consequence, there would also be an X sphere where the X particles are in equilibrium and the new particles would be thermally emitted from the surface of that sphere. If this sphere had a radius larger than the one of the neutrino sphere, then again energy would be more efficiently lost by neutrinos which escape the star earlier and the neutrino signal on earth would not be affected [118].

Internal stellar dynamics would also be changed drastically at such strong couplings, requiring a modification of the simulations. Hence, the bound in Equation (8.3) should only be applied for modest trapping.

To conclude, one can place limits for a novel kind of particle by calculating its luminosity L_X which can be compared to the bound in Equation (8.3) at least in the case of only weakly trapped particles. While this is a rough estimate, it is still appropriate given the non-negligible uncertainties in supernova modelling. The huge advantage of supernovae for Beyond the Standard Model physics is the high production number of particles which allows to test feebly interacting light particles and to place tight bounds on their couplings.

Any future nearby supernova would shed more light on the exact laws governing an explosion since more neutrino detectors are assembled and running nowadays [200]. For instance, the IceCube experiment is expected to record $\mathcal{O}(10^6)$ neutrinos from a supernova at a distance of 10 kpc which would allow for a measurement of the neutrino light curve and thus the resolution of the different phases in the collapse [200]. With that information at hand, also the reliability of the New Physics bound could be improved.

SN_{1987A} CONSTRAINTS ON FLAVOR-VIOLATING COUPLINGS

The constraint on the energy loss due to the emission of a new light particle has been used in the past to derive strong bounds on axion couplings to nucleons. Because of the sizable abundance of Λ baryons in the proto-neutron star, one can extend this analysis to flavor-violating couplings of axions which mediate transitions from strange to down quarks.

In Section 9.1, we present the basic formulas which yield the luminosity of a new particle produced in stars, also discussing effects due to the modified dispersion relation and trapping. In the presence of a flavor-violating coupling, axions are dominantly produced in Λ decays into neutrons and axions, which we use to place limits in Section 9.2. In Section 9.3, we finally estimate the bounds for Λ bremsstrahlung as a possibility to extend the constraints to axion-like particles with masses above the mass difference between the Λ hyperon and neutron.

9.1 ENERGY-LOSS FORMULA FOR A NEW PARTICLE

If a light particle X produced in the core is sufficiently weakly interacting to escape the stellar plasma, it can efficiently drain the energy of the star. In order to place bounds on the mass and couplings of the new particle, we have to calculate the energy loss of the stellar medium due to the emission of that particle from first principles. In the following, we evaluate the luminosity L_X which is the energy loss per unit time.

Since the thermodynamic properties of a star vary with its radius, we determine the energy loss rate per volume Q and integrate over the volume V_ν of the neutrino sphere with radius $R_\nu \sim \mathcal{O}(40 \text{ km})$ [55, 201],

$$L_X = \int_{V_\nu} d^3r Q(r) = 4\pi \int_0^{R_\nu} dr r^2 Q(r), \quad (9.1)$$

where in the last step we assumed spherical symmetry. The reason why this integral is cut at the neutrino sphere is that only particles produced within the neutrino sphere reduce the energy available to neutrino emission and thus affect the observed neutrino signal, see Section 8.2.

The energy loss rate per volume Q is obtained from the usual thermal average, taking the rate Γ_{prod} into account at which the light particle is produced. Specifically, this means that Q is given by the integration

The thermal average of a quantity O is the sum over all quantum numbers i, j, \dots of the distribution function $f(E)$ times that quantity, $\langle O \rangle = \sum_{i,j,\dots} O_{i,j,\dots} f(E_{i,j,\dots})$, with the particle energy E . The “ $1\pm$ ” occurs since we are considering a final state particle.

and summation of the light particle’s energy E_X and production rate Γ_{prod} over its phase space and internal degrees of freedom [55, 201],

$$Q = \sum_{\text{pol}_X} \int \frac{d^3 p_X}{(2\pi)^3} E_X \Gamma_{\text{prod}}. \quad (9.2)$$

In principle, one would have to consider also a distribution factor $(1 \pm f_X(\mathbf{p}_X))$, where the upper sign refers to bosons and the lower one to fermions. However, we neglect this factor since an escaping particle cannot build up a thermal population so that $f_X \simeq 0$.

The production rate Γ_{prod} is a straightforward generalization of the decay rate of a particle. It is proportional to the probability $|\langle f | S | i \rangle|^2 \sim (2\pi)^4 \delta^{(4)}(\sum_i k_i - \sum_f p_f) |\mathcal{M}|^2$ for the production process to occur, where \mathcal{M} is the Feynman amplitude and $\sum_i k_i$ and $\sum_f p_f$ are sums over the initial and final state momenta k_i and p_f , respectively. Moreover, we have to incorporate the occupation probabilities for the initial particles given by the Bose-Einstein (BE) or Fermi-Dirac (FD) distributions

$$f_i^{\text{BE/FD}}(\mathbf{p}_i) = \frac{1}{e^{\frac{E_i(\mathbf{p}_i) - \mu_i}{T}} \mp 1}, \quad (9.3)$$

with the chemical potential μ_i of the particle and temperature T . Similarly, Bose enhancement or Pauli blocking factors $(1 + f_f)$ and $(1 - f_f)$, respectively, need to be taken into account for the final state. Finally, we have to integrate over the phase space and sum over the internal degrees of freedom of each particle, yielding in total [201]

$$\Gamma_{\text{prod}} = \frac{1}{2E_X} \prod_i \int \frac{d^3 k_i}{(2\pi)^3 2E_i} f_i(\mathbf{k}_i) \prod_{f \neq X} \int \frac{d^3 p_f}{(2\pi)^3 2E_f} (1 \pm f_f(\mathbf{p}_f)) \times (2\pi)^4 \delta^{(4)}\left(\sum_i k_i - \sum_f p_f\right) \sum_{\text{pol}} |\mathcal{M}|^2, \quad (9.4)$$

Note that unlike for particle decays we do not average over initial state polarizations but only sum since we are considering an ensemble of particles instead of individual ones.

where the index i refers to all initial particles, while the index f runs over all final state particles including the new light particle X .

In order to calculate the luminosity L_X , one needs to know the chemical potential μ_i of each particle i and the temperature T of the star. While the temperature is the same for all particles in thermal equilibrium, five basic chemical potentials are sufficient to describe all particles due to conserved quantum numbers. These are given by μ_b , μ_q , μ_s , μ_{le} and $\mu_{l\mu}$ corresponding to baryon number, electric charge, strangeness, electron lepton number and muon lepton number symmetries, respectively [194]. Then, a particle i with baryon number B_i , electric charge Q_i , strangeness S_i , electron number L_i^e and muon number L_i^μ features a chemical potential [194]

$$\mu_i = B_i \mu_b + Q_i \mu_q + S_i \mu_s + L_i^e \mu_{le} + L_i^\mu \mu_{l\mu}. \quad (9.5)$$

The input quantities, that is temperature T and the chemical potentials μ_i , have to be obtained from a simulation of the star and generally depend on its radius r so that both Γ_{prod} and Q become radius-dependent. Moreover, the production rate Γ_{prod} also depends on the energy E_X of the new particle.

TRAPPING A light particle produced in the core of a proto-neutron star might be absorbed again in outer regions, thus reducing the luminosity of the new particle [201]. In particular, energy deposited by the absorption process would be available to neutrinos if it happens in a region where neutrino emission is still efficient, see Figure 9.1a. In this case, the neutrino pulse observed on earth would not be influenced despite the presence of a new particle. Hence, we need to take the reduction of the luminosity by absorption into account in order not to overestimate the effect of a new particle.

For weak couplings, absorption happens only rarely so that the energy loss rate Q per volume in Equation (9.2) yields a good approximation of the luminosity attributed to new particle emission. If instead the couplings are large, then trapping effects are efficient and the new particle scatters multiple times before it reaches a radius at which the star becomes transparent. The consequence is the formation of an X sphere within which the new particles cannot leave the star so that they are effectively emitted thermally from the surface of that sphere [202], see Figure 9.1b. This situation is analogous to neutrinos and photons which are mostly emitted from the surface of the neutrino sphere or from the surface of the star, respectively, due to their trapping.

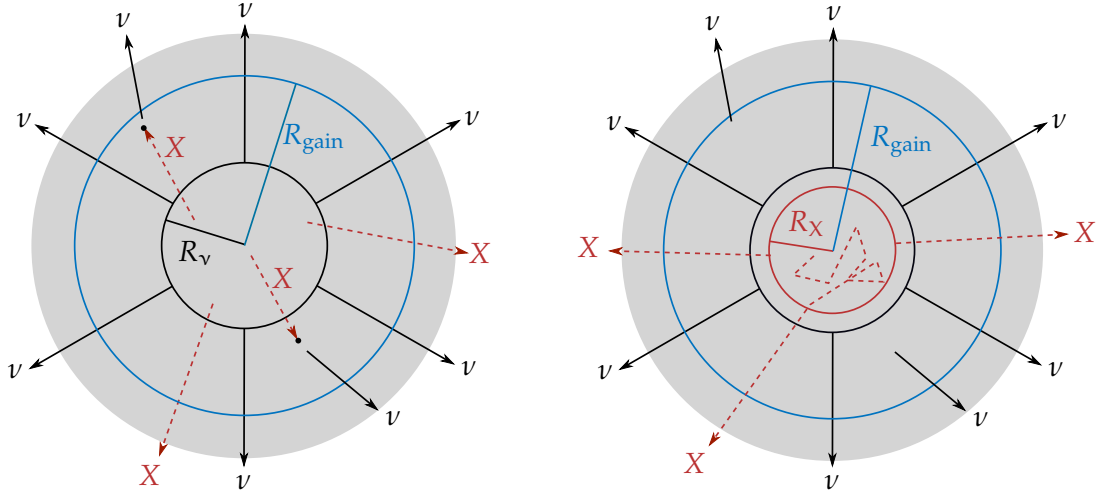
The quantity characterizing these trapping effects is the optical depth τ . For homogeneous materials it is defined as the product of the inverse of the mean-free path λ_{mfp} and the distance ΔR travelled, $\tau = \lambda_{\text{mfp}}^{-1} \Delta R$. If a particle covers a distance of the mean-free path, the optical depth becomes unity and the particle number gets suppressed by $e^{-\tau} = e^{-1}$. Therefore, we can include trapping in our calculations by multiplying the production rate Γ_{prod} by an exponential damping [201],

$$\Gamma_{\text{prod}} \rightarrow \Gamma_{\text{prod}} e^{-\tau}. \quad (9.6)$$

The energy-loss rate Q per volume in Equation (9.2) is modified to [201]

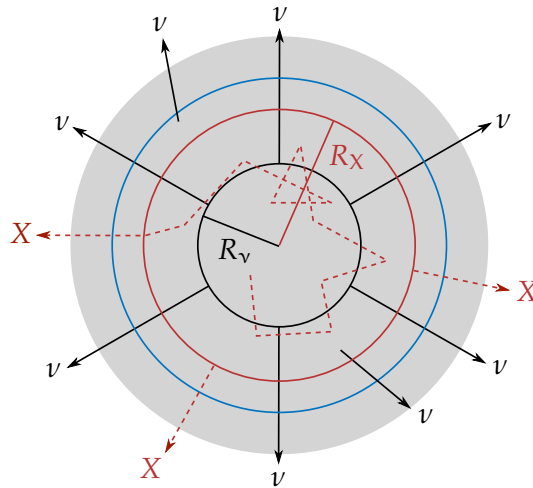
$$Q = \sum_{\text{pol}_X} \int \frac{d^3 p_X}{(2\pi)^3} E_X \Gamma_{\text{prod}}(E_X, r) e^{-\tau(E_X, r)}. \quad (9.7)$$

In this expression, we considered the general case of a non-constant optical depth that depends on the energy E_X and the radius r where



(a) Modest trapping. Energy deposited within the gain radius R_{gain} (blue) by X particle absorption is converted to neutrino energy and does not contribute to the X luminosity in the energy-loss criterion (8.3). Only X particles exiting the gain sphere (blue) drain the neutrino energy and affect the neutrino signal on earth.

(b) Large trapping. The X particles are effectively emitted from an X sphere (red) with radius R_X and scatter many times before reaching that radius. The neutrino signal on earth is affected since X particles are emitted from within the neutrino sphere (black) and thus drain its energy.



(c) Very large trapping. X particles are even trapped outside of the neutrino radius R_ν (black) and are emitted from an X sphere (red). Since neutrinos are emitted from within that sphere, the neutrino signal on earth is unchanged and no New Physics bound can be placed in this situation.

Figure 9.1: Visualization of the different trapping regimes. Neutrinos are mostly emitted from the neutrino sphere (black) at radius R_ν but also to a lesser extent at larger radii. Top left: For modest trapping, most of the X particles freely stream out of the star, while some are absorbed. The energy of X particles absorbed before the gain radius R_{gain} (blue) is available to neutrino emission so that they do not affect the neutrino signal. Top right: For large trapping, the X particles scatter many times before reaching the radius R_X at which the star becomes effectively transparent. Hence, an X sphere (red) forms and most of the X emission originates from its surface, which is similar to the neutrino sphere. Bottom: If the radius of that X sphere is larger than the one of the neutrino sphere, $R_X > R_\nu$, the neutrino signal is again unchanged. New Physics bounds can only be obtained in the situations (a) and (b) since the neutrino signal on earth is modified in these cases.

the new particle is produced. The reasons for these dependencies are on the one hand that the mean-free path λ_{mfp} varies with radius r due to the different densities and temperatures and on the other hand that the energy of the incoming particle provides an energy scale to the absorption process. The definition of the optical depth $\tau(E_X, r)$ above is thus only valid infinitesimally and we obtain [201]

$$\tau(E_X, r) = \int_r^{R_{\text{far}}} d\tilde{r} \lambda_{\text{mfp}}^{-1}(E_X, \tilde{r}) \quad (9.8)$$

for finite distances. Here, we integrate over the shell of possible absorption from the radius r of production to a radius R_{far} at which neutrino emission is not efficient anymore so that the deposited energy does not affect the neutrino signal on earth. While the value of the far radius R_{far} should be at least larger than the radius $R_\nu \sim \mathcal{O}(40 \text{ km})$ of the neutrino sphere, one should rather take a value of order $R_{\text{gain}} \sim \mathcal{O}(100 \text{ km})$ which marks the border at which neutrino capture is more efficient than neutrino emission [201], see Figure 9.1a.

If the new particle X is produced in $i_1 + i_2 + \dots \rightarrow X + f_1 + f_2 + \dots$ scattering with initial and final state particles i_j and f_j , respectively, its mean-free path λ_{mfp} is obtained from the rate Γ_{abs} of the absorption process $X + f_1 + f_2 + \dots \rightarrow i_1 + i_2 + \dots$. In particular, we have $\lambda_{\text{mfp}} = \Gamma_{\text{abs}}^{-1}$ so that the optical depth reads

$$\tau(E_X, r) = \int_r^{R_{\text{far}}} dr \Gamma_{\text{abs}}(E_X, r). \quad (9.9)$$

As we show in Appendix C.1, the absorption rate Γ_{abs} is proportional to the production rate Γ_{prod} given in Equation (9.4),

$$\Gamma_{\text{abs}} = e^{\frac{E_X}{T}} \Gamma_{\text{prod}}, \quad (9.10)$$

by the principle of detailed balance, which follows from thermal and chemical equilibrium as well as energy conservation and CP invariance of the matrix element. Note that we assumed the chemical potential of the new X particle to vanish, see Equation (9.5).

Turning to the case of strong coupling, an X sphere with radius R_X forms within which the new particle is approximately in thermal equilibrium. This corresponds to a large optical depth, $\tau(E_X, r) \gtrsim 1$, for particles produced at radii $r \lesssim R_X$. The radius R_X of this X sphere is usually chosen at the point where $\tau(E_X, R_X) = \frac{2}{3}$ [202], corresponding to the radius where the probability for the particle to leave the star without scattering drops below 50%. Since particles produced at such small radii are trapped, the main contribution to the luminosity of the new particles is given by particles emitted near the surface of this X sphere, see Figure 9.1b. This corresponds to a black body emitting

If we are to observe the new particles on earth, R_{far} would be the distance to the earth. Since we detect the neutrino signal, we are however only sensitive to modifications of neutrino emission.

these new particles and we can approximate the luminosity by the Stefan-Boltzmann law [202],

$$L_X = \frac{\pi^2}{120} 4\pi R_X^2 T^4(R_X), \quad (9.11)$$

This situation is similar to photon emission from the sun where the surface temperature enters the Stefan-Boltzmann luminosity since the surface is the outermost place of photon scattering.

However, the effect of the X particle should be included in the supernova simulation then since it provides an additional energy transport mechanism.

The potential energy V_{grav} is obtained as $V_{\text{grav}}(r) = m_X U_{\text{grav}}(r)$ from the gravitational potential U_{grav} .

Notice that $E_X \gtrsim 1.12m_X$ implies an Einstein gamma of $\gamma \gtrsim 1.12$, which corresponds to a velocity $v \gtrsim 0.45c = v_{\text{esc}}$ with the escape velocity v_{esc} .

where $T(R_X)$ is the temperature of the star at the radius R_X . Note that the Stefan-Boltzmann luminosity is only a valid approximation when the coupling is so strong that the transition from large to mild absorption occurs in a narrow region [186]. Between this strong trapping regime and the free-streaming regime one can only interpolate the luminosity as neither the Stefan-Boltzmann law (9.11) nor the modest trapping luminosity (9.7) are valid.

Since the probability for absorption increases with larger coupling, the X sphere grows in size for larger couplings. If the radius R_X exceeds the one of the neutrino sphere R_ν , the new particles cannot efficiently drain the neutrino luminosity anymore, see Figure 9.1c. Consequently, the neutrino signal on earth is not changed compared to the case without new particles and one cannot use the measurement of the neutrino luminosity to infer bounds on the new particle. This sets an upper bound of applicability of the supernova limits on couplings.

New X particles with masses of several 100 MeV can not only be trapped due to reabsorption but also due to their sizable gravitational interaction [203, 204]. In particular, their velocities must be large enough to overcome the escape velocity of $\mathcal{O}(0.5c)$. One can approximately include the gravitational effect by considering only X particles with a kinetic energy E_{kin} larger than the absolute value of the gravitational potential $U_{\text{grav}}(r) = -G_N \frac{M_{\text{encl}}(r)}{r}$ [204], where $M_{\text{encl}}(r)$ is the enclosed star mass within radius r and $G_N \simeq 6.67430 \times 10^{-11} \text{ m}^3 \text{ kg}^{-1} \text{ s}^{-2}$ [23] is Newton's constant.

From the simulation in Reference [186], we find that the minimal gravitational potential $U_{\text{grav}}^{\text{min}} = U_{\text{grav}}(R_{\text{min}}) \simeq -0.12$ occurs at a radius of about $R_{\text{min}} \simeq 14 \text{ km}$. Consequently, particles produced at radii $r \lesssim R_{\text{min}} = 14 \text{ km}$ need to have an energy [204]

$$E_X = m_X + E_{\text{kin}} \gtrsim m_X + m_X \left| U_{\text{grav}}^{\text{min}} \right| \simeq 1.12m_X \quad (9.12)$$

to escape the star. For radii r larger than this radius R_{min} of minimal gravitational potential, the kinetic energy must overcome the potential $U_{\text{grav}}(r)$ so that the X energy must fulfill [204]

$$E_X \geq m_X + m_X U_{\text{grav}}(r) = m_X \left(1 + G_N \frac{M_{\text{encl}}(r)}{r} \right). \quad (9.13)$$

These conditions introduce a lower cut-off to the phase-space integral of the new X particle in Equation (9.2).

MATTER EFFECTS Nucleons in the star cannot be viewed as free particles but are affected by the surrounding nuclear medium. Although this is a many-body problem, the particle can still be modeled by an effective single-particle dispersion relation. A particularly useful approach in hot and dense systems is given by relativistic mean field theory [205, 206] which is employed in many equations of state such as the SFHoY model [187] used in this work.

In this approach, the scalar and vector interactions between nucleons are modeled by the exchange of scalar and vector mesons φ and V^μ [206]. In high density environments, the meson fields can be replaced by their expectation values $\varphi \rightarrow \langle \varphi \rangle = \varphi_N$ and $(V^\mu) \rightarrow \langle (V^\mu) \rangle = (V_N^\mu) = (V_N, 0)$, where the spatial components of the vector expectation values vanish due to rotational symmetry.

This leads to a modification of the Dirac equation of a nucleon with mass m_N and spinor N ,

$$(i\partial - \not{V}_N - m_N - \varphi_N)N = 0. \quad (9.14)$$

As a consequence, the vector expectation value V_N enters the dispersion relation as a constant shift of the nucleon energy, $E_N \rightarrow E_N^* = E_N + V_N$, while the scalar mean value φ_N modifies the nucleon mass $m_N \rightarrow m_N^* = m_N + \varphi_N$. Hence, the effective dispersion relation of a nucleon in a high-density medium reads [205, 206]

$$E_N^*(\mathbf{p}_N) = \sqrt{(m_N^*)^2 + \mathbf{p}_N^2} + V_N. \quad (9.15)$$

At the technical level, φ_N and V_N are obtained from the self-energy of the particle by separating it into scalar and vector parts. The scalar part determines φ_N , while the zeroth component of the vector self-energy yields V_N . For these reasons, V_N and m^* are usually referred to as the vector self-energy and the effective Dirac mass of a particle, respectively. In general, these medium corrections have to be calculated for each particle separately, leading to different values for each class of particles.

Incorporating matter effects, one has to carefully identify all instances where the dispersion relation enters the calculation. On the one hand, the mass-shell condition $p^2 = m^2$ changes to

$$p^2 = (m^*)^2 + 2E^*V - V^2, \quad (9.16)$$

where $E^* = p^0$ is the particle energy including medium effects and V is the vector self-energy. Moreover, the modified dispersion relation changes the polarization sum of fermions which becomes

$$\sum_{\text{spin}} u\bar{u} = \not{p} - V\gamma^0 + m^*, \quad (9.17)$$

Here and in the following we denote medium quantities by an asterisk.

Sometimes the vector expectation value V_i is equivalently included into the chemical potential, $\mu_i \rightarrow \mu_i^* = \mu_i - V_i$.

Similarly, we find $\sum_{\text{spin}} v\bar{v} = \not{p} - V\gamma^0 - m^*$ for the v spinor

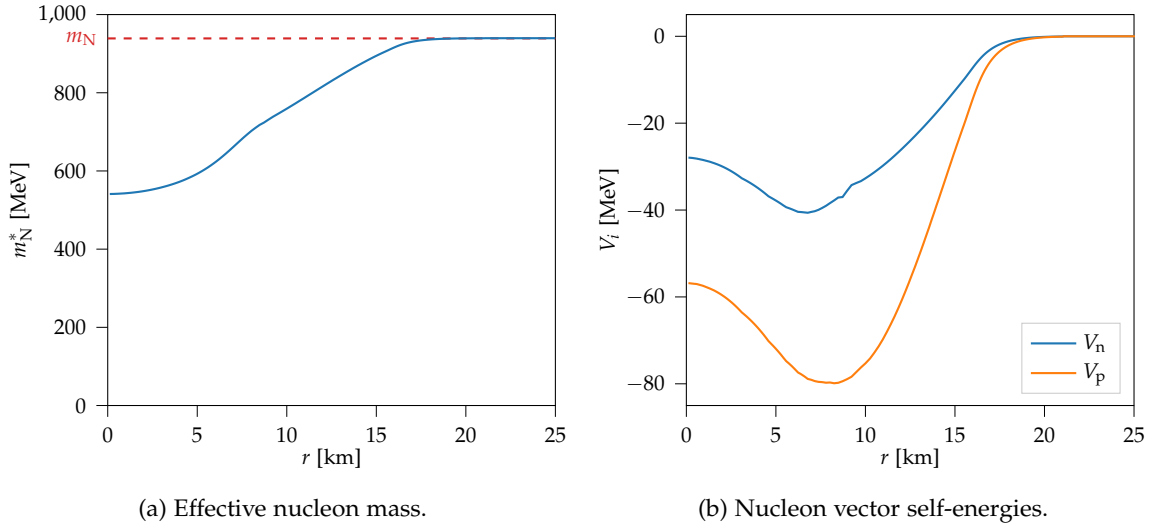


Figure 9.2: Profiles of the effective mass m_i^* of protons p and neutrons n and their vector self-energies V_i with radius r in the remnant of the supernova of a $18.8M_\odot$ mass progenitor star 1 s after the core bounce. The effective masses m_i^* for protons and neutrons are similar, $m_N^* = m_p^* \simeq m_n^*$, so we show only one curve. The vacuum nucleon mass $m_N \simeq 939$ MeV is indicated in red. The profiles were taken from the supernova simulation in Reference [186] with the SFHo equation of state.

for the u spinor.

In the center of the remnant proto-neutron star of a supernova, medium effects can be significant, reducing proton and neutron masses by almost a factor of 2 compared to their vacuum value, see Figure 9.2a for the results of the simulation in Reference [186]. This reduction is due to a strong dependence of the scalar interactions on the nuclear density. In contrast, the vector interaction changes the energy by at most 10% and differs for proton and neutron, see Figure 9.2b.

9.2 HYPERON DECAYS

As it was discussed in Section 8.1, the high temperature in the core of the proto-neutron star remnant of a supernova leads to a sizable population of Λ hyperons. While decays of the Λ baryon to Standard Model particles are in chemical equilibrium with the stellar medium, the decay of a Λ hyperon to a neutron and a feebly coupled light particle X can contribute to the energy loss of the star, see Section 8.2. The large abundance of hyperons allows to test rare decays so that tight bounds on the branching ratio $\text{Br}(\Lambda \rightarrow n + X)$ of the decay are expected. These decays were studied in Reference [66] in the context of QCD axions, axion-like particles (ALPs) and Dark Photons. In this section, we review this bound in the case of the axion, focussing on the size of the corrections due to trapping and matter effects. Moreover, we do not assume equal self-energies for Λ baryons and neutrons as it was done in Reference [66].

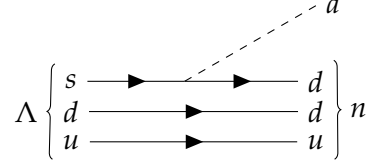


Figure 9.3: Feynman diagram for the tree-level decay of a Λ hyperon into a neutron and an axion due to flavor-violating couplings $g_{sd}^{V,A}$.

In order to derive a bound on the axion parameter space, we have to evaluate the luminosity (9.1) for the emission of a QCD axion from Λ decays to neutrons. In this analysis we set all axion couplings to zero except for the flavor-violating vector and axialvector strange-down couplings $g_{sd}^{V,A}$ so that axions are predominantly produced in these decays. Thus, the couplings of an axion a to strange quarks s and down quarks d are determined by the Lagrangian

$$\mathcal{L}_{\text{aff}} = \frac{\partial_\mu a}{2f_a} \bar{s} \gamma^\mu \left(g_{sd}^V + g_{sd}^A \gamma_5 \right) d + \text{h.c.}, \quad (9.18)$$

where f_a is the axion decay constant. In the presence of such flavor-violating couplings $g_{sd}^{V,A}$ the decay occurs at tree-level, see the Feynman diagram in Figure 9.3.

If the axion was also produced for instance in nucleon bremsstrahlung processes due to an axion-nucleon coupling, this would provide an additional production channel, adding to the production via decays and strengthening the bound on the axion coupling. Therefore, the restriction to only the flavor-violating couplings $g_{sd}^{V,A}$ provides a conservative upper limit.

Another possibility is the production from Λ bremsstrahlung, see Section 9.3.

The nucleon couplings are determined by the gluon and diagonal quark couplings [207].

PRODUCTION RATE The production rate Γ_{prod} of axions is determined from Equation (9.4). In order to assess the effects of the medium on the bounds, we evaluate the production rate for both cases of a vacuum and medium dispersion relation, where the latter is given in Equation (9.15).

In the vacuum case, the squared matrix element summed over fermion spins reads [66]

$$\sum_{\text{pol}} |\mathcal{M}|_{\text{free}}^2 = 2 \frac{|g_{sd}^V|^2 f_1^2 + |g_{sd}^A|^2 g_1^2}{4f_a^2} (m_\Lambda^2 - m_n^2)^2 \quad (9.19)$$

with the form factors $f_1 \simeq -1.22$ and $g_1 \simeq -0.89$ [54]. See Appendix C.2 for details on the derivation.

The production rate without matter effects simplifies to [66]

$$\Gamma_{\text{prod}}^{\text{free}} = \frac{2m_\Lambda^3 \Gamma_{\text{free}}(\Lambda \rightarrow n + a)}{(m_\Lambda^2 - m_n^2) E_a^2} \int_{E_\Lambda^{\text{min}}}^{\infty} dE_\Lambda f_\Lambda(E_\Lambda) (1 - f_n(E_\Lambda - E_a)),$$

(9.20)

where $\Gamma_{\text{free}}(\Lambda \rightarrow n + a)$ is the partial Λ decay rate into a neutron and an axion in vacuum as measured in collider experiments, see Equation (C.10) for the expression in terms of the coupling constants $g_{\text{sd}}^{\text{V},A}$. Moreover, E_{Λ}^{min} is the minimum Λ energy required to find an axion with energy E_a in the rest frame of the star, see Equation (C.19). All masses and energies in Expression (9.20) refer to vacuum values without matter effects and we derive this result in Appendix C.2. If instead we consider the mean-field dispersion relation (9.15) for particles in high-density environments, the matrix element is proportional to the vacuum matrix element,

$$\sum_{\text{pol}} |\mathcal{M}|_{\text{medium}}^2 = \alpha(E_{\Lambda}^*, E_a) \sum_{\text{pol}} |\mathcal{M}|_{\text{free}}^2 \quad (9.21)$$

with the energy-dependent proportionality factor $\alpha(E_{\Lambda}^*, E_a)$ in Equation (C.12).

Denoting the effective masses of Λ and neutron in a medium by $m_{\Lambda,n}^*$ and the energies in a medium by $E_{\Lambda,n}^*$, we find the production rate $\Gamma_{\text{prod}}^{\text{medium}}$ for axions in stellar media

$$\begin{aligned} \Gamma_{\text{prod}}^{\text{medium}} &= \frac{2m_{\Lambda}^3 \Gamma_{\text{free}}(\Lambda \rightarrow n + a)}{E_a^2 (m_{\Lambda}^2 - m_n^2)} \int_{E_{\Lambda,n}^{\text{min}}}^{E_{\Lambda,n}^{\text{max}}} dE_{\Lambda}^* \alpha(E_{\Lambda}^*, E_a) \\ &\times \frac{(E_{\Lambda}^* - V_{\Lambda})(E_{\Lambda}^* - V_n - E_a)}{E_{\Lambda}^* (E_{\Lambda}^* - E_a)} f_{\Lambda}(E_{\Lambda}^*) (1 - f_n(E_{\Lambda}^* - E_a)). \end{aligned} \quad (9.22)$$

Here, $m_{\Lambda,n}$ correspond to the vacuum masses of Λ and neutron and $\Gamma_{\text{free}}(\Lambda \rightarrow n + a)$ is again the partial decay rate in vacuum, see Equation (C.10). Moreover, $V_{\Lambda,n}$ are the vector self-energies of Λ and neutron and the minimal and maximal Λ energies are defined in Equation (C.24). This expression reduces to the one given in Reference [66] in the limit of equal self-energies $V_{\Lambda} = V_n$.

Note that the axion dispersion relation might also be subject to corrections in high-density media, for instance by a small reduction of the axion mass or a modification of baryonic couplings, see Reference [208]. We neglect this effect in this work and choose a vacuum dispersion for the axion.

LUMINOSITY In order to assess the effect of axion reabsorption, we determine the energy-loss rate Q per volume both for modestly trapped axions by including the exponential suppression with the optical depth $\tau(E_a, r) \neq 0$, see Equation (9.7), and for free-streaming axions with vanishing optical depth $\tau = 0$, see Equation (9.2). The integral over the axion momentum \mathbf{p}_a simplifies to

$$\int \frac{d^3 p_a}{(2\pi)^3} = \frac{1}{2\pi^2} \int_0^\infty dE_a E_a^2 \quad (9.23)$$

since the integrand only depends on the energy E_a of the massless axion.

Finally, we obtain the axion luminosity by integrating the energy loss rate Q per volume, see Equation (9.1). Since the Λ distribution function vanishes for radii larger than $R_\Lambda \gtrsim 12$ km, see Figure 8.1b, the upper limits of the radial integrals in the luminosity (9.1) and optical depth (9.8) are effectively given by this maximal radius R_Λ of Λ abundance, that is $R_v, R_{\text{far}} \rightarrow R_\Lambda$. This means that trapping of axions only occurs at radii below R_Λ , while they stream freely for larger radii. Note, however, that this statement depends on the validity of the detailed balance approximation (9.10) for the absorption rate, which is possibly not justified as Λ baryons produced from axion absorption do not have to be in thermal equilibrium at radii larger than R_Λ . Although this effect needs further investigation, we expect the absorption in outer regions to be small since the high-energetic neutrons needed to produce heavy Λ baryons are less abundant due to low temperatures.

The distribution functions f_Λ and f_n depend on the chemical potentials $\mu_{\Lambda,n}$ of the baryons and the temperature T of the star. According to Equation (9.5), the chemical potentials of Λ hyperon and neutron are both given by the baryon chemical potential, $\mu_\Lambda = \mu_n = \mu_b$, since the strangeness chemical potential is set to zero, $\mu_s = 0$ [194]. Since these parameters are inferred from simulations of a supernova and no closed expressions are available, we have to evaluate the integrals in the axion luminosity numerically.

Moreover, the effective Dirac masses m_i^* and self-energies V_i have to be extracted from supernova simulations. We use the CompOSE [194] code with the SFHoY equation of state [187] to calculate all stellar parameters with input values from the supernova simulations in References [186, 195]. Although these simulations were performed using the SFHo [192, 193] equation of state without hyperons, we do not expect a large influence of hyperons to stellar evolution since both the SFHo and SFHoY versions provide similar results at the densities of interest [187, 188].

All cases have been implemented in the programming language C++ using algorithms from the GNU Scientific Library. Specifically, we use the adaptive QAG routine for numerical integration, which implements an adaptive integration with Gauss-Kronrod quadrature rules. Moreover, we interpolate the stellar data provided by the simulations [186, 195] and CompOSE [194] as a grid in the radius r with the aid of linear splines from the GNU Scientific Library.

RESULTS In our analysis, we restrict ourselves to the simulation of an $18.8M_{\odot}$ progenitor star which features the lowest temperatures out of the three considered masses, see Figure 8.1a, and thus leads to the most conservative bounds [66]. Moreover, we calculate the luminosity at time $t \simeq 1$ s after the core bounce which is the conventional benchmark point, see for example References [186, 201, 204].

For the free-streaming regime, we determine the luminosity for the cases of vacuum and medium dispersion, both with and without trapping effects. Note that the cases in this work do not correspond to the ones in Reference [66]: The vacuum case in this work assumes all quantities to be at their vacuum values, while the “EoS” case in Reference [66] assumes a medium dispersion in the distribution functions. Moreover, the “EoS*” scenario in Reference [66] uses equal self-energies $V_{\Lambda} = V_n$, while we also consider differences in these quantities.

Instead of determining the bound for the axion couplings $g_{\text{sd}}^{\text{V,A}}$ directly, we first express the luminosity in terms of the vacuum branching ratio $\text{Br}(\Lambda \rightarrow n + X)$ of Λ baryons decaying into a neutron and an invisible particle X . This has the advantage that the bound can also be applied to other types of invisible particles in two-body decays. Note, however, that our discussion only applies to massless invisible particles. In particular, bounds were determined for Dark Photon couplings in Reference [66].

The luminosities for each of the four cases are shown in Figure 9.4. If one takes matter effects into account by choosing the mean-field dispersion relation (9.15), $E^*(\mathbf{p}_i) = \sqrt{(m^*)^2 + \mathbf{p}_i^2} + V_i$, the luminosity decreases by about 30 % compared to the pure vacuum dispersion $E(\mathbf{p}_i) = \sqrt{m_i^2 + \mathbf{p}_i^2}$. By contrast, effects from trapping parametrized by a non-vanishing optical depth τ , see Equation (9.7), only have a sizable impact on the luminosity in a regime which is excluded by the energy loss criterion (8.3). Trapping becomes important for branching ratios above $\mathcal{O}(10^{-7})$ and is the dominant effect for branching ratios above $\mathcal{O}(10^{-5})$ where matter effects lead to a slight increase of the luminosity.

At large couplings, axions are emitted from an axion sphere where trapping is efficient, see Figures 9.1b and 9.1c. Since axions cannot be absorbed by neutrons to produce Λ baryons at radii larger than $r \gtrsim R_{\Lambda} = 12$ km, the radius R_a of the axion sphere is bounded from above by this radius, $R_a \leq R_{\Lambda}$. In particular, the radius R_a of the axion sphere is always smaller than the radius $R_{\nu} \sim \mathcal{O}(40$ km) of the neutrino sphere and the neutrino signal is therefore affected by the energy loss of trapped axions for all couplings. In other words, the situation depicted in Figure 9.1c does not occur for Λ decays and thus the usual upper limit of applicability of the supernova bound is absent in this case. The luminosity derived from the Stefan-Boltzmann law (9.11) is constrained to be $L_a^{\text{trapping}} \gtrsim \mathcal{O}(10^{54} \text{ erg s}^{-1})$ [66], which

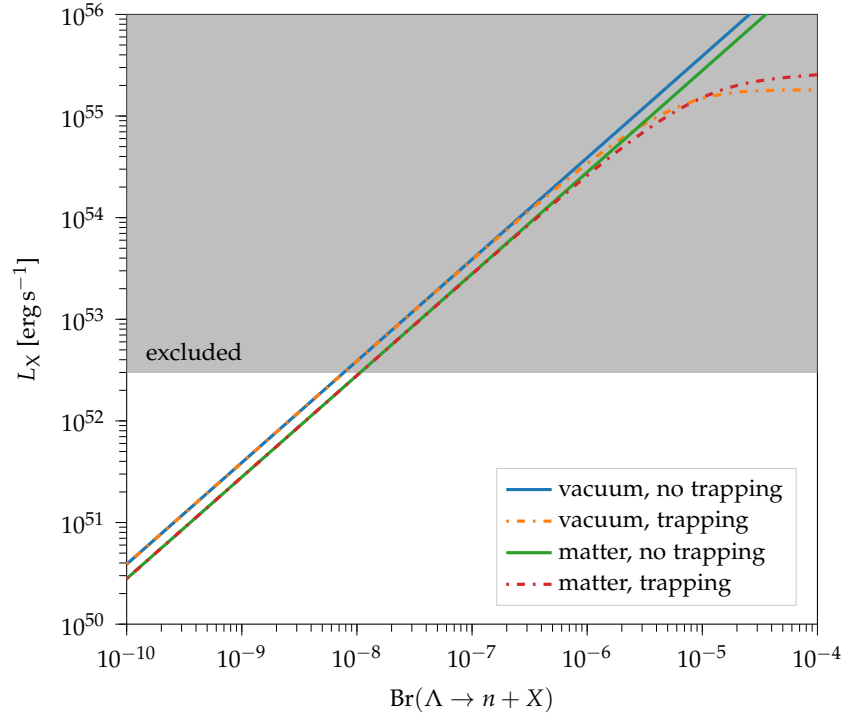


Figure 9.4: Luminosities in terms of the vacuum branching ratio $\text{Br}(\Lambda \rightarrow n + X)$ of a Λ hyperon decaying into a neutron and a massless invisible X particle. The gray region is excluded from the energy loss criterion (8.3). “Vacuum” refers to the use of a vacuum dispersion $E_i(\mathbf{p}_i) = \sqrt{m_i^2 + \mathbf{p}_i^2}$ for Λ and neutron, while “matter” incorporates the mean-field dispersion relation in Equation (9.15) for particles in high-density environments. “Trapping” means the inclusion of the exponential damping with the optical depth in Equation (9.7) which has been omitted in the “no trapping” case.

Table 9.1: Upper limits $\text{Br}(\Lambda \rightarrow n + a)_{\text{max}}$ on the branching ratio $\text{Br}(\Lambda \rightarrow n + X)$ of a Λ baryon decaying into a neutron and a light particle X from SN1987A observations. We separately show the effect of using a vacuum and a medium dispersion relation for the baryons and of neglecting trapping which is characterized by a non-zero optical depth τ . Note that our cases are different to the ones considered in Reference [66] which explains the different numbers, see text for details.

$\text{Br}(\Lambda \rightarrow n + X)_{\text{max}}$	dispersion relation	
	vacuum	medium
no trapping ($\tau = 0$)	7.6×10^{-9}	10.5×10^{-9}
trapping ($\tau \neq 0$)	7.1×10^{-9}	10.7×10^{-9}

violates the bound in Equation (8.3). As a consequence, the trapping regime and therefore large couplings are excluded.

While this reasoning depends on the validity of the detailed balance approximation (9.10), the luminosity in the regime where trapping becomes efficient exceeds the energy-loss criterion already by more than two orders of magnitude, see Figure 9.4. Hence, any effects beyond the detailed balance approximation would have to be large. In particular, the luminosity would have to develop a sharp dip to reach the allowed region since it has to saturate again at the trapping value $L_a^{\text{trapping}} \sim \mathcal{O}(10^{54} \text{ erg s}^{-1})$ for large couplings, which is unlikely. Moreover, the branching ratio of Λ decays is bounded from laboratory experiments to be smaller than $\text{Br}(\Lambda \rightarrow n + X) \lesssim 9 \times 10^{-3}$ [54], constraining the X coupling already to a value probably smaller than what is needed for strong trapping. Thus, this regime is also excluded by this argument.

Applying the energy loss criterion in Equation (8.3), one finds the upper limits on the branching ratio shown in Table 9.1. Including trapping and matter effects, our final result for the upper bound on the branching ratio is given by

$$\text{Br}(\Lambda \rightarrow n + a) \lesssim 1.1 \times 10^{-8}, \quad (9.24)$$

which is five orders of magnitude better than the current laboratory bound of $\text{Br}(\Lambda \rightarrow n + a)_{\text{lab}} \lesssim 9 \times 10^{-3}$ [54]. It is also one order of magnitude stronger than the projected bound of $\text{Br}(\Lambda \rightarrow n + a)_{\text{proj}} \lesssim 10^{-7}$ from the BESIII experiment [54] which is currently taking data. Note that the assumption of equal self-energies $V_\Lambda = V_n$ in Reference [66] leads to a limit of $\text{Br}(\Lambda \rightarrow n + a) \lesssim 0.8 \times 10^{-8}$ which is about 25% better than the result without this approximation. Thus, we conclude that the difference in the self-energies yields a significant effect.

Using the explicit expression for the decay rate in Equation (C.10), one can translate the upper bound on the branching ratio into lower bounds on the model-independent normalized axion scales

$$F_{\Lambda n} = \frac{2f_a}{\sqrt{|g_{sd}^V|^2 f_1^2 + |g_{sd}^A|^2 g_1^2}} \quad (9.25)$$

for the Λ -neutron coupling and

$$F_{sd}^{V,A} = \frac{2f_a}{|g_{sd}^{V,A}|} \quad (9.26)$$

for the quark couplings. We find

$$F_{\Lambda n} \gtrsim 5.0 \times 10^9 \text{ GeV} \quad (9.27)$$

and

$$F_{sd}^V \gtrsim 6.1 \times 10^9 \text{ GeV} \quad , \quad F_{sd}^A \gtrsim 4.4 \times 10^9 \text{ GeV} \quad , \quad (9.28)$$

with the form factors $f_1 \simeq -1.22$ and $g_1 \simeq -0.89$ [54]. For the latter bounds we assumed only one of the couplings $g_{sd}^{V,A}$ to be present at a time. Note that our constraints are slightly weaker than the ones in Reference [66] due to the inclusion of the difference in the self-energies in this work.

While the bound on the vector coupling is still about two orders of magnitude smaller than the best bound of $F_{sd}^V \gtrsim 6.8 \times 10^{11} \text{ GeV}$ from $K^+ \rightarrow \pi^+ + a$ decays [54], the constraint on the axialvector coupling surpasses all other constraints, especially the current best limit from kaon mixing of $F_{sd}^A \gtrsim 4 \times 10^7 \text{ GeV}$ [54]. The supernova bound is also particularly interesting for massless Dark Photons where the $K^+ \rightarrow \pi^+ + a$ constraints are absent, see Reference [66].

9.3 HYPERON BREMSSTRAHLUNG

As seen in the previous sections, the sizable abundance of Λ hyperons in the proto-neutron star remnant of a supernova allows to place strong limits on the flavor-violating strange-down coupling of axions. It is interesting to extend this bound for massive axion-like particles (ALPs) A , where the Peccei-Quinn symmetry is explicitly broken by a mass term so that the mass m_A of the axion-like particle becomes a free parameter. Since the $\Lambda \rightarrow n + A$ decay is kinematically forbidden if the mass m_A exceeds the mass difference $\Delta M_{\Lambda n} = m_\Lambda - m_n$ between the Λ baryon and neutron, one only obtains limits for axion-like particle masses smaller than this difference, $m_A \lesssim \Delta M_{\Lambda n} \simeq 180 \text{ MeV}$ [23].

The mass reach could be extended by considering heavier hyperons such as Σ baryons. However, their mass is just slightly larger than the

The abundance of Σ baryons was obtained analogously to those in Figure 8.1b.

one of the Λ baryon, while their abundance in stars is less than 0.1%. Thus, not much is gained by considering heavier hyperons. A more promising possibility is the addition of a spectator nucleon to the decay, see Figure 9.3. This process resembles nucleon bremsstrahlung [202, 209–212] with one of the initial nucleons replaced by a Λ baryon. The advantage of Λ bremsstrahlung compared to decays is the available kinetic energy of $\mathcal{O}(100 \text{ MeV})$, in addition to the larger phase space from the Λ -neutron mass difference.

Indeed, a recent study of massive axion-like particles in nucleon bremsstrahlung processes showed that strong bounds on the nucleon coupling are obtained for axion-like particle masses of up to about 400 MeV—although weakened by about one order of magnitude at the upper edge of this range [212]. If this mass reach can be equally translated to Λ bremsstrahlung, one would naively expect significant constraints on the flavor-violating couplings $g_{sd}^{V,A}$ for axion-like particle masses of up to $\Delta M_{\Lambda n} + 400 \text{ MeV} \sim \mathcal{O}(600 \text{ MeV})$.

This would even allow to extend the laboratory bound on the vector coupling g_{sd}^V from the two-body kaon decay into a pion and an axion-like particle, $K^+ \rightarrow \pi^+ + A$, which is only effective for masses below $m_A \lesssim 260 \text{ MeV}$ [213]. Although one could in principle extend this bound to the kaon-pion mass difference of $m_K - m_\pi \simeq 350 \text{ MeV}$ [23], the experimental analysis is cut at 260 MeV due to a large Standard Model background from $K^+ \rightarrow \pi^+ \pi^+ \pi^-$ decays [213]. As a consequence, the currently best bound for axion-like particle masses larger than 260 MeV is given by kaon mixing [54] which, however, suffers from large uncertainties and a potential sensitivity to the ultraviolet dynamics of axion models. Therefore, a supernova bound might provide a more robust limit in this to date weakly constrained part of the parameter space.

ESTIMATE OF LAMBDA BREMSSTRAHLUNG In this work, we estimate the bound from Λ bremsstrahlung processes on the flavor-violating $g_{sd}^{V,A}$ couplings. We restrict ourselves to the leading effects, closely following the classic analyses of nucleon bremsstrahlung [202, 209–212]. First, we consider only the one-pion exchange which is the dominant interaction between nucleons. Moreover, we include only spectator neutrons and neglect the diagrams with spectator protons which are suppressed by the smaller proton abundance. Since the Σ^0 hyperon is also a bound state of uds quarks like the Λ baryon, both the pion and the axion-like particle can mediate transitions between Λ and Σ^0 baryons. As a consequence, there are four diagrams for the Λ -neutron bremsstrahlung $\Lambda + n \rightarrow n + n + A$ possible at leading order. Two of them are depicted in Figure 9.5, while the other two are obtained from these by the exchange of the final-state neutrons.

As a further simplification, we expect the diagram involving the Σ^0 baryon in the intermediate state in Figure 9.5b to be smaller than the

In principle, there would also be multiple pion exchanges and exchanges of other mesons like kaons. The latter are suppressed by $\frac{m_\pi^2}{m_K^2} \sim 0.1$ due to the larger kaon masses.

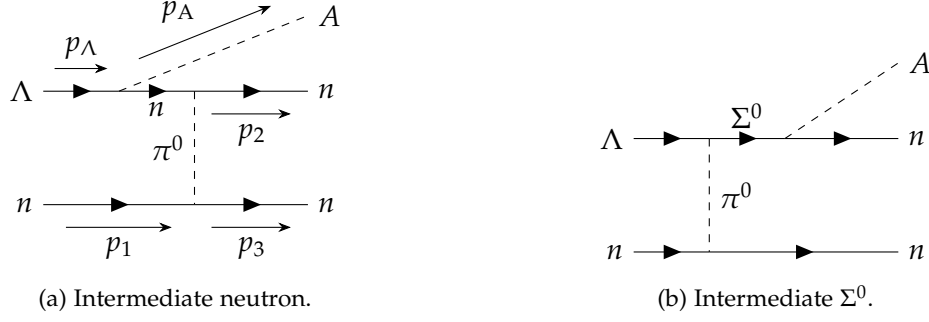


Figure 9.5: Possible Feynman diagrams for Λ -neutron bremsstrahlung of an axion-like particle A in the limit of one-pion exchanges. Two additional tree-level Feynman diagrams are obtained by exchanging the final state neutrons.

one with the intermediate neutron in Figure 9.5a due to the smaller Λ - Σ coupling to pions [214] and form factors [54]. Thus, we only consider the diagram in Figure 9.5a and its counterpart with crossed final-state neutron lines in our estimate.

In order to determine the matrix element of these diagrams, we have to specify the couplings. The flavor-violating axion couplings to Λ baryons and neutrons $C_{\Lambda n}^{V,A}$ are obtained from the quark coupling in Equation (9.18) by proper matching. As we expect the leading couplings to be given by the vector and axialvector parts of the baryonic matrix element (C.7a) and (C.7b) [66], we consider the Lagrangian

$$\mathcal{L}_{\Lambda n A} = \frac{\partial_\mu A}{2f_a} \bar{\Lambda} \gamma^\mu \left(C_{\Lambda n}^V + C_{\Lambda n}^A \gamma_5 \right) n + \text{h.c.} \quad (9.29)$$

in this work for the interaction between Λ baryons and neutrons n with the axion-like particle A .

The nucleon-pion interaction Lagrangian $\mathcal{L}_{NN\pi}$ was calculated in Reference [214] and reads

$$\mathcal{L}_{NN\pi} = -f_{NN\pi} (\partial_\mu \pi_j) \bar{N} \gamma^\mu \gamma_5 \sigma_j N. \quad (9.30)$$

Here, σ_j denotes the j -th Pauli matrix and we abbreviated the nucleon isospin doublet by $N = (p, n)$ with proton p and neutron n and the pion triplet π_i , where

$$\pi_1 = \frac{1}{\sqrt{2}} (\pi^+ + \pi^-) \quad , \quad \pi_2 = \frac{i}{\sqrt{2}} (\pi^+ - \pi^-) \quad , \quad \pi_3 = \pi^0, \quad (9.31)$$

with the charged pion fields π^\pm and neutral pion π^0 . Moreover, the pion-nucleon coupling $f_{NN\pi}$ is given in terms of the pion decay constant $f_\pi \simeq 92.1 \text{ MeV}$ [23] and the axialvector neutron coupling $g_A \simeq 1.26$ [214], $f_{NN\pi} = \frac{g_A}{2f_\pi}$.

In order to automate the calculation of the matrix element for the more involved case of all diagrams in a future work, we have implemented both the Λ -neutron coupling (9.29) and the pion-nucleon coupling (9.30) in a FeynRules [215] model file. From there it can be exported to a FeynArts [216] model, which we can use within FeynCalc [217–219] for the algebraic manipulation of the amplitudes.

In principle, there are fifteen possible scalar products but the diagonal scalar products are fixed by the mass-shell condition, $p_i^2 = m_i^2$.

MATRIX ELEMENT In general, the amplitude of the process depends on the ten free scalar products of the five particle momenta p_Λ , $p_{1,2,3}$ and p_A as indicated in Diagram 9.5a. However, momentum conservation imposes five conditions

$$p_i \cdot (p_\Lambda + p_1 - p_2 - p_3 - p_A) = 0 \quad (9.32)$$

for $i = \Lambda, 1, 2, 3, A$ on the ten scalar products $p_i \cdot p_j$ with $i \neq j$ so that only five of them are independent.

It is convenient to introduce the momentum transfers $k = p_1 - p_3$ and $l = p_1 - p_2$ of Diagram 9.5a and its exchanged counterpart, respectively. The advantage of this parametrization is the cancellation of the neutron mass in the energy components of the momentum transfers k and l , allowing for a clear separation of scales later. As in the classic analyses [202, 209–212], we choose k^2 , l^2 , $k \cdot l$, $k \cdot p_A$, and $l \cdot p_A$ as the five independent scalar products. We list all products in terms of these independent ones in Appendix C.4.

Since the masses of Λ baryons and neutrons are much larger than the other scales in the problem, we approximate the amplitude in the limit of $m_{\Lambda,n} \rightarrow \infty$, taking only the leading term. In order to do so, we have to identify the scaling of the scalar products. For this we note that the average kinetic energy E_{kin} of a free non-relativistic particle with mass m and temperature T is given by $E_{\text{kin}} = \frac{3}{2}T$ by means of the equipartition theorem, so that the momentum \mathbf{p} of the particle is of order $|\mathbf{p}| \sim \sqrt{3mT}$. Therefore, the momenta p_i for $i = \Lambda, 1, 2, 3$ for massive, non-relativistic particles in thermal equilibrium scale like

The equipartition theorem states that each quadratic degree of freedom contributes $\frac{1}{2}T$ to the internal energy of a system.

$$p_i \sim \left(\frac{m_i + T}{\sqrt{m_i T}} \right). \quad (9.33)$$

Using energy-momentum conservation and denoting the baryon masses by $m_b \sim m_n, m_\Lambda$, we infer the scaling of the axion-like particle's four-momentum as

$$p_A = p_\Lambda + p_1 - p_2 - p_3 \sim \left(\frac{\Delta M_{\Lambda n} + T}{\sqrt{m_b T}} \right). \quad (9.34)$$

From that we can determine the scaling of the scalar products k^2 , l^2 , $k \cdot l$, $k \cdot p_A$ and $l \cdot p_A$. First, we find

$$k \sim \left(\frac{T}{\sqrt{m_n T}} \right) \quad \text{and} \quad l \sim \left(\frac{T}{\sqrt{m_n T}} \right), \quad (9.35)$$

where the neutron mass drops out of the zeroth component. Since there is a hierarchy between the temperature T , the mass difference $\Delta M_{\Lambda n}$ and the neutron mass m_n , $T \ll \Delta M_{\Lambda n} \ll m_n$, the scalar products scale like

$$\begin{aligned} k^2, l^2, k \cdot l &\sim T^2 - m_n T \sim m_n T, \\ k \cdot p_A, l \cdot p_A &\sim \Delta M_{\Lambda n} T - m_b T \sim m_b T, \end{aligned} \quad (9.36)$$

and are thus of similar size. From these estimates we conclude that the zero components are subleading to the spatial components so that we can approximate the scalar products to be

$$\begin{aligned} k^2 &\simeq -|\mathbf{k}|^2, \quad l^2 \simeq -|\mathbf{l}|^2, \quad k \cdot l \simeq -\mathbf{k} \cdot \mathbf{l}, \\ k \cdot p_A &\simeq -\mathbf{k} \cdot \mathbf{p}_A, \quad l \cdot p_A \simeq -\mathbf{l} \cdot \mathbf{p}_A. \end{aligned} \quad (9.37)$$

Expanding the full amplitude of the Λ bremsstrahlung process for large baryon masses $m_n, m_\Lambda \sim m_b \rightarrow \infty$, we have to bear in mind that all scalar products are proportional to the baryon mass. Additionally assuming small axion-like particle masses $m_A \ll m_b$, we find the leading term of the squared amplitude summed over initial and final state polarizations

$$\begin{aligned} \sum_{\text{pol}} |\mathcal{M}|^2 &\simeq 16 f_{\text{NN}\pi}^4 \frac{|C_{\Lambda n}^V|^2 + |C_{\Lambda n}^A|^2}{4 f_a^2} m_n^4 (m_\Lambda^2 - m_n^2)^2 \\ &\times \left[\frac{\mathbf{k}^4 (m_\pi^4 + 3m_\pi^2 \mathbf{l}^2 + 3\mathbf{l}^4) + \mathbf{l}^2 (m_\pi^4 (\mathbf{k}^2 + \mathbf{l}^2) + 3m_\pi^2 \mathbf{k}^2 \mathbf{l}^2)}{(\mathbf{k} \cdot \mathbf{l})^2 (\mathbf{k}^2 + m_\pi^2)^2 (\mathbf{l}^2 + m_\pi^2)^2} \right. \\ &\quad \left. - \frac{2}{(\mathbf{k}^2 + m_\pi^2) (\mathbf{l}^2 + m_\pi^2)} \right]. \quad (9.38) \end{aligned}$$

Here, $m_\pi \simeq 135 \text{ MeV}$ [23] is the π^0 mass. Moreover, we replaced the scalar products of the four-vectors by the approximations in Equation (9.37).

For better comparison to other results, we also define the model-independent axion scale for Λ -neutron transitions as

$$F_{\Lambda n} = \frac{2f_a}{\sqrt{|C_{\Lambda n}^V|^2 + |C_{\Lambda n}^A|^2}}. \quad (9.39)$$

PRODUCTION RATE We evaluate the production rate Γ_{prod} of axion-like particles as defined in Equation (9.4). In order to simplify the problem, we note that the momentum \mathbf{p}_A of the axion-like particle can be neglected compared to the other momenta due to the following reasoning:

The axion-like particles are expected to be non-relativistic for masses in the interesting region of the parameter space of $m_A \gtrsim 260$ MeV due to the low temperature.

Assuming the axion-like particle to be non-relativistic and using energy conservation, we can infer its energy E_A from the momentum scalings (9.33) to be

$$E_A = E_\Lambda + E_1 - E_2 - E_3 \sim \Delta M_{\Lambda n} + T, \quad (9.40)$$

where E_i with $i = \Lambda, 1, 2, 3$ are the energies of the baryons. We obtain the momentum \mathbf{p}_A of the axion-like particle from the mass-shell condition,

$$|\mathbf{p}_A| \sim \sqrt{(\Delta M_{\Lambda n} + T)^2 - m_A^2}. \quad (9.41)$$

If its mass m_A is larger than the mass difference $\Delta M_{\Lambda n}$ between neutron and Λ hyperon, $m_A \gtrsim \Delta M_{\Lambda n}$, the kinetic energy of the baryons must also partially account for the rest mass of the axion-like particle. Consequently, the magnitude of the momentum \mathbf{p}_A is parametrically reduced with respect to the baryonic momenta \mathbf{p}_i , $i = \Lambda, 1, 2, 3$, which are of $\mathcal{O}(\sqrt{m_b T})$, see Equation (9.33). In this limit of small $\mathbf{p}_A \ll \mathbf{p}_i$, we neglect the axion-like particle momentum \mathbf{p}_A in the spatial part of the momentum conserving delta function,

$$\delta^{(3)}(\mathbf{p}_\Lambda + \mathbf{p}_1 - \mathbf{p}_2 - \mathbf{p}_3 - \mathbf{p}_A) \simeq \delta^{(3)}(\mathbf{p}_\Lambda + \mathbf{p}_1 - \mathbf{p}_2 - \mathbf{p}_3). \quad (9.42)$$

It is not a priori clear whether this simplification holds since it does not take the finite width of the momentum distribution into account or assumes the final state baryon momenta to be at the order of their values in thermal equilibrium. While this approximation needs to be justified in a full calculation, the complexity of the phase space integration is reduced since angles between the baryon and axion-like particle momenta do not appear in the integrand.

In contrast to the nucleon bremsstrahlung calculations performed in Reference [210], we need to take the different Λ momentum into account and modify the discussion accordingly. The final result reads

$$\begin{aligned} \Gamma_{\text{prod}} = & \frac{m_\Lambda m_n}{128\pi^6 \Delta M_{\Lambda n} E_A} \int_0^\infty d|\mathbf{p}_0| \int_0^\infty d|\mathbf{p}| \int_{|\mathbf{q}|_-}^{|\mathbf{q}|_+} d|\mathbf{q}| \\ & \times \int_{-1}^1 d\cos(\vartheta_q) \int_0^{2\pi} d\varphi_q |\mathbf{p}_0| |\mathbf{p}| |\mathbf{q}|^2 \\ & \times \left[\frac{f_\Lambda(E_\Lambda) f_n(E_1) (1 - f_n(E_2)) (1 - f_n(E_3))}{E_\Lambda E_1 E_2 E_3} \sum_{\text{pol}} |\mathcal{M}|^2 \right]_{\cos(\vartheta_p) = c_p}, \end{aligned} \quad (9.43)$$

where $f_i(E_i)$ is the Fermi-Dirac distribution of baryon i and the baryon momenta are expressed in terms of the center-of-mass coordinates of the final state neutrons, $\mathbf{p}_\Lambda = \mathbf{p}_0 + \mathbf{p}$, $\mathbf{p}_1 = \mathbf{p}_0 - \mathbf{p}$ and $\mathbf{p}_{2,3} = \mathbf{p}_0 \pm \mathbf{q}$, see Equations (C.43a)–(C.43d) and (C.44a)–(C.44c). The angles ϑ_p and ϑ_q refer to the polar angles of \mathbf{p} and \mathbf{q} , respectively, with respect to \mathbf{p}_0 , while the azimuthal angle φ_q is taken with respect to the \mathbf{p}_0 - \mathbf{p} plane, see Equations (C.45a)–(C.45c).

Furthermore, we defined the minimal and maximal momenta $|\mathbf{q}|_\pm$,

$$|\mathbf{q}|_\pm^2 = \max \left\{ 0, A \pm \frac{\Delta M_{\Lambda n} |\mathbf{p}| |\mathbf{p}_0|}{m_\Lambda} \right\}, \quad (9.44)$$

and the root c_p of the energy delta function,

$$c_p = \frac{m_\Lambda}{\Delta M_{\Lambda n} |\mathbf{p}| |\mathbf{p}_0|} (A - \mathbf{q}^2), \quad (9.45)$$

with $A = m_n(\Delta M_{\Lambda n} - E_A) + \frac{1}{2} \left(\frac{m_n}{m_\Lambda} - 1 \right) \mathbf{p}_0^2 + \frac{1}{2} \left(\frac{m_n}{m_\Lambda} + 1 \right) \mathbf{p}^2$. See Appendix C.5 for a derivation of this result.

Note that only the amplitude $\sum_{\text{pol}} |\mathcal{M}|^2$ depends on the angle φ_q . This integral can be performed analytically and yields

$$\int_0^{2\pi} d\varphi_q \sum_{\text{pol}} |\mathcal{M}|^2 = 96\pi f_{\text{NN}\pi}^4 \frac{|C_{\Lambda n}^V|^2 + |C_{\Lambda n}^A|^2}{4f_a^2} \frac{m_n^4 (m_\Lambda^2 - m_n^2)^2}{(|\mathbf{p}|^2 - |\mathbf{q}|^2)^2}. \quad (9.46)$$

LUMINOSITY In order to finally obtain the axion-like particle luminosity for this process, we have to integrate over the volume of the star and the phase space of the axion-like particle as given in Equations (9.1) and (9.2), neglecting trapping and matter effects. Note, however, that the phase space integration is modified due to the non-vanishing axion-like particle mass m_A and reads

$$\int \frac{d^3 p_A}{(2\pi)^3} = \frac{1}{2\pi^2} \int_{1.12m_A}^{\infty} dE_A \sqrt{E_A^2 - m_A^2} E_A. \quad (9.47)$$

Here, we also considered gravitational trapping as described in Section 9.1 by shifting the lower limit of the integral from m_A to $1.12m_A$, which removes axion-like particles with velocities below the escape velocity from the luminosity. Since Λ baryons are only abundant in the star for radii $r \lesssim 12$ km, all axion-like particles are produced before the minimum of the gravitational potential and we only need to consider the case of Equation (9.12).

Like in the previous section, we have to perform the integration numerically with stellar input parameters taken from simulations. The constant couplings can be factorized in the free-streaming limit so

At this point, we are only interested in the order of magnitude. That is why we neglect matter effects which we expect to be of $\mathcal{O}(30\%)$ as in the previous section, while trapping does not seem to be important.

that we only have to integrate once for each mass m_A of the axion-like particle. At the technical level, we employ the VEGAS algorithm as implemented in the GNU Scientific Library in C++ for the remaining six-dimensional numerical integration. Since we are not considering matter effects in this estimate, we set both the neutron and Λ hyperon mass to their vacuum values. Therefore, the only input values from supernova simulations are the temperature T and baryon chemical potential μ_b which are provided as a grid in the radius r in Reference [186] in the Garching Core-Collapse Supernova Archive [195]. We interpolate the radial dependence of these two quantities linearly with splines implemented in the GNU Scientific Library.

RESULTS In Figure 9.6, we show the lower bound on the model-independent axion scale $F_{\Lambda n}$ defined in Equation (9.39) as it is obtained from the energy-loss criterion (8.3) for the bremsstrahlung luminosity in terms of the mass m_A of the axion-like particle.

For masses below $m_A \lesssim \Delta M_{\Lambda n} \simeq 180 \text{ MeV}$, not only the validity of our Approximation (9.42) has to be questioned but we also encounter a singularity if the intermediate neutron goes on-shell, causing its propagator to be divergent. In this case, the situation resembles the decay in Section 9.2: The Λ hyperon decays into a physical neutron which afterwards scatters with another neutron. The latter process should not be considered since the scattering of neutrons is already part of the supernova simulations. Therefore, the case of small axion-like particle masses $m_A \lesssim \Delta M_{\Lambda n}$ needs further scrutiny and we restrict ourselves to the regime of large masses $m_A \gtrsim \Delta M_{\Lambda n}$ in this work.

Furthermore, we display the exclusion regions from two-body kaon decays $K^+ \rightarrow \pi^+ + A$ as measured in NA62 [213, 220] and $\Lambda \rightarrow n + A$ decays from the SN1987A supernova signal [66]. For the former, we have translated the upper bounds on the branching ratios in References [213, 220] into lower bounds on the effective vector axion scale $F_{\Lambda n} = \frac{F_{sd}^V}{|f_1|}$ with the vector form factor $f_1 \simeq -1.22$ using the formula [221]

$$\Gamma(K^+ \rightarrow \pi^+ + A) = \frac{(m_K^2 - m_\pi^2)^2}{16\pi m_K (F_{sd}^V)^2} \sqrt{1 - 2 \frac{m_\pi^2 + m_A^2}{m_K^2} + \frac{(m_\pi^2 - m_A^2)^4}{m_K^4}} \quad (9.48)$$

for the decay rate $\Gamma(K^+ \rightarrow \pi^+ + A)$ with the K^+ mass m_K and π^+ mass m_π . In both cases, we have further assumed a vanishing axialvector coupling.

For masses m_A larger than 250 MeV we observe an exponential decay of the luminosity, which is proportional to $e^{-\frac{m_A}{T}}$ with $T \simeq 32 \text{ MeV}$. This exponential decay confirms that the leading effects for large

In other words, the diagram 9.5a could be cut at the intermediate on-shell neutron, reducing to two independent processes: the decay of a Λ into a neutron and axion-like particle and a scattering between two neutrons via pion exchange. The neutron scattering is already part of the supernova simulation.

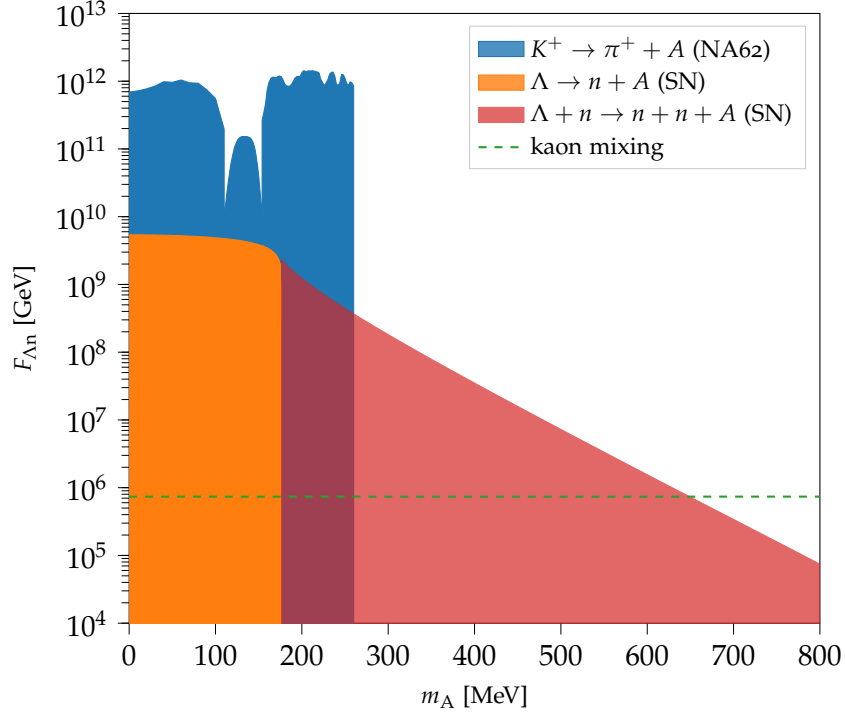


Figure 9.6: Excluded region (red) for the axion scale $F_{\Lambda n}$ of the Λ -neutron coupling in terms of the mass m_A of the axion-like particle as obtained by requiring the Λ bremsstrahlung luminosity to be smaller than the neutrino luminosity, see Equation (8.3). The bremsstrahlung bound is only calculated for axion-like particle masses above the Λ -neutron mass difference, $m_A \gtrsim \Delta M_{\Lambda n}$, since the intermediate neutron can be on-shell for smaller masses which leads to a singular propagator requiring further scrutiny. We also show the excluded areas from NA62 searches for $K^+ \rightarrow \pi^+ + A$ decays [213, 220] and the supernova (SN) bound from $\Lambda \rightarrow n + A$ decays [66] in orange. Moreover, the lower bound from kaon mixing [54] divided by the form factor $|f_1| \simeq 1.22$ is displayed in green, which is constantly extrapolated from its value at vanishing mass m_A and therefore only indicative.

masses are proportional to the exponential suppression of the phase space of a non-relativistic particle, see also References [117, 222]. Interestingly, the bound from Λ -neutron bremsstrahlung smoothly connects to the exclusion region from decays, yielding strong constraints in the regime where the decay is kinematically forbidden. In particular, we find tight limits of $F_{\Lambda n} \gtrsim \mathcal{O}(10^9 \text{ GeV})$ for masses $m_A \simeq \mathcal{O}(200 \text{ MeV})$, which are however still three orders of magnitude below the bounds from kaon decays in NA62 [213, 220]. Above masses of 260 MeV, these kaon decay constraints are absent due to large Standard Model backgrounds and the only available limit of $F_{sd}^V \gtrsim \mathcal{O}(10^5 \text{ GeV})$ on the flavor-violating coupling comes from kaon mixing [54]. In this regime, we find lower supernova bounds of $F_{\Lambda n} \gtrsim \mathcal{O}(10^8 \text{ GeV})$ for $m_A \simeq 260 \text{ MeV}$ which reduce to $F_{\Lambda n} \gtrsim 10^6 \text{ GeV}$ for $m_A \simeq 600 \text{ MeV}$. Thus, the supernova bound for axion-like parti-

cles surpasses the one from kaon mixing for masses of up to about 650 MeV.

Note, however, that the mixing constraint has been derived for a massless axion using Chiral Perturbation Theory. While this calculation exhibits large uncertainties already in the massless case, an extension to axion-like particles with masses of $\mathcal{O}(300 \text{ MeV})$ should be taken with caution and serves only as a reference point. Moreover, the kaon mixing bound is sensitive to ultraviolet dynamics from axion models where heavy degrees of freedom at the Peccei-Quinn scale could yield a contribution of similar size to the $\Delta S = 2$ operators relevant for kaon mixing.

Therefore, the supernova bound is highly relevant for axion-like particles with masses above 260 MeV, motivating a further investigation of the Λ bremsstrahlung process.

The exchange of a particle with a mass of $\mathcal{O}(f_a)$ becomes an $\mathcal{O}\left(\frac{1}{f_a^2}\right)$ contribution in the effective theory. The insertion of two axion couplings of $\mathcal{O}\left(\frac{1}{f_a}\right)$ is similar in size.

OUTLOOK We will extend this estimate in a future analysis by addressing several simplifications that can be expected to change our preliminary estimate by an $\mathcal{O}(1)$ factor:

1. We will calculate the full set of possible tree-level Feynman diagrams in the one-pion exchange approximation. This does not only include the evaluations of the diagram 9.5b but also the scattering with protons. While we neglected the proton diagrams due to the smaller proton abundance, they could yield a similar contribution to neutron scattering because of the larger multiplicity of diagrams and the reduced Pauli blocking of protons in the final state.
2. One should justify the omission of the axion-like particle momentum \mathbf{p}_A in the spatial delta function, see Equation (9.42). While we expect this to be a good approximation for masses m_A larger than the mass difference between neutron and Λ hyperon, it could be of similar size as the baryon momenta for smaller masses.
3. Matter effects should be added to the discussion since the lowered nucleon masses could potentially have an effect on the kinematics of the process and could also affect the mass difference $\Delta M_{\Lambda n}$. Similar to Λ decays we expect an effect of $\mathcal{O}(1)$.
4. We will translate the bound on the Λ -neutron coupling to the quark coupling $g_{sd}^{V,A}$ by performing a proper matching. This effect is relevant for large axion-like particle masses.

CONCLUSION AND OUTLOOK

In this part, we have studied constraints on flavor-violating couplings of axions and axion-like particles from the cooling of the proto-neutron star remnant of a supernova. If the energy loss by the emission of such hypothetical particles was too large, the expected duration of the supernova neutrino pulse of $\mathcal{O}(10\text{ s})$ would be shortened, contradicting observations. The detection of neutrinos from the SN1987A supernova confirmed the Standard Model expectation for the neutrino luminosity, imposing an upper limit on the additional energy loss due to the emission of new particles. Indeed, many analyses in the past have used the SN1987A neutrino signal to derive tight bounds on couplings of different types of new particles to ordinary matter, in particular axion couplings to nucleons and photons.

Recent simulations of supernovae have concluded that there exists a sizable population of Λ baryons in the core of a proto-neutron star due to high temperatures of $\mathcal{O}(40\text{ MeV})$. This large fraction of hyperons allows for an interesting probe of flavor-violating couplings of light particles, which up to now have been bounded only weakly by laboratory experiments. In this work, we have discussed the possibility to constrain the flavor-violating strange-down coupling of axions and axion-like particles in the light of the SN1987A signal.

In particular, we have studied two types of processes involving Λ baryons. First, we have analyzed axion production in decays of Λ baryons to neutrons, $\Lambda \rightarrow n + a$, which are mediated at tree-level by the flavor-violating vector and axialvector couplings $g_{\text{sd}}^{\text{V,A}}$. Specifically, we calculated the axion luminosity, taking corrections due to axion trapping and matter effects into account. As a result, we find that trapping can be neglected for Λ decays since Λ baryons cannot be reproduced at large radii, while matter effects account for an $\mathcal{O}(30\%)$ reduction of the luminosity. Using the energy loss argument, we were able to put lower limits of $F_{\text{sd}}^{\text{V}} \gtrsim 6.1 \times 10^9\text{ GeV}$ and $F_{\text{sd}}^{\text{A}} \gtrsim 4.4 \times 10^9\text{ GeV}$ on the effective axion scales, where $F_{\text{sd}}^{\text{V,A}}$ are the axion decay constants divided by the model-dependent dimensionless coupling constants $g_{\text{sd}}^{\text{V,A}}$. While the vector coupling is still constrained more stringently by $K^+ \rightarrow \pi^+ + a$ decays, the bounds on the axialvector coupling exceed not only the current best bounds from kaon mixing by two orders of magnitude, but also the expected future limit from BESIII by about a factor of ten. Moreover, there is no bound from kaon decays in the case of massless Dark Photons while the supernova analysis applies with minor modifications.

Turning to axion-like particles (ALPs) whose mass is a free parameter, we have explored the possibility to derive limits for axion-like particles with masses larger than the mass difference between Λ baryon and neutron, where Λ decays are kinematically forbidden. Adding a spectator neutron to the decay, the kinetic energy now allows for the production of axion-like particles heavier than 180 MeV. In this work, we have estimated the leading contributions to the axion luminosity of this bremsstrahlung process. The application of the energy loss argument leads to bounds of $F_{\Lambda n} \gtrsim \mathcal{O}(10^9 \text{ GeV})$, which are about three orders of magnitude below the bounds from kaon decays in NA62. Although the luminosity drops exponentially with increasing mass, we now also derive stringent limits of $\mathcal{O}(10^8 \text{ GeV})$ for axion-like particle masses above 260 MeV, where the $K^+ \rightarrow \pi^+ + A$ analysis does not place a limit due to large Standard Model backgrounds. The supernova bound also surpasses the one from kaon mixing for axion-like particle masses of up to $m_A \lesssim 650 \text{ MeV}$, which is the current best bound but suffers from large uncertainties and a sensitivity to potential ultraviolet dynamics. This makes the supernova bound highly relevant and motivates a further investigation of the Λ bremsstrahlung process.

While we have to wait for the next nearby supernova in our galaxy to improve on the experimental side, there are some points on the theoretical side that can be refined. First, more work is needed in the context of supernova modelling to obtain robust supernova models explaining all observations. On the particle physics side, one can improve the bremsstrahlung estimate by considering all relevant processes, scrutinizing the approximations made in this thesis, and by including matter effects. Moreover, one should translate the hyperon coupling to quark couplings by a proper treatment of hadronic effects. We expect these modifications to yield an $\mathcal{O}(1)$ correction to our estimate for the luminosity.

The variety of neutrino detectors that are running nowadays would allow for a precise test of supernova models by measuring the neutrino light curve of a nearby supernova—preferably within the Milky Way. As soon as such a supernova is observed with the plenty of modern neutrino detectors currently running, we will be able to significantly improve the energy loss criterion and increase the reliability of the supernova bounds on new particles.

CONCLUDING REMARKS

CONCLUDING REMARKS

The global efforts of building experiments at the intensity frontier led to vast progress in the exploration of light particles that are weakly coupled to the Standard Model. The prime example of such particles are neutrinos, but there are also many hypothetical particles of this class as well-motivated solutions of problems and puzzles of the Standard Model such as Dark Matter or the absence of CP-violation in strong interactions.

In this thesis, we have improved and extended previous studies on the phenomenology of light particles with masses below 1 GeV in several aspects. Specifically, we have generalized analyses of molecular spectra to more types of New Physics couplings and mediators. Moreover, we have extended existing texture studies in the neutrino sector with effects from charged leptons by assuming a well-motivated underlying $U(2)$ flavor symmetry. Finally, we have found novel bounds on flavor-violating axion couplings to light down-type quarks from the SN1987A supernova signal, which surpass existing laboratory limits by orders of magnitude.

Specifically, we have studied the implications of recent precision measurements of molecular spectra on the parameter space of new forces mediated by light particles in Part I. In contrast to other experimental methods like atomic spectroscopy, molecules have the advantage that couplings between two nuclei, two electrons and between an electron and a nucleus can be probed at the same time. While the coupling of a scalar mediator to nuclei has been discussed before in molecular spectroscopy, we have extended this analysis to other couplings and mediator types, namely pseudoscalar, vector and axialvector mediators. We have found upper limits on the different couplings of up to $\mathcal{O}(10^{-8})$ for mediators at the keV scale, which improve to $\mathcal{O}(10^{-11})$ for the axialvector electron-electron and nucleus-nucleus coupling. In all cases, our results are compatible with those obtained with other methods. For the electron-electron coupling, we find limits of the same order as those derived from Helium spectroscopy, while for nucleus-nucleus and electron-nucleus couplings other methods yield stronger bounds. However, we have also placed limits on the proton-proton coupling, while only neutron couplings are usually considered in the literature.

In Part II of this thesis, we have studied the predictions for neutrino observables in a broad class of models based on a $U(2)$ flavor symmetry, which work remarkably well in explaining the observed patterns in quark masses and mixings. For this purpose, we have assumed the

neutrino Yukawa matrix to share the features of viable $U(2)$ textures. The resulting texture has often been studied in the literature in the context of pure texture analyses. Here, it is the consequence of an underlying flavor symmetry which allowed us to include the effect of charged leptons in the resulting predictions. Specifically, we have considered two benchmark scenarios for charged leptons which are motivated from models compatible with Pati-Salam or $U(5)$ Grand Unification. In all cases, we find narrow ranges for the mass parameters at high confidence level. The sum of neutrino masses $\sum_i m_i$ is constrained to the small range of 63–69 meV in the special case of no effect from charged leptons to the PMNS matrix, where also the effective Majorana mass vanishes. This serves as a useful reference point for realistic unified scenarios which predict a similar range for the neutrino mass sum but a non-zero effective Majorana mass. All scenarios prefer normal ordering, while inverted ordering is only viable in the $U(5)$ compatible scenario, where the whole inverted ordering parameter space is excluded by cosmology. Finally, the correlation between the $(2,3)$ angle and the Dirac CP phase of the PMNS matrix—which is present in the case without charged leptons—is smeared out in the realistic unified scenarios due to additional phases in the charged lepton sector. As all predictions are below the reach of current and next-generation experiments, we conclude that only cosmological measurements can provide hints to the absolute neutrino mass scale in the near future if a $U(2)$ flavor symmetry is realized in nature. On the other hand, any signal in those experiments would exclude the entire class of models with $U(2)$ flavor symmetry.

In the final Part III, we have derived stellar bounds on the flavor-violating coupling of light pseudoscalar particles such as axions to light down-type quarks from the observation of the SN1987A supernova. For this purpose, we have first studied two-body decays of Λ hyperons into a neutron and an axion, which would occur frequently in the hot and dense proto-neutron star of a supernova due to the large abundance of Λ baryons. Thus, the cooling of the star would be significantly modified, resulting in tight lower bounds of $\mathcal{O}(10^9 \text{ GeV})$ on the effective vector and axialvector axion scales. While kaon decays yield stronger bounds for the vector coupling, our axialvector constraints surpass the corresponding current and future bounds by at least one order of magnitude. Moreover, we have estimated a bremsstrahlung-like process with Λ baryons as a possibility to extend this bound to axion-like particles with masses above 260 MeV, which is the upper limit reachable by kaon experiments. Indeed, our estimate yields constraints on the effective axion scale of $\mathcal{O}(10^8 \text{ GeV})$ that are better by about three orders of magnitude than the current best limit from kaon mixing, which itself suffers from large uncertainties in the calculation and from a potential sensitivity to the ultraviolet

theory. This preliminary result motivates a further and more thorough analysis in an upcoming publication.

To summarize, we have studied the phenomenology of light particles which can be probed in molecular spectroscopy, precision neutrino experiments and astrophysics, providing important information for a variety of experiments. Many of these experiments have already started taking data or will do so in the near future. Furthermore, there is the chance of observing a nearby galactic supernova which would significantly improve our understanding of the physics driving core-collapse supernova explosions. With these experimental results at hand, we will be able to substantially refine our knowledge about light particles and might even provide the first hints for Beyond the Standard Model Physics. The future of probing light degrees of freedom at the intensity frontier is definitely exciting!

APPENDIX

MOLECULAR SPECTROSCOPY

A.1 CALCULATION OF NON-RELATIVISTIC POTENTIALS

In this section, we exemplarily show the derivation of non-relativistic potentials for the cases of a scalar and pseudoscalar mediator, before we provide the steps that lead to the contact potential of the W box diagram given in Equation (3.25). The derivations of the scalar and pseudoscalar potential have also been considered in References [112, 223].

A.1.1 Scalar Mediator

The interaction of a scalar mediator S with mass m_S and two fermions f is described by the Lagrangian

$$\mathcal{L}_{\text{Sff}} = g_f^S S \bar{f} f. \quad (\text{A.1})$$

Given two fermions a and b with incoming momenta p_a, p_b and final state momenta p'_a, p'_b , the use of Feynman rules determines the amplitude of the diagram in Figure A.1 to read

$$\mathcal{M} = -\frac{g_a^S g_b^S}{q^2 - m_S^2 + i\epsilon} (\bar{u}'_a u_a) (\bar{u}'_b u_b). \quad (\text{A.2})$$

Here, $q = p_a - p'_a$ is the momentum transfer between the two interacting fermions, while $u_{a,b} = u(p_{a,b})$ and $u'_{a,b} = u(p'_{a,b})$ are the Dirac spinors of the incoming and outgoing particles, respectively.

In the non-relativistic limit, we can approximate $q^2 \simeq -\mathbf{q}^2$ with the spatial component \mathbf{q} of the momentum transfer q and

To see this, notice that the non-relativistic kinetic energy $\frac{\mathbf{p}^2}{2m}$ is suppressed by $\frac{v}{m}$ with respect to the momentum \mathbf{p} .

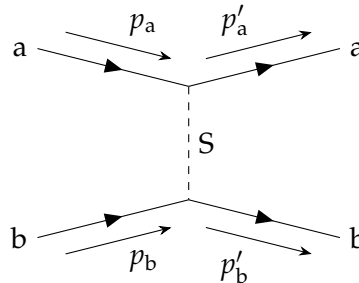


Figure A.1: Feynman diagram for the scattering of two particles a and b by the exchange of a scalar mediator S .

$$u(p) \simeq \begin{pmatrix} \xi \\ \frac{\mathbf{p} \cdot \boldsymbol{\sigma}}{2m} \xi \end{pmatrix}, \quad (\text{A.3})$$

where m is the mass of the considered fermion, ξ is a two-component Pauli spinor describing the particle's spin and $\boldsymbol{\sigma}$ is the tuple of Pauli matrices. Hence, we find

$$\bar{u}_i u_j \simeq \xi_i^\dagger \xi_j = (\xi_i^\dagger)_\alpha (\xi_j)_\beta \delta_{\alpha\beta} \quad (\text{A.4})$$

with spinor indices α, β and the Kronecker delta $\delta_{\alpha\beta}$. Plugging these approximations into the amplitude (A.2), we infer the Fourier-transformed non-relativistic potential $\tilde{V}(\mathbf{q})$ by comparison with Equation (3.1) as

$$[\tilde{V}(\mathbf{q})]_{\gamma\delta,\alpha\beta} \simeq -\frac{g_a^S g_b^S}{\mathbf{q}^2 + m_S^2} \delta_{\gamma\alpha} \delta_{\delta\beta}. \quad (\text{A.5})$$

As expected, the scalar interaction does not change the spin of the interacting particles which is reflected in the Kronecker deltas acting on the spin space of the fermions.

The Fourier transform of Equation (A.5) with respect to the momentum transfer \mathbf{q} finally yields the well-known Yukawa potential [107]

$$V(\mathbf{r}) = -\frac{g_a^S g_b^S}{4\pi} \frac{e^{-m_S r}}{r}, \quad (\text{A.6})$$

where we omitted the unit-operators on the spin space of the two particles.

A.1.2 Pseudoscalar Mediator

The Lagrangian

$$\mathcal{L}_{\text{Pff}} = i g_f^P \bar{P} \not{\gamma} f \quad (\text{A.7})$$

yields the interaction of a pseudoscalar particle P with mass m_P and a fermion species f . As a result, we find the matrix element

$$\mathcal{M} = \frac{g_a^P g_b^P}{q^2 - m_P^2 + i\epsilon} (\bar{u}'_a \not{\gamma}_5 u_a) (\bar{u}'_b \not{\gamma}_5 u_b) \quad (\text{A.8})$$

for the interaction between two fermion species a and b, following the notation of the previous section.

The Feynman diagram is the same as in Figure A.1 with the scalar S replaced by the pseudoscalar P.

Applying the same approximations as in the scalar case, the spinor product evaluates in the non-relativistic limit as

$$\bar{u}_i \gamma_5 u_j \simeq \frac{1}{2m} \xi_i^\dagger (\mathbf{p}_j - \mathbf{p}_i) \cdot \boldsymbol{\sigma} \xi_j, \quad (\text{A.9})$$

where we assumed the spinors u_i and u_j to refer to particles of the same mass, $m = m_i = m_j$. This corresponds to the assumption that the mediator particle cannot change flavor.

As a result, the momentum-space potential as defined in Equation (3.1) reads

$$\left[\tilde{V}(\mathbf{q}) \right]_{\gamma\delta, \alpha\beta} \simeq -\frac{1}{4m_a m_b} \frac{g_a^P g_b^P}{\mathbf{q}^2 + m_P^2} [\mathbf{q} \cdot \boldsymbol{\sigma}]_{\gamma\alpha} [\mathbf{q} \cdot \boldsymbol{\sigma}]_{\delta\beta}. \quad (\text{A.10})$$

Bearing in mind that the spin indices α, γ refer to the first particle a while β, δ refer to particle b, we can label the Pauli matrices by a and b to keep track of this. The Fourier transform to real space yields

$$V(\mathbf{r}) = \frac{g_a^P g_b^P}{4\pi} \frac{1}{4m_a m_b} (\boldsymbol{\sigma}_a \cdot \nabla) (\boldsymbol{\sigma}_b \cdot \nabla) \left(\frac{e^{-m_P r}}{r} \right) \quad (\text{A.11})$$

and using

$$\begin{aligned} \partial_j \partial_k \left(\frac{e^{-m_P r}}{r} \right) &= -m_P^2 \left[\delta_{jk} \left(\frac{1}{m_P r} + \frac{1}{m_P^2 r^2} + \frac{4\pi r}{3m_P^2} \delta^{(3)}(\mathbf{r}) \right) \right. \\ &\quad \left. - \frac{r_j r_k}{r^2} \left(1 + \frac{3}{m_P r} + \frac{3}{m_P^2 r^2} \right) \right] \frac{e^{-m_P r}}{r} \end{aligned} \quad (\text{A.12})$$

the pseudoscalar potential in Equation (3.17b) follows,

$$\begin{aligned} V_P(\mathbf{r}) &= -g_{ab}^P \frac{m_P^2}{4m_a m_b} \left[(\boldsymbol{\sigma}_a \cdot \boldsymbol{\sigma}_b) \left(\frac{1}{m_P^2 r^2} + \frac{1}{m_P r} + \frac{4\pi r}{3m_P^2} \delta^{(3)}(\mathbf{r}) \right) \right. \\ &\quad \left. - (\boldsymbol{\sigma}_a \cdot \hat{\mathbf{r}}) (\boldsymbol{\sigma}_b \cdot \hat{\mathbf{r}}) \left(1 + \frac{3}{m_P^2 r^2} + \frac{3}{m_P r} \right) \right] \frac{e^{-m_P r}}{4\pi r}, \end{aligned} \quad (\text{A.13})$$

with the abbreviation $g_{ab}^P = g_a^P g_b^P$.

A.1.3 Evaluation of the W Box Diagram

In this subsection, we sketch the evaluation of the box diagram in Figure 3.5 which leads to an estimate of the contact interaction. Denoting the loop momentum by l and choosing it to be the momentum of the W boson running at the top, we find the amplitude

This is appropriate in the non-relativistic limit even for mediators with flavor-changing couplings since the mass gap between different flavors cannot be overcome by keV energies.

$$\begin{aligned} i\mathcal{M} &= 8M_W^4 G_F^2 [\bar{u}(p_4) \gamma^\mu \gamma^\nu \gamma^\rho P_L u(p_1)] [\bar{u}(p_3) \gamma_\rho \gamma_\sigma \gamma_\mu P_L u(p_2)] \\ &\quad \times \int \frac{d^4 l}{(2\pi)^4} \frac{l_\nu l^\sigma}{(l^2 + i\varepsilon)^2 (l^2 - M_W^2 + i\varepsilon)^2}. \end{aligned} \quad (\text{A.14})$$

Here, M_W is the W boson mass, G_F is the Fermi constant, and P_L is the left-chiral projector, while $p_{1,2}$ and $p_{3,4}$ are the momenta of the initial and final state electrons, respectively. Moreover, we neglected the external momenta p_i in the propagators since we are interested in the high-energy behavior.

The loop integral is finite in four dimensions [224] leading to

$$i\mathcal{M} = -i \frac{2\pi}{3} G_F^2 M_W^2 [\bar{u}(p_4) \gamma^\mu \gamma^\nu \gamma^\rho P_L u(p_1)] [\bar{u}(p_3) \gamma_\rho \gamma_\nu \gamma_\mu P_L u(p_2)]. \quad (\text{A.15})$$

Using the identity [225]

$$[\gamma^\mu \gamma^\nu \gamma^\rho P_L]_{ij} [\gamma_\rho \gamma_\nu \gamma_\sigma P_L]_{kl} = 4 [\gamma^\mu P_L]_{ij} [\gamma_\mu P_L]_{kl} \quad (\text{A.16})$$

we can finally express the amplitude as

$$i\mathcal{M} = -i \frac{8\pi}{3} G_F^2 M_W^2 [\bar{u}(p_4) \gamma^\mu P_L u(p_1)] [\bar{u}(p_3) \gamma_\mu P_L u(p_2)]. \quad (\text{A.17})$$

In the non-relativistic limit, the spinor product simplifies to

$$\begin{aligned} &[\bar{u}(p_4) \gamma^\mu P_L u(p_1)] [\bar{u}(p_3) \gamma_\mu P_L u(p_2)] \\ &\simeq \frac{1}{4} \left[(\xi_4^\dagger \xi_1) (\xi_3^\dagger \xi_2) + (\xi_4^\dagger \sigma^i \xi_1) (\xi_3^\dagger \sigma^i \xi_2) \right] = \frac{1}{2} (\xi_3^\dagger \xi_1) (\xi_4^\dagger \xi_2), \end{aligned} \quad (\text{A.18})$$

where in the last step the identity $\sigma_{\alpha\beta}^i \sigma_{\gamma\delta}^i = 2\delta_{\alpha\delta} \delta_{\gamma\beta} - \delta_{\alpha\beta} \delta_{\gamma\delta}$ [226] was applied.

Comparing to the definition of the potential in Equation (3.1), we find the potential in momentum space

$$\left[\tilde{V}(\mathbf{q}) \right]_{\gamma\delta, \alpha\beta} \simeq \frac{4}{3} \pi G_F^2 M_W^2 \delta_{\gamma\alpha} \delta_{\delta\beta}. \quad (\text{A.19})$$

Finally, the Fourier transform of a constant yields the Dirac delta distribution. Suppressing the unit matrices in spin space, we hence find the potential

$$V(\mathbf{r}) = \frac{4}{3} \pi G_F^2 M_W^2 \delta^{(3)}(\mathbf{r}) \quad (\text{A.20})$$

which is a contact potential as expected for the high-energy contribution.

A.2 SPIN MATRIX ELEMENTS

In this section, we briefly discuss the possible spin states for the isotopologues in their unperturbed ground states (2.13). For this purpose, we explicitly write the spin parts of the wave functions, that is

$$|\Psi^{(0)}\rangle = |\varphi_{\text{el}}\rangle \otimes |\text{spin}\rangle_{\text{el}} \otimes |\chi\rangle \otimes |\text{spin}\rangle_{\text{N}}, \quad (\text{A.21})$$

where $|\text{spin}\rangle_{\text{el}}$ is the spin state of the spin- $\frac{1}{2}$ electrons and $|\text{spin}\rangle_{\text{N}}$ is the spin state of the nuclei with spins S_1 and S_2 . In the following, we refer to the spin operators of the electrons $i = 1, 2$ as $\hat{\mathbf{S}}_i^{\text{e}}$ and to those of the nuclei $i = A, B$ as $\hat{\mathbf{S}}_i^{\text{N}}$.

ELECTRONIC SPIN STATE Since the electronic ground state wave function is symmetric under the exchange of the two electrons, the electronic spin state must be antisymmetric to fulfill the Pauli principle. Hence, the electrons must have vanishing total spin and their state is given by the spin singlet

$$|\text{spin}\rangle_{\text{el}} = |s_{\text{e}} = 0, m_{\text{e}} = 0\rangle = \frac{1}{2} (|\uparrow\downarrow\rangle - |\downarrow\uparrow\rangle), \quad (\text{A.22})$$

where s_{e} is the total spin quantum number linked to the operator $\hat{\mathbf{S}}^{\text{e}} = \hat{\mathbf{S}}_1^{\text{e}} + \hat{\mathbf{S}}_2^{\text{e}}$ and m_{e} is the corresponding eigenvalue of the z component \hat{S}_z^{e} . The first arrow in the kets indicates the spin state of the first electron with \uparrow and \downarrow being spin up and down, respectively, while the second arrow refers to the second electron.

As a consequence, the spin matrix elements $\langle \text{spin} |_{\text{el}} [\hat{\mathbf{S}}_i^{\text{e}}]_{\alpha} [\hat{\mathbf{S}}_j^{\text{e,N}}]_{\beta} | \text{spin} \rangle_{\text{el}}$ of one electron $i = 1, 2$ interacting with either the other electron or a nucleus $j = 1, 2, A, B$ and where α, β are the components of the spin vector read as follows:

1. **ELECTRON-NUCLEUS FORCE** In this case, the index j refers to nucleus A or B so that the nucleus spin operator can be factored out. Since $\langle 0, 0 |_{\text{el}} \hat{\mathbf{S}}_i^{\text{e}} | 0, 0 \rangle_{\text{el}} = 0$, all matrix elements vanish,

$$\langle 0, 0 |_{\text{el}} [\hat{\mathbf{S}}_i^{\text{e}}]_{\alpha} [\hat{\mathbf{S}}_j^{\text{N}}]_{\beta} | 0, 0 \rangle_{\text{el}} \sim \langle 0, 0 |_{\text{el}} [\hat{\mathbf{S}}_i^{\text{e}}]_{\alpha} | 0, 0 \rangle_{\text{el}} = 0. \quad (\text{A.23})$$

Thus, all spin-dependent terms vanish for couplings between one electron and one nucleus.

2. **ELECTRON-ELECTRON FORCE** Here, we evaluate

$$\langle 0, 0 |_{\text{el}} [\hat{\mathbf{S}}_1^{\text{e}}]_{\alpha} [\hat{\mathbf{S}}_2^{\text{e}}]_{\beta} | 0, 0 \rangle_{\text{el}} = -\frac{1}{4} \delta_{\alpha\beta} \quad (\text{A.24})$$

yielding

$$\langle 0, 0 |_{\text{el}} \hat{\mathbf{S}}_1^{\text{e}} \cdot \hat{\mathbf{S}}_2^{\text{e}} | 0, 0 \rangle_{\text{el}} = -\frac{3}{4}. \quad (\text{A.25})$$

For instance, the electronic matrix element of the pseudoscalar potential (3.17b) with $\mathbf{r} = \mathbf{r}_{12} = \mathbf{r}_2 - \mathbf{r}_1$ simplifies to

$$\begin{aligned} & (\langle \varphi_{\text{el}} | \otimes \langle 0, 0 |_{\text{el}}) V_P(\mathbf{r}) (| \varphi_{\text{el}} \rangle \otimes | 0, 0 \rangle_{\text{el}}) \\ & \sim \langle \varphi_{\text{el}} | \left[-\frac{3}{4} \left(\frac{1}{m^2 r^2} + \frac{1}{mr} + \frac{4\pi r}{3m^2} \delta^{(3)}(\mathbf{r}) \right) \right. \\ & \quad \left. + \frac{1}{4} \left(1 + \frac{3}{m^2 r^2} + \frac{3}{mr} \right) \right] \frac{e^{-mr}}{4\pi r} | \varphi_{\text{el}} \rangle \\ & = \frac{1}{4} \left[\langle \varphi_{\text{el}} | \frac{e^{-mr}}{4\pi r} | \varphi_{\text{el}} \rangle - \frac{1}{4m^2} \langle \varphi_{\text{el}} | \delta^{(3)}(\mathbf{r}) | \varphi_{\text{el}} \rangle \right], \quad (\text{A.26}) \end{aligned}$$

where we dropped constant terms and used the Dirac distribution to cancel the exponential.

NUCLEAR SPIN STATES In the case of spin-dependent forces coupling to nuclei, we encounter two types of angular momentum matrix elements. The matrix element of the operator $\hat{\mathbf{S}}_A^N \cdot \hat{\mathbf{S}}_B^N$ only depends on nuclear spins, while the one of the operator $(\hat{\mathbf{S}}_A^N \cdot \hat{\mathbf{r}})(\hat{\mathbf{S}}_B^N \cdot \hat{\mathbf{r}})$ can be factorized into a spin and an orbital angular momentum part,

$$\begin{aligned} & (\langle J, M_1 | \otimes \langle S, m_1 |_{\text{N}}) (\hat{\mathbf{S}}_A^N \cdot \hat{\mathbf{r}})(\hat{\mathbf{S}}_B^N \cdot \hat{\mathbf{r}}) (| J, M_2 \rangle \otimes | S, m_2 \rangle_{\text{N}}) \\ & = \langle J, M_1 | \frac{r_\alpha r_\beta}{r^2} | J, M_2 \rangle \langle S, m_1 |_{\text{N}} [\hat{\mathbf{S}}_A^N]_\alpha [\hat{\mathbf{S}}_B^N]_\beta | S, m_2 \rangle_{\text{N}}. \quad (\text{A.27}) \end{aligned}$$

The orbital part can be evaluated by decomposing the tensor $r_i r_j$ in terms of spherical harmonics Y_l^m ,

$$\frac{r_i r_j}{r^2} = \sum_{l,m} \lambda_l^m Y_l^m(\vartheta, \varphi), \quad (\text{A.28})$$

with coefficients λ_l^m . For instance,

$$\frac{x^2}{r^2} = \frac{2\sqrt{\pi}}{3} Y_0^0 + \sqrt{\frac{2\pi}{15}} Y_2^{-2} - \frac{2}{3} \sqrt{\frac{\pi}{5}} Y_2^0 + \sqrt{\frac{2\pi}{15}} Y_2^2 \quad \text{or} \quad (\text{A.29})$$

$$\frac{xy}{r^2} = i \sqrt{\frac{2\pi}{15}} Y_2^{-2} - i \sqrt{\frac{2\pi}{15}} Y_2^2. \quad (\text{A.30})$$

The integrals can afterwards be solved by using the formula [227]

$$\begin{aligned} & \langle J, M_1 | Y_l^m | J, M_2 \rangle = \int d\Omega (Y_J^{M_1})^* Y_l^m Y_J^{M_2} \\ & = \sqrt{\frac{2l+1}{4\pi}} C_{00, J0}^{lJ} C_{m M_2, J M_1}^{lJ}, \quad (\text{A.31}) \end{aligned}$$

where $C_{m_1 m_2, j m}^{j_1 j_2}$ are the Clebsch-Gordan coefficients for the addition of two spins with quantum numbers $|j_1, m_1\rangle$ and $|j_2, m_2\rangle$ to a state $|j, m\rangle$.

For the spin-state matrix element, we must distinguish between bosonic and fermionic nuclei. Since the potentials listed in Sections 3.2 and 3.3 are only valid for fermions, we cannot consider the couplings to deuterium being a spin-1 nucleus. This leaves us with H₂, T₂ and HT to consider.

Starting with the homonuclear isotopologues H₂ and T₂, their quantum states must be antisymmetric under the exchange of the nuclei to comply with the Pauli principle. The spatial part of the nuclear wave function χ can be split into spherical harmonics Y_J^m and a radial part, see Equation (2.22). Interchanging the two nuclei, the nuclear wave function gets a factor $(-1)^J$ from the spherical harmonics and is thus antisymmetric for odd angular momentum J and symmetric for even angular momentum J . In order to obtain an overall antisymmetric state, the nuclear spin state $|\text{spin}\rangle_{\text{N}}$ must therefore be symmetric for odd J and antisymmetric for even J .

1. **EVEN ANGULAR MOMENTUM** In this case, the nuclear spins are in the singlet $S_{\text{N}} = 0$ state $|0, 0\rangle_{\text{N}}$. The spin matrix elements for this case are the same as for the electronic case, see Equations (A.23), (A.24) and (A.25). In particular, we find

$$\begin{aligned} & (\langle J, M_1 | \otimes \langle 0, 0 |_{\text{N}}) (\hat{\mathbf{S}}_{\text{A}}^{\text{N}} \cdot \hat{\mathbf{r}}) (\hat{\mathbf{S}}_{\text{B}}^{\text{N}} \cdot \hat{\mathbf{r}}) (|J, M_2\rangle \otimes |0, 0\rangle_{\text{N}}) \\ &= -\frac{1}{4} \delta_{\alpha\beta} \langle J, M_1 | \frac{r_{\alpha} r_{\beta}}{r^2} |J, M_2\rangle = -\frac{1}{4} \delta_{M_1 M_2} \end{aligned} \quad (\text{A.32})$$

so that the perturbation stays diagonal in this case.

2. **ODD ANGULAR MOMENTUM** For odd J , the nuclear spin state is given by the symmetric $S_{\text{N}} = 1$ triplet state. Since there is now an additional degeneracy given by the spin multiplicity, the matrix elements become more involved. In particular, we find

$$\begin{aligned} & (\langle J, M_1 | \otimes \langle 1, m_1 |_{\text{N}}) (\hat{\mathbf{S}}_{\text{A}}^{\text{N}} \cdot \hat{\mathbf{S}}_{\text{B}}^{\text{N}}) (|J, M_2\rangle \otimes |1, m_2\rangle) \\ &= \frac{1}{4} \delta_{m_1 m_2} \delta_{M_1 M_2}. \end{aligned} \quad (\text{A.33})$$

The other relevant operator $(\hat{\mathbf{S}}_{\text{A}}^{\text{N}} \cdot \hat{\mathbf{r}}) (\hat{\mathbf{S}}_{\text{B}}^{\text{N}} \cdot \hat{\mathbf{r}})$ is not diagonal anymore in this case and due to the lengthy expressions we refrain from listing it in this thesis.

For the heteronuclear molecule HT, there is no restriction on the exchange of the two nuclei from the Pauli principle. Hence, there are no restrictions on the symmetry of the spin state which could be a singlet or triplet state. Since all these states are now degenerate, we have to calculate the matrix of each potential for all these states. For example, the operator $\hat{\mathbf{S}}_{\text{A}}^{\text{N}} \cdot \hat{\mathbf{S}}_{\text{B}}^{\text{N}}$ yields a matrix

$$\begin{aligned}
& (\langle J, M_1 | \otimes \langle m_1, m_2 |_{\text{N}}) (\hat{\mathbf{S}}_{\text{A}}^{\text{N}} \cdot \hat{\mathbf{S}}_{\text{B}}^{\text{N}}) (|J, M_2\rangle \otimes |m'_1, m'_2\rangle_{\text{N}}) \\
& \hat{=} \begin{pmatrix} \frac{1}{4}\delta_{M_1 M_2} & 0 & 0 & 0 \\ 0 & -\frac{1}{4}\delta_{M_1 M_2} & \frac{1}{2}\delta_{M_1 M_2} & 0 \\ 0 & \frac{1}{2}\delta_{M_1 M_2} & -\frac{1}{4}\delta_{M_1 M_2} & 0 \\ 0 & 0 & 0 & \frac{1}{4}\delta_{M_1 M_2} \end{pmatrix} \quad (\text{A.34})
\end{aligned}$$

in the basis of the nuclear spins. In particular, we arranged the spin basis in the form $\{|\uparrow\uparrow\rangle, |\uparrow\downarrow\rangle, |\downarrow\uparrow\rangle, |\downarrow\downarrow\rangle\}$ where the first and second entry in the states correspond to the z projection of the hydrogen and tritium spin, respectively.

The matrix element of the second operator $(\hat{\mathbf{S}}_{\text{A}}^{\text{N}} \cdot \hat{\mathbf{r}})(\hat{\mathbf{S}}_{\text{B}}^{\text{N}} \cdot \hat{\mathbf{r}})$ again evaluates to lengthy expressions and we refrain from showing it here.

A.3 LIST OF EXPERIMENTAL DATA

Here, all experimental data used in our analysis are listed.

Table A.1: List of all measurements used in our analysis. The transitions $(v_1, J_1) \rightarrow (v_2, J_2)$ are characterized by the vibrational quantum numbers v_i and the angular momentums J_i of the involved levels (v_i, J_i) .

molecule	transition	energy [cm^{-1}]	reference
H ₂	(3, 5) \rightarrow (0, 3)	12 559.749 52(5)	[228]
H ₂	(1, 0) \rightarrow (0, 0)	4161.166 36(15)	[98]
H ₂	(1, 1) \rightarrow (0, 1)	4155.254 00(21)	[98]
H ₂	(1, 2) \rightarrow (0, 2)	4143.465 53(15)	[98]
H ₂	(11, 1) \rightarrow (0, 0)	32 937.7554(16)	[229]
H ₂	(11, 3) \rightarrow (0, 0)	33 186.4791(16)	[229]
H ₂	(11, 4) \rightarrow (0, 0)	33 380.1025(33)	[229]
H ₂	(11, 5) \rightarrow (0, 0)	33 615.5371(18)	[229]
HD	(1, 0) \rightarrow (0, 0)	3632.160 52(22)	[98]
HD	(1, 1) \rightarrow (0, 1)	3628.304 50(22)	[98]
HD	(2, 2) \rightarrow (0, 1)	7241.849 350 87(67)	[99]
HD	(2, 3) \rightarrow (0, 2)	7306.483 222 50(93)	[99]
HD	(2, 4) \rightarrow (0, 3)	7361.903 173 35(93)	[99]
D ₂	(1, 0) \rightarrow (0, 0)	2993.617 06(15)	[98]
D ₂	(1, 1) \rightarrow (0, 1)	2991.507 06(15)	[98]
D ₂	(1, 2) \rightarrow (0, 2)	2987.293 52(15)	[98]
D ₂	(0, 2) \rightarrow (0, 0)	179.068(2)	[101]

molecule	transition	energy [cm ⁻¹]	reference
D ₂	(0, 3) → (0, 1)	297.533(3)	[101]
D ₂	(0, 4) → (0, 2)	414.648(2)	[101]
T ₂	(1, 0) → (0, 0)	2464.503 94(67)	[105]
T ₂	(1, 1) → (0, 1)	2463.348 17(42)	[105]
T ₂	(1, 2) → (0, 2)	2461.039 17(42)	[105]
T ₂	(1, 3) → (0, 3)	2457.581 35(42)	[105]
T ₂	(1, 4) → (0, 4)	2452.982 33(42)	[105]
T ₂	(1, 5) → (0, 5)	2447.250 61(42)	[105]
T ₂	(1, 6) → (0, 6)	2440.397(5)	[105]
T ₂	(1, 7) → (0, 7)	2432.442(5)	[105]
T ₂	(1, 2) → (0, 0)	2581.114(5)	[105]
T ₂	(1, 3) → (0, 1)	2657.281(5)	[105]
T ₂	(1, 4) → (0, 2)	2731.716(5)	[105]
T ₂	(1, 5) → (0, 3)	2804.164(5)	[105]
DT	(1, 0) → (0, 0)	2743.341 60(42)	[105]
DT	(1, 1) → (0, 1)	2741.732 04(39)	[105]
DT	(1, 2) → (0, 2)	2738.516 62(42)	[105]
DT	(1, 3) → (0, 3)	2733.704 79(42)	[105]
DT	(1, 4) → (0, 4)	2727.307 45(42)	[105]
DT	(1, 5) → (0, 5)	2719.342 21(42)	[105]
DT	(1, 6) → (0, 6)	2709.828 35(67)	[105]
DT	(1, 7) → (0, 7)	2698.7870(5)	[105]
HT	(1, 0) → (0, 0)	3434.812 48(53)	[105]
HT	(1, 1) → (0, 1)	3431.575 09(53)	[105]
HT	(1, 2) → (0, 2)	3425.112 65(53)	[105]
HT	(1, 3) → (0, 3)	3415.452 58(53)	[105]

NEUTRINO OBSERVABLES FROM A $U(2)$ TEXTURE

B.1 RELATIONS BETWEEN NEUTRINO AND PMNS PARAMETERS

The PMNS matrix U can be obtained from the left-handed rotations V_L^ℓ in the charged lepton sector and V^ν in the neutrino sector as

$$U = (V_L^\ell)^\dagger V^\nu. \quad (\text{B.1})$$

One can express the neutrino parameters in terms of those of the charged lepton rotation and PMNS matrix by inverting this relation,

$$V^\nu = V_L^\ell U. \quad (\text{B.2})$$

Parametrizing all matrices in the standard form (5.7), one can determine the neutrino parameters. For instance, the angles can be obtained as

$$\sin(\vartheta_{13}^\nu) = |V_{13}^\nu|, \quad (\text{B.3})$$

$$\sin(\vartheta_{12}^\nu) = \frac{|V_{12}^\nu|}{\cos(\vartheta_{13}^\nu)}, \quad (\text{B.4})$$

$$\sin(\vartheta_{23}^\nu) = \frac{|V_{23}^\nu|}{\cos(\vartheta_{13}^\nu)}. \quad (\text{B.5})$$

PATI-SALAM SCENARIO In the $U(2)_{\text{PS}}$ scenario, the angles in terms of the PMNS parameters ϑ_{ij} , δ and $\alpha_{1,2}$ as well as the charged lepton angle $\vartheta_{23}^{\ell,R}$ and the effective phase β read

$$s_{23}^\nu = \frac{c_{12}^{\ell,L} c_{13}}{c_{13}^\nu} \left| s_{23} - t_{12}^{\ell,L} t_{13} e^{i\beta} \right|, \quad (\text{B.6})$$

$$s_{12}^\nu = \frac{s_{12}^{\ell,L} s_{12}}{c_{13}^\nu} \left| \frac{c_{13}}{t_{12}^{\ell,L}} e^{i\beta} + \frac{c_{23}}{t_{12}} e^{-i\delta} - s_{23} s_{13} \right|, \quad (\text{B.7})$$

$$s_{13}^\nu = c_{12}^{\ell,L} c_{13} \left| t_{13} e^{i\beta} + t_{12}^{\ell,L} s_{23} \right|, \quad (\text{B.8})$$

where $s_{ij} = \sin(\vartheta_{ij})$, $c_{ij} = \cos(\vartheta_{ij})$ and $t_{ij} = \tan(\vartheta_{ij})$ and analogously for the charged lepton angles. Moreover, the (1,2) charged lepton angle reads

$$s_{12}^{\ell,L} = \sqrt{\frac{c_{23}^{\ell,R} m_e}{m_\mu}} \quad (\text{B.9})$$

with electron and muon masses m_e and m_μ , respectively. The phases can be obtained by

$$\delta^y = \delta + \gamma_1 + \gamma_2, \quad (\text{B.10})$$

$$\alpha_1^y = \alpha_1 - \gamma_1, \quad (\text{B.11})$$

$$\alpha_2^y = \alpha_2 - \gamma_1 + \gamma_3, \quad (\text{B.12})$$

where we abbreviated

$$\gamma_1 = \arg \left(\frac{c_{13}t_{12}e^{i\beta} - s_{23}s_{13}t_{12}t_{12}^{\ell,L} + c_{23}t_{12}^{\ell,L}e^{-i\delta}}{s_{23}t_{12}^{\ell,L}t_{12}e^{i\beta} - (t_{12}^{\ell,L})^2 t_{12}t_{13}} \right), \quad (\text{B.13})$$

$$\gamma_2 = \arg \left(\frac{c_{13}e^{i\beta} - s_{23}s_{13}t_{12}^{\ell,L} - c_{23}t_{12}t_{12}^{\ell,L}e^{-i\delta}}{t_{13}t_{12}^{\ell,L}e^{i\beta} + (t_{12}^{\ell,L})^2 s_{23}} \right), \quad (\text{B.14})$$

$$\gamma_3 = \arg \left(\frac{c_{13}t_{12}e^{i\beta} - s_{23}s_{13}t_{12}t_{12}^{\ell,L} + c_{23}t_{12}^{\ell,L}e^{-i\delta}}{c_{13}t_{12}e^{i\beta} - s_{23}s_{13}t_{12}t_{12}^{\ell,L} - c_{23}(t_{12})^2 t_{12}^{\ell,L}e^{-i\delta}} \right). \quad (\text{B.15})$$

$U(5)$ COMPATIBLE SCENARIO In the $U(2)_5$ scenario, the angles in terms of the PMNS parameters ϑ_{ij} , δ and $\alpha_{1,2}$ as well as the charged lepton angle $\vartheta_{23}^{\ell,L}$ and the two effective phases $\beta_{1,2}$ are given by

$$s_{23}^y = \frac{c_{23}^{\ell,L} c_{12}^{\ell,L} c_{13}}{c_{13}^y} \left| s_{23} - t_{12}^{\ell,L} t_{13} e^{i\beta_1} + \frac{c_{23} t_{23}^{\ell,L}}{c_{12}^{\ell,L}} e^{-i\beta_2} \right|, \quad (\text{B.16})$$

$$s_{12}^y = \frac{s_{12}^{\ell,L} s_{12}}{c_{13}^y} \left| \frac{c_{13}}{t_{12}^{\ell,L}} e^{i\beta_1} + \frac{c_{23}}{t_{12}} e^{-i\delta} - s_{13} s_{23} \right|, \quad (\text{B.17})$$

$$s_{13}^y = c_{12}^{\ell,L} c_{13} \left| t_{13} e^{i\beta_1} + t_{12}^{\ell,L} s_{23} \right|, \quad (\text{B.18})$$

where $s_{ij} = \sin(\vartheta_{ij})$, $c_{ij} = \cos(\vartheta_{ij})$ and $t_{ij} = \tan(\vartheta_{ij})$ and analogously for the charged lepton angles. Moreover, the $(1,2)$ charged lepton angle reads

$$s_{12}^{\ell,L} = \sqrt{\frac{m_e}{c_{23}^{\ell,L} m_\mu}} \quad (\text{B.19})$$

with electron and muon masses m_e and m_μ , respectively. The phases can be obtained by

$$\delta^y = \delta + \gamma_1 + \gamma_2, \quad (\text{B.20})$$

$$\alpha_1^y = \alpha_1 - \gamma_1, \quad (\text{B.21})$$

$$\alpha_2^y = \alpha_2 - \gamma_1 + \gamma_3, \quad (\text{B.22})$$

where we abbreviated

$$\begin{aligned} \gamma_1 = & \arg \left(\frac{s_{13}s_{23}t_{12}t_{12}^{\ell,L}t_{23}^{\ell,L} - c_{13}t_{12}t_{23}^{\ell,L}e^{i\beta_1} - c_{23}t_{12}^{\ell,L}t_{23}^{\ell,L}e^{-i\delta}}{t_{13}t_{12}s_{12}^{\ell,L}t_{12}^{\ell,L}t_{23}^{\ell,L} + c_{23}t_{12}t_{12}^{\ell,L}e^{i(\beta_1+\beta_2)} - s_{23}t_{12}s_{12}^{\ell,L}t_{23}^{\ell,L}e^{i\beta_1}} \right) \\ & + \arg \left(t_{13}s_{12}^{\ell,L}e^{i(\beta_1+\beta_2)} - s_{23}c_{12}^{\ell,L}e^{i\beta_2} - c_{23}t_{23}^{\ell,L} \right), \end{aligned} \quad (\text{B.23})$$

$$\gamma_2 = \arg \left(\frac{-s_{13}s_{23}t_{12}t_{12}^{\ell,L} + c_{13}t_{12}e^{i\beta_1} - c_{23}t_{12}^{\ell,L}e^{-i\delta}}{s_{23}t_{12}s_{12}^{\ell,L}t_{12}^{\ell,L} + t_{12}t_{13}s_{12}^{\ell,L}e^{i\beta_1}} \right), \quad (\text{B.24})$$

$$\gamma_3 = \arg \left(\frac{s_{13}s_{23}t_{12}t_{12}^{\ell,L} - c_{13}t_{12}e^{i\beta_1} - c_{23}t_{12}^{\ell,L}e^{-i\delta}}{s_{13}s_{23}t_{12}t_{12}^{\ell,L} - c_{13}t_{12}e^{i\beta_1} + (t_{12})^2c_{23}t_{12}^{\ell,L}e^{-i\delta}} \right). \quad (\text{B.25})$$

SUPERNOVA CONSTRAINTS

C.1 THE PRINCIPLE OF DETAILED BALANCE

For particles in thermal and chemical equilibrium, one can relate the absorption rate Γ_{abs} to the production rate Γ_{prod} by the principle of detailed balance.

Considering a production process for the new particle X of the form $i_1 + i_2 + \dots \rightarrow X + f_1 + f_2 + \dots$ with initial state particles i_j with momenta k_j and final state particles f_j with momenta p_j , we obtain the absorption rate Γ_{abs} by exchanging initial and final states in the formula of the production rate Γ_{prod} in Equation (9.4) [201],

$$\Gamma_{\text{abs}} = \frac{1}{2E_X} \prod_{f \neq X} \int \frac{d^3 p_f}{(2\pi)^3 2E_f} f_f(\mathbf{p}_f) \prod_i \int \frac{d^3 k_i}{(2\pi)^3 2E_i} (1 \pm f_i(\mathbf{k}_i)) \times (2\pi)^4 \delta^{(4)}\left(\sum_i k_i - \sum_f p_f\right) \sum_{\text{pol}} |\mathcal{M}|^2. \quad (\text{C.1})$$

Chemical equilibrium requires that the sums of the chemical potentials of initial and final state particles are equal,

$$\mu_{i_1} + \mu_{i_2} + \dots = \mu_X + \mu_{f_1} + \mu_{f_2} + \dots. \quad (\text{C.2})$$

Moreover, the relation

$$1 \pm f_{\text{BE/FD}}(E) = e^{\frac{E-\mu}{T}} f_{\text{BE/FD}}(E) \quad (\text{C.3})$$

holds for both the Bose-Einstein (BE) and the Fermi-Dirac (FD) distribution. Assuming vanishing chemical potential $\mu_X = 0$ for the new particle X , we therefore find

$$\begin{aligned} \prod_i f_i(E_i) \prod_{f \neq X} (1 \pm f_f(E_f)) &= \prod_i f_i(E_i) \prod_{f \neq X} e^{\frac{\sum_{f \neq X} E_f - \sum_{f \neq X} \mu_f}{T}} f_f(E_f) \\ &= e^{-\frac{E_X - \mu_X}{T}} \prod_i e^{\frac{\sum_i (E_i - \mu_i)}{T}} f_i(E_i) \prod_{f \neq X} f_f(E_f) \\ &= e^{-\frac{E_X}{T}} \prod_{f \neq X} f_f(E_f) \prod_i (1 \pm f_i(E_i)), \end{aligned} \quad (\text{C.4})$$

where we used energy conservation in the second step and thermal equilibrium.

Assuming CP invariance for the matrix element, $|\mathcal{M}_{f \rightarrow i}|^2 = |\mathcal{M}_{i \rightarrow f}|^2$, we therefore find

$$\Gamma_{\text{abs}} = e^{\frac{E_X}{T}} \Gamma_{\text{prod}} \quad (\text{C.5})$$

when we compare to the definition of the production rate in Equation (9.4).

C.2 LAMBDA PRODUCTION RATES FROM DECAYS

The matrix element for a Λ baryon with momentum p_Λ decaying into a neutron and an axion with momenta p_n and p_a , respectively, is obtained from

$$\begin{aligned} & i(2\pi)^4 \delta^{(4)}(p_\Lambda - p_n - p_a) \mathcal{M}(\Lambda \rightarrow n + a) \\ &= \int d^4x \langle n(p_n), a(p_a) | i\mathcal{L}_{\text{aff}} | \Lambda(p_\Lambda) \rangle \end{aligned} \quad (\text{C.6})$$

with the Lagrangian \mathcal{L}_{aff} defined in Equation (9.18).

For the calculation of the amplitude, one needs the baryonic matrix elements $\langle n(p_n) | \bar{d}\gamma^\mu(\gamma_5)s | \Lambda(p_\Lambda) \rangle$ of vector and axialvector quark currents. They can be expressed in terms of three form factors $f_{1,2,3}(q^2)$ for the vector and $g_{1,2,3}(q^2)$ for the axialvector currents and read [66]

$$\begin{aligned} & \langle n(p_n) | \bar{d}\gamma^\mu s | \Lambda(p_\Lambda) \rangle \\ &= \bar{u}_n(p_n) \left[f_1(q^2)\gamma^\mu + \frac{f_2(q^2)}{m_\Lambda}\sigma^{\mu\nu}q_\nu + \frac{f_3(q^2)}{m_\Lambda}q^\mu \right] u_\Lambda(p_\Lambda), \quad (\text{C.7a}) \\ & \langle n(p_n) | \bar{d}\gamma^\mu\gamma_5 s | \Lambda(p_\Lambda) \rangle \\ &= \bar{u}_n(p_n) \left[g_1(q^2)\gamma^\mu + \frac{g_2(q^2)}{m_\Lambda}\sigma^{\mu\nu}q_\nu + \frac{g_3(q^2)}{m_\Lambda}q^\mu \right] \gamma_5 u_\Lambda(p_\Lambda), \end{aligned} \quad (\text{C.7b})$$

where $q = p_\Lambda - p_n$.

Therefore, the amplitude $\mathcal{M}(\Lambda \rightarrow n + a)$ for a massless axion is given by

$$\begin{aligned} & i\mathcal{M}(\Lambda \rightarrow n + a) \\ &= \frac{-iq_\mu}{2f_a} \bar{u}_n(p_n)\gamma^\mu \left[(g_{\text{sd}}^V)^* f_1 + (g_{\text{sd}}^A)^* g_1\gamma_5 \right] u_\Lambda(p_\Lambda), \end{aligned} \quad (\text{C.8})$$

where the terms proportional to the tensor form factors f_2 and g_2 cancel due to antisymmetry and the ones proportional to f_3 and g_3 due to the vanishing axion mass, $q^2 = p_a^2 = m_a^2 = 0$. Moreover, we defined the charges $f_1 = f_1(0)$ and $g_1 = g_1(0)$ as in Reference [66].

VACUUM DECAY RATE Until now, no assumptions on the dispersion relation have been made. When we square the matrix element and sum over polarizations, we however have to consider the modified polarization sum and mass-shell condition due to medium effects, see Section 9.1 for a discussion and in particular Equations (9.16) and (9.17). Since we want to relate the Λ decay in stars to the one in vacuum which is measured in collider experiments, we first calculate the vacuum case.

The squared matrix element summed over final state polarizations can be readily obtained in this case to read [66]

$$\sum_{\text{pol}} |\mathcal{M}|_{\text{free}}^2 = \frac{|g_{\text{sd}}^{\text{V}}|^2 f_1^2 + |g_{\text{sd}}^{\text{A}}|^2 g_1^2}{2f_a^2} (m_\Lambda^2 - m_n^2)^2. \quad (\text{C.9})$$

The phase space integration finally yields the vacuum decay rate [66]

$$\begin{aligned} \Gamma_{\text{free}}(\Lambda \rightarrow n + a) &= \frac{1}{32\pi m_\Lambda} \frac{m_\Lambda^2 - m_n^2}{m_\Lambda^2} \sum_{\text{pol}} |\mathcal{M}|_{\text{free}}^2 \\ &= \frac{1}{16\pi} \frac{|g_{\text{sd}}^{\text{V}}|^2 f_1^2 + |g_{\text{sd}}^{\text{A}}|^2 g_1^2}{4f_a^2} \frac{(m_\Lambda^2 - m_n^2)^3}{m_\Lambda^3}. \end{aligned} \quad (\text{C.10})$$

MEDIUM MATRIX ELEMENT In the determination of the squared matrix element in matter, we have to employ the mean field dispersion relation in Equation (9.15) resulting in the modified norm (9.16) of the four-momentum and polarization sum (9.17). The evaluation leads to

$$\sum_{\text{pol}} |\mathcal{M}|_{\text{medium}}^2 = \alpha(E_\Lambda^*, E_a) \sum_{\text{pol}} |\mathcal{M}|_{\text{free}}^2 \quad (\text{C.11})$$

in terms of the vacuum matrix element $\sum_{\text{pol}} |\mathcal{M}|_{\text{free}}^2$ in Equation (C.9) with

$$\begin{aligned} \alpha(E_\Lambda^*, E_a) &= \frac{1}{(m_\Lambda^2 - m_n^2)^2} (2E_\Lambda^* \Delta V + (m_\Lambda^*)^2 - (m_n^*)^2 - V_\Lambda^2 + V_n^2) \\ &\quad \times (\Delta V (2E_\Lambda^* - 2E_a - V_\Lambda - V_n) + (m_\Lambda^*)^2 - (m_n^*)^2). \end{aligned} \quad (\text{C.12})$$

Here, E_Λ^* and $m_{\Lambda,n}^*$ refer to the Λ energy as well as Λ and neutron masses with matter effects, respectively, see Equation (9.15), while $m_{\Lambda,n}$ are the vacuum masses. Moreover, we defined $\Delta V = V_\Lambda - V_n$ with the Λ and neutron vector self-energies V_Λ and V_n , respectively, as well as the axion energy E_a for which we neglect matter effects.

Note that the proportionality factor α reduces to

$$\alpha(E_\Lambda^*, E_a) \rightarrow \left(\frac{(m_\Lambda^*)^2 - (m_n^*)^2}{m_\Lambda^2 - m_n^2} \right)^2 \quad (\text{C.13})$$

in the limit of equal self-energies $V_\Lambda = V_n$, so that the medium matrix element is the vacuum matrix element with vacuum masses m_i replaced by their corresponding effective masses m_i^* in this case. This confirms the result in Reference [66].

C.3 PRODUCTION RATES FOR LAMBDA DECAYS

The production rate Γ_{prod} for decays of Λ baryons with momenta p_Λ into neutrons and axions with momenta p_n and p_a , $\Lambda \rightarrow n + a$, reads

$$\Gamma_{\text{prod}} = \frac{1}{2E_a} \int \frac{d^3 p_\Lambda}{(2\pi)^3 2E_\Lambda} f_\Lambda(E_\Lambda) \int \frac{d^3 p_n}{(2\pi)^3 2E_n} (1 - f_n(E_n)) \times (2\pi)^4 \delta^{(4)}(p_\Lambda - p_n - p_a) \sum_{\text{pol}} |\mathcal{M}|^2 \quad (\text{C.14})$$

according to the general expression in Equation (9.4).

Performing the trivial angular integral over the azimuthal angle of the Λ momentum and the integration over the neutron momentum p_n using the spatial delta function, one arrives at

$$\Gamma_{\text{prod}} = \frac{1}{16\pi E_a} \int_0^\infty d|\mathbf{p}_\Lambda| |\mathbf{p}_\Lambda|^2 \int_{-1}^1 d(\cos(\vartheta_\Lambda)) \sum_{\text{pol}} |\mathcal{M}|^2 \times \frac{f_\Lambda(E_\Lambda)(1 - f_n(E_\Lambda - E_a))}{E_\Lambda(E_\Lambda - E_a)} \delta(E_\Lambda - E_n - E_a) \Big|_{\mathbf{p}_n = \mathbf{p}_\Lambda - \mathbf{p}_a}. \quad (\text{C.15})$$

Note that we did not yet assume a specific dispersion relation in the evaluation.

VACUUM PRODUCTION RATE In order to evaluate the remaining delta function, we first restrict ourselves to a vacuum dispersion before turning to the medium case. Using

$$E_n = \sqrt{m_n^2 + |\mathbf{p}_\Lambda|^2 + E_a^2 - 2|\mathbf{p}_\Lambda|E_a \cos(\vartheta_\Lambda)} \quad (\text{C.16})$$

in vacuum, we rewrite the delta function as

$$\delta(E_\Lambda - E_n - E_a) = \frac{E_\Lambda - E_a}{|\mathbf{p}_\Lambda|E_a} \delta\left(\cos(\vartheta_\Lambda) - \frac{m_n^2 - m_\Lambda^2 + 2E_a E_\Lambda}{2\sqrt{E_\Lambda^2 - m_\Lambda^2} E_a}\right). \quad (\text{C.17})$$

In the rest frame of a particle, the kinematics of a two-body decay is completely fixed. In our case, one of the final state particles is

massless, $m_a = 0$, and we obtain its energy E_a^{CM} in the rest frame of the Λ hyperon as

$$E_a^{\text{CM}} = \frac{m_\Lambda^2 - m_n^2}{2m_\Lambda}. \quad (\text{C.18})$$

For a given axion energy E_a in the stellar rest frame, the Λ decay can only happen if the energy E_Λ of the Λ hyperon is such that there exists a boost to its rest frame where the axion energy becomes E_a^{CM} . This enforces a lower bound on the possible E_Λ energy of

$$E_\Lambda \geq E_\Lambda^{\text{min}} = m_\Lambda \frac{(E_a^{\text{CM}})^2 + E_a^2}{2E_a E_a^{\text{CM}}}. \quad (\text{C.19})$$

Indeed, a root of the delta function (C.17) exists only for $E_\Lambda \geq E_\Lambda^{\text{min}}$. Expressing the matrix element in terms of the vacuum decay rate $\Gamma_{\text{free}}(\Lambda \rightarrow n + a)$ in Equation (C.10) and performing the angular integration, we arrive at the final result [66]

$$\Gamma_{\text{prod}}^{\text{free}} = \frac{2m_\Lambda^3 \Gamma_{\text{free}}(\Lambda \rightarrow n + a)}{(m_\Lambda^2 - m_n^2) E_a^2} \int_{E_\Lambda^{\text{min}}}^{\infty} dE_\Lambda f_\Lambda(E_\Lambda) (1 - f_n(E_\Lambda - E_a)). \quad (\text{C.20})$$

MEDIUM PRODUCTION RATE Using the mean-field dispersion relation for particles in high density media, $E^*(\mathbf{p}) = \sqrt{(m^*)^2 + \mathbf{p}^2} + V$ with the effective Dirac mass m^* and vector self-energy V , see Equation (9.15), the delta function reads

$$\delta(E_\Lambda^* - E_n^* - E_a) = \frac{E_\Lambda^* - V_n - E_a}{|\mathbf{p}_\Lambda| E_a} \delta(\cos(\vartheta_\Lambda) - c_\Lambda), \quad (\text{C.21})$$

where V_n is the effective neutron potential and where we abbreviated the root as

$$c_\Lambda = \frac{2(E_\Lambda^* - V_\Lambda)(E_a - \Delta V) + \tilde{M}^2}{2E_a \sqrt{(E_\Lambda^* - V_\Lambda)^2 - (m_\Lambda^*)^2}} \quad (\text{C.22})$$

with $\Delta V = V_\Lambda - V_n$ and

$$\tilde{M}^2 = 2E_a \Delta V - (\Delta V)^2 + (m_n^*)^2 - (m_\Lambda^*)^2. \quad (\text{C.23})$$

The requirement $|\cos(\vartheta_\Lambda)| = |c_\Lambda| \leq 1$ evaluates to upper and lower bounds $E_{\Lambda, \text{min}}^*$ and $E_{\Lambda, \text{max}}^*$ for E_Λ^* , $E_{\Lambda, \text{min}}^* \leq E_\Lambda^* \leq E_{\Lambda, \text{max}}^*$ of

$$E_{\Lambda, \min/\max}^* = \max \left\{ m_{\Lambda}^* + V_{\Lambda}, -\frac{B}{2} \pm \sqrt{\frac{B^2}{4} - C} + V_{\Lambda} \right\}. \quad (\text{C.24})$$

Here, we abbreviated

$$B = \frac{(E_a - \Delta V) \tilde{M}^2}{\Delta V (\Delta V - 2E_a)}, \quad C = \frac{\tilde{M}^4 + 4(m_{\Lambda}^*)^2 E_a^2}{4\Delta V (\Delta V - 2E_a)}. \quad (\text{C.25})$$

Note that we have

$$E_{\Lambda, \min}^* \rightarrow \frac{((m_n^*)^2 - (m_{\Lambda}^*)^2)^2 + 4(m_{\Lambda}^*)^2 E_a^2}{4E_a((m_{\Lambda}^*)^2 - (m_n^*)^2)} + V_{\Lambda} \quad (\text{C.26})$$

and $E_{\Lambda, \max}^* \rightarrow \infty$ in the limit of equal self-energies $V_{\Lambda} = V_n$ [66]. The medium matrix element is proportional to the vacuum matrix element, $\sum_{\text{pol}} |\mathcal{M}|_{\text{medium}}^2 = \alpha(E_{\Lambda}^*, E_a) \sum_{\text{pol}} |\mathcal{M}|_{\text{free}}^2$, see Equation (C.11) and we can express it in terms of the vacuum decay rate $\Gamma_{\text{free}}(\Lambda \rightarrow n + a)$ again. Putting everything together and performing the angular integral using the delta function, we finally find

$$\begin{aligned} \Gamma_{\text{prod}}^{\text{medium}} &= \frac{2m_{\Lambda}^3 \Gamma_{\text{free}}(\Lambda \rightarrow n + a)}{E_a^2 (m_{\Lambda}^2 - m_n^2)} \int_{E_{\Lambda, \min}^*}^{E_{\Lambda, \max}^*} dE_{\Lambda}^* \alpha(E_{\Lambda}^*, E_a) \\ &\times \frac{(E_{\Lambda}^* - V_{\Lambda})(E_{\Lambda}^* - V_n - E_a)}{E_{\Lambda}^* (E_{\Lambda}^* - E_a)} f_{\Lambda}(E_{\Lambda}^*) (1 - f_n(E_{\Lambda}^* - E_a)) \end{aligned} \quad (\text{C.27})$$

in terms of the vacuum decay rate $\Gamma_{\text{free}}(\Lambda \rightarrow n + a)$, which yields the result of Reference [66] in the limit of equal self-energies, $V_{\Lambda} \rightarrow V_n$.

C.4 INDEPENDENT SCALAR PRODUCTS FOR BREMSSTRAHLUNG

Given five momenta p_i with $i = 1, \dots, 5$, there are 15 possible scalar products $p_i \cdot p_j$ of which five are determined by the mass-shell condition $p_i^2 = m_i^2$. Momentum conservation yields five constraints of the form

$$p_i \cdot (p_1 + p_2 - p_3 - p_4 - p_5) = 0 \quad (\text{C.28})$$

on these scalar products.

Moreover, we define the momentum transfers $k = p_2 - p_4$ and $l = p_2 - p_3$ and we choose $k^2, l^2, k \cdot l, k \cdot p_5$ and $l \cdot p_5$ as the independent scalar products. Denoting the scalar products by $p_{ij} = p_i \cdot p_j$, this leads to a set of equations,

$$\left\{ \begin{array}{l}
 m_1^2 + p_{12} - p_{13} - p_{14} - p_{15} = 0 \\
 p_{12} + m_2^2 - p_{23} - p_{24} - p_{25} = 0 \\
 p_{13} + p_{23} - m_3^2 - p_{34} - p_{35} = 0 \\
 p_{14} + p_{24} - p_{34} - m_4^2 - p_{45} = 0 \\
 p_{15} + p_{25} - p_{35} - p_{45} - m_5^2 = 0 \\
 m_2^2 + m_4^2 - 2p_{24} = k^2 \\
 m_2^2 + m_3^2 - 2p_{23} = l^2 \\
 m_2^2 - p_{23} - p_{24} + p_{34} = k \cdot l \\
 p_{25} - p_{45} = k \cdot p_5 \\
 p_{25} - p_{35} = l \cdot p_5
 \end{array} \right. , \quad (C.29)$$

which can be readily solved for the scalar products p_{ij} . We find

$$p_1 \cdot p_2 = \frac{1}{2} (-k^2 - 2k \cdot l + 2k \cdot p_5 - l^2 + 2l \cdot p_5 + m_1^2 + m_2^2 - m_5^2) , \quad (C.30)$$

$$p_1 \cdot p_3 = \frac{1}{2} (-k^2 + 2k \cdot p_5 + m_1^2 + m_3^2 - m_5^2) , \quad (C.31)$$

$$p_1 \cdot p_4 = \frac{1}{2} (-l^2 + 2l \cdot p_5 + m_1^2 + m_4^2 - m_5^2) , \quad (C.32)$$

$$p_1 \cdot p_5 = \frac{1}{2} (-2k \cdot l + m_1^2 + m_2^2 - m_3^2 - m_4^2 + m_5^2) , \quad (C.33)$$

$$p_2 \cdot p_3 = \frac{1}{2} (-l^2 + m_2^2 + m_3^2) , \quad (C.34)$$

$$p_2 \cdot p_4 = \frac{1}{2} (-k^2 + m_2^2 + m_4^2) , \quad (C.35)$$

$$p_2 \cdot p_5 = \frac{1}{2} (-2k \cdot l + 2k \cdot p_5 + 2l \cdot p_5 + m_1^2 + m_2^2 - m_3^2 - m_4^2 - m_5^2) , \quad (C.36)$$

$$p_3 \cdot p_4 = \frac{1}{2} (-k^2 + 2k \cdot l - l^2 + m_3^2 + m_4^2) , \quad (C.37)$$

$$p_3 \cdot p_5 = \frac{1}{2} (-2k \cdot l + 2k \cdot p_5 + m_1^2 + m_2^2 - m_3^2 - m_4^2 - m_5^2) , \quad (C.38)$$

$$p_4 \cdot p_5 = \frac{1}{2} (-2k \cdot l + 2l \cdot p_5 + m_1^2 + m_2^2 - m_3^2 - m_4^2 - m_5^2) , \quad (C.39)$$

where we have to replace $p_1 \rightarrow p_\Lambda$, $p_2 \rightarrow p_1$, $p_3 \rightarrow p_2$, $p_4 \rightarrow p_3$ and $p_5 \rightarrow p_A$ to match the notation in the text.

C.5 PHASE SPACE OF HYPERON BREMSSTRAHLUNG

In this section, we show the derivation of the production rate Γ_{prod} as given in Equation (9.43). We start by considering the general ex-

pression for the production rate in Equation (9.4) adapted for a $2 \rightarrow 3$ process,

$$\begin{aligned} \Gamma_{\text{prod}} &= \frac{1}{2E_A} \int \frac{d^3 p_\Lambda}{(2\pi)^3 2E_\Lambda} f_\Lambda(E_\Lambda) \int \frac{d^3 p_1}{(2\pi)^3 2E_1} f_n(E_1) \\ &\times \int \frac{d^3 p_2}{(2\pi)^3 2E_2} (1 - f_n(E_2)) \int \frac{d^3 p_3}{(2\pi)^3 2E_3} (1 - f_n(E_3)) \\ &\times (2\pi)^4 \delta^{(4)}(p_\Lambda + p_1 - p_2 - p_3 - p_A) \sum_{\text{pol}} |\mathcal{M}|^2, \quad (\text{C.40}) \end{aligned}$$

employing the notation indicated in the Feynman diagram in Figure 9.5a.

First, we use the simplification of the spatial delta function in Equation (9.42),

$$\delta^{(3)}(\mathbf{p}_\Lambda + \mathbf{p}_1 - \mathbf{p}_2 - \mathbf{p}_3 - \mathbf{p}_A) \simeq \delta^{(3)}(\mathbf{p}_\Lambda + \mathbf{p}_1 - \mathbf{p}_2 - \mathbf{p}_3), \quad (\text{C.41})$$

which is valid for large axion-like particle masses $m_A \gtrsim \Delta M_{\Lambda n}$ as discussed in Section 9.3.

Next, we evaluate the \mathbf{p}_3 integral using the spatial delta function and change coordinates to the center-of-mass system of the final-state neutrons,

$$\mathbf{p}_\Lambda = \mathbf{p}_0 + \mathbf{p}, \quad \mathbf{p}_1 = \mathbf{p}_0 - \mathbf{p}, \quad \mathbf{p}_{2,3} = \mathbf{p}_0 \pm \mathbf{q}, \quad (\text{C.42})$$

where the choice for the initial momenta reflects momentum conservation in the approximation of small axion-like particle momentum \mathbf{p}_A . After this substitution, the energies E_i are obtained as

$$E_\Lambda = m_\Lambda + \frac{\mathbf{p}_0^2 + \mathbf{p}^2 + 2\mathbf{p}_0 \cdot \mathbf{p}}{2m_\Lambda}, \quad (\text{C.43a})$$

$$E_1 = m_n + \frac{\mathbf{p}_0^2 + \mathbf{p}^2 - 2\mathbf{p}_0 \cdot \mathbf{p}}{2m_n}, \quad (\text{C.43b})$$

$$E_2 = m_n + \frac{\mathbf{p}_0^2 + \mathbf{q}^2 + 2\mathbf{p}_0 \cdot \mathbf{q}}{2m_n}, \quad (\text{C.43c})$$

$$E_3 = m_n + \frac{\mathbf{p}_0^2 + \mathbf{q}^2 - 2\mathbf{p}_0 \cdot \mathbf{q}}{2m_n}. \quad (\text{C.43d})$$

Furthermore, the scalar products \mathbf{k}^2 , \mathbf{l}^2 and $\mathbf{k} \cdot \mathbf{l}$ occurring in the matrix element (9.38) read

$$\mathbf{k}^2 = \mathbf{p}^2 + \mathbf{q}^2 - 2\mathbf{p} \cdot \mathbf{q}, \quad (\text{C.44a})$$

$$\mathbf{l}^2 = \mathbf{p}^2 + \mathbf{q}^2 + 2\mathbf{p} \cdot \mathbf{q}, \quad (\text{C.44b})$$

$$\mathbf{k} \cdot \mathbf{l} = \mathbf{p}^2 - \mathbf{q}^2. \quad (\text{C.44c})$$

The relative positioning of three vectors to each other is characterized by three angles—two polar angles and one azimuthal angle. In particular, we choose the center-of-mass momentum \mathbf{p}_0 as a reference direction so that \mathbf{p} and \mathbf{q} are determined by the polar angles ϑ_p and ϑ_q to the reference vector. Moreover, the location of the vector \mathbf{q} is given by an azimuthal angle φ_q relative to the plane spanned by \mathbf{p}_0 and \mathbf{p} . With these definitions, the scalar products of these three vectors read

$$\mathbf{p}_0 \cdot \mathbf{p} = |\mathbf{p}_0| |\mathbf{p}| \cos(\vartheta_p), \quad (\text{C.45a})$$

$$\mathbf{p}_0 \cdot \mathbf{q} = |\mathbf{p}_0| |\mathbf{q}| \cos(\vartheta_q), \quad (\text{C.45b})$$

$$\mathbf{p} \cdot \mathbf{q} = |\mathbf{p}| |\mathbf{q}| (\cos(\vartheta_p) \cos(\vartheta_q) + \sin(\vartheta_p) \sin(\vartheta_q) \sin(\varphi_q)). \quad (\text{C.45c})$$

Subsequently, we rewrite the energy delta function in terms of the new variables,

$$\begin{aligned} \delta(E_\Lambda + E_1 - E_2 - E_3 - E_A) \\ = \frac{m_\Lambda m_n}{\Delta M_{\Lambda n} |\mathbf{p}| |\mathbf{p}_0|} \delta(\cos(\vartheta_p) - c_p), \end{aligned} \quad (\text{C.46})$$

where we abbreviated the root of the delta function

$$c_p = \frac{m_\Lambda}{\Delta M_{\Lambda n} |\mathbf{p}| |\mathbf{p}_0|} (A - \mathbf{q}^2) \quad (\text{C.47})$$

with

$$A = m_n (\Delta M_{\Lambda n} - E_A) + \frac{1}{2} \left(\frac{m_n}{m_\Lambda} - 1 \right) \mathbf{p}_0^2 + \frac{1}{2} \left(\frac{m_n}{m_\Lambda} + 1 \right) \mathbf{p}^2. \quad (\text{C.48})$$

The requirement $|\cos(\vartheta_p)| \leq 1$ restricts the possible values for $|\mathbf{q}|$ to lie in the interval $|\mathbf{q}| \in [|\mathbf{q}|_-, |\mathbf{q}|_+]$ with

$$|\mathbf{q}|_\pm^2 = \max \left\{ 0, A \pm \frac{\Delta M_{\Lambda n} |\mathbf{p}| |\mathbf{p}_0|}{m_\Lambda} \right\}. \quad (\text{C.49})$$

For the final result, we perform the trivial angular integrals over the solid angle of the center-of-mass momentum \mathbf{p}_0 and over the azimuthal angle φ_p of the vector \mathbf{p} , yielding

$$\begin{aligned} \Gamma_{\text{prod}} = & \frac{m_\Lambda m_n}{128 \pi^6 \Delta M_{\Lambda n} E_A} \int_0^\infty d|\mathbf{p}_0| \int_0^\infty d|\mathbf{p}| \int_{|\mathbf{q}|_-}^{|\mathbf{q}|_+} d|\mathbf{q}| \\ & \times \int_{-1}^1 d(\cos(\vartheta_q)) \int_0^{2\pi} d\varphi_q |\mathbf{p}_0| |\mathbf{p}| |\mathbf{q}|^2 \\ & \times \left[\frac{f_\Lambda(E_\Lambda) f_n(E_1) (1 - f_n(E_2)) (1 - f_n(E_3))}{E_\Lambda E_1 E_2 E_3} \sum_{\text{pol}} |\mathcal{M}|^2 \right]_{\cos(\vartheta_p) = c_p}. \end{aligned} \quad (\text{C.50})$$

BIBLIOGRAPHY

- [1] N. Aghanim et al. “Planck 2018 results. VI. Cosmological parameters.” *Astron. Astrophys.* 641 (2020), A6. DOI: [10.1051/0004-6361/201833910](https://doi.org/10.1051/0004-6361/201833910). arXiv: [1807.06209](https://arxiv.org/abs/1807.06209) [[astro-ph.CO](#)].
- [2] F. Zwicky. “Die Rotverschiebung von extragalaktischen Nebeln.” *Helv. Phys. Acta* 6 (1933), pp. 110–127. DOI: [10.1007/s10714-008-0707-4](https://doi.org/10.1007/s10714-008-0707-4).
- [3] Vera C. Rubin and W. Kent Ford Jr. “Rotation of the Andromeda Nebula from a Spectroscopic Survey of Emission Regions.” *Astrophys. J.* 159 (1970), pp. 379–403. DOI: [10.1086/150317](https://doi.org/10.1086/150317).
- [4] Jaco de Swart, Gianfranco Bertone, and Jeroen van Dongen. “How Dark Matter Came to Matter.” *Nature Astron.* 1 (2017), p. 0059. DOI: [10.1038/s41550017-0059](https://doi.org/10.1038/s41550017-0059). arXiv: [1703.00013](https://arxiv.org/abs/1703.00013) [[astro-ph.CO](#)].
- [5] Joshua D. Simon. “The Faintest Dwarf Galaxies.” *Ann. Rev. Astron. Astrophys.* 57.1 (2019), pp. 375–415. DOI: [10.1146/annurev-astro-091918-104453](https://doi.org/10.1146/annurev-astro-091918-104453). arXiv: [1901.05465](https://arxiv.org/abs/1901.05465) [[astro-ph.GA](#)].
- [6] Paolo Salucci. “The distribution of dark matter in galaxies.” *Astron. Astrophys. Rev.* 27.1 (2019), p. 2. DOI: [10.1007/s00159-018-0113-1](https://doi.org/10.1007/s00159-018-0113-1). arXiv: [1811.08843](https://arxiv.org/abs/1811.08843) [[astro-ph.GA](#)].
- [7] Steven W. Allen, August E. Evrard, and Adam B. Mantz. “Cosmological Parameters from Observations of Galaxy Clusters.” *Ann. Rev. Astron. Astrophys.* 49 (2011), pp. 409–470. DOI: [10.1146/annurev-astro-081710-102514](https://doi.org/10.1146/annurev-astro-081710-102514). arXiv: [1103.4829](https://arxiv.org/abs/1103.4829) [[astro-ph.CO](#)].
- [8] Simon D. M. White and M. J. Rees. “Core condensation in heavy halos: A Two stage theory for galaxy formation and clusters.” *Mon. Not. Roy. Astron. Soc.* 183 (1978), pp. 341–358. DOI: [10.1093/mnras/183.3.341](https://doi.org/10.1093/mnras/183.3.341).
- [9] Alessandro Strumia and Francesco Vissani. *Neutrino masses and mixings and...* arXiv: [hep-ph/0606054](https://arxiv.org/abs/hep-ph/0606054).
- [10] Q. R. Ahmad et al. “Measurement of the rate of $\nu_e + d \rightarrow p + p + e^-$ interactions produced by ^8B solar neutrinos at the Sudbury Neutrino Observatory.” *Phys. Rev. Lett.* 87 (2001), p. 071301. DOI: [10.1103/PhysRevLett.87.071301](https://doi.org/10.1103/PhysRevLett.87.071301). arXiv: [nuclex/0106015](https://arxiv.org/abs/nuclex/0106015).
- [11] S. Fukuda et al. “Solar B-8 and hep neutrino measurements from 1258 days of Super-Kamiokande data.” *Phys. Rev. Lett.* 86 (2001), pp. 5651–5655. DOI: [10.1103/PhysRevLett.86.5651](https://doi.org/10.1103/PhysRevLett.86.5651). arXiv: [hep-ex/0103032](https://arxiv.org/abs/hep-ex/0103032).

- [12] Ivan Esteban, M. C. Gonzalez-Garcia, Michele Maltoni, Thomas Schwetz, and Albert Zhou. “The fate of hints: updated global analysis of three-flavor neutrino oscillations.” *JHEP* 09 (2020), p. 178. DOI: [10.1007/JHEP09\(2020\)178](https://doi.org/10.1007/JHEP09(2020)178). arXiv: [2007.14792](https://arxiv.org/abs/2007.14792) [hep-ph].
- [13] E. Aprile et al. “Excess electronic recoil events in XENON1T.” *Phys. Rev. D* 102.7 (2020), p. 072004. DOI: [10.1103/PhysRevD.102.072004](https://doi.org/10.1103/PhysRevD.102.072004). arXiv: [2006.09721](https://arxiv.org/abs/2006.09721) [hep-ex].
- [14] A. T. Yue, M. S. Dewey, D. M. Gilliam, G. L. Greene, A. B. Laptev, J. S. Nico, W. M. Snow, and F. E. Wietfeldt. “Improved Determination of the Neutron Lifetime.” *Phys. Rev. Lett.* 111.22 (2013), p. 222501. DOI: [10.1103/PhysRevLett.111.222501](https://doi.org/10.1103/PhysRevLett.111.222501). arXiv: [1309.2623](https://arxiv.org/abs/1309.2623) [nucl-ex].
- [15] R. W. Pattie Jr. et al. “Measurement of the neutron lifetime using a magneto-gravitational trap and in situ detection.” *Science* 360.6389 (2018), pp. 627–632. DOI: [10.1126/science.aan8895](https://doi.org/10.1126/science.aan8895). arXiv: [1707.01817](https://arxiv.org/abs/1707.01817) [nucl-ex].
- [16] B. Abi et al. “Measurement of the Positive Muon Anomalous Magnetic Moment to 0.46 ppm.” *Phys. Rev. Lett.* 126.14 (2021), p. 141801. DOI: [10.1103/PhysRevLett.126.141801](https://doi.org/10.1103/PhysRevLett.126.141801). arXiv: [2104.03281](https://arxiv.org/abs/2104.03281) [hep-ex].
- [17] G. Mention, M. Fechner, Th. Lasserre, Th. A. Mueller, D. Lhuillier, M. Cribier, and A. Letourneau. “The Reactor Antineutrino Anomaly.” *Phys. Rev. D* 83 (2011), p. 073006. DOI: [10.1103/PhysRevD.83.073006](https://doi.org/10.1103/PhysRevD.83.073006). arXiv: [1101.2755](https://arxiv.org/abs/1101.2755) [hep-ex].
- [18] Ferruccio Feruglio. “Pieces of the Flavour Puzzle.” *Eur. Phys. J. C* 75.8 (2015), p. 373. DOI: [10.1140/epjc/s10052-015-3576-5](https://doi.org/10.1140/epjc/s10052-015-3576-5). arXiv: [1503.04071](https://arxiv.org/abs/1503.04071) [hep-ph].
- [19] Robert N. Cahn. “The Eighteen arbitrary parameters of the standard model in your everyday life.” *Rev. Mod. Phys.* 68 (1996), pp. 951–960. DOI: [10.1103/RevModPhys.68.951](https://doi.org/10.1103/RevModPhys.68.951).
- [20] Luca Di Luzio, Maurizio Giannotti, Enrico Nardi, and Luca Visinelli. “The landscape of QCD axion models.” *Phys. Rept.* 870 (2020), pp. 1–117. DOI: [10.1016/j.physrep.2020.06.002](https://doi.org/10.1016/j.physrep.2020.06.002). arXiv: [2003.01100](https://arxiv.org/abs/2003.01100) [hep-ph].
- [21] Stephen L. Adler. “Axial vector vertex in spinor electrodynamics.” *Phys. Rev.* 177 (1969), pp. 2426–2438. DOI: [10.1103/PhysRev.177.2426](https://doi.org/10.1103/PhysRev.177.2426).
- [22] J. S. Bell and R. Jackiw. “A PCAC puzzle: $\pi^0 \rightarrow \gamma\gamma$ in the σ model.” *Nuovo Cim. A* 60 (1969), pp. 47–61. DOI: [10.1007/BF02823296](https://doi.org/10.1007/BF02823296).
- [23] P. A. Zyla et al. “Review of Particle Physics.” *PTEP* 2020.8 (2020), p. 083C01. DOI: [10.1093/ptep/ptaa104](https://doi.org/10.1093/ptep/ptaa104).

- [24] M. Milgrom. "A Modification of the Newtonian dynamics as a possible alternative to the hidden mass hypothesis." *Astrophys. J.* 270 (1983), pp. 365–370. DOI: [10.1086/161130](https://doi.org/10.1086/161130).
- [25] Wayne Hu, Rennan Barkana, and Andrei Gruzinov. "Cold and fuzzy dark matter." *Phys. Rev. Lett.* 85 (2000), pp. 1158–1161. DOI: [10.1103/PhysRevLett.85.1158](https://doi.org/10.1103/PhysRevLett.85.1158). arXiv: [astro-ph/0003365](https://arxiv.org/abs/astro-ph/0003365).
- [26] Paul H. Frampton, Masahiro Kawasaki, Fuminobu Takahashi, and Tsutomu T. Yanagida. "Primordial Black Holes as All Dark Matter." *JCAP* 04 (2010), p. 023. DOI: [10.1088/1475-7516/2010/04/023](https://doi.org/10.1088/1475-7516/2010/04/023). arXiv: [1001.2308](https://arxiv.org/abs/1001.2308) [hep-ph].
- [27] Giorgio Arcadi, Máira Dutra, Pradipta Ghosh, Manfred Lindner, Yann Mambrini, Mathias Pierre, Stefano Profumo, and Farialdo S. Queiroz. "The waning of the WIMP? A review of models, searches, and constraints." *Eur. Phys. J. C* 78.3 (2018), p. 203. DOI: [10.1140/epjc/s10052-018-5662-y](https://doi.org/10.1140/epjc/s10052-018-5662-y). arXiv: [1703.07364](https://arxiv.org/abs/1703.07364) [hep-ph].
- [28] Mark Srednicki, Richard Watkins, and Keith A. Olive. "Calculations of Relic Densities in the Early Universe." *Nucl. Phys. B* 310 (1988). Ed. by M. A. Srednicki, p. 693. DOI: [10.1016/0550-3213\(88\)90099-5](https://doi.org/10.1016/0550-3213(88)90099-5).
- [29] Katherine Garrett and Gintaras Duda. "Dark Matter: A Primer." *Adv. Astron.* 2011 (2011), p. 968283. DOI: [10.1155/2011/968283](https://doi.org/10.1155/2011/968283). arXiv: [1006.2483](https://arxiv.org/abs/1006.2483) [hep-ph].
- [30] Lawrence J. Hall, Karsten Jedamzik, John March-Russell, and Stephen M. West. "Freeze-In Production of FIMP Dark Matter." *JHEP* 03 (2010), p. 080. DOI: [10.1007/JHEP03\(2010\)080](https://doi.org/10.1007/JHEP03(2010)080). arXiv: [0911.1120](https://arxiv.org/abs/0911.1120) [hep-ph].
- [31] Z. Tang et al. "Search for the Neutron Decay $n \rightarrow X + \gamma$ where X is a dark matter particle." *Phys. Rev. Lett.* 121.2 (2018), p. 022505. DOI: [10.1103/PhysRevLett.121.022505](https://doi.org/10.1103/PhysRevLett.121.022505). arXiv: [1802.01595](https://arxiv.org/abs/1802.01595) [nucl-ex].
- [32] Dario Buttazzo, Paolo Panci, Daniele Teresi, and Robert Ziegler. "Xenon1T excess from electron recoils of non-relativistic Dark Matter." *Phys. Lett. B* 817 (2021), p. 136310. DOI: [10.1016/j.physletb.2021.136310](https://doi.org/10.1016/j.physletb.2021.136310). arXiv: [2011.08919](https://arxiv.org/abs/2011.08919) [hep-ph].
- [33] Asimina Arvanitaki, Savas Dimopoulos, Sergei Dubovsky, Nemanja Kaloper, and John March-Russell. "String Axiverse." *Phys. Rev. D* 81 (2010), p. 123530. DOI: [10.1103/PhysRevD.81.123530](https://doi.org/10.1103/PhysRevD.81.123530). arXiv: [0905.4720](https://arxiv.org/abs/0905.4720) [hep-th].
- [34] R. D. Peccei and Helen R. Quinn. "CP Conservation in the Presence of Instantons." *Phys. Rev. Lett.* 38 (1977), pp. 1440–1443. DOI: [10.1103/PhysRevLett.38.1440](https://doi.org/10.1103/PhysRevLett.38.1440).

- [35] R. D. Peccei and Helen R. Quinn. “Constraints Imposed by CP Conservation in the Presence of Instantons.” *Phys. Rev. D* 16 (1977), pp. 1791–1797. DOI: [10.1103/PhysRevD.16.1791](https://doi.org/10.1103/PhysRevD.16.1791).
- [36] Frank Wilczek. “Problem of Strong P and T Invariance in the Presence of Instantons.” *Phys. Rev. Lett.* 40 (1978), pp. 279–282. DOI: [10.1103/PhysRevLett.40.279](https://doi.org/10.1103/PhysRevLett.40.279).
- [37] Steven Weinberg. “A New Light Boson?” *Phys. Rev. Lett.* 40 (1978), pp. 223–226. DOI: [10.1103/PhysRevLett.40.223](https://doi.org/10.1103/PhysRevLett.40.223).
- [38] Frank Wilczek. “Axions and Family Symmetry Breaking.” *Phys. Rev. Lett.* 49 (1982), pp. 1549–1552. DOI: [10.1103/PhysRevLett.49.1549](https://doi.org/10.1103/PhysRevLett.49.1549).
- [39] Lorenzo Calibbi, Florian Goertz, Diego Redigolo, Robert Ziegler, and Jure Zupan. “Minimal axion model from flavor.” *Phys. Rev. D* 95.9 (2017), p. 095009. DOI: [10.1103/PhysRevD.95.095009](https://doi.org/10.1103/PhysRevD.95.095009). arXiv: [1612.08040](https://arxiv.org/abs/1612.08040) [hep-ph].
- [40] Yohei Ema, Koichi Hamaguchi, Takeo Moroi, and Kazunori Nakayama. “Flaxion: a minimal extension to solve puzzles in the standard model.” *JHEP* 01 (2017), p. 096. DOI: [10.1007/JHEP01\(2017\)096](https://doi.org/10.1007/JHEP01(2017)096). arXiv: [1612.05492](https://arxiv.org/abs/1612.05492) [hep-ph].
- [41] Matthias Linster and Robert Ziegler. “A Realistic $U(2)$ Model of Flavor.” *JHEP* 08 (2018), p. 058. DOI: [10.1007/JHEP08\(2018\)058](https://doi.org/10.1007/JHEP08(2018)058). arXiv: [1805.07341](https://arxiv.org/abs/1805.07341) [hep-ph].
- [42] Prateek Agrawal et al. “Feebly-Interacting Particles:FIPs 2020 Workshop Report” (Feb. 2021). arXiv: [2102.12143](https://arxiv.org/abs/2102.12143) [hep-ph].
- [43] E. J. Salumbides, J. C. J. Koelemeij, J. Komasa, K. Pachucki, K. S. E. Eikema, and W. Ubachs. “Bounds on fifth forces from precision measurements on molecules.” *Phys. Rev. D* 87.11 (2013), p. 112008. DOI: [10.1103/PhysRevD.87.112008](https://doi.org/10.1103/PhysRevD.87.112008). arXiv: [1304.6560](https://arxiv.org/abs/1304.6560) [physics.atom-ph].
- [44] E. J. Salumbides, A. N. Schellekens, B. Gato-Rivera, and W. Ubachs. “Constraints on extra dimensions from precision molecular spectroscopy.” *New J. Phys.* 17.3 (2015), p. 033015. DOI: [10.1088/1367-2630/17/3/033015](https://doi.org/10.1088/1367-2630/17/3/033015). arXiv: [1502.02838](https://arxiv.org/abs/1502.02838) [physics.atom-ph].
- [45] Cédric Delaunay, Claudia Fruguele, Elina Fuchs, and Yotam Soreq. “Probing new spin-independent interactions through precision spectroscopy in atoms with few electrons.” *Phys. Rev. D* 96.11 (2017), p. 115002. DOI: [10.1103/PhysRevD.96.115002](https://doi.org/10.1103/PhysRevD.96.115002). arXiv: [1709.02817](https://arxiv.org/abs/1709.02817) [hep-ph].
- [46] Julian C. Berengut et al. “Probing New Long-Range Interactions by Isotope Shift Spectroscopy.” *Phys. Rev. Lett.* 120 (2018), p. 091801. DOI: [10.1103/PhysRevLett.120.091801](https://doi.org/10.1103/PhysRevLett.120.091801). arXiv: [1704.05068](https://arxiv.org/abs/1704.05068) [hep-ph].

- [47] Matthew P. A. Jones, Robert M. Potvliege, and Michael Spannowsky. “Probing new physics using Rydberg states of atomic hydrogen.” *Phys. Rev. Res.* 2.1 (2020), p. 013244. DOI: [10.1103/PhysRevResearch.2.013244](https://doi.org/10.1103/PhysRevResearch.2.013244). arXiv: [1909.09194](https://arxiv.org/abs/1909.09194) [hep-ph].
- [48] Cyrille Solaro, Steffen Meyer, Karin Fisher, Julian C. Berengut, Elina Fuchs, and Michael Drewsen. “Improved isotope-shift-based bounds on bosons beyond the Standard Model through measurements of the $^2D_{3/2}$ – $^2D_{5/2}$ interval in Ca^+ .” *Phys. Rev. Lett.* 125.12 (2020), p. 123003. DOI: [10.1103/PhysRevLett.125.123003](https://doi.org/10.1103/PhysRevLett.125.123003). arXiv: [2005.00529](https://arxiv.org/abs/2005.00529) [physics.atom-ph].
- [49] Y. Kamiya, K. Itagami, M. Tani, G. N. Kim, and S. Komamiya. “Constraints on New Gravitylike Forces in the Nanometer Range.” *Phys. Rev. Lett.* 114 (2015), p. 161101. DOI: [10.1103/PhysRevLett.114.161101](https://doi.org/10.1103/PhysRevLett.114.161101). arXiv: [1504.02181](https://arxiv.org/abs/1504.02181) [hep-ex].
- [50] M. Aker et al. “Improved Upper Limit on the Neutrino Mass from a Direct Kinematic Method by KATRIN.” *Phys. Rev. Lett.* 123.22 (2019), p. 221802. DOI: [10.1103/PhysRevLett.123.221802](https://doi.org/10.1103/PhysRevLett.123.221802). arXiv: [1909.06048](https://arxiv.org/abs/1909.06048) [hep-ex].
- [51] M. Aker et al. “First direct neutrino-mass measurement with sub-eV sensitivity” (May 2021). arXiv: [2105.08533](https://arxiv.org/abs/2105.08533) [hep-ex].
- [52] A. Gando et al. “Search for Majorana Neutrinos near the Inverted Mass Hierarchy Region with KamLAND-Zen.” *Phys. Rev. Lett.* 117.8 (2016). [Addendum: *Phys. Rev. Lett.* 117, 109903 (2016)], p. 082503. DOI: [10.1103/PhysRevLett.117.082503](https://doi.org/10.1103/PhysRevLett.117.082503). arXiv: [1605.02889](https://arxiv.org/abs/1605.02889) [hep-ex].
- [53] M. Agostini et al. “Final Results of GERDA on the Search for Neutrinoless Double- β Decay.” *Phys. Rev. Lett.* 125.25 (2020), p. 252502. DOI: [10.1103/PhysRevLett.125.252502](https://doi.org/10.1103/PhysRevLett.125.252502). arXiv: [2009.06079](https://arxiv.org/abs/2009.06079) [nucl-ex].
- [54] Jorge Martin Camalich, Maxim Pospelov, Pham Ngoc Hoa Vuong, Robert Ziegler, and Jure Zupan. “Quark Flavor Phenomenology of the QCD Axion.” *Phys. Rev. D* 102.1 (2020), p. 015023. DOI: [10.1103/PhysRevD.102.015023](https://doi.org/10.1103/PhysRevD.102.015023). arXiv: [2002.04623](https://arxiv.org/abs/2002.04623) [hep-ph].
- [55] G. G. Raffelt. *Stars as laboratories for fundamental physics*. Chicago, USA: Univ. Pr. (1996) 664 p, 1996. ISBN: 9780226702728. URL: <http://wwwth.mpp.mpg.de/members/raffelt/mypapers/199613.pdf>.
- [56] T. A. Wagner, S. Schlamminger, J. H. Gundlach, and E. G. Adelberger. “Torsion-balance tests of the weak equivalence principle.” *Class. Quant. Grav.* 29 (2012), p. 184002. DOI: [10.1088/0264-9381/29/18/184002](https://doi.org/10.1088/0264-9381/29/18/184002). arXiv: [1207.2442](https://arxiv.org/abs/1207.2442) [gr-qc].

- [57] G. L. Klimchitskaya and V. M. Mostepanenko. “Constraints on axionlike particles and non-Newtonian gravity from measuring the difference of Casimir forces.” *Phys. Rev. D* 95.12 (2017), p. 123013. DOI: [10.1103/PhysRevD.95.123013](https://doi.org/10.1103/PhysRevD.95.123013). arXiv: [1704.05892](https://arxiv.org/abs/1704.05892) [hep-ph].
- [58] Brian Batell, Rouven Essig, and Ze’ev Surujon. “Strong Constraints on Sub-GeV Dark Sectors from SLAC Beam Dump E137.” *Phys. Rev. Lett.* 113.17 (2014), p. 171802. DOI: [10.1103/PhysRevLett.113.171802](https://doi.org/10.1103/PhysRevLett.113.171802). arXiv: [1406.2698](https://arxiv.org/abs/1406.2698) [hep-ph].
- [59] A. A. Aguilar-Arevalo et al. “Dark Matter Search in a Proton Beam Dump with MiniBooNE.” *Phys. Rev. Lett.* 118.22 (2017), p. 221803. DOI: [10.1103/PhysRevLett.118.221803](https://doi.org/10.1103/PhysRevLett.118.221803). arXiv: [1702.02688](https://arxiv.org/abs/1702.02688) [hep-ex].
- [60] W. Altmannshofer et al. “The Belle II Physics Book.” *PTEP* 2019.12 (2019). Ed. by E. Kou and P. Urquijo. [Erratum: *PTEP* 2020, 029201 (2020)], p. 123C01. DOI: [10.1093/ptep/ptz106](https://doi.org/10.1093/ptep/ptz106). arXiv: [1808.10567](https://arxiv.org/abs/1808.10567) [hep-ex].
- [61] Xabier Cid Vidal et al. “Report from Working Group 3: Beyond the Standard Model physics at the HL-LHC and HE-LHC.” *CERN Yellow Rep. Monogr.* 7 (2019). Ed. by Andrea Dainese, Michelangelo Mangano, Andreas B. Meyer, Aleandro Nisati, Gavin Salam, and Mika Anton Vesterinen, pp. 585–865. DOI: [10.23731/CYRM-2019-007.585](https://doi.org/10.23731/CYRM-2019-007.585). arXiv: [1812.07831](https://arxiv.org/abs/1812.07831) [hep-ph].
- [62] A. Cerri et al. “Report from Working Group 4: Opportunities in Flavour Physics at the HL-LHC and HE-LHC.” *CERN Yellow Rep. Monogr.* 7 (2019). Ed. by Andrea Dainese, Michelangelo Mangano, Andreas B. Meyer, Aleandro Nisati, Gavin Salam, and Mika Anton Vesterinen, pp. 867–1158. DOI: [10.23731/CYRM-2019-007.867](https://doi.org/10.23731/CYRM-2019-007.867). arXiv: [1812.07638](https://arxiv.org/abs/1812.07638) [hep-ph].
- [63] V. Anastassopoulos et al. “New CAST Limit on the Axion-Photon Interaction.” *Nature Phys.* 13 (2017), pp. 584–590. DOI: [10.1038/nphys4109](https://doi.org/10.1038/nphys4109). arXiv: [1705.02290](https://arxiv.org/abs/1705.02290) [hep-ex].
- [64] T. Braine et al. “Extended Search for the Invisible Axion with the Axion Dark Matter Experiment.” *Phys. Rev. Lett.* 124.10 (2020), p. 101303. DOI: [10.1103/PhysRevLett.124.101303](https://doi.org/10.1103/PhysRevLett.124.101303). arXiv: [1910.08638](https://arxiv.org/abs/1910.08638) [hep-ex].
- [65] Ferruccio Feruglio and Andrea Romanino. “Lepton Flavour Symmetries” (Dec. 2019). arXiv: [1912.06028](https://arxiv.org/abs/1912.06028) [hep-ph].
- [66] Jorge Martin Camalich, Jorge Terol-Calvo, Laura Tolos, and Robert Ziegler. “Supernova Constraints on Dark Flavored Sectors” (Dec. 2020). arXiv: [2012.11632](https://arxiv.org/abs/2012.11632) [hep-ph].

- [67] Asimina Arvanitaki, Savas Dimopoulos, and Ken Van Tilburg. “Resonant absorption of bosonic dark matter in molecules.” *Phys. Rev. X* 8.4 (2018), p. 041001. DOI: [10.1103/PhysRevX.8.041001](https://doi.org/10.1103/PhysRevX.8.041001). arXiv: [1709.05354](https://arxiv.org/abs/1709.05354) [hep-ph].
- [68] Sylvain Fichtel. “Quantum Forces from Dark Matter and Where to Find Them.” *Phys. Rev. Lett.* 120.13 (2018), p. 131801. DOI: [10.1103/PhysRevLett.120.131801](https://doi.org/10.1103/PhysRevLett.120.131801). arXiv: [1705.10331](https://arxiv.org/abs/1705.10331) [hep-ph].
- [69] Philippe Brax, Sylvain Fichtel, and Guillaume Pignol. “Bounding Quantum Dark Forces.” *Phys. Rev. D* 97.11 (2018), p. 115034. DOI: [10.1103/PhysRevD.97.115034](https://doi.org/10.1103/PhysRevD.97.115034). arXiv: [1710.00850](https://arxiv.org/abs/1710.00850) [hep-ph].
- [70] Wolfgang Gregor Hollik, Matthias Linster, and Mustafa Tabet. “A Study of New Physics Searches with Tritium and Similar Molecules.” *Eur. Phys. J. C* 80.7 (2020), p. 661. DOI: [10.1140/epjc/s10052-020-8215-0](https://doi.org/10.1140/epjc/s10052-020-8215-0). arXiv: [2004.11274](https://arxiv.org/abs/2004.11274) [hep-ph].
- [71] Jacek Komasa, Mariusz Puchalski, Paweł Czachorowski, Grzegorz Łach, and Krzysztof Pachucki. “Rovibrational energy levels of the hydrogen molecule through nonadiabatic perturbation theory.” *Phys. Rev. A* 100 (3 Sept. 2019), p. 032519. DOI: [10.1103/PhysRevA.100.032519](https://doi.org/10.1103/PhysRevA.100.032519). URL: <https://link.aps.org/doi/10.1103/PhysRevA.100.032519>.
- [72] Philip M. Morse. “Diatomic Molecules According to the Wave Mechanics. II. Vibrational Levels.” *Phys. Rev.* 34 (1 July 1929), pp. 57–64. DOI: [10.1103/PhysRev.34.57](https://doi.org/10.1103/PhysRev.34.57). URL: <https://link.aps.org/doi/10.1103/PhysRev.34.57>.
- [73] W. Heitler and F. London. “Wechselwirkung neutraler Atome und homöopolare Bindung nach der Quantenmechanik.” *Zeitschrift für Physik* 44.6 (June 1927), pp. 455–472. ISSN: 0044-3328. DOI: [10.1007/BF01397394](https://doi.org/10.1007/BF01397394). URL: <https://doi.org/10.1007/BF01397394>.
- [74] Hubert M. James and Albert Sprague Coolidge. “The Ground State of the Hydrogen Molecule.” *The Journal of Chemical Physics* 1.12 (1933), pp. 825–835. DOI: [10.1063/1.1749252](https://doi.org/10.1063/1.1749252). eprint: <https://doi.org/10.1063/1.1749252>. URL: <https://doi.org/10.1063/1.1749252>.
- [75] M. Born and R. Oppenheimer. “Zur Quantentheorie der Molekeln.” *Annalen der Physik* 389.20 (1927), pp. 457–484. DOI: <https://doi.org/10.1002/andp.19273892002>. eprint: <https://onlinelibrary.wiley.com/doi/pdf/10.1002/andp.19273892002>. URL: <https://onlinelibrary.wiley.com/doi/abs/10.1002/andp.19273892002>.
- [76] W. Kolos and L. Wolniewicz. “A complete non-relativistic treatment of the H₂ molecule.” *Physics Letters* 2.5 (1962), pp. 222–223. URL: [https://doi.org/10.1016/0031-9163\(62\)90235-4](https://doi.org/10.1016/0031-9163(62)90235-4).

- [77] W. Kołos and L. Wolniewicz. "Nonadiabatic theory for diatomic molecules and its application to the hydrogen molecule." *Reviews of Modern Physics* 35.3 (1963), pp. 473–483. URL: <https://doi.org/10.1103/RevModPhys.35.473>.
- [78] W. Kołos and L. Wolniewicz. "Accurate Adiabatic Treatment of the Ground State of the Hydrogen Molecule." *The Journal of chemical physics* 41.12 (1964), pp. 3663–3673. URL: <https://doi.org/10.1063/1.1725796>.
- [79] W. Kołos and L. Wolniewicz. "Accurate computation of vibronic energies and of some expectation values for H₂, D₂, and T₂." *The Journal of chemical physics* 41.12 (1964), pp. 3674–3678. URL: <https://doi.org/10.1063/1.1725797>.
- [80] W. Kołos and L. Wolniewicz. "Improved theoretical ground-state energy of the hydrogen molecule." *The Journal of chemical physics* 49.1 (1968), pp. 404–410. URL: <https://doi.org/10.1063/1.1669836>.
- [81] K. Pachucki, M. Zientkiewicz, and V.A. Yerokhin. "H₂SOLV: Fortran solver for diatomic molecules in explicitly correlated exponential basis." *Computer Physics Communications* 208 (July 2016). DOI: [10.1016/j.cpc.2016.07.024](https://doi.org/10.1016/j.cpc.2016.07.024).
- [82] K. Pachucki and J. Komasa. "Nonadiabatic corrections to the wave function and energy." *Journal of Chemical Physics* 129.3 (2008). cited By 47. DOI: [10.1063/1.2952517](https://www.scopus.com/inward/record.uri?eid=2-s2.0-47849090977&doi=10.1063%2f1.2952517&partnerID=40&md5=e010a4eb52b57211614b28f17a58e5b3). URL: <https://www.scopus.com/inward/record.uri?eid=2-s2.0-47849090977&doi=10.1063%2f1.2952517&partnerID=40&md5=e010a4eb52b57211614b28f17a58e5b3>.
- [83] Krzysztof Pachucki and Jacek Komasa. "Nonadiabatic corrections to rovibrational levels of H₂." *The Journal of Chemical Physics* 130.16 (2009), p. 164113. DOI: [10.1063/1.3114680](https://doi.org/10.1063/1.3114680). eprint: <https://doi.org/10.1063/1.3114680>. URL: <https://doi.org/10.1063/1.3114680>.
- [84] Krzysztof Pachucki and Jacek Komasa. "Rovibrational levels of HD." *Phys. Chem. Chem. Phys.* 12 (32 2010), pp. 9188–9196. DOI: [10.1039/C0CP00209G](https://doi.org/10.1039/C0CP00209G). URL: <http://dx.doi.org/10.1039/C0CP00209G>.
- [85] Krzysztof Pachucki and Jacek Komasa. "Leading order nonadiabatic corrections to rovibrational levels of H₂, D₂, and T₂." *The Journal of Chemical Physics* 143.3 (2015), p. 034111. DOI: [10.1063/1.4927079](https://doi.org/10.1063/1.4927079). eprint: <https://doi.org/10.1063/1.4927079>. URL: <https://doi.org/10.1063/1.4927079>.
- [86] Mariusz Puchalski, Jacek Komasa, Paweł Czachorowski, and Krzysztof Pachucki. "Complete α^6 m Corrections to the Ground State of H₂." *Phys. Rev. Lett.* 117 (26 Dec. 2016), p. 263002. DOI:

- 10.1103/PhysRevLett.117.263002. URL: <https://link.aps.org/doi/10.1103/PhysRevLett.117.263002>.
- [87] Mariusz Puchalski, Jacek Komasa, and Krzysztof Pachucki. "Relativistic corrections for the ground electronic state of molecular hydrogen." *Phys. Rev. A* 95 (5 May 2017), p. 052506. DOI: 10.1103/PhysRevA.95.052506. URL: <https://link.aps.org/doi/10.1103/PhysRevA.95.052506>.
- [88] Mariusz Puchalski, Jacek Komasa, Paweł Czachorowski, and Krzysztof Pachucki. "Nonadiabatic QED correction to the dissociation energy of the hydrogen molecule." *Phys. Rev. Lett.* 122.10 (2019), p. 103003. DOI: 10.1103/PhysRevLett.122.103003. arXiv: 1812.02980 [physics.atom-ph].
- [89] Mariusz Puchalski, Anna Spyszkievicz, Jacek Komasa, and Krzysztof Pachucki. "Nonadiabatic Relativistic Correction to the Dissociation Energy of H₂, D₂, and HD." *Phys. Rev. Lett.* 121 (7 Aug. 2018), p. 073001. DOI: 10.1103/PhysRevLett.121.073001. URL: <https://link.aps.org/doi/10.1103/PhysRevLett.121.073001>.
- [90] Mariusz Puchalski, Jacek Komasa, Anna Spyszkievicz, and Krzysztof Pachucki. "Dissociation energy of molecular hydrogen isotopologues." *Phys. Rev. A* 100 (2 Aug. 2019), p. 020503. DOI: 10.1103/PhysRevA.100.020503. URL: <https://link.aps.org/doi/10.1103/PhysRevA.100.020503>.
- [91] Mariusz Puchalski, Jacek Komasa, Paweł Czachorowski, and Krzysztof Pachucki. "Nonadiabatic QED Correction to the Dissociation Energy of the Hydrogen Molecule." *Phys. Rev. Lett.* 122 (10 Mar. 2019), p. 103003. DOI: 10.1103/PhysRevLett.122.103003. URL: <https://link.aps.org/doi/10.1103/PhysRevLett.122.103003>.
- [92] Paweł Czachorowski. "Relativistic nonadiabatic corrections to the ground state of molecular hydrogen." PhD thesis. University of Warsaw, 2019.
- [93] Mariusz Puchalski, Jacek Komasa, Paweł Czachorowski, and Krzysztof Pachucki. "Complete $\alpha^6 m$ corrections to the ground state of H₂." *Phys. Rev. Lett.* 117.26 (2016), p. 263002. DOI: 10.1103/PhysRevLett.117.263002. arXiv: 1608.07081 [physics.chem-ph].
- [94] Paweł Czachorowski, Mariusz Puchalski, Jacek Komasa, and Krzysztof Pachucki. "Nonadiabatic relativistic correction in H₂, D₂, and HD." *Phys. Rev. A* 98.5 (2018), p. 052506. DOI: 10.1103/PhysRevA.98.052506. arXiv: 1810.02604 [physics.atom-ph].

- [95] Paweł Czachorowski, Jacek Komasa, Grzegorz Łach, Krzysztof Pachucki, and Mariusz Puchalski. *H2SPECTRE*. <https://www.fuw.edu.pl/~krp/codes.html>; https://qcg.home.amu.edu.pl/qcg/public_html/H2Spectre.html.
- [96] Wolfgang Gregor Hollik. *Finding hints of New Physics in Tritium molecular spectra*. Talk at DESY Theory Workshop - Quantum field theory meets gravity (2019), Hamburg, Deutschland, 24.–27. September 2019. 51.01.01; LK 01. 2019.
- [97] G. D. Dickenson, M. L. Niu, E. J. Salumbides, J. Komasa, K. S. E. Eikema, K. Pachucki, and W. Ubachs. “Fundamental Vibration of Molecular Hydrogen.” *Phys. Rev. Lett.* 110 (19 May 2013), p. 193601. DOI: [10.1103/PhysRevLett.110.193601](https://doi.org/10.1103/PhysRevLett.110.193601). URL: <https://link.aps.org/doi/10.1103/PhysRevLett.110.193601>.
- [98] M. L. Niu, E. J. Salumbides, G. D. Dickenson, K. S. E. Eikema, and W. Ubachs. “Precision spectroscopy of the $X1\Sigma_g^+, v = 0 \rightarrow 1(J = 0 - 2)$ rovibrational splittings in H₂, HD and D₂.” *Journal of Molecular Spectroscopy* 300 (2014). Spectroscopic Tests of Fundamental Physics, pp. 44–54. ISSN: 0022-2852. DOI: <https://doi.org/10.1016/j.jms.2014.03.011>. URL: <http://www.sciencedirect.com/science/article/pii/S0022285214000630>.
- [99] F. M. J. Cozijn, P. Dupré, E. J. Salumbides, K. S. E. Eikema, and W. Ubachs. “Sub-Doppler Frequency Metrology in HD for Tests of Fundamental Physics.” *Phys. Rev. Lett.* 120 (15 Apr. 2018), p. 153002. DOI: [10.1103/PhysRevLett.120.153002](https://doi.org/10.1103/PhysRevLett.120.153002). URL: <https://link.aps.org/doi/10.1103/PhysRevLett.120.153002>.
- [100] François Biraben. “The first decades of Doppler-free two-photon spectroscopy.” *Comptes Rendus Physique* 20.7 (2019). La science en mouvement 2 : de 1940 aux premières années 1980 à Avancées en physique, pp. 671–681. ISSN: 1631-0705. DOI: <https://doi.org/10.1016/j.crhy.2019.04.003>. URL: <http://www.sciencedirect.com/science/article/pii/S1631070519300283>.
- [101] Raúl Z. Martínez, Dionisio Bermejo, Piotr Wcisło, and Franck Thibault. “Accurate wavenumber measurements for the So(0), So(1), and So(2) pure rotational Raman lines of D₂.” *Journal of Raman Spectroscopy* 50.1 (), pp. 127–129. DOI: [10.1002/jrs.5499](https://doi.org/10.1002/jrs.5499). URL: <https://onlinelibrary.wiley.com/doi/abs/10.1002/jrs.5499>.
- [102] M. Schlösser, X. Zhao, M. Trivikram, W. Ubachs, and E. J. Salumbides. “CARS spectroscopy of the ($v = 0 \rightarrow 1$) band in T₂.” *Journal of Physics B: Atomic, Molecular and Optical Physics* 50.21 (Oct. 2017), p. 214004. DOI: [10.1088/1361-6455/aa8d80](https://doi.org/10.1088/1361-6455/aa8d80). URL: <https://doi.org/10.1088/1361-6455/aa8d80>.

- [103] T. Madhu Trivikram, M. Schlösser, W. Ubachs, and E. J. Salumbides. “Relativistic and QED Effects in the Fundamental Vibration of T_2 .” *Phys. Rev. Lett.* 120 (16 Apr. 2018), p. 163002. DOI: [10.1103/PhysRevLett.120.163002](https://doi.org/10.1103/PhysRevLett.120.163002). URL: <https://link.aps.org/doi/10.1103/PhysRevLett.120.163002>.
- [104] K.-F. Lai, P. Czachorowski, M. Schlösser, M. Puchalski, J. Komasa, K. Pachucki, W. Ubachs, and E. J. Salumbides. “Precision tests of nonadiabatic perturbation theory with measurements on the DT molecule.” *Phys. Rev. Research* 1 (3 Nov. 2019), p. 033124. DOI: [10.1103/PhysRevResearch.1.033124](https://doi.org/10.1103/PhysRevResearch.1.033124). URL: <https://link.aps.org/doi/10.1103/PhysRevResearch.1.033124>.
- [105] K.-F. Lai, V. Hermann, T.M. Trivikram, M. Diouf, M. Schlösser, W. Ubachs, and E.J. Salumbides. “Precision measurement of the fundamental vibrational frequencies of tritium-bearing hydrogen molecules: T_2 , DT, HT” (Mar. 2020). arXiv: [2003.11060](https://arxiv.org/abs/2003.11060) [physics.chem-ph].
- [106] Michael E. Peskin and Daniel V. Schroeder. *An Introduction to quantum field theory*. Reading, USA: Addison-Wesley, 1995. ISBN: 978-0-201-50397-5.
- [107] Hideki Yukawa. “On the Interaction of Elementary Particles I.” *Proc. Phys. Math. Soc. Jap.* 17 (1935), pp. 48–57. DOI: [10.1143/PTPS.1.1](https://doi.org/10.1143/PTPS.1.1).
- [108] *hyc.py - Hydrogen Yukawa-like Corrections*. 2020. URL: <https://git.particle.kit.edu/new-physics-in-tritium/hydrogen-yukawa-corrections>.
- [109] Vanda Silveira and A. Zee. “SCALAR PHANTOMS.” *Phys. Lett.* 161B (1985), pp. 136–140. DOI: [10.1016/0370-2693\(85\)90624-0](https://doi.org/10.1016/0370-2693(85)90624-0).
- [110] John McDonald. “Gauge singlet scalars as cold dark matter.” *Phys. Rev. D* 50 (1994), pp. 3637–3649. DOI: [10.1103/PhysRevD.50.3637](https://doi.org/10.1103/PhysRevD.50.3637). arXiv: [hep-ph/0702143](https://arxiv.org/abs/hep-ph/0702143) [HEP-PH].
- [111] Y. Chikashige, Rabindra N. Mohapatra, and R. D. Peccei. “Are There Real Goldstone Bosons Associated with Broken Lepton Number?” *Phys. Lett.* 98B (1981), pp. 265–268. DOI: [10.1016/0370-2693\(81\)90011-3](https://doi.org/10.1016/0370-2693(81)90011-3).
- [112] Pavel Fadeev, Yevgeny V. Stadnik, Filip Ficek, Mikhail G. Kozlov, Victor V. Flambaum, and Dmitry Budker. “Revisiting spin-dependent forces mediated by new bosons: Potentials in the coordinate-space representation for macroscopic- and atomic-scale experiments.” *Phys. Rev. A* 99.2 (2019), p. 022113. DOI: [10.1103/PhysRevA.99.022113](https://doi.org/10.1103/PhysRevA.99.022113). arXiv: [1810.10364](https://arxiv.org/abs/1810.10364) [hep-ph].

- [113] Joerg Jaeckel and Sabyasachi Roy. "Spectroscopy as a test of Coulomb's law: A Probe of the hidden sector." *Phys. Rev. D* 82 (2010), p. 125020. DOI: [10.1103/PhysRevD.82.125020](https://doi.org/10.1103/PhysRevD.82.125020). arXiv: [1008.3536 \[hep-ph\]](https://arxiv.org/abs/1008.3536).
- [114] Bob Holdom. "Two $U(1)$'s and Epsilon Charge Shifts." *Phys. Lett.* 166B (1986), pp. 196–198. DOI: [10.1016/0370-2693\(86\)91377-8](https://doi.org/10.1016/0370-2693(86)91377-8).
- [115] E. C. G. Stueckelberg. "Interaction energy in electrodynamics and in the field theory of nuclear forces." *Helv. Phys. Acta* 11 (1938), pp. 225–244. DOI: [10.5169/seals-110852](https://doi.org/10.5169/seals-110852).
- [116] Boris Kors and Pran Nath. "A Stueckelberg extension of the standard model." *Phys. Lett.* B586 (2004), pp. 366–372. DOI: [10.1016/j.physletb.2004.02.051](https://doi.org/10.1016/j.physletb.2004.02.051). arXiv: [hep-ph/0402047 \[hep-ph\]](https://arxiv.org/abs/hep-ph/0402047).
- [117] Georg G. Raffelt. "Astrophysical methods to constrain axions and other novel particle phenomena." *Phys. Rept.* 198 (1990), pp. 1–113. DOI: [10.1016/0370-1573\(90\)90054-6](https://doi.org/10.1016/0370-1573(90)90054-6).
- [118] Georg G. Raffelt. "Astrophysical axion bounds." *Lect. Notes Phys.* 741 (2008), pp. 51–71. DOI: [10.1007/978-3-540-73518-2_3](https://doi.org/10.1007/978-3-540-73518-2_3). arXiv: [hep-ph/0611350 \[hep-ph\]](https://arxiv.org/abs/hep-ph/0611350).
- [119] Paul Frederik Depta, Marco Hufnagel, and Kai Schmidt-Hoberg. "Robust cosmological constraints on axion-like particles" (2020). arXiv: [2002.08370 \[hep-ph\]](https://arxiv.org/abs/2002.08370).
- [120] G. Feinberg and J. Sucher. "Long-Range Forces from Neutrino-Pair Exchange." *Phys. Rev.* 166 (1968), pp. 1638–1644. DOI: [10.1103/PhysRev.166.1638](https://doi.org/10.1103/PhysRev.166.1638).
- [121] Shau-Jin Chang and R. Rajaraman. "Long-range corrections to the coulomb potential and their implications about weak interactions." *Phys. Rev.* 183 (1969), pp. 1442–1445. DOI: [10.1103/PhysRev.183.1442](https://doi.org/10.1103/PhysRev.183.1442).
- [122] Stephen D. H. Hsu and Pierre Sikivie. "Long range forces from two neutrino exchange revisited." *Phys. Rev. D* 49 (1994), pp. 4951–4953. DOI: [10.1103/PhysRevD.49.4951](https://doi.org/10.1103/PhysRevD.49.4951). arXiv: [hep-ph/9211301 \[hep-ph\]](https://arxiv.org/abs/hep-ph/9211301).
- [123] J. A. Grifols, E. Masso, and R. Toldra. "Majorana neutrinos and long range forces." *Phys. Lett.* B389 (1996), pp. 563–565. DOI: [10.1016/S0370-2693\(96\)01304-4](https://doi.org/10.1016/S0370-2693(96)01304-4). arXiv: [hep-ph/9606377 \[hep-ph\]](https://arxiv.org/abs/hep-ph/9606377).
- [124] F. Ferrer and M. Nowakowski. "Higgs and Goldstone bosons mediated long range forces." *Phys. Rev. D* 59 (1999), p. 075009. DOI: [10.1103/PhysRevD.59.075009](https://doi.org/10.1103/PhysRevD.59.075009). arXiv: [hep-ph/9810550 \[hep-ph\]](https://arxiv.org/abs/hep-ph/9810550).

- [125] Yevgeny V. Stadnik. “Probing Long-Range Neutrino-Mediated Forces with Atomic and Nuclear Spectroscopy.” *Phys. Rev. Lett.* 120.22 (2018), p. 223202. DOI: [10.1103/PhysRevLett.120.223202](https://doi.org/10.1103/PhysRevLett.120.223202). arXiv: [1711.03700](https://arxiv.org/abs/1711.03700) [physics.atom-ph].
- [126] Quan Le Thien and Dennis E. Krause. “Spin-Independent Two-Neutrino Exchange Potential with Mixing and CP -Violation.” *Phys.Rev.D* 99.11 (2019), p. 116006. DOI: [10.1103/PhysRevD.99.116006](https://doi.org/10.1103/PhysRevD.99.116006). arXiv: [1901.05345](https://arxiv.org/abs/1901.05345) [hep-ph].
- [127] Mitrajyoti Ghosh, Yuval Grossman, and Walter Tangarife. “Probing the two-neutrino exchange force using atomic parity violation” (2019). arXiv: [1912.09444](https://arxiv.org/abs/1912.09444) [hep-ph].
- [128] Alejandro Segarra and José Bernabéu. “Absolute neutrino mass and the Dirac/Majorana distinction from the weak interaction of aggregate matter.” *Phys. Rev. D* 101.9 (2020), p. 093004. DOI: [10.1103/PhysRevD.101.093004](https://doi.org/10.1103/PhysRevD.101.093004). arXiv: [2001.05900](https://arxiv.org/abs/2001.05900) [hep-ph].
- [129] Patrick D. Bolton, Frank F. Deppisch, and Chandan Hati. “Probing New Physics with Long-Range Neutrino Interactions: An Effective Field Theory Approach” (Apr. 2020). arXiv: [2004.08328](https://arxiv.org/abs/2004.08328) [hep-ph].
- [130] M. Abramowitz and I.A. Stegun. *Handbook of Mathematical Functions with Formulas, Graphs, and Mathematical Tables*. Applied mathematics series. U.S. Government Printing Office, 1964.
- [131] A. Pineda and J. Soto. “Potential NRQED: The Positronium case.” *Phys. Rev. D* 59 (1999), p. 016005. DOI: [10.1103/PhysRevD.59.016005](https://doi.org/10.1103/PhysRevD.59.016005). arXiv: [hep-ph/9805424](https://arxiv.org/abs/hep-ph/9805424).
- [132] T. Asaka, M. Tanaka, K. Tsumura, and M. Yoshimura. “Precision electroweak shift of muonium hyperfine splitting” (Oct. 2018). arXiv: [1810.05429](https://arxiv.org/abs/1810.05429) [hep-ph].
- [133] Alexandria Costantino and Sylvain Fichet. “The Neutrino Casimir Force” (Mar. 2020). arXiv: [2003.11032](https://arxiv.org/abs/2003.11032) [hep-ph].
- [134] Matthias Linster, Jacobo Lopez-Pavon, and Robert Ziegler. “Neutrino Observables from a $U(2)$ Flavor Symmetry.” *Phys. Rev. D* 103.1 (2021), p. 015020. DOI: [10.1103/PhysRevD.103.015020](https://doi.org/10.1103/PhysRevD.103.015020). arXiv: [2009.10437](https://arxiv.org/abs/2009.10437) [hep-ph].
- [135] M. Bona et al. “The Unitarity Triangle Fit in the Standard Model and Hadronic Parameters from Lattice QCD: A Reappraisal after the Measurements of $\Delta m(s)$ and $BR(B \rightarrow \tau \nu(\tau))$.” *JHEP* 10 (2006), p. 081. DOI: [10.1088/1126-6708/2006/10/081](https://doi.org/10.1088/1126-6708/2006/10/081). arXiv: [hep-ph/0606167](https://arxiv.org/abs/hep-ph/0606167).
- [136] NuFIT 5.0 (2020), www.nu-fit.org. URL: <http://www.nu-fit.org>.

- [137] Adam Falkowski, Marco Nardecchia, and Robert Ziegler. "Lepton Flavor Non-Universality in B-meson Decays from a U(2) Flavor Model." *JHEP* 11 (2015), p. 173. DOI: [10.1007/JHEP11\(2015\)173](https://doi.org/10.1007/JHEP11(2015)173). arXiv: [1509.01249](https://arxiv.org/abs/1509.01249) [hep-ph].
- [138] Riccardo Barbieri and Robert Ziegler. "Quark masses, CKM angles and Lepton Flavour Universality violation." *JHEP* 07 (2019), p. 023. DOI: [10.1007/JHEP07\(2019\)023](https://doi.org/10.1007/JHEP07(2019)023). arXiv: [1904.04121](https://arxiv.org/abs/1904.04121) [hep-ph].
- [139] C. D. Froggatt and Holger Bech Nielsen. "Hierarchy of Quark Masses, Cabibbo Angles and CP Violation." *Nucl. Phys. B* 147 (1979), pp. 277–298. DOI: [10.1016/0550-3213\(79\)90316-X](https://doi.org/10.1016/0550-3213(79)90316-X).
- [140] Nima Arkani-Hamed and Martin Schmaltz. "Hierarchies without symmetries from extra dimensions." *Phys. Rev. D* 61 (2000), p. 033005. DOI: [10.1103/PhysRevD.61.033005](https://doi.org/10.1103/PhysRevD.61.033005). arXiv: [hep-ph/9903417](https://arxiv.org/abs/hep-ph/9903417).
- [141] Lisa Randall and Raman Sundrum. "A Large mass hierarchy from a small extra dimension." *Phys. Rev. Lett.* 83 (1999), pp. 3370–3373. DOI: [10.1103/PhysRevLett.83.3370](https://doi.org/10.1103/PhysRevLett.83.3370). arXiv: [hep-ph/9905221](https://arxiv.org/abs/hep-ph/9905221).
- [142] David Elazzar Kaplan and Timothy M. P. Tait. "New tools for fermion masses from extra dimensions." *JHEP* 11 (2001), p. 051. DOI: [10.1088/1126-6708/2001/11/051](https://doi.org/10.1088/1126-6708/2001/11/051). arXiv: [hep-ph/0110126](https://arxiv.org/abs/hep-ph/0110126).
- [143] Gerard 't Hooft. "Renormalizable Lagrangians for Massive Yang-Mills Fields." *Nucl. Phys. B* 35 (1971). Ed. by J. C. Taylor, pp. 167–188. DOI: [10.1016/0550-3213\(71\)90139-8](https://doi.org/10.1016/0550-3213(71)90139-8).
- [144] Steven Weinberg. "Electromagnetic and weak masses." *Phys. Rev. Lett.* 29 (1972), pp. 388–392. DOI: [10.1103/PhysRevLett.29.388](https://doi.org/10.1103/PhysRevLett.29.388).
- [145] Howard Georgi and Sheldon L. Glashow. "Attempts to calculate the electron mass." *Phys. Rev. D* 7 (1973), pp. 2457–2463. DOI: [10.1103/PhysRevD.7.2457](https://doi.org/10.1103/PhysRevD.7.2457).
- [146] S. M. Barr and Almas Khan. "A Realistic Radiative Fermion Mass Hierarchy in Non-supersymmetric SO(10)." *Phys. Rev. D* 79 (2009), p. 115005. DOI: [10.1103/PhysRevD.79.115005](https://doi.org/10.1103/PhysRevD.79.115005). arXiv: [0807.5112](https://arxiv.org/abs/0807.5112) [hep-ph].
- [147] K. S. Babu. "TASI Lectures on Flavor Physics." *Theoretical Advanced Study Institute in Elementary Particle Physics: The Dawn of the LHC Era*. Oct. 2009. DOI: [10.1142/9789812838360_0002](https://doi.org/10.1142/9789812838360_0002). arXiv: [0910.2948](https://arxiv.org/abs/0910.2948) [hep-ph].
- [148] Riccardo Barbieri, G. R. Dvali, and Lawrence J. Hall. "Predictions from a U(2) flavor symmetry in supersymmetric theories." *Phys. Lett. B* 377 (1996), pp. 76–82. DOI: [10.1016/0370-2693\(96\)00318-8](https://doi.org/10.1016/0370-2693(96)00318-8). arXiv: [hep-ph/9512388](https://arxiv.org/abs/hep-ph/9512388).

- [149] Riccardo Barbieri, Lawrence J. Hall, and Andrea Romanino. “Consequences of a $U(2)$ flavor symmetry.” *Phys. Lett. B* 401 (1997), pp. 47–53. DOI: [10.1016/S0370-2693\(97\)00372-9](https://doi.org/10.1016/S0370-2693(97)00372-9). arXiv: [hep-ph/9702315](https://arxiv.org/abs/hep-ph/9702315).
- [150] R. G. Roberts, A. Romanino, Graham G. Ross, and L. Velasco-Sevilla. “Precision Test of a Fermion Mass Texture.” *Nucl. Phys. B* 615 (2001), pp. 358–384. DOI: [10.1016/S0550-3213\(01\)00408-4](https://doi.org/10.1016/S0550-3213(01)00408-4). arXiv: [hep-ph/0104088](https://arxiv.org/abs/hep-ph/0104088).
- [151] Radovan Dermisek and Stuart Raby. “Fermion masses and neutrino oscillations in $SO(10)$ SUSY GUT with $D(3) \times U(1)$ family symmetry.” *Phys. Rev. D* 62 (2000), p. 015007. DOI: [10.1103/PhysRevD.62.015007](https://doi.org/10.1103/PhysRevD.62.015007). arXiv: [hep-ph/9911275](https://arxiv.org/abs/hep-ph/9911275).
- [152] Emilian Dudas, Gero von Gersdorff, Stefan Pokorski, and Robert Ziegler. “Linking Natural Supersymmetry to Flavour Physics.” *JHEP* 01 (2014), p. 117. DOI: [10.1007/JHEP01\(2014\)117](https://doi.org/10.1007/JHEP01(2014)117). arXiv: [1308.1090](https://arxiv.org/abs/1308.1090) [hep-ph].
- [153] Steven Weinberg. “Baryon and Lepton Nonconserving Processes.” *Phys. Rev. Lett.* 43 (1979), pp. 1566–1570. DOI: [10.1103/PhysRevLett.43.1566](https://doi.org/10.1103/PhysRevLett.43.1566).
- [154] Paul H. Frampton, Sheldon L. Glashow, and Danny Marfatia. “Zeroes of the neutrino mass matrix.” *Phys. Lett. B* 536 (2002), pp. 79–82. DOI: [10.1016/S0370-2693\(02\)01817-8](https://doi.org/10.1016/S0370-2693(02)01817-8). arXiv: [hep-ph/0201008](https://arxiv.org/abs/hep-ph/0201008).
- [155] Wan-lei Guo and Zhi-zhong Xing. “Implications of the KamLAND measurement on the lepton flavor mixing matrix and the neutrino mass matrix.” *Phys. Rev. D* 67 (2003), p. 053002. DOI: [10.1103/PhysRevD.67.053002](https://doi.org/10.1103/PhysRevD.67.053002). arXiv: [hep-ph/0212142](https://arxiv.org/abs/hep-ph/0212142).
- [156] S. Dev, Sanjeev Kumar, Surender Verma, and Shivani Gupta. “Phenomenology of two-texture zero neutrino mass matrices.” *Phys. Rev. D* 76 (2007), p. 013002. DOI: [10.1103/PhysRevD.76.013002](https://doi.org/10.1103/PhysRevD.76.013002). arXiv: [hep-ph/0612102](https://arxiv.org/abs/hep-ph/0612102).
- [157] Harald Fritzsch, Zhi-zhong Xing, and Shun Zhou. “Two-zero Textures of the Majorana Neutrino Mass Matrix and Current Experimental Tests.” *JHEP* 09 (2011), p. 083. DOI: [10.1007/JHEP09\(2011\)083](https://doi.org/10.1007/JHEP09(2011)083). arXiv: [1108.4534](https://arxiv.org/abs/1108.4534) [hep-ph].
- [158] D. Meloni and G. Blankenburg. “Fine-tuning and naturalness issues in the two-zero neutrino mass textures.” *Nucl. Phys. B* 867 (2013), pp. 749–762. DOI: [10.1016/j.nuclphysb.2012.10.011](https://doi.org/10.1016/j.nuclphysb.2012.10.011). arXiv: [1204.2706](https://arxiv.org/abs/1204.2706) [hep-ph].
- [159] Teruyuki Kitabayashi and Masaki Yasuè. “Formulas for flavor neutrino masses and their application to texture two zeros.” *Phys. Rev. D* 93.5 (2016), p. 053012. DOI: [10.1103/PhysRevD.93.053012](https://doi.org/10.1103/PhysRevD.93.053012). arXiv: [1512.00913](https://arxiv.org/abs/1512.00913) [hep-ph].

- [160] Shun Zhou. “Update on two-zero textures of the Majorana neutrino mass matrix in light of recent T2K, Super-Kamiokande and NOvA results.” *Chin. Phys. C* 40.3 (2016), p. 033102. DOI: [10.1088/1674-1137/40/3/033102](https://doi.org/10.1088/1674-1137/40/3/033102). arXiv: [1509.05300](https://arxiv.org/abs/1509.05300) [hep-ph].
- [161] Madan Singh, Gulsheen Ahuja, and Manmohan Gupta. “Revisiting the texture zero neutrino mass matrices.” *PTEP* 2016.12 (2016), 123Bo8. DOI: [10.1093/ptep/ptw180](https://doi.org/10.1093/ptep/ptw180). arXiv: [1603.08083](https://arxiv.org/abs/1603.08083) [hep-ph].
- [162] Julien Alcaide, Jordi Salvado, and Arcadi Santamaria. “Fitting flavour symmetries: the case of two-zero neutrino mass textures.” *JHEP* 07 (2018), p. 164. DOI: [10.1007/JHEP07\(2018\)164](https://doi.org/10.1007/JHEP07(2018)164). arXiv: [1806.06785](https://arxiv.org/abs/1806.06785) [hep-ph].
- [163] Zhi-zhong Xing. “Flavor structures of charged fermions and massive neutrinos.” *Phys. Rept.* 854 (2020), pp. 1–147. DOI: [10.1016/j.physrep.2020.02.001](https://doi.org/10.1016/j.physrep.2020.02.001). arXiv: [1909.09610](https://arxiv.org/abs/1909.09610) [hep-ph].
- [164] Patrick Dunne. *Latest Neutrino Oscillation Results from T2K*. July 2020. DOI: [10.5281/zenodo.3959558](https://doi.org/10.5281/zenodo.3959558).
- [165] Alex Himmel. *New Oscillation Results from the NOvA Experiment*. July 2020. DOI: [10.5281/zenodo.4142045](https://doi.org/10.5281/zenodo.4142045).
- [166] K. Abe et al. “A Long Baseline Neutrino Oscillation Experiment Using J-PARC Neutrino Beam and Hyper-Kamiokande.” Dec. 2014. arXiv: [1412.4673](https://arxiv.org/abs/1412.4673) [physics.ins-det].
- [167] B. Abi et al. “Long-baseline neutrino oscillation physics potential of the DUNE experiment.” *Eur. Phys. J. C* 80.10 (2020), p. 978. DOI: [10.1140/epjc/s10052-020-08456-z](https://doi.org/10.1140/epjc/s10052-020-08456-z). arXiv: [2006.16043](https://arxiv.org/abs/2006.16043) [hep-ex].
- [168] Ali Ashtari Esfahani et al. “Determining the neutrino mass with cyclotron radiation emission spectroscopy—Project 8.” *J. Phys. G* 44.5 (2017), p. 054004. DOI: [10.1088/1361-6471/aa5b4f](https://doi.org/10.1088/1361-6471/aa5b4f). arXiv: [1703.02037](https://arxiv.org/abs/1703.02037) [physics.ins-det].
- [169] Luca Amendola et al. “Cosmology and fundamental physics with the Euclid satellite.” *Living Rev. Rel.* 21.1 (2018), p. 2. DOI: [10.1007/s41114-017-0010-3](https://doi.org/10.1007/s41114-017-0010-3). arXiv: [1606.00180](https://arxiv.org/abs/1606.00180) [astro-ph.CO].
- [170] Amir Aghamousa et al. “The DESI Experiment Part I: Science, Targeting, and Survey Design” (Oct. 2016). arXiv: [1611.00036](https://arxiv.org/abs/1611.00036) [astro-ph.IM].
- [171] N. Abgrall et al. “The Large Enriched Germanium Experiment for Neutrinoless Double Beta Decay (LEGEND).” *AIP Conf. Proc.* 1894.1 (2017). Ed. by Osvaldo Civitarese, Ivan Stekl, and Jouni Suhonen, p. 020027. DOI: [10.1063/1.5007652](https://doi.org/10.1063/1.5007652). arXiv: [1709.01980](https://arxiv.org/abs/1709.01980) [physics.ins-det].

- [172] J.B. Albert et al. "Sensitivity and Discovery Potential of nEXO to Neutrinoless Double Beta Decay." *Phys. Rev. C* 97.6 (2018), p. 065503. DOI: [10.1103/PhysRevC.97.065503](https://doi.org/10.1103/PhysRevC.97.065503). arXiv: [1710.05075](https://arxiv.org/abs/1710.05075) [nucl-ex].
- [173] Rene Brun and Fons Rademakers. "ROOT — An object oriented data analysis framework." *Nuclear Instruments and Methods in Physics Research Section A: Accelerators, Spectrometers, Detectors and Associated Equipment* 389.1 (1997). New Computing Techniques in Physics Research V, pp. 81–86. ISSN: 0168-9002. DOI: [https://doi.org/10.1016/S0168-9002\(97\)00048-X](https://doi.org/10.1016/S0168-9002(97)00048-X). URL: <https://www.sciencedirect.com/science/article/pii/S016890029700048X>.
- [174] Fons Rademakers et al. *root-project/root: v6.20/04*. 2020. DOI: [10.5281/ZENODO.3895855](https://doi.org/10.5281/ZENODO.3895855). URL: <https://zenodo.org/record/3895855>.
- [175] Hans-Thomas Janka. "Neutrino-Driven Explosions." *Handbook of Supernovae*. Ed. by Athem W. Alsabti and Paul Murdin. Cham: Springer International Publishing, 2017, pp. 1095–1150. ISBN: 978-3-319-21846-5. DOI: [10.1007/978-3-319-21846-5_109](https://doi.org/10.1007/978-3-319-21846-5_109). URL: https://doi.org/10.1007/978-3-319-21846-5_109.
- [176] Thierry Foglizzo. "Explosion Physics of Core-Collapse Supernovae." *Handbook of Supernovae*. Ed. by Athem W. Alsabti and Paul Murdin. Cham: Springer International Publishing, 2017, pp. 1053–1073. ISBN: 978-3-319-21846-5. DOI: [10.1007/978-3-319-21846-5_52](https://doi.org/10.1007/978-3-319-21846-5_52). URL: https://doi.org/10.1007/978-3-319-21846-5_52.
- [177] R. Bollig, N. Yadav, D. Kresse, H. -Th. Janka, B. Mueller, and A. Heger. "Self-consistent 3D Supernova Models From -7 Minutes to +7 Seconds: a 1-bethe Explosion of a ~19 Solar-mass Progenitor" (Oct. 2020). arXiv: [2010.10506](https://arxiv.org/abs/2010.10506) [astro-ph.HE].
- [178] Hans-Thomas Janka, K. Langanke, A. Marek, G. Martinez-Pinedo, and B. Mueller. "Theory of Core-Collapse Supernovae." *Phys. Rept.* 442 (2007), pp. 38–74. DOI: [10.1016/j.physrep.2007.02.002](https://doi.org/10.1016/j.physrep.2007.02.002). arXiv: [astro-ph/0612072](https://arxiv.org/abs/astro-ph/0612072).
- [179] Hans-Thomas Janka. "Explosion Mechanisms of Core-Collapse Supernovae." *Ann. Rev. Nucl. Part. Sci.* 62 (2012), pp. 407–451. DOI: [10.1146/annurev-nucl-102711-094901](https://doi.org/10.1146/annurev-nucl-102711-094901). arXiv: [1206.2503](https://arxiv.org/abs/1206.2503) [astro-ph.SR].
- [180] Adam Burrows and David Vartanyan. "Core-Collapse Supernova Explosion Theory." *Nature* 589.7840 (2021), pp. 29–39. DOI: [10.1038/s41586-020-03059-w](https://doi.org/10.1038/s41586-020-03059-w). arXiv: [2009.14157](https://arxiv.org/abs/2009.14157) [astro-ph.SR].

- [181] H. A. Bethe and R. F. Bacher. "Nuclear Physics A. Stationary States of Nuclei." *Rev. Mod. Phys.* 8 (1936), pp. 82–229. DOI: [10.1103/RevModPhys.8.82](https://doi.org/10.1103/RevModPhys.8.82).
- [182] Subrahmanyan Chandrasekhar. *An introduction to the study of stellar structure*. 1939.
- [183] Hans-Thomas Janka. "Neutrino Emission from Supernovae." *Handbook of Supernovae*. Ed. by Athem W. Alsabti and Paul Murdin. Cham: Springer International Publishing, 2017, pp. 1575–1604. ISBN: 978-3-319-21846-5. DOI: [10.1007/978-3-319-21846-5_4](https://doi.org/10.1007/978-3-319-21846-5_4). URL: https://doi.org/10.1007/978-3-319-21846-5_4.
- [184] Hans A. Bethe and James R. Wilson. "Revival of a stalled supernova shock by neutrino heating." *Astrophys. J.* 295 (1985), pp. 14–23. DOI: [10.1086/163343](https://doi.org/10.1086/163343).
- [185] R. Bollig, H. -Th. Janka, A. Lohs, G. Martinez-Pinedo, C. J. Horowitz, and T. Melson. "Muon Creation in Supernova Matter Facilitates Neutrino-driven Explosions." *Phys. Rev. Lett.* 119.24 (2017), p. 242702. DOI: [10.1103/PhysRevLett.119.242702](https://doi.org/10.1103/PhysRevLett.119.242702). arXiv: [1706.04630](https://arxiv.org/abs/1706.04630) [astro-ph.HE].
- [186] Robert Bollig, William DeRocco, Peter W. Graham, and Hans-Thomas Janka. "Muons in Supernovae: Implications for the Axion-Muon Coupling." *Phys. Rev. Lett.* 125.5 (2020). [Erratum: *Phys.Rev.Lett.* 126, 189901 (2021)], p. 051104. DOI: [10.1103/PhysRevLett.125.051104](https://doi.org/10.1103/PhysRevLett.125.051104). arXiv: [2005.07141](https://arxiv.org/abs/2005.07141) [hep-ph].
- [187] M. Fortin, M. Oertel, and C. Providência. "Hyperons in hot dense matter: what do the constraints tell us for equation of state?" *Publ. Astron. Soc. Austral.* 35 (2018), p. 44. DOI: [10.1017/pasa.2018.32](https://doi.org/10.1017/pasa.2018.32). arXiv: [1711.09427](https://arxiv.org/abs/1711.09427) [astro-ph.HE].
- [188] M. Oertel, M. Hempel, T. Klähn, and S. Typel. "Equations of state for supernovae and compact stars." *Rev. Mod. Phys.* 89.1 (2017), p. 015007. DOI: [10.1103/RevModPhys.89.015007](https://doi.org/10.1103/RevModPhys.89.015007). arXiv: [1610.03361](https://arxiv.org/abs/1610.03361) [astro-ph.HE].
- [189] James M. Lattimer and F. Douglas Swesty. "A generalized equation of state for hot, dense matter." *Nuclear Physics A* 535.2 (1991), pp. 331–376. ISSN: 0375-9474. DOI: [https://doi.org/10.1016/0375-9474\(91\)90452-C](https://doi.org/10.1016/0375-9474(91)90452-C). URL: <https://www.sciencedirect.com/science/article/pii/037594749190452C>.
- [190] M. Oertel, A. F. Fantina, and J. Novak. "An extended equation of state for core-collapse simulations." *Phys. Rev. C* 85 (2012), p. 055806. DOI: [10.1103/PhysRevC.85.055806](https://doi.org/10.1103/PhysRevC.85.055806). arXiv: [1202.2679](https://arxiv.org/abs/1202.2679) [nucl-th].

- [191] Miguel Marques, Micaela Oertel, Matthias Hempel, and Jérôme Novak. “New temperature dependent hyperonic equation of state: Application to rotating neutron star models and I - Q relations.” *Phys. Rev. C* 96.4 (2017), p. 045806. DOI: [10.1103/PhysRevC.96.045806](https://doi.org/10.1103/PhysRevC.96.045806). arXiv: 1706.02913 [nucl-th].
- [192] Matthias Hempel and Jürgen Schaffner-Bielich. “A statistical model for a complete supernova equation of state.” *Nuclear Physics A* 837.3 (2010), pp. 210–254. ISSN: 0375-9474. DOI: <https://doi.org/10.1016/j.nuclphysa.2010.02.010>. URL: <https://www.sciencedirect.com/science/article/pii/S0375947410003325>.
- [193] A. W. Steiner, M. Hempel, and T. Fischer. “CORE-COLLAPSE SUPERNOVA EQUATIONS OF STATE BASED ON NEUTRON STAR OBSERVATIONS.” *The Astrophysical Journal* 774.1 (Aug. 2013), p. 17. DOI: [10.1088/0004-637x/774/1/17](https://doi.org/10.1088/0004-637x/774/1/17). URL: <https://doi.org/10.1088/0004-637x/774/1/17>.
- [194] *CompOSE — CompStar Online Supernovæ Equations of State*. 2018. URL: <https://compose.obspm.fr>.
- [195] *The Garching Core-Collapse Supernova Archive*. URL: <https://wwwmpa.mpa-garching.mpg.de/ccsnarchive/archive.html>.
- [196] K. Hirata et al. “Observation of a Neutrino Burst from the Supernova SN 1987a.” *Phys. Rev. Lett.* 58 (1987). Ed. by K. C. Wali, pp. 1490–1493. DOI: [10.1103/PhysRevLett.58.1490](https://doi.org/10.1103/PhysRevLett.58.1490).
- [197] R. M. Bionta et al. “Observation of a Neutrino Burst in Coincidence with Supernova SN 1987a in the Large Magellanic Cloud.” *Phys. Rev. Lett.* 58 (1987), p. 1494. DOI: [10.1103/PhysRevLett.58.1494](https://doi.org/10.1103/PhysRevLett.58.1494).
- [198] E. N. Alekseev, L. N. Alekseeva, V. I. Volchenko, and I. V. Krivosheina. “Possible detection of a neutrino signal on February 23, 1987 with the Baksan underground scintillation telescope of the Nuclear Research Institute of the Soviet Academy of Sciences.” *Pisma v Zhurnal Eksperimentalnoi i Teoreticheskoi Fiziki* 45 (May 1987), pp. 461–464.
- [199] T. J. Loredo and D. Q. Lamb. “Neutrino from SN1987A: Implications for cooling of the nascent neutron star and the mass of the electron anti-neutrino.” *Annals N. Y. Acad. Sci.* 571 (1989). Ed. by E. J. Fenyves, pp. 601–630. DOI: [10.1111/j.1749-6632.1989.tb50547.x](https://doi.org/10.1111/j.1749-6632.1989.tb50547.x).
- [200] Francis Halzen and Kate Scholberg. “Neutrinos from Core-Collapse Supernovae and Their Detection.” *Handbook of Supernovae*. Ed. by Athem W. Alsabti and Paul Murdin. Cham: Springer International Publishing, 2017, pp. 1655–1670. ISBN: 978-3-319-21846-5. DOI: [10.1007/978-3-319-21846-5_8](https://doi.org/10.1007/978-3-319-21846-5_8). URL: https://doi.org/10.1007/978-3-319-21846-5_8.

- [201] Jae Hyeok Chang, Rouven Essig, and Samuel D. McDermott. “Revisiting Supernova 1987A Constraints on Dark Photons.” *JHEP* 01 (2017), p. 107. DOI: [10.1007/JHEP01\(2017\)107](https://doi.org/10.1007/JHEP01(2017)107). arXiv: [1611.03864](https://arxiv.org/abs/1611.03864) [hep-ph].
- [202] Pierluca Carenza, Tobias Fischer, Maurizio Giannotti, Gang Guo, Gabriel Martínez-Pinedo, and Alessandro Mirizzi. “Improved axion emissivity from a supernova via nucleon-nucleon bremsstrahlung.” *JCAP* 10.10 (2019). [Erratum: *JCAP* 05, E01 (2020)], p. 016. DOI: [10.1088/1475-7516/2019/10/016](https://doi.org/10.1088/1475-7516/2019/10/016). arXiv: [1906.11844](https://arxiv.org/abs/1906.11844) [hep-ph].
- [203] H. K. Dreiner, C. Hanhart, U. Langenfeld, and Daniel R. Phillips. “Supernovae and light neutralinos: SN1987A bounds on supersymmetry revisited.” *Phys. Rev. D* 68 (2003), p. 055004. DOI: [10.1103/PhysRevD.68.055004](https://doi.org/10.1103/PhysRevD.68.055004). arXiv: [hep-ph/0304289](https://arxiv.org/abs/hep-ph/0304289).
- [204] Giuseppe Lucente, Pierluca Carenza, Tobias Fischer, Maurizio Giannotti, and Alessandro Mirizzi. “Heavy axion-like particles and core-collapse supernovae: constraints and impact on the explosion mechanism.” *JCAP* 12 (2020), p. 008. DOI: [10.1088/1475-7516/2020/12/008](https://doi.org/10.1088/1475-7516/2020/12/008). arXiv: [2008.04918](https://arxiv.org/abs/2008.04918) [hep-ph].
- [205] J. D. Walecka. “A theory of highly condensed matter.” *Annals of Physics* 83.2 (1974), pp. 491–529. ISSN: 0003-4916. DOI: [https://doi.org/10.1016/0003-4916\(74\)90208-5](https://doi.org/10.1016/0003-4916(74)90208-5). URL: <https://www.sciencedirect.com/science/article/pii/0003491674902085>.
- [206] Brian D. Serot and John Dirk Walecka. “Relativistic Nuclear Many-Body Theory.” *Recent Progress in Many-Body Theories: Volume 3*. Ed. by T. L. Ainsworth, C. E. Campbell, B. E. Clements, and E. Krotscheck. Boston, MA: Springer US, 1992, pp. 49–92. ISBN: 978-1-4615-3466-2. DOI: [10.1007/978-1-4615-3466-2_5](https://doi.org/10.1007/978-1-4615-3466-2_5). URL: https://doi.org/10.1007/978-1-4615-3466-2_5.
- [207] Giovanni Grilli di Cortona, Edward Hardy, Javier Pardo Vega, and Giovanni Villadoro. “The QCD axion, precisely.” *JHEP* 01 (2016), p. 034. DOI: [10.1007/JHEP01\(2016\)034](https://doi.org/10.1007/JHEP01(2016)034). arXiv: [1511.02867](https://arxiv.org/abs/1511.02867) [hep-ph].
- [208] Reuven Balkin, Javi Serra, Konstantin Springmann, and Andreas Weiler. “The QCD axion at finite density.” *JHEP* 07 (2020), p. 221. DOI: [10.1007/JHEP07\(2020\)221](https://doi.org/10.1007/JHEP07(2020)221). arXiv: [2003.04903](https://arxiv.org/abs/2003.04903) [hep-ph].
- [209] N. Iwamoto. “Axion Emission from Neutron Stars.” *Phys. Rev. Lett.* 53 (1984), pp. 1198–1201. DOI: [10.1103/PhysRevLett.53.1198](https://doi.org/10.1103/PhysRevLett.53.1198).
- [210] Georg Raffelt and David Seckel. “Bounds on Exotic Particle Interactions from SN 1987a.” *Phys. Rev. Lett.* 60 (1988), p. 1793. DOI: [10.1103/PhysRevLett.60.1793](https://doi.org/10.1103/PhysRevLett.60.1793).

- [211] Ralf Peter Brinkmann and Michael S. Turner. “Numerical Rates for Nucleon-Nucleon Axion Bremsstrahlung.” *Phys. Rev. D* 38 (1988), p. 2338. DOI: [10.1103/PhysRevD.38.2338](https://doi.org/10.1103/PhysRevD.38.2338).
- [212] Jun Seok Lee. “Revisiting Supernova 1987A Limits on Axion-Like-Particles” (Aug. 2018). arXiv: [1808.10136](https://arxiv.org/abs/1808.10136) [hep-ph].
- [213] Eduardo Cortina Gil et al. “Search for a feebly interacting particle X in the decay $K^+ \rightarrow \pi^+ X$.” *JHEP* 03 (2021), p. 058. DOI: [10.1007/JHEP03\(2021\)058](https://doi.org/10.1007/JHEP03(2021)058). arXiv: [2011.11329](https://arxiv.org/abs/2011.11329) [hep-ex].
- [214] Henk Polinder, Johann Haidenbauer, and Ulf-G. Meissner. “Hyperon-nucleon interactions: A Chiral effective field theory approach.” *Nucl. Phys. A* 779 (2006), pp. 244–266. DOI: [10.1016/j.nuclphysa.2006.09.006](https://doi.org/10.1016/j.nuclphysa.2006.09.006). arXiv: [nuc1-th/0605050](https://arxiv.org/abs/nuc1-th/0605050).
- [215] Adam Alloul, Neil D. Christensen, Céline Degrande, Claude Duhr, and Benjamin Fuks. “FeynRules 2.0 - A complete toolbox for tree-level phenomenology.” *Comput. Phys. Commun.* 185 (2014), pp. 2250–2300. DOI: [10.1016/j.cpc.2014.04.012](https://doi.org/10.1016/j.cpc.2014.04.012). arXiv: [1310.1921](https://arxiv.org/abs/1310.1921) [hep-ph].
- [216] Thomas Hahn. “Generating Feynman diagrams and amplitudes with FeynArts 3.” *Comput. Phys. Commun.* 140 (2001), pp. 418–431. DOI: [10.1016/S0010-4655\(01\)00290-9](https://doi.org/10.1016/S0010-4655(01)00290-9). arXiv: [hep-ph/0012260](https://arxiv.org/abs/hep-ph/0012260).
- [217] R. Mertig, M. Bohm, and Ansgar Denner. “FEYN CALC: Computer algebraic calculation of Feynman amplitudes.” *Comput. Phys. Commun.* 64 (1991), pp. 345–359. DOI: [10.1016/0010-4655\(91\)90130-D](https://doi.org/10.1016/0010-4655(91)90130-D).
- [218] Vladyslav Shtabovenko, Rolf Mertig, and Frederik Orellana. “New Developments in FeynCalc 9.0.” *Comput. Phys. Commun.* 207 (2016), pp. 432–444. DOI: [10.1016/j.cpc.2016.06.008](https://doi.org/10.1016/j.cpc.2016.06.008). arXiv: [1601.01167](https://arxiv.org/abs/1601.01167) [hep-ph].
- [219] Vladyslav Shtabovenko, Rolf Mertig, and Frederik Orellana. “FeynCalc 9.3: New features and improvements.” *Comput. Phys. Commun.* 256 (2020), p. 107478. DOI: [10.1016/j.cpc.2020.107478](https://doi.org/10.1016/j.cpc.2020.107478). arXiv: [2001.04407](https://arxiv.org/abs/2001.04407) [hep-ph].
- [220] Eduardo Cortina Gil et al. “Search for π^0 decays to invisible particles.” *JHEP* 02 (2021), p. 201. DOI: [10.1007/JHEP02\(2021\)201](https://doi.org/10.1007/JHEP02(2021)201). arXiv: [2010.07644](https://arxiv.org/abs/2010.07644) [hep-ex].
- [221] Jernej F. Kamenik and Christopher Smith. “FCNC portals to the dark sector.” *JHEP* 03 (2012), p. 090. DOI: [10.1007/JHEP03\(2012\)090](https://doi.org/10.1007/JHEP03(2012)090). arXiv: [1111.6402](https://arxiv.org/abs/1111.6402) [hep-ph].
- [222] Lorenzo Calibbi, Diego Redigolo, Robert Ziegler, and Jure Zupan. “Looking forward to Lepton-flavor-violating ALPs” (June 2020). arXiv: [2006.04795](https://arxiv.org/abs/2006.04795) [hep-ph].

- [223] Ryuji Daido and Fuminobu Takahashi. "The sign of the dipole-dipole potential by axion exchange." *Phys. Lett. B* 772 (2017), pp. 127–129. DOI: [10.1016/j.physletb.2017.06.027](https://doi.org/10.1016/j.physletb.2017.06.027). arXiv: [1704.00155](https://arxiv.org/abs/1704.00155) [hep-ph].
- [224] V. A. Smirnov. *Feynman integral calculus*. 2006.
- [225] M. Beneke, G. Buchalla, C. Greub, A. Lenz, and U. Nierste. "Next-to-leading order QCD corrections to the lifetime difference of B(s) mesons." *Phys. Lett. B* 459 (1999), pp. 631–640. DOI: [10.1016/S0370-2693\(99\)00684-X](https://doi.org/10.1016/S0370-2693(99)00684-X). arXiv: [hep-ph/9808385](https://arxiv.org/abs/hep-ph/9808385).
- [226] V. I. Borodulin, R. N. Rogalyov, and S. R. Slabospitskii. "CORE 3.1 (Compendium of RELations, Version 3.1)" (Feb. 2017). arXiv: [1702.08246](https://arxiv.org/abs/1702.08246) [hep-ph].
- [227] J. J. Sakurai and Jim Napolitano. *Modern Quantum Mechanics*. 2nd ed. Cambridge University Press, 2017. DOI: [10.1017/9781108499996](https://doi.org/10.1017/9781108499996).
- [228] C.-F. Cheng, Y. R. Sun, H. Pan, J. Wang, A.-W. Liu, A. Campargue, and S.-M. Hu. "Electric-quadrupole transition of H₂ determined to 10⁻⁹ precision." *Phys. Rev. A* 85 (2 Feb. 2012), p. 024501. DOI: [10.1103/PhysRevA.85.024501](https://doi.org/10.1103/PhysRevA.85.024501). URL: <https://link.aps.org/doi/10.1103/PhysRevA.85.024501>.
- [229] T. Madhu Trivikram, M. L. Niu, P. Wcislo, W. Ubachs, and E. J. Salumbides. "Precision measurements and test of molecular theory in highly excited vibrational states of H₂ ($v = 11$)." *Applied Physics B* 122.12 (2016), p. 294. ISSN: 1432-0649. DOI: [10.1007/s00340-016-6570-1](https://doi.org/10.1007/s00340-016-6570-1). URL: <https://doi.org/10.1007/s00340-016-6570-1>.

DANKSAGUNG

Zunächst möchte ich Ulrich Nierste danken, dass du mir die Möglichkeit einer etwas mehr als dreijährigen Promotion in deiner Arbeitsgruppe gegeben hast und mir die Freiheit gegeben hast, mir meine Promotionsprojekte und Kollaborateure selbstständig auszusuchen. Ebenso möchte ich dir für die ermöglichten Dienstreisen danken, was angesichts spärlicher Mittel nicht selbstverständlich ist.

Darüber hinaus möchte ich Thomas Schwetz-Mangold danken, dass Sie wie bei meiner Masterarbeit wieder das Koreferat übernommen haben und mir insbesondere am Ende hilfreiche Kommentare zur Arbeit gegeben haben. Ebenso möchte ich Ihnen danken für die Hilfestellung zur Statistik zu Beginn der Promotion.

Mein größter Dank gilt Robert Ziegler, dass du zwei meiner Projekte betreut und vorgeschlagen hast. Auch dafür, dass du am Ende meine Arbeit teils mehrfach durchgesehen hast und viele Kommentare gegeben hast, die die Arbeit deutlich verbessern. Ebenso möchte ich Wolfgang (G.) Hollik danken für die gute Zusammenarbeit im Molekülprojekt und das Probelesen des entsprechenden Teils meiner Arbeit.

Ganz besonders möchte ich auch den weiteren Korrekturlesern Paul Pöpperl und Martin Lang danken, dafür dass ihr teils spontan und mehrfach meine Arbeit gelesen habt und viele sprachliche Fehler angemerkt habt. Ohne euch wäre meine Arbeit deutlich schlechter . . .

Danken möchte ich auch meinen weiteren Kollaborateuren Jacobo Lopez-Pavon und Mustafa Tabet für die gute Zusammenarbeit, physikalischen und nicht-physikalischen Diskussionen sowie Jacobo für die Einladung nach Valencia. Und natürlich Sonia Rani und Aman Sardwal, die anfangs im Rahmen des Internship Grants mit am Molekülprojekt gearbeitet haben und mir außerdem die indische Kultur näher bringen konnten.

Ganz wichtig ist natürlich das Arbeitsumfeld. Hierfür möchte ich allen Mitgliedern des TTP danken für die angenehme Atmosphäre und die vielen interessanten Gespräche, insbesondere meinen Bürokollegen im Raum 12/19 Daniel Baranowski, Marco Bonetti und Marvin Gerlach und denen in 11/04, die ich nur deshalb nicht namentlich aufzähle, damit ich niemanden vergesse. Des Weiteren gilt mein Dank allen Admins, dass ihr die Computerinfrastruktur und insbesondere den Cluster stets am Laufen gehalten habt.

Wen man auch nicht vergessen sollte, sind die Sekretärinnen: Hier bedanke ich mich bei Martina Schorn, Barbara Lepold, Isabelle Junge und Zahra Donyai, dass ihr/Sie den Verwaltungsaufwand im Hinter-

grund für mich abgefangen habt und bei Problemen stets eine Antwort wusstet.

Ebenso möchte ich mich bei KSETA und dem SFB TRR 257 für die Finanzierung meiner Doktorandenstelle und auch der nun anschließenden dreimonatigen Postdocstelle danken sowie dem Graduiertenkolleg GRK1694, insbesondere für die Finanzierung einiger meiner Dienstreisen. Ebenso danke ich stellvertretend für KSETA Irmgard Langbein als Geschäftsführerin für die vielen Angebote, die man als Doktorand geboten bekommt.

Zu guter Letzt möchte ich meinen Eltern danken, dass ihr mir diesen Weg ermöglicht habt und mich immer dabei unterstützt habt. Danke!

COLOPHON

Figure 9.1 has been drawn using Inkscape, while all other figures were typeset in TikZ. All Feynman diagrams are drawn using the L^AT_EX package {TikZ-Feynman}. All plots have been exported from Matplotlib to pgfplots using the Python package tikzplotlib.

This document was typeset using the typographical look-and-feel classicthesis developed by André Miede and Ivo Pletikosić. The style was inspired by Robert Bringhurst's seminal book on typography "*The Elements of Typographic Style*". classicthesis is available for both L^AT_EX and L^YX:

<https://bitbucket.org/amiede/classicthesis/>

Matthias Linster: *Phenomenology of Light Particles on Earth and in the Sky*, © 28. November 2021